X-RAY SCATTERING TECHNIQUES FOR COHERENT IMAGING IN REFLECTION GEOMETRY, MEASUREMENT OF MUTUAL INTENSITY, AND SYMMETRY DETERMINATION IN DISORDERED MATERIALS

by

DANIEL H. PARKS

A DISSERTATION

Presented to the Department of Physics
and the Graduate School of the University of Oregon
in partial fulfillment of the requirements
for the degree of
Doctor of Philosophy

June 2013

DISSERTATION APPROVAL PAGE

Student: Daniel H. Parks

Title: X-ray Scattering Techniques for Coherent Imaging in Reflection Geometry, Measurement of Mutual Intensity, and Symmetry Determination in Disordered Materials

This dissertation has been accepted and approved in partial fulfillment of the requirements for the Doctor of Philosophy degree in the Department of Physics by:

Michael Raymer	Chair
Stephen Kevan	Advisor
Stephen Gregory	Member
George Nazin	Outside Member

and

Kimberly Andrews Espy	Vice President for Research & Innovation/ Dean of the Graduate School

Original approval signatures are on file with the University of Oregon Graduate School.

Degree awarded June 2013

© 2013 Daniel H. Parks

DISSERTATION ABSTRACT

Daniel H. Parks

Doctor of Philosophy

Department of Physics

June 2013

Title: X-ray Scattering Techniques for Coherent Imaging in Reflection Geometry, Measurement of Mutual Intensity, and Symmetry Determination in Disordered Materials

The advent of highly-coherent x-ray light sources, such as those now available world-wide in modern third-generation synchrotrons and increasingly available in free-electron lasers, is driving the need for improved analytical and experimental techniques which exploit the coherency of the generated light. As the light illuminating a sample approaches full coherence, a simple Fourier transform describes the diffraction pattern generated by the scattered light in the far field; because the Fourier transform of an object is unique, coherent scattering can directly probe local structure in the scattering object instead of bulk properties.

In this dissertation, we exploit the coherence of Advanced Light Source beamline 12.0.2 to build three types of novel coherent scattering microscopes. First, we extend the techniques of coherent diffractive imaging and Fourier transform holography, which uses iterative computational methods to invert oversampled coherent speckle patterns, into reflection geometry. This proof-of-principle experiment demonstrates a method by which reflection Bragg peaks, such as those from the orbitally-ordered phase of complex metal oxides, might eventually be imaged. Second, we apply a similar imaging method to the x-ray beam itself

to directly image the mutual coherence function with only a single diffraction pattern. This technique supersedes the double-slit experiments commonly seen in the scattering literature to measure the mutual intensity function by using a set of apertures which effectively contains all possible double slit geometries. Third, we show how to evaluate the speckle patterns taken from a labyrinthine domain pattern for "hidden" rotational symmetries. For this measurement, we modify the iterative algorithms used to invert speckle patterns to generate a large number of domain configurations with the same incoherent scattering profile as the candidate pattern and then use these simulations as the basis for a statistical inference of the degree of ordering in the domain configuration. We propose extending this measurement to position-resolved speckle patterns, creating a symmetry-sensitive microscope. The three new techniques described herein may be employed at current and future light sources.

CURRICULUM VITAE

NAME OF AUTHOR: Daniel H. Parks

GRADUATE AND UNDERGRADUATE SCHOOLS ATTENDED:

University of Oregon, Eugene, OR
Whitman College, Walla Walla, WA

DEGREES AWARDED:

Doctor of Philosophy in Physics, 2013, University of Oregon
Bachelor of Arts in Physics, 2005, Whitman College

AREAS OF SPECIAL INTEREST:

Coherent x-ray scattering, Fourier optics, correlated electron physics, magnetic thin films, GPU computing

PROFESSIONAL EXPERIENCE:

Graduate Research Assistant 2006-2013

Advanced Light Source Doctoral Fellow 2010-2012

Graduate Teaching Fellow 2005-2006

GRANTS, AWARDS AND HONORS:

Advanced Light Source Doctoral Fellow

Phi Beta Kappa, 2005

PUBLICATIONS:

R. Su, K. A. Seu, D. Parks, J. J. Kan, E. E. Fullerton, S. Roy, and S. D. Kevan, "Emergent rotational symmetries in disordered magnetic domain patterns," *Phys. Rev. Lett.*, vol. 107, p. 257204, 2011.

J. J. Turner, X. Huang, O. Krupin, K. A. Seu, D. Parks, S. Kevan, E. Lima, K. Kisslinger, I. McNulty, R. Gambino, S. Mangin, S. Roy, and P. Fischer, "X-ray diffraction microscopy of magnetic structures," *Phys. Rev. Lett.*, vol. 107, p. 033904, Jul 2011.

S. Roy, D. Parks, K. A. Seu, R. Su, J. J. Turner, W. Chao, E. H. Anderson, S. Cabrini, and S. D. Kevan, "Lensless x-ray imaging in reflection geometry," *Nat. Phot.*, vol. 5, pp. 243–245, 04 2011.

K. A. Seu, S. Roy, R. Su, D. H. Parks, E. Shipton, E. E. Fullerton, and S. D. Kevan, "Momentum transfer resolved memory in a magnetic system with perpendicular anisotropy," *Applied Physics Letters*, vol. 98, no. 12, p. 122505, 2011.

K. A. Seu, R. Su, S. Roy, D. Parks, E. Shipton, E. E. Fullerton, and S. D. Kevan, "Microscopic return point memory in co/pd multilayer films," *New Journal of Physics*, vol. 12, no. 3, p. 035009, 2010.

D. K. Hore, D. K. Beaman, D. H. Parks, and G. L. Richmond, "Whole-molecule approach for determining orientation at isotropic surfaces by nonlinear vibrational spectroscopy," *The Journal of Physical Chemistry B*, vol. 109, no. 35, pp. 16846–16851, 2005.

ACKNOWLEDGEMENTS

Scientific research relies on the collaboration on many participants, not any one person working alone. In the course of conducting the experiments described in this dissertation, I have been grateful for the assistance and advice of both members of our research group as well as external collaborators.

I am first most grateful for the advice and guidance of Professor Kevan, who allowed me a long leash to follow my nose in a series of very challenging experiments.

At the Advanced Light Source, I have worked closely with beamline scientist Sujoy Roy who has been a strong advocate in developing the reflection imaging technique described in Chapter IV, with post-doctoral researcher Keoki Seu, whose savant-like ability to understand and operate the complex synchrotron beamline was a great help during many late-night experiments, and with fellow graduate student Run Su, who assisted during long periods of beam time. Former group member Josh Turner, with whom I overlapped at the beginning of my tenure at the beamline, helped in getting my feet wet with beamline techniques and speckle metrology.

At the Center for X-Ray Optics, the nano-fabrication skills of collaborators Weilun Chao and Eric Anderson were invaluable in manufacturing the test-pattern imaged in Chapter IV and the apertures used to measure the beamline coherence function in Chapter V, as well as in fabricating the pinholes we used to establish a coherent beam in many other experiments.

At the Molecular Foundry, Stefano Cabrini manufactured the set of Fourier-transform holography apertures we still use today and was extremely helpful in

fabricating other apertures which pressed the focused-ion beam technique to its limits.

Professor Eric Fullerton at the University of California San Diego and his students Eric Shipton and Jimmy Kan grew the magnetic multilayer samples whose speckle patterns provided the impetus for the investigation of rotational symmetries in Chapter VII.

The strong coupling between coherent scattering and Fourier transforms has meant that analysis of experimental data has often been highly computational and in fact required custom analytical algorithms. For help and collaboration in coding I am grateful to Keoki Seu, with whom I co-wrote the *speckle* analytical library as a foundation for future on-line analysis of coherence experiments at beamline 12.0.2 and its planned successor.

The *speckle* analysis library used in this dissertation is based on several open-source software packages which should be acknowledged, primarily the *numpy* and *scipy* Python libraries for numerical calculuations, *matplotlib* for plotting, and *pyopencl* and *pyfft* for Python access to GPU computation.

TABLE OF CONTENTS

LIST OF FIGURES

Figure Page

Figure Page

LIST OF TABLES

Table Page

CHAPTER I

INTRODUCTION AND OUTLINE

The classical wave nature of light as evidenced by its ability to diffract and form interference patterns was conclusively demonstrated long ago, by Young in 1807 [1] and soon thereafter by Arago's confirmation of Fresnel's spot [2]. While these and other discoveries laid the groundwork for the development of modern optical theory, the diffraction of light as a tool for investigations in material science was strongly constrained by the lack of bright point sources to those applications, such as crystallography, which did not require tremendous transverse coherence. With the revolution of the visible-light lasers in 1960 [3–5] and the consequent high temporal and spatial coherence they provided, theories of coherent diffraction and speckle [6] took on new urgency. However, at x-ray energies the extremely limited coherence available at first- and second-generation synchrotron light sources made the resulting weakly visible interference effects a nuisance rather than a resource.

Today, with high brightness and moderately coherent x-rays available from undulators at third-generation synchrotrons such as the Advanced Light Source at Lawrence Berkeley National Laboratory and the promise of fully-coherent x-rays in the near future from free-electron lasers, the synchrotron community is dedicating enormous effort to develop and implement techniques which exploit the ability of coherent diffraction not to probe just bulk structure, as in crystallography, but to image materials at nanometer resolution with chemical sensitivity.

In this dissertation we describe three experiments using coherent x-rays in novel forms of microscopy. First, we demonstrate lensless imaging techniques in a reflection geometry, opening the door to imaging of a wealth of systems

such as the electronic ordering phases in complex transition metal oxides. Second, we demonstrate the use of holographic techniques to directly image the coherence function of the x-ray beam. Third, we combine numerical modeling and simulation with innovative speckle metrology to evaluate the presence of apparent "hidden" rotational symmetries in speckle pattern of a magnetic thin film sample; coupled with position-resolved measurement, this would constitute a "symmetry microscope" for nominally disordered materials.

We organize this dissertation as follows.

In Chapter II, we consider the fundamental background of coherent diffraction at synchrotron light sources. This includes: fundamental results from scalar diffraction theory (including the Kirchoff diffraction integral, the near-field Fresnel approximation, the far-field Fraunhofer approximation, fast methods of calculating diffraction patterns, and the role of partial coherence in the far-field intensity), and the beamline and experimental endstation apparatus used in these experiments. Because one of the experiments discussed in this dissertation involves scattering from magnetic thin-film samples, we also briefly review the basics of resonant magnetic diffraction.

In Chapter III, we consider the theoretical background specific to the inversion of speckle patterns by finding numerical solutions to the phase problem. We review a variety of iterative algorithms which can successfully invert suitable diffraction patterns and discuss the conditions necessary to form an invertible diffraction pattern. We then conduct several simulations to demonstrate the performance of the iterative phasing algorithms and how the phase retrieval transfer function estimates the resolution of a reconstructed image. We conclude by reviewing an alternative solution to the phase problem, Fourier transform

holography, and consider how it overlaps with the other iterative methods in the case of non-ideal reference waves.

In Chapter IV, we apply the techniques of Chapter III to reflection geometry, imaging a known test sample through a highly novel method which has applicability to a variety of interesting condensed matter samples. In this chapter we discuss the factors behind our choice of geometry and apertures; how best to mount the sample to maximize recovered image fidelity, the collection and conditioning of a high-quality diffraction pattern, and the reconstruction of the wavefield leaving the sample. We also dedicate considerable length to understanding exactly how all the experimental parameters contribute to the achievable resolution in the final recovered image.

In Chapter V, we apply the holographic techniques introduced in Chapter III to the imaging the x-ray beam's degree of coherence, a second order property of the electric field. We show how to fabricate a set of holographic apertures which function as a continuous set Young's double-slits to measure the degree of correlation between all possible separation vectors simultaneously. From an initial experiment, we recover an estimate of the coherence factor along both principal axes, and discuss how future improvements could eliminate the effect of the direct synchrotron beam bleeding through the apertures, which we did not consider in the initial design of the experiment.

In Chapter VI, we adopt the iterative algorithms introduced in Chapter III and used in Chapter IV to the simulation of labyrinthine magnetic domains in thin films with perpendicular magnetic anisotropy. With the domain generator algorithm we aim to produce domain configurations belonging to the class of

solutions described by an arbitrary incoherent scattering lineshape. We discuss at length gory and tedious algorithmic details.

In Chapter VII, we use the domain generator developed in Chapter VI to interpret the presence of a possible "hidden" angular symmetry in a speckle pattern taken from a magnetic thin-film sample. Due to the ability to find similar candidate symmetries in the speckle patterns generated from random numbers, we endeavor to answer two basic questions about the experimental candidate: what would such a symmetry look like in the real space domain configuration, and how can we determine whether any particular candidate symmetry reflects an ordering mechanism in the sample or a random fluctuation in the speckle pattern?

In Chapter VIII, we summarize the research and provide an outlook to future research in these areas.

CHAPTER II

BACKGROUND

In this chapter we review the fundamental background behind the three experiments described in the later chapters of this dissertation. As all of three experiments operate within the domain of coherent x-ray scattering, we first derive several key results in coherent scalar diffraction theory, show how both near- and far-field diffraction patterns may be rapidly calculated with numerical methods, and consider the effect of partial coherence on the far-field intensity pattern. Next, we briefly discuss resonant magnetic scattering, and how this can be modeled realistically as a coherent scattering process; coherent magnetic resonant scattering is a key component in the final chapter of the dissertation. Finally, we review the basic physics of x-ray radiation as produced by an undulator source such as those at the Advanced Light Source, and discuss specifically how this radiation is delivered through ALS beamline 12.0.2 to the 12.0.0.2 experimental endstation. The chapter concludes with a section on the capabilities of the scattering endstation used in these experiments.

2.1. Scalar Diffraction Theory

As the experiments in this dissertation were all conducted at beamline 12.0.2 of the Advanced Light Source and beamline 12.0.2 is a coherent scattering beamlne, in this section we will derive some useful results in coherent scalar diffraction theory. From the scalar wave equation and Green's Theorem, we will find the exact Kirchoff diffraction integral. We will then consider two limiting forms of the integral applicable to the near- and far-fields. This treatment mainly follows

that of Goodman [7], although there are many excellent resources on the history and development of this theory [8–12]. For simplicity, we do not consider the full vectoral nature of the electric and magnetic fields which arises under inclusion of field polarization.

2.1.1. The Kirchoff Diffraction Integral

Many advanced treatments of scalar diffraction theory derive the exact Kirchoff diffraction integral. The standard derivation proceeds along the following steps. First, from Maxwell's equations, they show an optical disturbance in the monochromatic limit follows the Helmholtz equation. Combined with Green's theorem, the Helmholtz equation permit several choices of Green's functions for the optical disturbance in the forms of expanding spherical waves. In physically realistic diffraction situations, such as the diffraction of light through an aperture in an opaque screen, the expanding waves fall off in intensity sufficiently quickly that we may treat them as outgoing and consider only the waves passing through the aperture as contributing to the electric field at a point past the aperture. The integral in Green's theorem then reduces to the well-known Kirchoff diffraction integral:

$$U(x,y) = \frac{1}{i\lambda}\iint_{aperture} U(u,v)\frac{\exp(ikr)}{r}\cos(\theta)\,ds \qquad \text{(Equation 2.1.)}$$

where λ is the wavelength of the monochromatic wave, $U(u,v)$ is the value of the wavefield within the (u,v) source plane, $U(x,y)$ is the value of the wavefield in the (x,y) observation plane, and r and θ are the distance and angle between any given pair of points (u,v) and (x,y). We illustrate this geometry in Figure 2.1..

In addition to its mathematical rigor, Equation 2.1. expresses the Huygens-Fresnel principle by stating that the diffracted field at some point behind the aperture may be expressed by treating each point in the aperture as the source of an expanding spherical wave which then adds in superposition. In fact, up to the cosine term and the prefactor, we could write down Equation 2.1. directly from the Huygens-Fresnel principle. That cosine term is sometimes referred to as the obliquity factor, which changes somewhat depending on the particular choice of Green's function used in the derivation of Equation 2.1.. Different choices of G and thereby different obliquity factors lead to nearly identical results in the far field but may show small differences very close to the aperture [13], ultimately due to differences in the treatment of the complicated fringing fields near the rim of the aperture.

We reproduce the full derivation of Equation 2.1. as described above in Appendix A.

2.1.2. Fresnel and Fraunhofer Approximations

While accurate, the Kirchoff integral presents serious difficulties in terms of calculation. As the integral generally permits no analytic solutions, we must employ numerical techniques. Each point in the observation plane requires an independent two-dimensional integral over the source plane, as both the distance r_{01} and the obliquity factor change for each point. Consequently, direct numerical evaluation of the integral runs in very slow $O(N^2)$ time, where N is the total number of pixels in the discretized source plane. However, as the distance between the source plane and the observation plane becomes significantly larger than the size of the aperture, fast approximations to the integral become available.

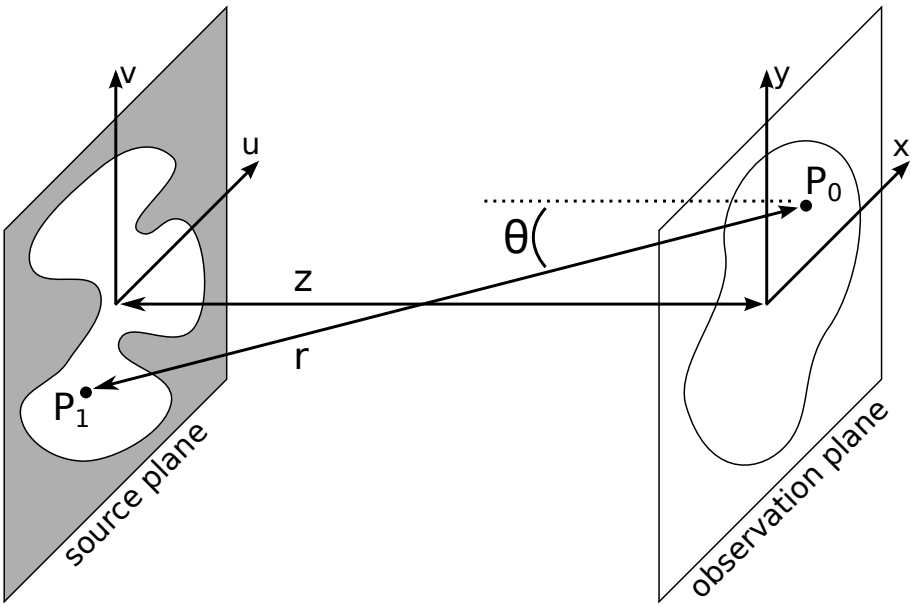

FIGURE 2.1.. Coordinates and planes for the Kirchoff, Fresnel, and Fraunhofer diffraction integrals.

2.1.2.1. The Fresnel Approximation

We define the coordinates used the upcoming approximations in Figure 2.1.. In the source plane with the aperture, we index points with cartesian coordinates (u, v). In the observation plane where we measure the diffraction pattern, we index points with cartesian coordinates (x, y). Some distance z separates the two planes. For ease of notation, we replace $\cos\theta = z/r$, making the diffraction integral:

$$U(x,y) = \frac{z}{i\lambda}\iint_{source} U(u,v)\frac{\exp(ikr)}{r^2}\,du\,dv \qquad \text{(Equation 2.2.)}$$

To simplify Equation 2.2. we make approximations to the distance r. First, we write the exact form of r in terms of the plane coordinates:

$$\begin{aligned} r &= \sqrt{(x-u)^2 + (y-v)^2 + z^2} \\ &= z\sqrt{1 + \left(\frac{x-u}{z}\right)^2 + \left(\frac{y-v}{z}\right)^2} \end{aligned}$$

As z increases, $r \to z$. In the Fresnel approximation, we first expand r as a Taylor series:

$$r = z\left[1 + \frac{1}{2}\left(\left(\frac{x-u}{z}\right)^2 + \left(\frac{y-v}{z}\right)^2\right) - \frac{1}{8}\left(\left(\frac{x-u}{z}\right)^2 + \left(\frac{y-v}{z}\right)^2\right)^2 + ...\right] \qquad \text{(Equation 2.3.)}$$

In Equation 2.2., r occurs in two places. For the polynomial r in the denominator, we must keep only the first-order of Equation 2.3., particularly when the aperture size much smaller than the propagation distance. For the r in the exponential, the high susceptibility of the complex exponential to errors in the distance approximation requires us to keep to second order. After factoring out a constant phase factor, the approximations to r give the Fresnel integral

$$U(x,y) \approx \frac{e^{ikz}}{iz\lambda}\iint_{source} U(u,v)\exp\left[\frac{ik}{2z}\left((x-u)^2 + (y-v)^2\right)\right] \qquad \text{(Equation 2.4.)}$$

Equation 2.4. is generally accurate for separation distances z greater than the size of the aperture. We will discuss a numerical method for rapidly evaluating Equation 2.4. in a later section.

2.1.2.2. The Fraunhofer Approximation

In the case when z becomes very large with respect to the size of the aperture, a further approximation becomes available. Expanding the phase factor in Equation 2.4., we write:

$$e^{\frac{ik}{2z}\left((x-u)^2+(y-v)^2\right)} = e^{\frac{ik}{2z}(x^2+y^2)} \times e^{\frac{ik}{2z}(u^2+v^2)} \times e^{\frac{-ik}{z}(xu+yv)}$$

Assuming $z \gg k(u^2+v^2)$, the middle term on the right hand side has no effect on the integrand. The left-most term has no variables of integration and may be pulled into the pre-factor of the integral. This leaves only the last term:

$$U(x,y) = \frac{e^{ikz}e^{ik(x^2+y^2)/2z}}{iz\lambda} \iint_{source} U(u,v) \exp\left[-\frac{ik}{2z}(xu+yv)\right] du\, dv \qquad \text{(Equation 2.5.)}$$

So for very large separation z, the wavefield at the observation plane is proportional to the Fourier transform of the wavefield passing through the aperture in the source plane.

The region of applicability for this approximation may be further clarified. Returning to the assumption which eliminated part of the phase factor, we define the Fresnel number N_f as

$$N_f = \frac{r^2}{z\lambda} \qquad \text{(Equation 2.6.)}$$

where r is now the characteristic size of the aperture (for a circular aperture, its radius). Generally, the Fresnel regime is considered those combinations of r, z, λ for which $N_f \geq 1$. The Fraunhofer regime is considered $N_f \ll 1$.

The reduction of the diffraction integral to a single Fourier transform is a tremendous result in optics due to the vast base of knowledge surrounding

the Fourier transform. In addition to the known analytic Fourier transforms, there exist fast numerical algorithms to calculate the Fourier transform of an arbitrary function in $O(N \log N)$ time instead of $O(N^2)$ [14–16]. Most scientific and numerical programming packages include Fast Fourier transform (FFT) algorithms, and the highly parallel nature of the algorithm presents a nearly-ideal use case for GPU computation [17].

2.1.3. Detection

At x-ray wavelengths, current detector technology cannot measure the full complex wavefield found in the far field. This results from averaging over many cycles of the wavefield in order to form an estimate of its amplitude. In fact, any sort of detector will respond not to the electric field, but the intensity at a point in space, given by:

$$\begin{aligned} I(x,y) &= \langle U(x,y,t)U^*(x,y,t)\rangle \\ &= |U(x,y)|^2 \end{aligned} \qquad \text{(Equation 2.7.)}$$

We therefore lose information about the phase of the electric field. In crystallography, this was originally referred to as "the phase problem." We will return to its importance in discussing coherent imaging techniques.

2.2. Near-field Propagation

In the experiments described in this dissertation, we will propagate coherent wavefields in the near-field regime. In contrast to far-field Fraunhofer diffraction where we find asymptotically exact solutions by fast numerical implementations of

the Fourier transform, near-field diffraction patterns resist simple calculation. Any attempt to calculate the near field diffraction pattern must reinsert the quadratic phase factor which we dropped in making the Fraunhofer approximation. This term creates the difficulty in finding analytic solutions to the integral. Direct numerical calculations of the Fresnel integral are prohibitively expensive and efficient FFT-based methods are highly desirable. Here, we review a common FFT-based algorithm for near-field coherent wave propagation and summarize its strengths, weaknesses, and zone of applicability. The treatment of this section primarily follows Mas [18]; the same information can also be found in many sources dealing with coherent optics [7, 8]

2.2.1. Discretization of the Integral

To use FFT methods we must first discretize the integral. Assuming the array over which the function is being evaluated is $N \times N$ pixels in size, we define the following discrete variables:

$$u = n\delta_0, \quad v = m\delta_0$$
$$x = a\delta_z, \quad y = b\delta_z$$

Here, δ_0 and δ_z describe the size of a pixel in the source plane and observation plane, respectively. The pixel indices n and m run between 0 and $N-1$. The size in pixels of the propagated array is the same size as the source array. After discretization, Equation 2.2. becomes:

$$U(a\delta_z, b\delta_z) = \frac{e^{ikz} e^{\frac{ik}{2z}(a^2+b^2)\delta_z}}{i\lambda z} \sum_{n=0}^{N-1} \sum_{m=0}^{N-1} U(n\delta_0, m\delta_0)\, e^{\frac{i\pi}{\lambda z}\left(n^2+m^2\right)\delta_0^2} e^{\frac{-2i\pi}{\lambda z}(na+mb)\delta_0\delta_z}$$

(Equation 2.8.)

The canonical form of the discrete fourier transform (DFT) of a series of sampled data x_n is [19]:

$$F(k) = \sum_{n=0}^{N-1} x_n e^{-2\pi ikn/N} \qquad \text{(Equation 2.9.)}$$

Matching Equation 2.8. and Equation 2.9. requires the following equality:

$$\delta_z = \frac{\lambda z}{N\delta_0} \qquad \text{(Equation 2.10.)}$$

So by discretizing the integral it initially seems we must accept a change in pixel size according to Equation 2.10..

Often, convenient evaluation of the discrete Fourier sum involves shifting the indices n and m from the range $(0, N-1)$ to $(-N/2, N/2-1)$. This change of variables allows the visual center of the array to be the coordinate origin, and more accurately reflects the behavior of the fourier transform in decomposing signals into both positive and negative frequencies.

2.2.2. Fresnel Integral as Convolution

For reasons relating to the accuracy of the phase component [18], we avoid direct calculation of the Fresnel integral and instead use the convolution theorem. Given two functions $f(u), g(u)$, their convolution $\{f * g\}$ is given by

$$\{f * g\}(x) = \int f(u)g(x-u)du \qquad \text{(Equation 2.11.)}$$

Using Equation 2.11., we rewrite Fresnel integral in Equation 2.4. as:

$$U(x,y,z) = U(x,y,0) * H(x,y,z) \qquad \text{(Equation 2.12.)}$$
$$H(x,y,z) = \frac{e^{ikz}}{i\lambda z} e^{\frac{ik}{2z}\left(x^2+y^2\right)}$$

$H(x,y,z)$ is called the Fresnel propagator. The convolution theorem allows Equation 2.12. to be calculated via Fourier transforms as

$$U(x,y,z) = \mathscr{F}^{-1}\left\{\mathscr{F}\left\{U(x,y,0)\right\}\mathscr{F}\left\{H(x,y,z)\right\}\right\} \qquad \text{(Equation 2.13.)}$$

We can analytically solve the Fourier transform of the propagator $H(x,y,z)$, which greatly speeds up the calculation.

$$\begin{aligned}
\mathscr{F}\{H(x,y,z)\}(f_x,f_y) &= \frac{e^{ikz}}{i\lambda z}\iint_{-\infty}^{\infty} e^{\frac{i\pi}{\lambda z}(x^2+y^2)} e^{-2i\pi(xf_x+yf_y)}\,dx\,dy \\
&= \frac{e^{ikz}}{i\lambda z}\iint_{-\infty}^{\infty} \exp\left[\frac{i\pi}{\lambda z}\left(x^2 - 2xf_x\lambda z + y^2 - 2yf_y\lambda z\right)\right]\,dx\,dy \\
&= \frac{e^{ikz}}{i\lambda z}\iint_{-\infty}^{\infty} \exp\left[\frac{i\pi}{\lambda z}\left((x-f\lambda z)^2 + (y-f\lambda z)^2 - \lambda^2 z^2(f_x^2+f_y^2)\right)\right]\,dx\,dy \\
&= \exp\left[-i\pi\lambda z\left(f_x^2+f_y^2\right)\right]\frac{e^{ikz}}{i\lambda z}\iint_{-\infty}^{\infty} \exp\left[\frac{i\pi}{\lambda z}\left(x^2+y^2\right)\right]\,dx\,dy \\
&= C\exp\left[-i\pi\lambda z\left(f_x^2+f_y^2\right)\right] \qquad \text{(Equation 2.14.)}
\end{aligned}$$

In Equation 2.14., we have buried both the exponential prefactor and the integral into a multiplicative constant, which we ignore as the conservation of energy determines the overall magnitude of the diffraction pattern and the global phase

is irrelevant. Inserting Equation 2.14. into Equation 2.13. gives

$$U(x,y,z) \propto \mathscr{F}^{-1}\left\{\mathscr{F}\left\{U(x,y,0)\right\}\exp\left[-i\pi\lambda z\left(f_x^2+f_y^2\right)\right]\right\} \qquad \text{(Equation 2.15.)}$$

The scaling factor λz governs the relationship between the coordinates x, y and their conjugate frequencies $f_x = \frac{x}{\lambda z}, f_y = \frac{y}{\lambda z}$. However, the pixels in the observation plane also obey the scaling law expressed in Equation 2.10.. With these relationship and the discrete variables introduced earlier, we discretize Equation 2.15. as

$$E(a\delta_z, b\delta_z) \propto \text{DFT}^{\text{-1}}\left\{\text{DFT}\left\{U(m\delta_0, n\delta_0)\right\}\exp\left(\frac{-i\pi\lambda z}{N^2\delta_0^2}\left(\tilde{m}^2+\tilde{n}^2\right)\right)\right\} \qquad \text{(Equation 2.16.)}$$

where $\tilde{m}, \tilde{n}$ are the coordinate indices in the Fourier domain after applying the first DFT. The near field diffraction pattern can therefore be calculated through a convolution nominally requiring three Fourier transforms. When propagating the same wavefield through a spectrum of distances, we can precompute the Fourier transform of the wavefield and directly evaluate the Fresnel kernel in the far field. Consequently, propagating through a spectrum of N distances requires only $N + 1$ rather than $3N$ Fourier transforms.

2.2.3. Nyquist Limitations on the Region of Applicability

For the numerical evaluation of the integral to remain valid, the phase term in Equation 2.16. must be properly sampled within the Nyquist limit, meaning the argument of the exponential can vary only up to $i\pi$ between any two adjacent points. As only propagation distance z varies, we calculate how large z may become

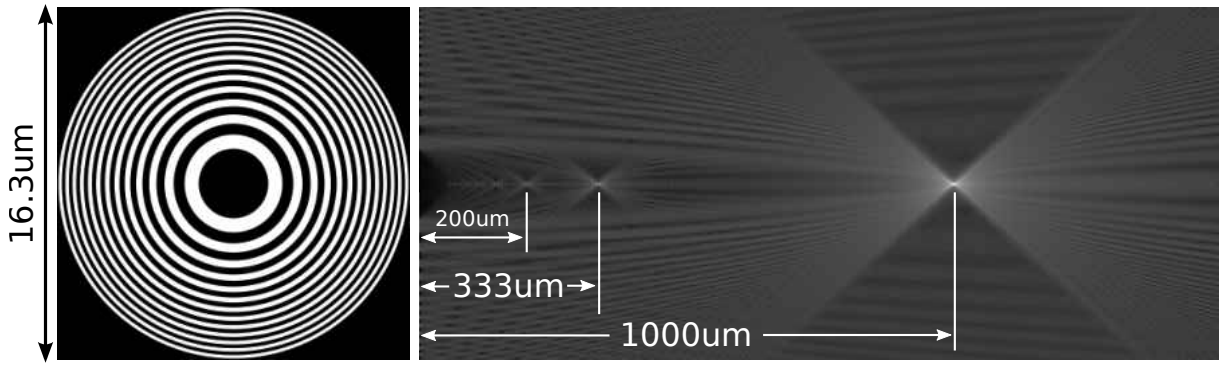

FIGURE 2.2.. Simulation of near-field diffraction from a Fresnel zone plate. At left, a view of the simulated zone plate. At right, slices through the diffraction pattern as a function of distance.

without violating the Nyquist sampling condition at the edge of the array:

$$i\pi \geq \frac{d}{d\tilde{m}} \left[\frac{-i\pi\lambda z}{N^2\delta_0^2} \left(\tilde{m}^2 + \tilde{n}^2 \right) \delta_0^2 \right]_{\tilde{n}=0,\, \tilde{m}=N/2} \qquad \text{(Equation 2.17.)}$$

$$z \leq \frac{N\delta_0^2}{\lambda} \qquad \text{(Equation 2.18.)}$$

This limit applies to both the magnitude and the phase of the propagated wave; above this limit, the propagated wavefield becomes unreliable due to aliasing in the phase factor, and other algorithms must be used to reach the far field.

While Equation 2.10. implies that the pixel size of the propagation increases linearly with z, Equation 2.15. in fact experiences no such stretching. This is because the use of both a forward and inverse DFT to implement the convolution cancels the scale factor which stretched the field of view of the plane propagated through direct evaluation.

2.2.4. Example

We show the near field diffraction patterns from a Fresnel zone-plate in Figure 2.2.. Fresnel zone plates act as diffractive elements to focus the x-rays at

a desired focal distance f from the aperture [12]. The transmittivity in a zone plate with binary transmittivity is given by:

$$T(r) = \frac{1}{2} \pm \frac{1}{2} \operatorname{sgn}\left[\cos\left(\frac{\pi r^2}{\lambda f + \lambda^2/4}\right)\right] \qquad \text{(Equation 2.19.)}$$

The inclusion of $\pm$ allows the central zone to be either opaque or transmissive. Because $\cos(x^2)$ oscillates very rapidly as x increases, we limit the simulation of the zone plate according to the Nyquist condition. In analogy to Equation 2.17. we calculate the maximum radial extent R_0 in pixels of a properly sampled zone plate:

$$\pi \geq \frac{d}{dR}\left[\frac{\pi(\delta_0 R)^2}{\lambda f + \lambda^2/4}\right]_{R=R_0} \qquad \text{(Equation 2.20.)}$$

$$R_0 \leq \frac{\lambda f + \lambda^2/4}{2\delta_0^2} \qquad \text{(Equation 2.21.)}$$

Figure 2.2. shows the binary zone plate described by Equation 2.19. with focal length 1mm at $\lambda = 2.48\mu m$. We have truncated to radial extent $R_0/3$, well short of the Nyquist limit. The magnitude of the near-field diffraction pattern as a function of z from the Nyquist-limited zone plate (not shown) is in the right panel on a log scale. For the parameters used in this simulation, the Nyquist limit for the propagation according to Equation 2.18. is $2064\mu m$. We easily observe not just the primary focal spot at $1000\mu m$ but also odd harmonics $f/3, f/5, f/7$, etc with decreasing power in successive harmonics. The existence of multiple focus points is equivalent to the spectral decomposition of a periodic square wave.

2.3. Partial Coherence

The Kirchoff diffraction integral Equation 2.1., the Fresnel approximation Equation 2.4., the Fraunhofer approximation Equation 2.5., and the detection formula Equation 2.7. assume the ideal case of perfectly coherent illumination. In fact, no wavefield exhibits perfect coherence, and a more accurate treatment of the formation of far-field intensity patterns must include a consideration of the role of imperfect, or partial, coherence. In this section, we briefly discuss the canonical qualitative example of partially coherent diffraction, Young's double slit experiment, then derive a highly useful formula, Schell's Theorem, to describe how a partially coherent far-field intensity pattern is produced from the fully-coherent idealization.

The theory of partially coherent diffraction has been advanced by many researchers, most importantly Wolf [9]. This treatment mainly follows Goodman [7]. Due to the ability of synchrotron beamlines to produce highly monochromatic light, we will derive the desired result under the assumption of only a single frequency of light in the experiment which is referred to as the quasimonochromatic assumption. Elaboration of the theory of partial coherence in the case of pink light may be found in the above cited sources.

2.3.1. Coherence, Qualitatively: Young's Double Slit Experiment

To illustrate the way speckle formation depends on coherence, we qualitatively consider the canonical Young's double-slit experiment shown in Figure 2.3.. In this experiment, monochromatic light of wavelength λ from a distant source is incident from the left on a pair of thin slits s_1 and s_2, from which it diffracts into the far field to form a band of light and dark interference stripes

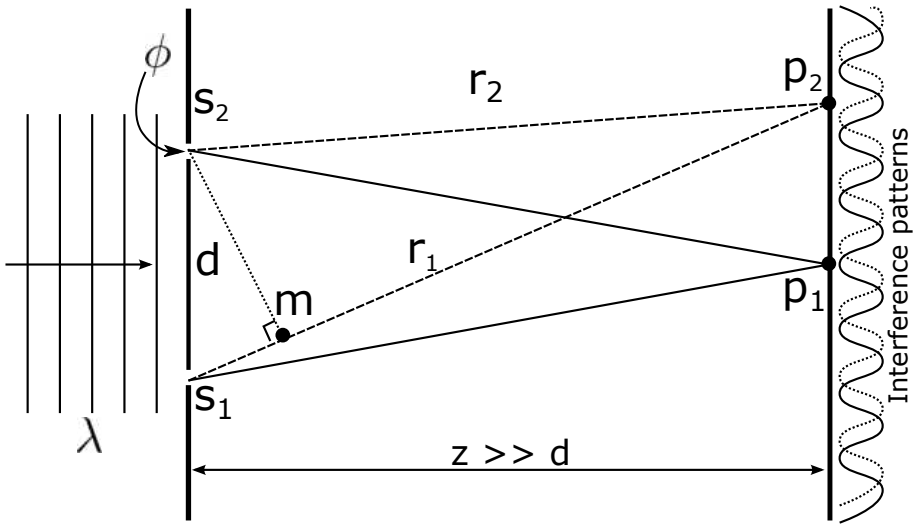

FIGURE 2.3.. Young's double slit experiment illustrates spatial coherence. Light of wavelength λ is incident from left on two slits s_1 and s_2, from which it diffracts into the far field to form a series of interference fringes. Points p_1 and p_2 in this schematic mark an interference maximum and minimum, respectively. The introduction of a constant relative phase shift ϕ into the light passing through s_2 moves the location of the fringes.

on a detector. Examining the solid interference curve, at p_1 the interference is constructive because the path lengths $\overline{s_1 p_2}$ and $\overline{s_2 p_2}$ differ by an even number of wavelengths (the path length difference is $\overline{s_1 m}$); at p_2, the interference is destructive because the path lengths differ by an odd number of wavelengths. However, if the phase of the wave at s_2 is retarded by some amount ϕ, the location of the maxima and minima shift as shown in the dashed interference pattern. When the relative phase between s_1 and s_2 is completely stable, we say that the wavefront is fully coherent. If the phase retardation ϕ varies randomly in time, however, the interference pattern also varies in location. In this case, a suitably long measurement of the intensity averages over all the movement of the pattern and shows reduced fringe contrast. In this latter case of random phase variations across the wavefront, we say that the wavefront is partially coherent.

Such random variations in ϕ may also be understood qualitatively by imagining the point source illuminating the apertures as an extended collection of point sources, all emitting incoherently from the others. Each source generates a wavefront which passes through the slits at some oblique angle, forming an interference pattern at a different location on the far field screen. Summing the interference patterns gives the reduced contrast. Given the time-averaging nature of recording the interference pattern, this view is equivalent to a single source point randomly changing its position relative to the slits and thereby introducing the phase variation ϕ. This geometric interpretation of the experiment grants a limiting relationship for describing when we may consider as fully coherent the illumination over an aperture subtending an angle θ relative to some source with extent d [12]:

$$d\theta = \lambda/2\pi$$

2.3.1.1. Coherence, Quantitatively: Schell's Theorem

We now conduct a more formal analysis of the far-field intensity under partially coherent illumination. First, we define some common terms. The amount of phase correlation between two points of an electric field is given by the so-called mutual coherence function, first introduced by Wolf [20, 21]

$$\Gamma_{12}(\tau) = \langle U_1(t+\tau)U_2^*(t)\rangle \qquad \text{(Equation 2.22.)}$$

where U_1 is the electric field at some point 1, U_2 is the electric field at some point 2, τ is a time delay, and the angle brackets indicate a time average. Because the fields at different points in space can change in magnitude without disrupting

the phase relationship, we often normalize the mutual coherence function by the intensities of the fields to give the complex degree of coherence $\gamma_{12}(\tau)$:

$$\gamma_{12}(\tau) = \frac{\langle U_1(t+\tau)U_2^*(t)\rangle}{\sqrt{\langle|U_1(t)|^2\rangle\,\langle|U_2(t)|^2\rangle}} \qquad \text{(Equation 2.23.)}$$

Although a complex number in general, the magnitude of γ_{12} lies between 0 and 1 by the Cauchy-Schwartz inequality. Assuming quasimonochromatic illumination, we often wish to consider the degree of coherence between two points at $\tau = 0$. This refers only to the retardation between the two points resulting from path length difference, and still requires a time average:

$$J_{12} = \Gamma_{12}(0) = \langle U_1(t)U_2^*(t)\rangle \qquad \text{(Equation 2.24.)}$$

$$\mu_{12} = \gamma_{12}(0) = \frac{\langle U_1(t)U_2^*(t)\rangle}{\sqrt{\langle|U_1(t)|^2\rangle\,\langle|U_2(t)|^2\rangle}} \qquad \text{(Equation 2.25.)}$$

J_{12} is called the mutual intensity and μ_{12} is called the complex coherence factor.

In mathematical treatments of the double slit experiment [7, 10], the visibility of neighboring fringes crucially contains the coherence factor:

$$\mathcal{V} = \frac{2\sqrt{I_1 I_2}}{I_1 + I_2}|\mu_{12}|$$

When careful fabrication makes identical pinholes and careful technique illuminates them equally, this reduces to:

$$\mathcal{V} = |\mu_{12}|; \quad (I_1 = I_2) \qquad \text{(Equation 2.26.)}$$

Equation 2.26. provides a straightforward and widely-used method of measuring the degree of partial coherence. In a traditional experiment of this type, a set of pairs of small, identical pinholes are fabricated with various separation distances, and each pair carefully aligned to maximize interference fringe visibility [22, 23]. However, ensuring each pinhole is equally illuminated so that $I_1 = I_2$ is a tedious task which makes measurements of the coherence low resolution.

Better techniques for measuring the coherence factor rely on a general consideration of the impact of partial coherence on the recorded far-field intensity. Under the assumption that the degree of coherence between any two points in the source plane depends only on the difference of their coordinates $(\Delta u, \Delta v)$, we may produce the partially coherent far-field intensity fully-coherent far-field I_{fc} through a convolution:

$$I_{pc}(x, y) = I_{fc}(x, y) * \mathscr{F}\{\mu(\Delta u, \Delta v)\} \qquad \text{(Equation 2.27.)}$$

We fully derive Equation 2.27., which Goodman refers to as Schell's Theorem, in Appendix A. In terms of the application of Equation 2.27. to the measurement of the degree of coherence, rewriting using the convolution theorem solves for the coherence factor:

$$\mu(\Delta u, \Delta v) = \frac{\mathscr{F}^{-1}\{I_{pc}(x, y)\}}{\mathscr{P}(\Delta u, \Delta v)} \qquad \text{(Equation 2.28.)}$$

where $\mathscr{P}(\Delta u, \Delta v)$ is the autocorrelation of the wavefield leaving the source plane. Consequently, through clever choice of the source apertures, we can easily measure the coherence of the illumination.

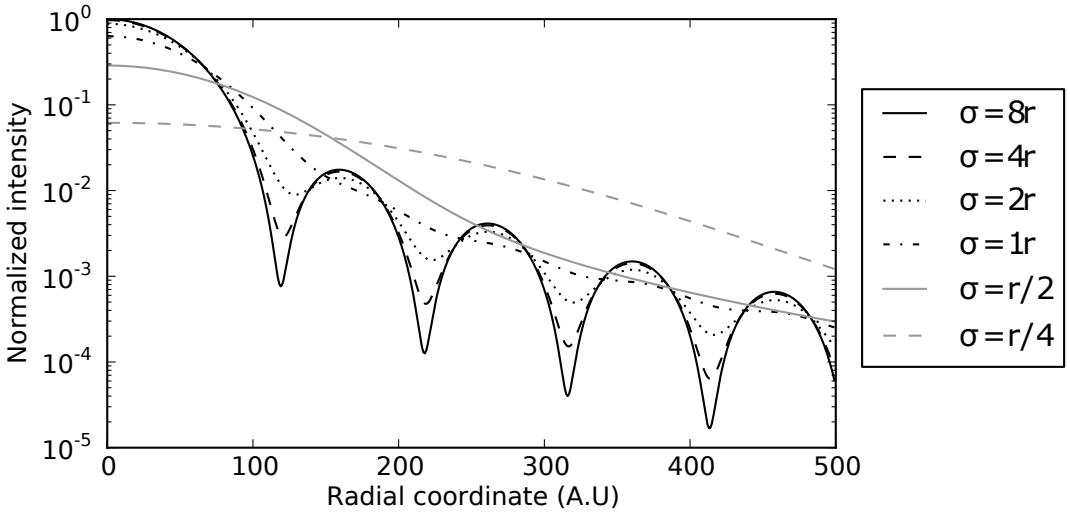

FIGURE 2.4.. Pinhole diffraction with partially coherent illumination; the pinhole radius is r and the coherence function is a gaussian with standard deviation σ.

2.3.2. Example

Figure 2.4. shows the results of simulations using Equation 2.27. to calculate the partially coherent intensity pattern formed from a circular pinhole of radius r. In the fully coherent case, the functional form of the intensity goes as the well-known Airy pattern $\left(J_1(\rho)/\sqrt{\rho}\right)^2$, where J_1 is a Bessel function of the first kind of first order and ρ is the radial coordinate on the detector. The coherence factor $\mu(\Delta u, \Delta v)$ in these simulations is a gaussian with standard deviation σ. By varying σ, we generate diffraction patterns of very high coherence ($\sigma = 8r$), diffraction patterns of very low coherence ($\sigma = r/4$), and diffraction patterns where the degree of coherence takes some intermediate value relative to the size of the aperture. As the coherence decreases, so does the visibility of the Airy fringes until the fringes eventually disappear.

2.4. Resonant Magnetic Scattering

In Chapter VII we will consider resonant scattering from magnetic thin film samples with perpendicular anisotropy. Hannon [24] first gave the proper scattering factors for resonant magnetic scattering in terms of the polarization $\mathbf{e}_n$ of the incoming photons, the polarization $\mathbf{e}'_n$ of the outgoing photons, the magnetization vector $\mathbf{M}$ and various transition matrix elements f_i^j:

$$f^{(n)} = (\mathbf{e}_n \cdot \mathbf{e}'_n) f_c^n + i(\mathbf{e}_n \times \mathbf{e}'_n) \cdot \mathbf{M}^n f_{m_1}^n + (\mathbf{e}_n \cdot \mathbf{M}^n)(\mathbf{e}'_n \cdot \mathbf{M}^n) f_{m_2}^n \quad \text{(Equation 2.29.)}$$

The first term of Equation 2.29. is nonzero only in the case when the polarization of the incoming light is not rotated by the scattering process, as it is for magnetic scattering. For the linear σ polarization on beamline 12.0.2, this term therefore corresponds entirely to charge scattering alone, as indicated by the f_c scattering factor. The second factor gives rise to XMCD in the case of circularly polarized light. However, as we use linear σ light and will be scattering from thin-film samples in which the magnetization is strongly favored to be out of plane ($\mathbf{M} = |M|\hat{k}$), this scattering factor requires that a magnetic signal rotate the outgoing polarization $\mathbf{e}_n$ into π orientation. In ordinary scattering, the matrix element f_c overwhelms the matrix element f_{m_1}. However, the L_3 electronic resonance strongly enhances the magnetic scattering. The third factor, quadratic in $\mathbf{M}$, is much weaker than the other two terms and generally close to zero anyways as $\sigma \cdot \hat{k} = 0$. In other situations away from normal incidence this term gives rise to magnetic linear dichroism.

Because the charge scattering remains on the σ polarization but the magnetic scattering rotates into π polarization, the two scattering signals do not interfere.

Consequently, Equation 2.29. predicts that in the case of linear polarization the charge and magnetic scattering intensities become separable:

$$I = |\mathbf{M}^n f^n_{m_1}|^2 + |f^n_c|^2 \qquad \text{(Equation 2.30.)}$$

To set the groundwork for simulating the scattering pattern, we also consider the scattering process explicitly from the point-of-view of the index of refraction and XMCD. Following the example of Lovesey and Collins [25], we decompose the linearly-polarized incident illumination into equally weighted left- and right-circularly polarized fields labeled $U_+(u,v)$ and $U_-(u,v)$, respectively. The index of refraction seen by each polarization depends on parallel or anti-parallel alignment between the magnetization at a given point in the sample and the angular momentum of the incident field. We model the effect of the magnetization on the index of refraction as a shift Δn in the base index of refraction n_0 that would be observed in the absence of magnetic dichroism. Dichroism here enters as a change in the sign of the shift to the optical constants.

$$\begin{aligned} n_{\uparrow\uparrow} &= n_0 + \Delta n \\ n_{\uparrow\downarrow} &= n_0 - \Delta n \\ n_0 &= 1 - \delta + i\beta \\ \Delta n &= -\Delta\delta + i\Delta\beta \end{aligned}$$

For simplicity, we express the shift in δ and β as a simple scalar multiplication:

$$n_{\uparrow\uparrow} = 1 - (1 + \Delta)\delta + i(1 + \Delta)\beta$$
$$n_{\uparrow\downarrow} = 1 - (1 - \Delta)\delta + i(1 - \Delta)\beta$$

Parallel and anti-parallel alignments of the spins relative to the propagation direction of the beam have value ± 1. Labeling the magnetization as a function of position $m(u, v)$, the index of refraction as a function of polarization and position becomes:

$$n_+(u, v) = 1 + (1 + \Delta \times m(u, v))\,\delta - i(1 + \Delta \times m(u, v))\beta \qquad \text{(Equation 2.31.)}$$
$$n_-(u, v) = 1 + (1 - \Delta \times m(u, v))\delta - i(1 - \Delta \times m(u, v))\beta \qquad \text{(Equation 2.32.)}$$

In the Born approximation, the relationship between the field incident on the sample and the field leaving the sample is given by:

$$U_{out}(u, v) = U_{in}(u, v) \exp\left[ikt(u, v)n(u, v)\right] \qquad \text{(Equation 2.33.)}$$

where k is the usual wavevector $2\pi/\lambda$, $t(u, v)$ is the thickness of the sample, and $n(u, v)$ is the index of refraction. We will use thin samples of approximately constant thickness t where we assume the Born approximation holds. Due to the orthogonality of the left- and right-circular polarizations, the incoherent sum of the

intensity of each polarization gives the total far-field intensity [7]:

$$I(x,y) = |\mathscr{F}\{U_+(u,v)\}|^2 + |\mathscr{F}\{U_-(u,v)\}|^2 \qquad \text{(Equation 2.34.)}$$

$$U_+(u,v) \propto U_{in}(u,v)\exp[iktn_+(u,v)]$$

$$U_-(u,v) \propto U_{in}(u,v)\exp[iktn_-(u,v)]$$

Finally, by setting $m(u,v)$ to a constant across space, we can simulate the effect of saturating the sample to record just the charge-scattering component of the signal in the absence of magnetic contrast. Generally speaking, the lack of charge ordering in the sample which could cause additional modulation in the illumination makes the saturation image just the Fourier transform of the aperture.

2.5. Beamline and Endstation

In this section we take a virtual tour of beamline 12.0.2 at the Advanced Light Source in Berkeley, CA. The beamline was originally constructed by the Center for X-Ray Optics at Lawrence Berkeley National Laboratory in 2002 as a demonstration instrument for coherent scattering at soft x-ray wavelengths. The beamline has two branches; branch 12.0.2.1 was used to test optical elements and filters for coherent scattering, and branch 12.0.2.2 was designed for coherent scattering from magnetic and complex-oxide systems. In this dissertation, we describe results from the 12.0.2.2 branch only. For some discussion of the design considerations in the scattering branch, see Chesnel [26].

The x-ray radiation used on this beamline is produced by a 55-period undulator insertion device. Like all undulator sources, the emitted beamline displays high brightness due to its low divergence. As the undulator functions as

essentially a "black box" source of radiation which we do not alter except for the undulator gap to tune the energy, we do not review undulator physics here. We do, however, present some fundamental undulator results in Appendix A. Attwood [12] provides a good introduction to undulator radiation specifically and synchrotron radiation more generally.

2.5.1. Beamline Elements

In Figure 2.5.(a), we show a rough cartoon schematic of the beamline. The first element of the beamline is a $N = 55$, $\lambda_u = 8.0cm$ undulator. X-rays emitted from the sector 12 undulator first impinge upon a water-cooled four-jaw aperture, which functions to accept only the central cone of the undulator beam. This aperture is set by hand. Following the four-jaw, a retractable, planar, gold-coated mirror M_0 deflects the beam between the 12.0.2 branches and the 12.0.1 branch. The planar design of the mirror allows deflection without disrupting the focus of the beam. A secondary role of M_0 is attenuating high harmonics of the undulator beam. These elements do not appear in Fig. 2.5.(b)

Downstream of M_0 comes the monochromator assembly, consisting of the iridium spherical focusing mirror M_2 [27], a varied line-space grating, and a set of adjustable exit slits. In Fig. 2.5.(b), M_2 is the box marked A, and the grating and slits are found in the box marked B. M_2 focuses the beam on the grating, from which the beam diffracts similarly to optical light through a prism. By adjusting the width of the exit slit, we define narrow acceptance angle and therefore allow to pass a narrow range of wavelength. By rotating the grating, we can select different wavelengths without disrupting the focus of the beam (cite someone). The grating was designed as a collaboration between CXRO and Hitachi, and is

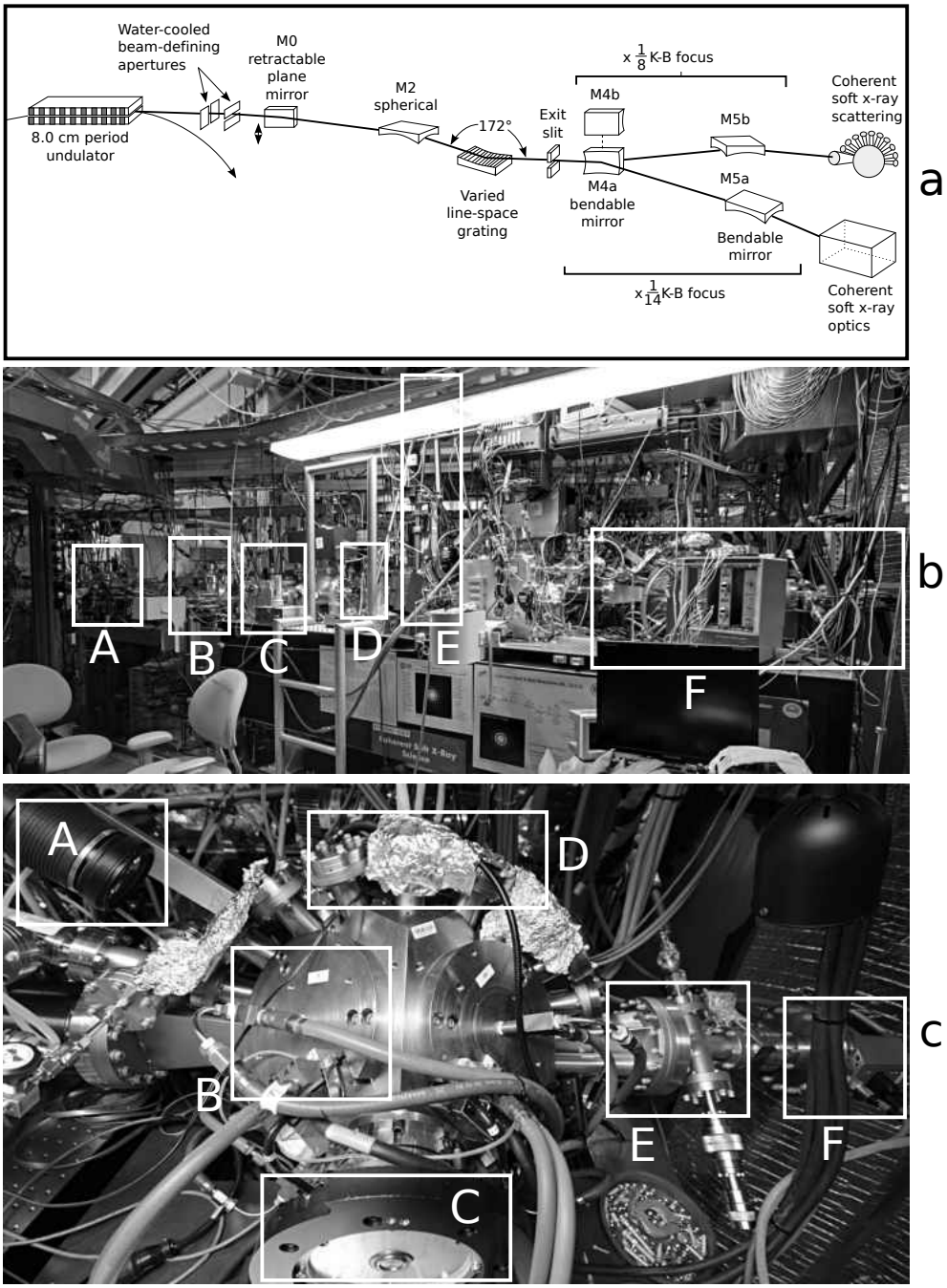

FIGURE 2.5.. Beamline schematic and photographs with salient features marked. Explanations provided in text.

fabricated from an extremely low-roughness gold film [28]. To measure the energy resolution established by the monochromating elements, we insert a thin titanium film between the monochromator slits and the next downstream element, focusing mirror M_4. The L_3 electronic resonance of titanium is centered at $453.8eV$ with width $0.22eV$ [29]. By measuring the photocurrent on the downstream mirror as a function of energy, we are able to determine the spectrum of the incoming radiation.

M_4 and M_5 together form a Kirkpatrick-Baez pair [30] which focuses the beam at the center of the chamber via grazing incidence reflection; M_4 focuses in the horizontal direction, and M_5 in the vertical. Both mirrors have spherical shape and are coated with tungsten. M_4 images the beam emitted from the undulator source, approximately ten meters upstream, while M_5 images the exit slits from the monochromator. The ratio of the distance between the undulator source and the enstation determines the degree of demagnification; on branchline 12.0.2.2, the demagnification is a factor of eight, while on branchline 12.0.2.1 the demagnification is by a factor of fourteen. However, both depth-of-focus effects and aberrations in the focusing optics ultimately result in a spot size somewhat larger than might be predicted by the source size and demagnification ratio. In Figure 2.5.(b), M_4 is found in the box marked C and M_5 is found in the box marked D. While the focus of the beamline should nominally not require adustment, the K-B system does permit fine-tuning via a CXRO controller.

Box E labels the location of a multilayer mirror and vertical beampipe leading to a phosphorescent YAG crystal and microscope which we use to monitor the focus of the beamline. As the total path length from the multilayer mirror to the YAG is nominally the same as that from the multilayer mirror to the center

of the chamber and the depth of focus is relatively large, we assume that a well-focused beam image on the YAG crystal indicates a well-focused beam on the sample. As a multilayer mirror, the reflectively depends strongly on energy in order to generate constructive interference through the Bragg condition. The optimum reflectivity of this mirror is at $250eV$.

2.5.2. Beamline Optical Parameters

The following beamline optical parameters are reproduced from Rosfjord [27]. In the time since publication, upgrades to the source and the inevitable contamination of mirrors have surely altered the values somewhat, but they are useful in ball-parking the performance of the 12.0.2.2 beamline.

In Figure 2.6. we show the coherent power in the central radiation cone as a function of photon energy at both the first and third undulator harmonics [31].

Energy (eV)	λ (nm)	Beamline Efficiency	θ_{cen} (μrad) $n = 3$	Coherent flux (focal plane; BW = 0.1%)
500	2.48	0.00567	33.57	4.39E10
600	2.07	0.00534	30.65	2.54E10
700	1.77	0.00433	28.37	1.20E10
800	1.55	0.00251	26.54	3.80E09

TABLE 2.1. Optical parameters for ALS beamline 12.0.2.2

2.5.3. Endstation

The 12.0.2.2 endstation, nicknamed "flangosaurus," is in the F box of Fig. 2.5.(b) and is photographed in more detail in Fig. 2.5.(c). The design of the endstation centers around the requirements of coherent scattering from complex materials; namely, scattering angles up to $2\theta = 180°$, the use liquid nitrogen or

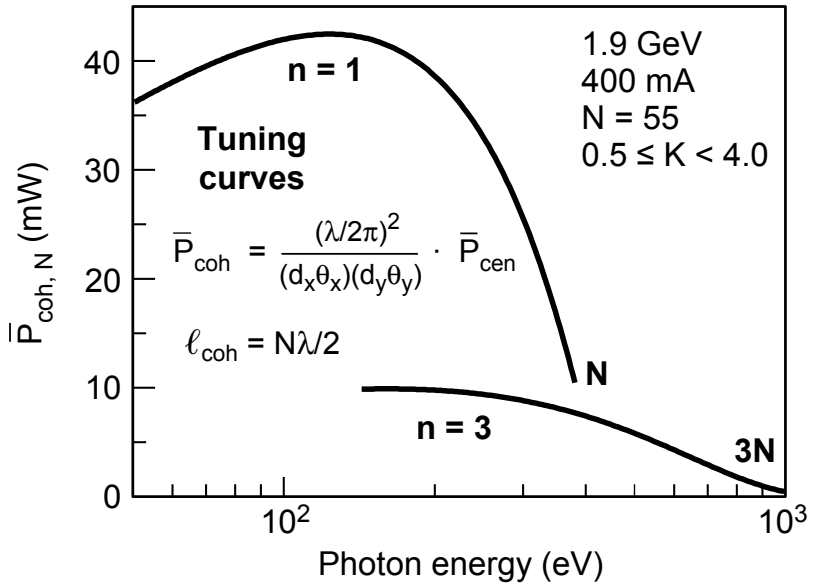

FIGURE 2.6.. Tuning curves for ALS undulator U8 at first and third harmonics.

helium cryogens to reach low-temperature phases, upstream pinholes to define illumination with a high degree of coherence, and vectoral electromagnets to apply magnetic fields.

2.5.3.1. Angular Range

The chamber itself is a titanium ultra-high vacuum scattering chamber with a series of external flanges mounted along the scattering plane at intervals of $2\theta = 180°$, to any of which a CCD detector may be mounted. Some of these flanges are labeled D in Fig. 2.5.(b). The chamber rotates on a set of rotary seals, labeled C, by an additional $2\theta \approx \pm 7°$, which in combination with the flange series provides access to most 2θ between 0° and 180°. On occasion, we have failed to reach particular Bragg peaks which at resonance fall into one of the 2θ dead-zones. The choice of titanium as the construction material reflects its non-magnetic character.

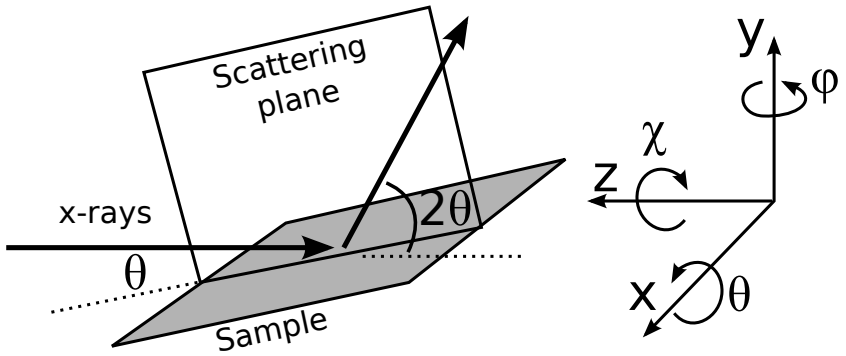

FIGURE 2.7.. Degrees of freedom in the 12.0.2.2 endstation. The 12.0.2.2 endstation has motorized control of x, y, z, and θ, but not χ or ϕ

2.5.3.2. Vectoral Magnets

The bulk of the endstation's volume is dedicated by a set of octupolar vectoral electromagnets, one of which is labeled B in Fig. 2.5.(c). The experiments in this dissertation use only a fraction of the capability of the magnets. For more extensive details on magnet capabilities and calibration, see Turner [32] or Arenholz [33]. By applying different amounts of current to the eight different magnets, we can create a magnetic field of arbitrary orientation with sustained magnitude of approximately $0.4T$ at the center of the chamber. We can apply slightly higher fields for short periods of time; however, excessive current eventually causes the water coolant to reach $100°C$ at which point the current supply turns off automatically via interlock and must be reset.

2.5.3.3. Sample Manipulation

We show the coordinate system describing the scattering plane and motorized degrees of freedom in Figure 2.7.. The sample is moved between experimental position and transfer position by means of a motorized, cantilevered manipulator. The primary directions of motion for the manipulator are the two dimensions

transverse to the beam; the $\hat{x}$ direction is parallel to the ground, and the $\hat{y}$ direction is perpendicular to the ground. The manipulator can also move parallel to the beam along the $\hat{z}$ axis, but this direction of motion is uncommon.

Along $\hat{x}$, the experimental position at the center of the chamber is approximately $x = 4mm$, while the transfer position is at $x = -364mm$. Given the large range of travel along this direction, we do not expect this motor to produce accurate positions at resolution below about $50\mu m$. Additionally, this motor exhibits backlash when undergoing small motions. Along $\hat{y}$, the range of motion is much less, ranging between $y = -2mm$ and $y = 2mm$. We trust the accuracy of the y motor to a much greater extent than x, and in experiments where we use the manipulator motor to align pinholes mounted directly on the sample with the beam, we see reproducible movements at $\Delta y < 5\mu m$ resolution.

We associate a rotation with each cardinal direction. Rotations about x we label θ; rotations about y we label ϕ; and rotations about z we label χ. The 12.0.2.2 endstation has motorized control only of θ. ϕ may be varied through the load-lock mechanism whereby samples are moved from the manipulator out of vacuum, but this control is manual and there is no read-back. No *in-situ* control of χ is possible, and so all alignment of χ must be done *ex-situ* through shims or various other ad-hoc means. Lack of χ control in particular presents serious difficulties to scattering experiments, as small misalignments of the sample may deflect the signal entirely off the detector. For scattering from a Bragg peak, such misalignment may not be discovered until beamtime because discovery of the alignment requries the beam. Further complicating the χ problem is a slight misalignment of the chamber in either ϕ or χ, which become coupled at large θ.

2.5.3.4. Pinholes

The sample manipulator also holds two high-precision piezoelectric motors manufactured by Attocube AG, on which we mount an array of pinholes. Currently, this array includes pinholes of $3\mu m$, $5\mu m$, and $10\mu m$ diameter. The horizontal attocube uses an optical encoder for position readback, while the vertical attocube is resistive. We use the pinholes to select the degree of coherence with which the sample is illuminated, or to select the size of the illumination and thereby the size of the speckles in the far field intensity pattern.

2.5.3.5. Cryogens

In order to reach low-temperature phases, the sample manipulator may be cooled with either liquid nitrogen or liquid helium. We measure temperature both the end of the cryostat as well as on the sample-holder, which is connected to the cryostat via a copper braid. Typically, the temperature reading at the sample rides about ten Kelvin higher than on the cryostat, presumably due to greater radiative transfer. With liquid helium, the minimum achievable temperature is around twenty Kelvin.

2.5.3.6. Detectors

The most common detector used on the endstation and the only detector used in the experiments in this dissertation is a high-sensitivity, high efficiency CCD, labeled F is Fig. 2.5.(c). CCD detectors are now commonplace at synchrotron sources. For a review of CCD physics, see Janesick [34]. The detector used on 12.0.2.2 was manufactured by Andor Technology, and is an area detector with 2048×2048 pixels each of side-length $12.5\mu m$. The readout time for the detector

at full-resolution is approximately five seconds, which is considered very slow by modern standards. The dynamic range of the detector is set by a combination of the pixel well-depth and the analog-digital converter in the detector's readout electronics. As the AD converter functions only up to 2^{16}, we can measure a maximum of 65536 counts/pixel before saturating the camera. A rough conversion between the number of incident photons recorded in a pixel and the number of registered AD counts is counts $\approx E/3.64$, where E is the energy of the incoming photons. At x-ray energies, this means that the a few hundred photons will saturate a pixel; combined with the slow readout speed, the extreme dynamic range present in a typical far-field signal requires multiple exposures to accurately reproduce across the full field of view. To this end, we often physically block the central portion of the diffraction signal; the beam block apparatus is labeled E in Fig. 2.5.(c).

A recent addition to the endstation capabilities is the long focal-length photographic macro lens labeled A in Fig. 2.5.(c). The use of this lens in concert with a CCTV detector allows real-time visual monitoring of the sample inside the chamber. Recently, we have begun combining small phosphorescent samples on the same mount with the experimental sample in order to precisely align the beam to a specific position on the experimental sample. Use of this lens requires that a 2θ flange be terminated with a glass window.

CHAPTER III

COHERENT DIFFRACTIVE IMAGING

3.1. Introduction

In this chapter we will review method, algorithms, and requirements broadly grouped as *coherent diffractive imaging* whereby we can invert properly prepared speckle patterns through numerical solutions to the phase problem. We structure this chapter as follows. First, we show the importance of the lost phase component in generating an image of the scatterer. Second, we show the iterative nature of the phase reconstruction algorithms and provide explicit forms for several of these algorithms commonly seen in the literature. Third, we discuss the requirements for a speckle pattern to be invertible with the listed algorithms, including oversampling and coherence requirements. Fourth, we present a good metric for judging the resolution of an image after phase reconstruction, the phase-retrieval transfer function. Fifth, we present some sample reconstructions of simulated data and judge their resolution; primarily, we focus on the impact of the support constraint with an eye towards the interpretation the experimental data reconstructed in the next chapter. Sixth, we present the theory of an alternative method of phase retrieval through holography, and examine how it overlaps with the iterative inversion methods in the limit of non-ideal reference waves.

The methods presented in this chapter do not represent original research, but rather a limited and specific introduction to the techniques used later. Coherent imaging algorithms have become a mature microscopy applicable to a vast range of materials at both synchrotron and free-electron laster facilities, including test-

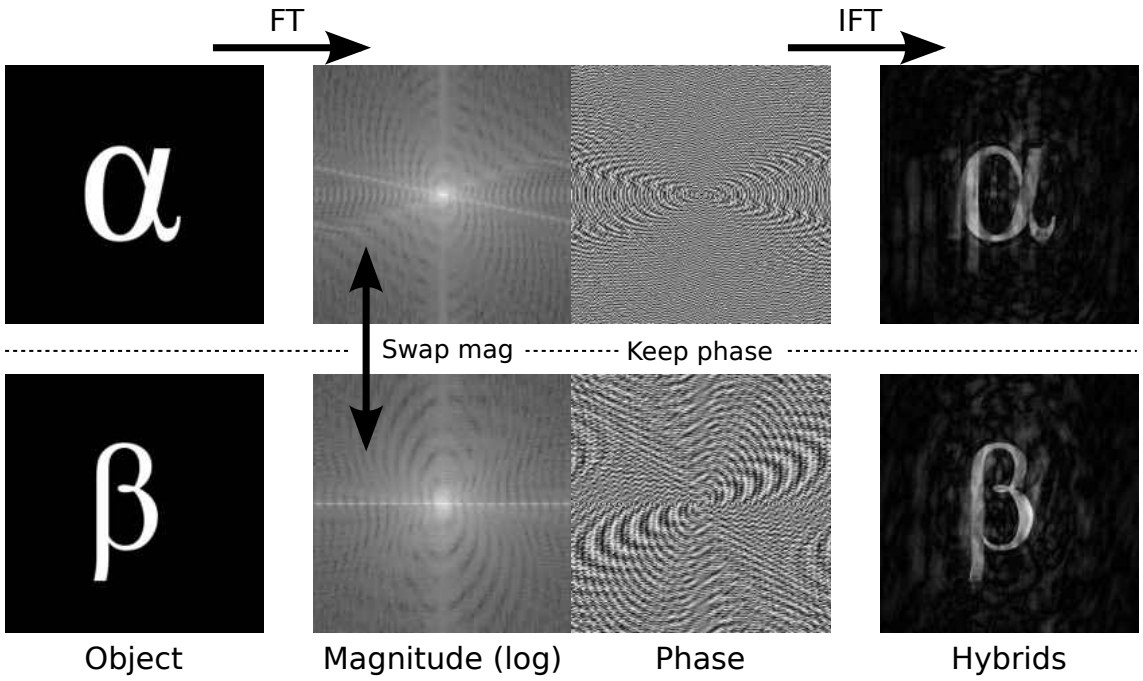

FIGURE 3.1.. The importance of the phase in image formation. Swapping the Fourier magnitudes of the two images exerts surprisingly little effect on the hybrid image.

patterns [35–37], biological samples such as yeast cells [38–41] and viruses [42, 43], magnetic nanostructures [44–49], quantum dots [50, 51], ceramic nanofoams [52, 53], radiation damage in nanowires [54], and the strain and deformation in nanoparticles [55]. References in the citations above give many additional examples. For a review of coherent imaging in the context of coherent scattering techniques more broadly, see Nugent [56]. For an in-depth review of imaging algorithms in particular, see Quiney [57].

3.2. The Importance of the Fourier Phase Component

We return to the phase problem originally exposed in Equation 2.7.

Because we may write any complex number $x + iy$ in polar coordinates as $A\exp(i\phi)$, where $A = \sqrt{x^2 + y^2}$ and $\phi = \tan^{-1}(y/x)$, the loss of the

phase information ϕ during the detection process initially seem a relatively inconsequential concern. After all, the phase represents only half the information of the complex wavefield. However, a brief demonstration will quickly disabuse this notion. In Figure 3.1., we show the effect of swapping the magnitude component of the Fourier transform of two fictitious real-valued objects, forming hybrid Fourier signals containing the magnitude of one transform and the phase of the other. After taking the inverse Fourier transform of the mixed signals, the real-space hybrids still most closely resemble the original image from which we retrained the phase component . While swapping the magnitude component introduces obvious distortions into the hybrid image, the phase component truly encodes the image. For this reason, in terms of forming a real-space image of the scattering object, the loss of the phase component in the detection process appears catastrophic.

Information about the real-space object remains in the modulus of the speckle pattern; for example, an inverse transformation of the intensity gives the autocorrelation.

3.3. Imaging Algorithms

Following a suggestion by Sayre [58] that the phase of a diffraction pattern could be reconstructed given a suitable level of oversampling beyond the Nyquist-Shannon limit, researchers have developed a variety of algorithms which, under the correct experimental conditions, iteratively reconstruct the phase information destroyed during the detection process. Post phase reconstruction, a simple Fourier transform of the complex diffraction pattern generates a real-space image of the scattering object. Here, we review several of these algorithms and describe their applicability to coherent scattering experiments at beamline 12.0.2.

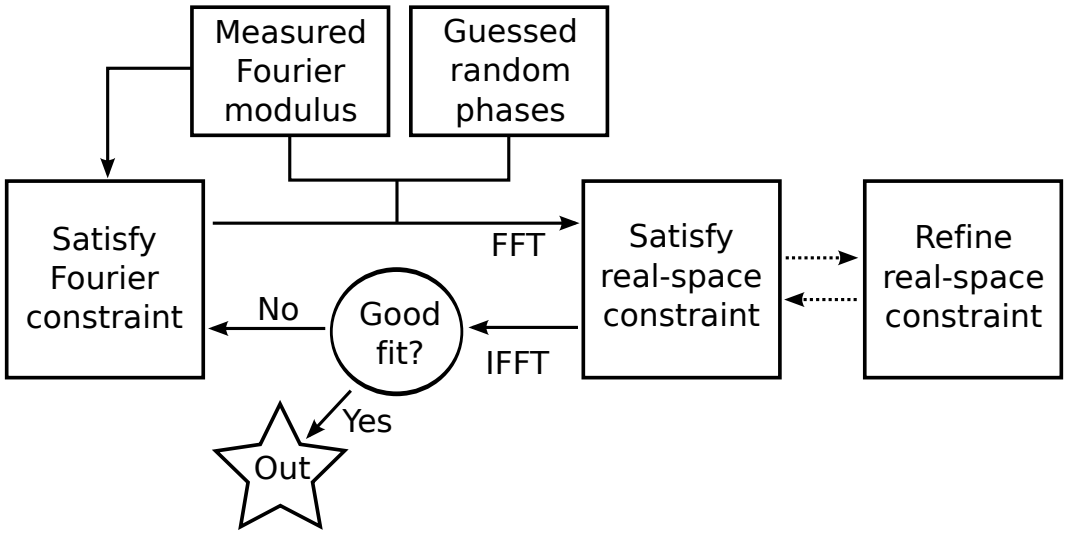

FIGURE 3.2.. The structure of phase retrieval algorithms. We find solutions by iterating between real- and Fourier- space, applying constraints in each until we reach convergence.

3.3.1. Iterative Algorithm Overview

Phase retrieval algorithms all share at their core a common strategy to solving the phase problem: iterative enforcement of constraints in both real- and Fourier-space derived from *a priori* information about the nature of the scattering object. For example, in Fourier-space we know that the modulus of the estimate must match that recorded on the detector during the experiment; in real-space, researchers often construct experiments which confine the scattering object to a small area of space with well-defined boundaries. Schematically, we understand the approach as follows. We form an initial guess at a solution from the Fourier modulus and a random set of phases. We then propagate the guess solution to the sample plane under the assumption of fully coherent illumination by a Fourier transform. In real-space, we require that the estimate of the object meet the constraints imposed by the *a priori* knowledge. Some algorithms may refine the real-space constraint [59]. We then propagate the constrained estimate back to

Fourier space, where the modulus of the estimate must match the measured Fourier modulus. If, after meeting the real space constraints, the estimate satisfies some termination condition such as a threshold in an error metric or self-consistency, we consider the estimate a solution.

We define the Fourier-space constraint operator P_m which replaces the Fourier modulus with that measured on the detector as

$$\rho'(r) = P_m \{\rho(r)\} = \mathscr{F}^{-1} \left\{ \sqrt{I(q)} \frac{\mathscr{F} \{\rho(r)\}}{|\mathscr{F} \{\rho(r)\}|} \right\} \qquad \text{(Equation 3.1.)}$$

where $I(q)$ is the intensity recorded on the detector and $\rho(r)$ is the solution estimate in real space. We introduce the $\rho'(r)$ notation to simplify the following equations.

The real-space constraint is weaker and more subtle, and we can understand much of the history of phase retrieval algorithms as ways to strengthen it and consequently improve the robustness of the solution. To satisfy the oversampling condition required by the Shannon theorem, we confine the real-space object to a limited region within the image called the support, which we label S. Outside the support, the object does not exist, and so we know that the value of the estimate there must be zero. Given the nature of the scattering experiment, additional constraints may apply to the real-space image; for example, some reconstructed images may contain only pixels with positive real value. Such constraints help the convergence of the algorithm by reducing the size of the search space. In this case, we understand the set S to describe the intersection of the pixels inside the support and pixels which have positive real value. Different approaches to enforcing this constraint give the various algorithms seen in the literature. Although we present several algorithms to emphasize the diversity of thought found in the literature, in

practice most reconstructions seem to be performed either by alternating several iterations of the hybrid input-output algorithm with an iteration of the error-reduction algorithm, or with the difference map algorithm.

3.3.1.1. The Error Reduction Algorithm

The *error reduction* algorithm (abbreviated ER) [60–62] approaches the real-space constraint as simply as possible, setting the value of the estimate outside the support to zero during every iteration. If $\rho^{(n)}(r)$ demarcates the estimate of the solution at some iteration n of the algorithm, the updated estimate $\rho^{(n+1)}(r)$ given by the error reduction algorithm is:

$$\rho^{(n+1)} = \begin{cases} \rho'^{(n)}(r) & r \in S \\ 0 & r \notin S \end{cases} \qquad \text{(Equation 3.2.)}$$

Fienup demonstrated that this algorithm is equivalent to a gradient descent along a particular error metric [63]. As a gradient search method, this algorithm stagnates in local minima within the solution space without finding the global minimum which corresponds to the solution.

3.3.1.2. The Solvent Flipping Algorithm

The *solvent flipping* algorithm [64], which ultimately takes its name from crystallographic phasing methods in which a solvent is placed in the crystal, flips

the value of the estimate outside the support:

$$\rho^{(n+1)} = \begin{cases} \rho'^{(n)}(r) & r \in S \\ -\rho'^{(n)}(r) & r \notin S \end{cases} \qquad \text{(Equation 3.3.)}$$

3.3.1.3. The Averaged Successive Reflections Algorithm

The *averaged successive reflections* algorithm [65], combines the input and the output to gradually relax the region outside the support to its required value of zero:

$$\rho^{(n+1)} = \begin{cases} \rho'^{(n)}(r) & r \in S \\ \rho^{(n)}(r) - \rho'^{(n)}(r) & r \notin S \end{cases} \qquad \text{(Equation 3.4.)}$$

3.3.1.4. The Hybrid Input-Output Algorithm

Proposed by Fienup [63, 66], the *hybrid input-output* algorithm (abbreviated HIO) draws on nonlinear feedback control theory to mix the current estimate $\rho^{(n)}$ with the semi-updated estimate $P_m\left\{\rho^{(n)}\right\}$. This algorithm uses a feedback parameter β; $\beta = 0.8$ is common. HIO essentially generalizes ASR which allows for an optimal amount of feedback instead of the fixed amount in the earlier algorithm.

$$\rho^{(n+1)} = \begin{cases} \rho'^{(n)}(r) & r \in S \\ \rho^{(n)}(r) - \beta\rho'^{(n)}(r) & r \notin S \end{cases} \qquad \text{(Equation 3.5.)}$$

We will use this highly successful and popular algorithm extensively in analyzing the forthcoming experiment.

3.3.1.5. The Relaxed Averaged Alternating Reflectors Algorithm

The *relaxed averaged alternating reflectors* algorithm [67] (abbreviated RAAR) also incorporates a feedback parameter β. This algorithm coincides with the hybrid input-output algorithm in the case of $\beta = 1$.

$$\rho^{(n+1)} = \begin{cases} \rho'^{(n)}(r) & r \in S \\ \beta\rho^{(n)}(r) + (1-2\beta)\rho'^{(n)}(r) & r \notin S \end{cases} \qquad \text{(Equation 3.6.)}$$

3.3.1.6. The Difference Map

Introduced by Elser [68], the *difference map* (abbreviated DM) is an umbrella term for a general set of algorithms with several parameters and two instances of the Fourier constraint operator P_m rather than the single instance found in the other algorithms. First, we build a modified version of $\rho(r)$ by

$$\rho_m(r) = \begin{cases} \rho(r) & r \in S \\ -\gamma_m\rho(r) & r \notin S \end{cases} \qquad \text{(Equation 3.7.)}$$

and then, in analogy to the definition of $\rho'(r)$ in Equation 3.1., we define

$$\rho''(r) = P_m\left\{\rho_m(r)\right\} \qquad \text{(Equation 3.8.)}$$

We can then express the difference map using the ρ' and ρ'' terms as

$$\rho^{(n+1)} = \begin{cases} 2\rho'^{(n)}(r) - \beta\rho''^{(n)}(r) + \beta\left(\left(1+\gamma_s\right)\rho'^{(n)}(r) - \gamma_s\rho^{(n)}(r)\right) & r \in S \\ \rho^{(n)}(r) - \beta\rho''^{(n)}(r) & r \notin S \end{cases} \qquad \text{(Equation 3.9.)}$$

Elser recommends as optimal values $\gamma_m = \beta^{-1}$ and $\gamma_s = -\beta^{-1}$.

3.3.1.7. Performance of Reconstruction Algorithms

Several publications have examined the performance of the various reconstruction algorithms in great depth. For a review of the convergence properties of several algorithms, as well as recommended improvements to the HIO algorithm from a conjugate-gradient and saddle-point optimization point of view, see Marchesini [69, 70]. For an evaluation of the HIO, ER, DM, and RAAR algorithms in the presence of both an inaccurate support and missing data behind a central beam-stop, see Huang [40].

3.3.1.8. Uniqueness

In 1982, Bates published a series of articles [71–73] which demonstrated the uniqueness of the phase retrieval problem, excepting several trivial degeneracies. First, shifting the original (or reconstructed) image within the image plane results in the same far-field intensity pattern:

$$\begin{aligned} |\mathscr{F}\{f(x-x_0, y-y_0)\}|^2 &= \left| \iint f(x-x_0, y-y_0) e^{-i(k_x x + k_y y)} dx\, dy \right|^2 \\ &= \left| e^{-i(k_x x_0 + k_y y_0))} \iint f(x', y') e^{-i(k_x x' + k_y y')} dx'\, dy' \right|^2 \\ &= |\mathscr{F}\{f(x,y)\}|^2 \qquad \text{(Equation 3.10.)} \end{aligned}$$

Second, multiplying the image by an overall phase factor $\exp(i\phi)$ results in the intensity pattern as the phase disappears by the same argument as above. Third, the dual of a function $f(x, y)$, which we write $f^*(-x, -y)$, produces the same far-field intensity pattern through a well-known symmetry in the Fourier transform.

In more than one dimension, Barakat and Newsam [74] demonstrated that only the pathologically rare case of data with a separable Fourier amplitude breaks the uniqueness of phase retrieval. They demonstrate that if we can decompose a Fourier signal $F(k)$ into the product $A(k)B(k)$, each of which have inverse transforms $a(x) = \mathscr{F}^{-1}\{A(k)\}$ and $b(x) = \mathscr{F}^{-1}\{B(k)\}$, then both $A(k)B(k)$ and $A^*(k)B(k)$ share a far field intensity but generally correspond to different real space images unless $a(x) = a^*(-x)$ or $b(x) = b^*(-x)$. Such a degeneracy is the only possible source of non-uniqueness in more than one dimension for perfect data.

Of course, experimental data has many sources of non-perfection, including shot noise in the intensity pattern and partially coherent illumination. Generally speaking, these sources of error do not permit multiple solutions, but rather prevent the existence of any exact solution. This being the case, the reconstruction algorithms will produce only a close estimate of the image upon convergence.

3.3.2. Oversampling

Reconstruction of the lost phase requires oversampling of the signal with respect to the Nyquist limit. Qualitatively, the speckle pattern recorded on the detector must have speckles larger than one pixel in order to accurately record the minima between the speckles. Quantitatively, we can state two equivalent formulations of the oversampling requirement. First, if we reconstruct a speckle pattern of size $N \times N$ pixels, the reconstructed image must fit entirely within a box of size $\frac{N}{2} \times \frac{N}{2}$ pixels. Second, the autocorrelation of the image, given by the inverse Fourier transform of the speckle intensity, must not overlap itself through the circular boundary conditions at the image edge, as this creates aliasing.

When diffracting from an isolated sample, we often know its size in real space *a priori* from optical microscopy, and may then verify oversampling condition prior to performing the scattering experiment as $2\pi/|\mathbf{q}|_{max}$ gives the pixel size in the reconstruction. In practice, for the coherence lengths of the beam and the corresponding sample size we can image and the value of $|\mathbf{q}|$ recorded by the detector, scattering experiments at 12.0.2 always oversample the diffraction pattern. Only when we perform highly incoherent scattering does the diffraction pattern become undersampled in the Nyquist sense, but as incoherent scattering does not generate speckle, we cannot do imaging experiments anyways.

Occasionally, researchers report a reduced two-dimensional oversampling ratio, typically calculated by $N^2/(\sum S)$, where N^2 gives the total number of pixels in the reconstructed image and $\sum S$ gives the total number of pixels within only the support region.

3.3.3. Coherence and Signal Level Requirements

Because third-generation x-ray light sources have both incomplete coherence and a small coherent fraction, substantial attention has now been paid to adapting the coherent algorithms listed above to work with less than fully-coherent conditions. When using the above algorithms, the object should fit within the coherence length of the beam, as deviations from full coherence seriously disrupt the reconstruction [75] However, given a well-specified coherence function, we can modify the the propagator between the near and far fields and the constraint operator P_m to more realistically reflect the degree of coherence [76, 77].

Researchers have investigated the level of signal necessary to obtain a reliable reconstruction [78], and better estimators of the intensity to improve

reconstructions from sparse measurements [79]. As we conduct scattering at soft x-ray energies on hard condensed matter samples, we have no pressing need to avoid radiation damage by limiting the time the sample spends in the beam. In the hard x-ray regime or for experiments using biological specimens, radiation damage and the amount of time the sample spends in the beam become critical concerns.

3.4. The PRTF and RFTF: Estimating Resolution

Phase retrieval algorithms of the type just discussed will recover the phase of the speckle pattern only imperfectly for a variety of reasons, including: limited coherence, distortions of the Fourier modulus from dust on the CCD or non-linearities in the CCD photoresponse, shot noise, and misestimation of the real-space constraints such as an inaccurate support. The phasing algorithms will therefore reliably reconstruct only a portion of the Fourier phases, while other phases will vary randomly with the starting seed. Generally speaking, the phases at reciprocal space points with high scattering intensity will reconstruct more reliably as they are less subject to SNR issues from counting statistics. For many samples of interest, we find the highest scattering intensity near the center of the diffraction pattern at reciprocal magnitudes corresponding to large real-space features.

Several metrics have been proposed to evaluate the reliability of the phase retrieval process as a function of reciprocal space magnitude; as the reconstructed phase increasingly fluctuates along with $|\mathbf{q}|$, we interpret the reconstruction as untrustworthy below a certain length-scale, setting the nominal resolution of the image. Given a large number of solution estimates $E_i(u, v)$ converged from random, independent seeds, the so-called "phase retrieval transfer function," or PRTF [38, 52, 80], attempts to quantify the degree of phase reliability in Fourier space

by averaging together the various Fourier phase components.

$$\mathrm{PRTF}(\mathbf{q}) = \left| \left\langle \frac{\mathscr{F}\left\{E_i(u,v)\right\}}{\left|\mathscr{F}\left\{E_i(u,v)\right\}\right|} \right\rangle_i \right| \qquad \text{(Equation 3.11.)}$$

Equation 3.11. gives the form of the PRTF; i labels the independent reconstructions. Dividing the Fourier transform of a reconstruction by its modulus leaves just the phase component. The phase component must always have magnitude unity, but as we averaged together many random phases the modulus of the average naturally approaches zero by the usual statistics of phasor addition. We therefore interpret the value of the PRTF in a straightforward way: highly reproducible phases at reciprocal space point $\mathbf{q}$ give $\mathrm{PRTF}(\mathbf{q}) = 1$, while points with highly varying phases give $\mathrm{PRTF}(\mathbf{q}) = 0$. Subtlety enters the interpretation when deciding at what intermediate value we should declare the phase unreproducing; no strict agreement exists in the literature, so we adopt a value of 0.5 as a reasonable limit on the resolution of the average reconstruction.

While measuring the randomness in phase reconstructions helps establish the resolution of the final averaged image, the reproducibility of the phase component does not guarantee correctness. We must instead examine the extent to which the average of many reconstructions satisfies the known constraint: the measured far-field speckle pattern. Defined in analogy to the R-factor in crystallography, the "R-factor transfer function," abbreviated RFTF, measures the agreement between the Fourier modulus of the average of the many reconstructions $E_i(u,v)$ and the

speckle pattern [80, 81].

$$\mathrm{RFTF}(\mathbf{q}) = \frac{1}{\sqrt{1+\sigma^2(\mathbf{q})}} \qquad \text{(Equation 3.12.)}$$

$$\sigma^2(\mathbf{q}) = \frac{\left|\left|\mathscr{F}\left\{\langle E_i(u,v)\rangle_i\right\}\right| - \sqrt{I}(\mathbf{q})\right|^2}{I(\mathbf{q})} \qquad \text{(Equation 3.13.)}$$

Equation 3.12. and Equation 3.13. taken together mathematically define the RFTF; $I(\mathbf{q})$ denotes the measured speckle intensity pattern. While the PRTF in Equation 3.11. naturally varies between zero and unity, the RFTF in Equation 3.12. behaves in a slightly more complicated fashion. At points $\mathbf{q}$ where the fourier modulus of the average estimate exactly matches the measured experimental fourier modulus, $\sigma^2 = 0$ and $\mathrm{RFTF}(\mathbf{q}) = 1$. At points $\mathbf{q}$ where the fourier modulus of the average estimate exactly falls towards zero, as often happens at large $|\mathbf{q}|$ when averaging many independent reconstuctions, $\sigma^2 = 1$ and $\mathrm{RFTF}(\mathbf{q}) = 1/\sqrt{2}$. It is unlikely but not forbidden for an average reconstruction to place more Fourier power at some $\mathbf{q}$ than exists in the speckle pattern, in which case $\sigma^2 \to \infty$ and so $\mathrm{RFTF}(\mathbf{q}) \to 0$.

Both Equation 3.11. and Equation 3.12. define the transfer functions at all measured points $\mathbf{q}$. However, common practice reduces the dimensionality of the analysis via an azimuthal average and presents results as $\mathrm{PRTF}(|\mathbf{q}|)$ or $\mathrm{RFTF}(|\mathbf{q}|)$ instead.

3.5. The Impact of the Support Constraint on Reconstruction

As mentioned above, a variety of experimental factors can lead to poor reconstruction or a reconstruction which fails outright. Among the most important of these are the size and shape of the support constraint; the former may be set during the reconstruction calculation, while the choice of sample or illuminating

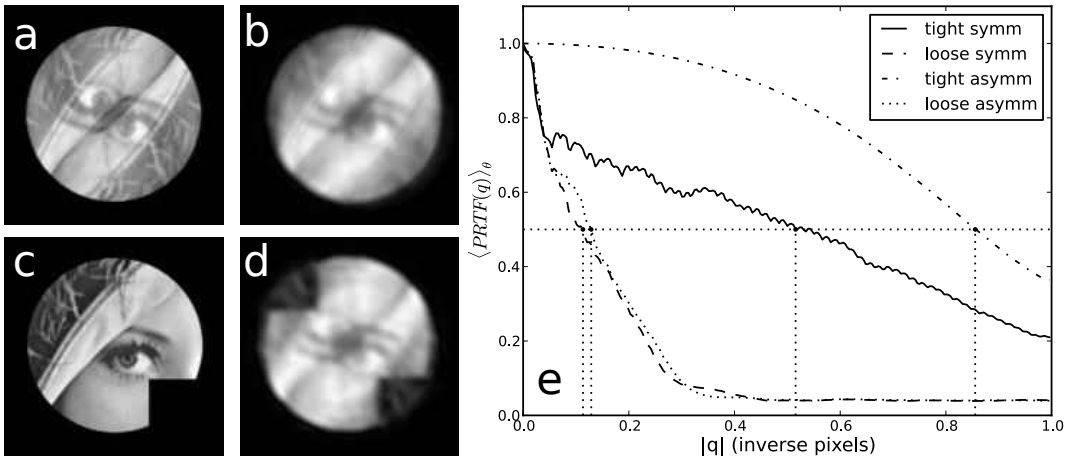

FIGURE 3.3.. Reconstructions for various supports. (a) shows a symmetric object with tight support; (b) a symmetric object with loose support; (c) an asymmetric object with tight support; (d) an asymmetric object with loose support. (e) shows the PRTF for the four reconstructions, calculated from 500 independent reconstructions each with 1000 iterations.

apertures predominately set the latter. Here, we show in-depth the effect of the support constraint on the resolution of the reconstruction. Several researchers have explored the impact of a correct support on the quality of the reconstruction [82, 83].

3.5.1. Support Requirements

In the following simulations, we use as the test object a portion the classical "Lena" image often used as a canonical test object in coherent imaging. The size of the test object is 512 by 512 pixels. The results we show are each the average of five-hundred independent reconstructions, each with a thousand total iterations alternating between nineteen iterations of the HIO algorithm and a single iteration of the ER algorithm. In these simulations, we do not show a RFTF plot as it closely tracks the shown PRTF.

Two factors dominate the impact of the support constraint on the quality of the reconstruction: symmetry and looseness. In Figure 3.3. we show reconstructions from four support permutations. Fig. 3.3.(a) and (b) show reconstructions which use a symmetric support. In these two simulations, the true support of the object is a circle of radius sixty pixels, making the diffraction pattern highly oversampled. Fig. 3.3.(a) shows the reconstruction using the true, tight support, while in Fig. 3.3.(b) we substantially loosened the support. Immediately, we note the low resolution of the reconstruction with the loose support; we find confirmation of this judgment in Fig. 3.3.(e), which shows the PRTF of the reconstructions. While the simulation with the tight support reaches the PRTF cutoff at approximately half an inverse pixel, that with the loose support hits the cutoff at 0.1 inverse pixels. To some degree, the loose support allows the reconstruction to shift in space, an allowed symmetry of the Fourier modulus, and the resulting low resolution subsequently reflects imperfect alignment of the independent reconstructions. Mostly, however, the low resolution reflects bad reconstructions due to insufficient constraint in real-space. Critically, both Fig. 3.3.(a) and (b) demonstrate a rotational symmetry not present in the original object, arising from a superposition of the original object and its dual. We will discuss this more in the next section.

Fig. 3.3.(c) and (d) show reconstructions which use an asymmetric support. The true support of the object is again a circle of radius sixty pixels, but with a notch cut from the corner. We modify the support constraint similarly to follow the incursion with a small gap of several pixels between the perimeter of the object and the boundary of the support used in Fig. 3.3.(c), while we make the gap very large in Fig. 3.3.(d). This notch breaks the symmetry of the support and forbids the simulation from superposing the original object and its dual. Breaking the

symmetry and maintaining a tight support allows for a very good reconstruction with PRTF cutoff at 0.85 inverse pixels. However, Fig. 3.3.(d) attests that an asymmetric object and support do not guarantee a quality reconstruction when the support becomes excessively loose. By making the support asymmetric but much larger than the object, the same problems manifest in (d) as in (b).

Consequently, for the best and most easily achieved reconstruction we require both a tight and asymmetric support constraint.

3.5.2. Twinned Solutions

Fig. 3.3.(a), (b), and (c) expose a dangerous pathology in the phase-retrieval process: the presence of a twinned solution [84, 85]. If some function $f(r)$ generates a speckle pattern $F(q)$, the symmetry of the Fourier transform says that $f^*(-r)$ must generate $F(q)$ as well. Consequently, when inverting the speckle pattern $F(q)$, any given reconstruction may generate $f(r)$, the rotated conjugate $f^*(-r)$, or even a linear combination $c_1 f(r) + c_2 f^*(-r)$. In this latter case, the reconstructed image gives a bad solution to the inversion of the speckle pattern but the reconstruction algorithms may stagnate at a local minimum in the optimization from which uniquely recovering $f(r)$ or $f(-r)$ becomes impossible.

We can imagine strategies to avoid twinned solutions; for example, calculating pairwise cross-correlations between all the independent reconstructions may help in identifying to which configuration each reconstruction belongs. In Figure 3.4. we show the effect on the PRTF of isolating and averaging the three possible solution configurations using such a cross-correlation scheme applied to the reconstructions after 1000 iterations. Defining the normalized cross-correlation of two independent

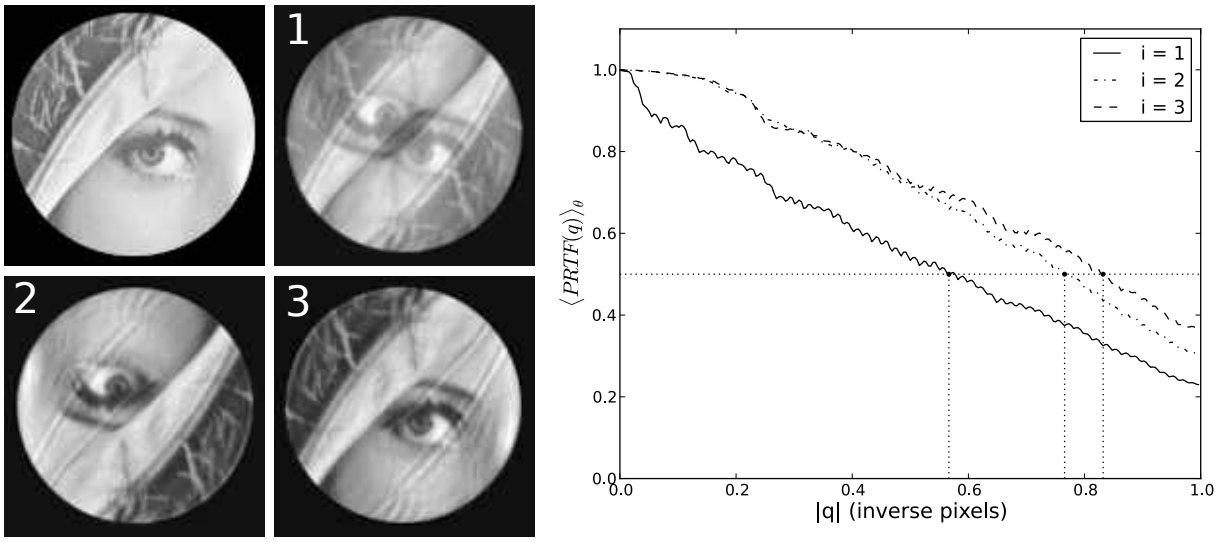

FIGURE 3.4.. Isolating the reconstruction configurations permitted by a symmetric support. (0), (1), (2), and (3) show the original object and the three configuration averages. The cut-off value of $|\mathbf{q}|$ in the PRTF moves outward compared to Fig. 3.3..

reconstructions E_i and E_j as

$$CC_{i,j} = \frac{\max(E_i \star E_j)}{\sqrt{\max(E_i \star E_i) \times \max(E_j \star E_j)}} \qquad \text{(Equation 3.14.)}$$

we identified three modal values in the distribution of the CC_{ij}. When E_i and E_j were of the same configuration, $CC_{i,j} > 0.98$. When E_i and E_j were $f(r)$ and $f(-r)$ (or vice versa), $CC_{i,j} \approx 0.87$. When either E_i or E_j, but not both, was the superposition, $CC_{i,j} \approx 0.94$. We found that the superposition solution appeared in approximately half the reconstructions, and $f(r)$ and $f^*(-r)$ equally split the remaining half. In comparing the PRTF of Fig. 3.4. to that of the tight symmetric reconstruction in Fig. 3.3.(e), we see that the cutoff value of $|\mathbf{q}|$ has shifted from approximately 0.5 inverse pixels outwards to approximately 0.8 inverse pixels for the non-superposed configurations.

While we can separate configurations in simulation, we prefer to avoid solutions poisoned by twinning through designs which discourage the twinning pathology in the first place. This pathology most acutely effects any support constraint which displays even approximate inversion symmetry, and for this reason simple, symmetric shapes such as circles and squares often used in other coherence experiments represent a nearly worst-case scenario in terms of imaging. Asymmetric objects, such as the support used in Fig. 3.3.(c), forbid the simulation from selecting either $f^*(-r)$ or the superposition $f(r) + f^*(-r)$.

3.5.3. Updating the Support

The poor PRTF and visually twinned solution in Fig. 3.3.(d) indicate it would be appropriate to tighten the estimate of the support and further iterate the independent estimates to generate an improved reconstruction. Following the approach of Marchesini [59], we update the support in the following way. To generate an updated support $S(u, v)$ from an ensemble of independent reconstructions $E_i(u, v)$, we blur the magnitude component of the average reconstruction through a convolution, then threshold the blurred image with respect to some fraction t of the maximum.

$$S(u,v) = \begin{cases} 1, & |\langle E_i(u,v)\rangle| * K > t \max\{|\langle E_i(u,v)\rangle * K\} \\ 0, & \text{otherwise} \end{cases} \qquad \text{(Equation 3.15.)}$$

Here, K is some convolution kernel suitable for blurring; we typically use a gaussian with a standard deviation of two or three pixels. Achieving a good refinement of the support requires some trial and error with respect to the size of the convolution kernel and the value of the threshold fraction t. This method of updating the

support finds common use in the context of forward-scattering experiments in which the central maximum of the diffraction pattern has been blocked to prevent damage to the detector from high x-ray intensity. The missing low spatial frequencies contain information about the support, and the iterative algorithms must reconstruct that information along with the rest of the speckle pattern. In our experiments, we avoid the need to reconstruct missing diffraction intensities but automatically updating the support from the loose initial estimate does increase the reliability of the reconstructed real-space image.

3.6. Fourier Transform Holography

The imaging algorithms presented above represent one way to recover the phase information from a far-field diffraction measurement given suitable constraints on the solution and certain considerations during the experiment. However, iterative phasing algorithms present formidable computational requirements due to the large number of Fourier transforms required, the non-convexity of the optimization problem, and the lack of a guarantee of convergence. In this section we review an alternative method recovering the phase information of a diffraction pattern using holographic techniques. This method, called Fourier transform holography, was first proposed by Stroke in 1965 [86]; early examples at x-ray wavelengths are Trebes [87] and McNulty [88]. Our interest in the technique was piqued by Eisebitt [89], who successfully employed this technique in imaging labyrinthine magnetic domains. For more information, also see Schlotter [90, 91]

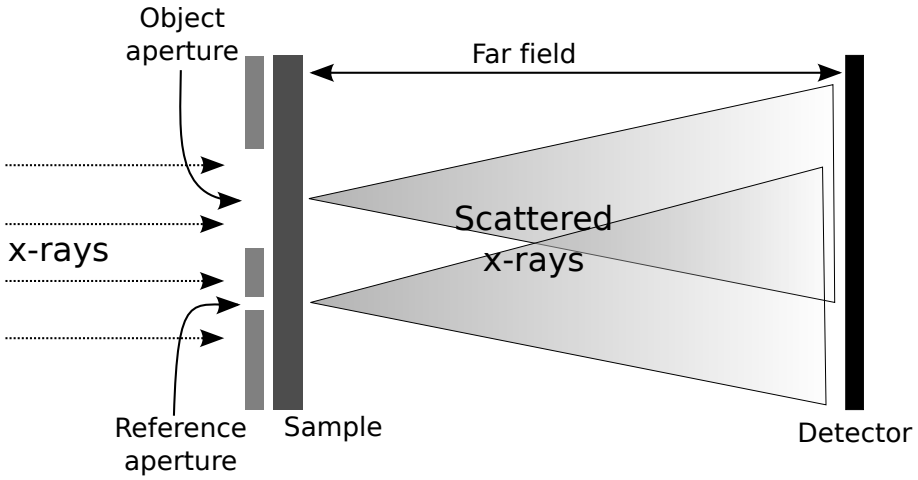

FIGURE 3.5.. The basic geometry of Fourier transform holography, showing object and reference apertures, the sample, and the far-field detector.

3.6.1. Theory of Holographic Image Formation

In familiar visible-light holography, the light scattered from an illuminated object interferes with light from a known reference [10, 92, 93]. Fourier transform holography adapts this approach to the Fourier domain by coherently illuminating at least two objects, one of which forms a reference wave by virtue of sufficiently small size. We demonstrate how to achieve this requirement in principle at soft x-ray wavelengths in Figure 3.5.. A gold film with two holes masks some sample under investigation; in the film, we fabricate two apertures. Still in analogy to visible-light holography, we refer to the large aperture as the object aperture and the small aperture as the reference aperture. In this simple geometry, the superposition of the illumination passing through the object aperture and the illumination passing through the reference aperture gives the total exiting electric field at the aperture plane.

$$U(u,v) = O(u,v) + R(u,v) \qquad \text{(Equation 3.16.)}$$

To calculate the far-field diffraction pattern, we simply Fourier transform the field $U(u,v)$, then square the magnitude of the transform. Here, we use the tilde notation to signify a field propagated to the Fourier domain and we leave the (u,v) and the (x,y) coordinates implicit after first use.

$$\begin{aligned} I(x,y) &= \left|\mathscr{F}\left\{U(u,v)\right\}\right|^2 \\ &= \left|\mathscr{F}\left\{O(u,v)+R(u,v)\right\}\right|^2 \\ &= |\tilde{O}+\tilde{R}|^2 \\ &= \tilde{O}\tilde{O}^* + \tilde{O}\tilde{R}^* + \tilde{O}^*\tilde{R} + \tilde{O}^*\tilde{R}^* \end{aligned} \qquad \text{(Equation 3.17.)}$$

Recognizing the Fourier formulation of the cross-correlation integral, we inverse transform the intensity in Equation 3.17.:

$$\begin{aligned} \mathscr{F}^{-1}\left\{I(x,y)\right\} &= \mathscr{F}^{-1}\left\{\tilde{O}\tilde{O}^* + \tilde{O}\tilde{R}^* + \tilde{O}^*\tilde{R} + \tilde{O}^*\tilde{R}^*\right\} \\ &= O\star O + O\star R + R\star O + R\star R \end{aligned} \qquad \text{(Equation 3.18.)}$$

From left to right, we identify the four terms of the Equation 3.18.: the autocorrelation of the object, the cross-correlation of the object and reference, the cross-correlation of the reference and the object, and the autocorrelation of the reference. We now consider the relationship between the two cross-correlation terms, which due to the non-commutativity of the cross-correlation operator are not equal. Instead, we recall that the distributive property of the complex conjugate provides $(ab)^* = a^*b^*$, and that the complex conjugate operates under the Fourier transform as $\mathscr{F}\left\{f^*(x)\right\} = \tilde{f}^*(-k)$, where x and k are the conjugate variables of the

transform. These two properties require that $O \star R$ and $R \star O$ are rotated complex conjugates of each other.

The critical mathematical insight into Fourier transform holography comes in formalizing the assumption of a small reference aperture. We take this to the limit where $R(u,v) \approx \delta(u-u_0, v-v_0)$; (u_0, v_0) are the coordinates of the reference relative to the object aperture. Under this approximation, the object-reference cross-correlation becomes

$$\begin{aligned} O \star R &= \iint_{-\infty}^{\infty} O^*(u,v)\delta(u-u_0-u', v-v_0-v')\,du'\,dv' \\ &= O^*(u-u_0, v-v_0) \end{aligned} \qquad \text{(Equation 3.19.)}$$

So by using an infinitesimal reference we recover an exact image of the full complex wavefield leaving the object aperture, solving the phase problem through a unique encoding of the zeros the phase in the far field diffraction pattern. We also recover the rotated conjugate of the wavefield in the object aperture, but this second image contains no additional information as it exists solely a consequence of the symmetry of the Fourier transform.

3.6.2. Image Formation with Large References

In practice, we cannot make references well-approximated by a delta function $\delta(u-u_0, v-v_0)$, and must accept that any physical implementation of the reference apertures will have some shape function $S(u,v)$. We include this shape function in the calculation by defining the reference as the convolution of the shape S with the δ-function describing the position relative to the object; the object-reference

cross-correlation then becomes:

$$\begin{aligned} O \star R &= O^*(u,v) * [\delta(u-u_0, v-v_0) * S(u,v)] \\ &= [O^*(u,v) * \delta(u-u_0, v-v_0)] * S(u,v) \\ &= O^*(u-u_0, v-v_0) * S(u,v) \end{aligned} \qquad \text{(Equation 3.20.)}$$

Here, we have relied upon the associativity of the convolution operator.

Equation 3.20. simply says that as the reference becomes larger, the object-reference cross-correlation becomes blurrier. For experiments which perform no further analysis of the hologram besides inverting the far-field diffraction pattern, this presents a fundamental trade-off in the Fourier transform holography strategy. Making the reference aperture larger increases the illumination it transmits and thereby increases the intensity of the cross-correlation which gives the image of the field in the object aperture. However, making the reference larger simultaneously decreases the resolution of the final image by convolving the image of the object with a more extended function, leading to a blurry image. The situation becomes substantially complicated when the shape function $S(u,v)$ becomes sufficiently large that it may also include structure, whether directly in the shape or in the field passing through the aperture. More advanced schemes for using larger references to increase flux have been described by several researchers [94, 95]. Due to the increased difficulty of fabrication and analysis, we do not attempt to implement those techniques.

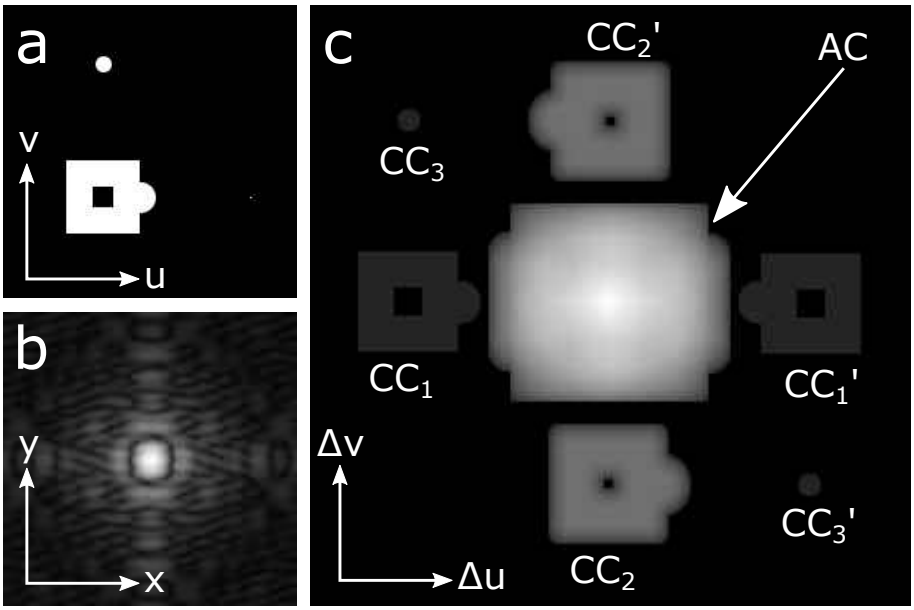

FIGURE 3.6.. A basic Fourier transform holography simulation with a δ-like and large circular reference. (a) shows the simulated test object with both a δ-like reference and a larger circular reference, (b) the central portion of the far-field diffraction pattern, (c) the inverse Fourier transform of (b) with the various terms of Equation 3.18. labeled.

3.6.3. Simulation of Image Formation

We illustrate these core Fourier transform holography concepts with a simulation shown in Figure 3.6.. Fig. 3.6.(a) shows the fictitious test object, which we have made a square donut with a protuberance to provide orientation; it transmits in an essentially binary fashion, with the white region having transmittivity one and the black regions having zero. We include two reference apertures with the test object: along the horizontal axis we place a small, δ-like aperture, and along the vertical axis we place a much larger circular aperture. Fig. 3.6.(b) shows the modulus of the central region of the Fourier transform of (a) (contrast has been reduced for visibility). The Fourier modulus displays the interference fringes characteristic of separated apertures. We easily observe

fringes with their periodicity along the vertical axis, particularly in the ring of intensity surrounding the central scattering maximum; however, we find no fringes with periodicity along the horizontal axis by visual inspection alone. The much larger integrated area of the large reference versus the small reference causes this difference in fringe visibility.

Fig. 3.6.(c) shows the inverse Fourier transform of (b) and the visual representation of Equation 3.18.; the various terms of that equation are labeled on the image. At center we find AC, the sum of the autocorrelations of the three apertures, all co-centered. CC_1 and CC_1' denote the cross-correlation of the test object and the small δ-like reference and its rotated complex conjugate. CC_2 and CC_2' denote the cross-correlation of the test object and the large circular reference and its rotated complex conjugate. CC_3 and CC_3' denote a term missing from Equation 3.18.: the cross-correlation of the two references and its complex conjugate. Generalizing the reference function $R(u, v)$ in Equation 3.16. to allow for multiple reference apertures will produce a cross-correlation between every possible pair of references. The various cross-correlations are displaced from the center of the $(\Delta u, \Delta v)$ coordinate system by the relative displacement between the aperture pair. In the case of the autocorrelations, there exists no relative displacement between the aperture and itself, centering the autocorrelations at $(\Delta u, \Delta v) = (0, 0)$. Convolution with the tiny δ-like reference makes CC_1' and CC_1' sharp but dim. In contrast, convolution with the larger aperture makes CC_2 and CC_2' much brighter but blurry; this confirms the intensity-resolution trade-off predicted by Equation 3.20..

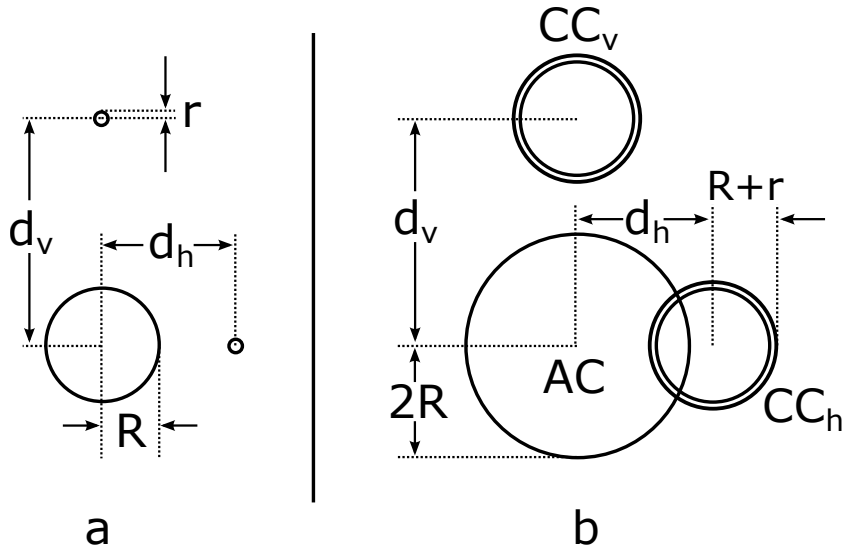

FIGURE 3.7.. The holographic separability condition. For object-reference cross-correlation to avoid overlappingthe autocorrelation of the object, the center-to-center distance between the object and reference apertures must exceed $3R + r$.

3.6.4. The Holographic Separability Condition

We implicitly assume in the simulation of Fig. 3.6. that the autocorrelations and the various cross-correlations do not overlap in the $(\Delta u, \Delta v)$ plane. In experimental realizations of Fourier transform holography, we generally strive to meet this condition as there exists no method for decomposing an arbitrary sum of the autocorrelation and a cross-correlation within the overlap region. Consequently, the need for separability of the hologram terms imposes a constraint on the design of the apertures. We graphically consider the holographic separability condition in Figure 3.7., showing the basic aperture arrangement in Fig. 3.7.(a) and the holographic images in Fig. 3.7.(b). The aperture arrangement extends that in Fig. 3.6., with a large object aperture, here a circle of radius R, and two small reference apertures of radius r. Some distance d_v separates the object and vertical reference, while d_h separates the object and horizontal reference. In the holographic domain, the autocorrelation region remains circular in shape but now has radius

$2R$. The center-to-center distance between the autocorrelation region and the cross-correlation terms CC_v and CC_h remains d_v and d_h, respectively, and the radius of the cross-correlations is $R + r$. The ring graphic used for the cross-correlations illustrates the increase in extent from convolution with the finite-size reference. From Fig. 3.7., the derive the condition for an object-reference cross-correlation to stay wholly separate from the object autocorrelation:

$$d_{obj-ref} \geq 3R + r \qquad \text{(Equation 3.21.)}$$

In Fig. 3.7.(b), $d_v > d_{obj-ref}$ and $d_h < d_{obj-ref}$. As a result, the horizontal cross-correlation fails the separability condition and overlaps with the autocorrelation.

3.6.5. Hybrid Holography-Imaging in the Large Reference Limit

We now consider the usefulness of the Fourier transform holography geometry even in the case of non-ideal apertures. In particular, due to the difficulty of fabricating very small, high quality references using standard techniques such as focused-ion beam milling, we examine options for analyzing diffraction patterns using references significantly larger than the δ-like assumption of Equation 3.19.. Fig. 3.6. already illustrates this situation. In this case, the convolution with the large reference serves to reduce the resolution of the object-reference cross-correlation. However, combining the initial Fourier transform holography result as in Fig. 3.6. with the iterative algorithms demonstrated earlier allows the deconvolution of the object and reference by more exactly solving the phase problem in the large-reference limit. From this point of view, we should consider the object-reference aperture system more generally as a single, large, asymmetric

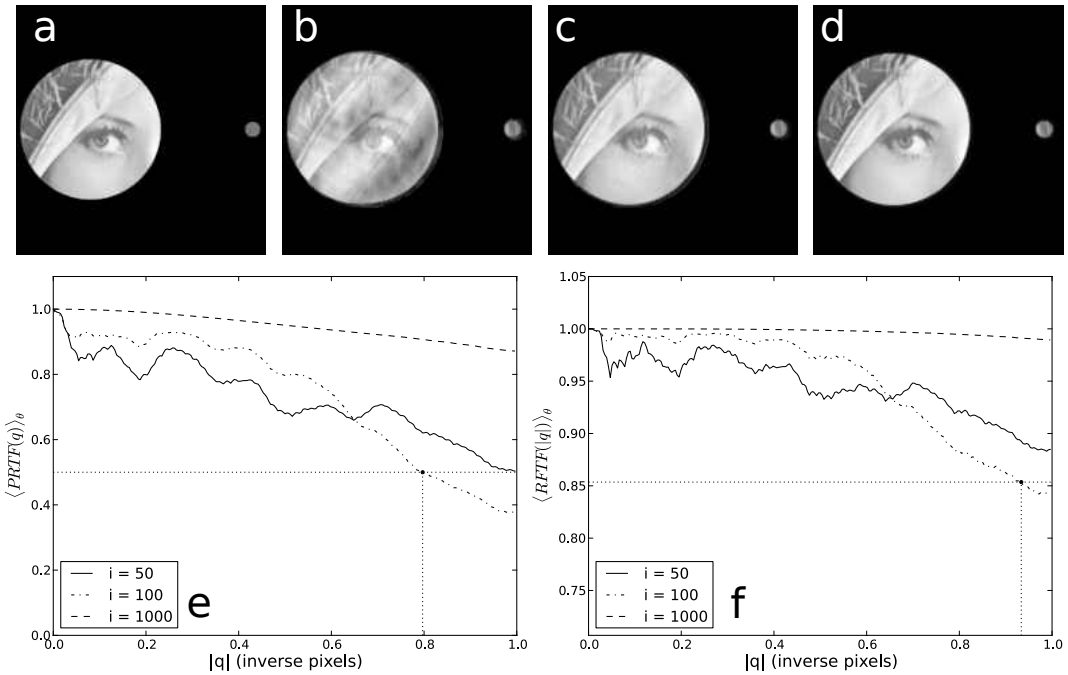

FIGURE 3.8.. Combining holography and iterative phasing with a tight support. (a) shows the original object; (b), (c), and (d) the averaged reconstruction (magnitude component) from 500 independent trials after 50, 100, and 1000 iterations, respectively. (e) and (f) show the PRTF and RFTF for the recovered test objects, respectively.

aperture, in which the "reference" aperture provides a powerful symmetry-breaking component to the real-space image.

We simulate the effect of a large reference aperture in Figure 3.8.. Extending the previous simulations of iterative phasing algorithms, we use as the object aperture a circular pinhole of radius 60 pixels but now include a large reference of radius 6 pixels inside the holographic separability distance given in Equation 3.21.. In addition to being much larger than a single-pixel δ approximation, the reference may also contain structure from the underlying test image. We show the original object in Fig. 3.8.(a), and the average reconstruction of 500 independent trials after 50, 100, and 1000 iterations each in (b), (c), and (d), respectively. After just 50 iterations the we recognize the average reconstruction, and after 100 iterations the

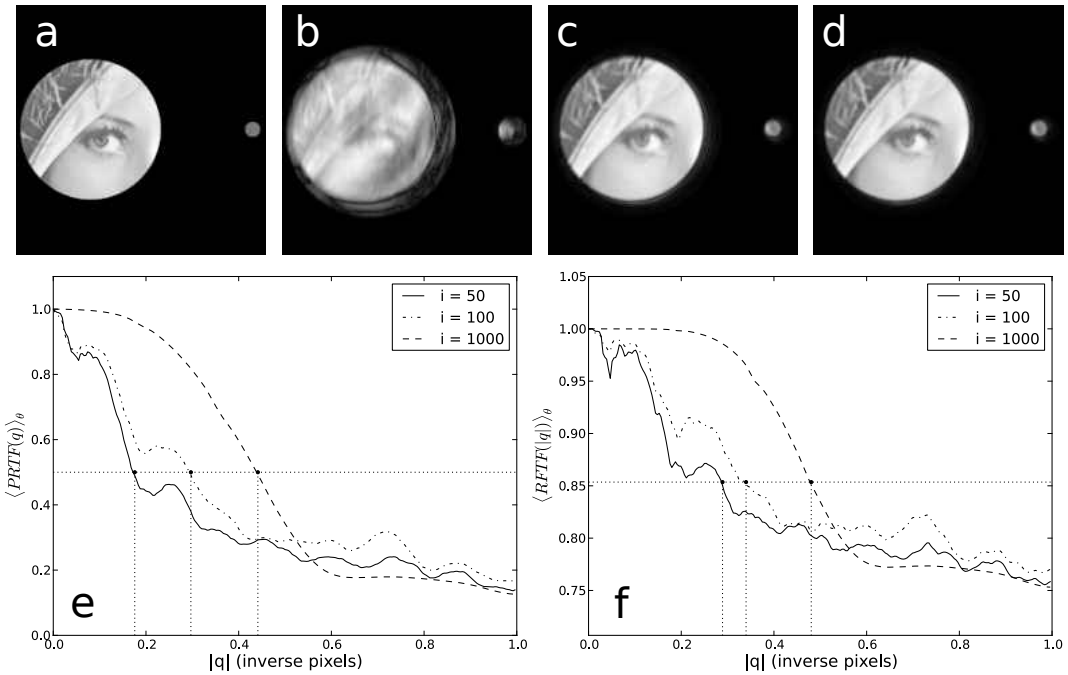

FIGURE 3.9.. Combining holography and iterative phasing with a loose support. (a) shows the original object; (b), (c), and (d) the averaged reconstruction (magnitude component) from 500 independent trials after 50, 100, and 1000 iterations, respectively. (e) and (f) show the PRTF and RFTF for the recovered test objects, respectively.

averaged reconstruction has, according to the PRTF in Fig. 3.8.(e) and RFTF in (f), achieved nearly perfect reconstruction; after 1000 iterations, the PRTF does not pass the cutoff at any $|\mathbf{q}|$. Qualitatively, the reconstruction behavior of the Fourier transform hologram closely resembles that seen in the asymmetric notched support in Fig. 3.3.(c). However, using a multipartite support seems to give even faster, better reconstructions [85].

The Fourier transform holography approach also provides an easy method for generating a good initial estimate of the size and shape of the support. Referring back to Fig. 3.7., the we can estimate object aperture by the perimeter of the object-reference cross-correlation and the object-reference separation distance by finding the distance between the center of the cross-correlation and the

autocorrelation. We have more difficulty estimating the size of the reference aperture. However, as the simulation in Figure 3.9. shows, even a relatively poor estimate of the support can lead to good reconstructions with the Fourier transform holography apertures. In this simulation, we repeat that of Fig. 3.8. but enlarge the support. We can glimpse the extent of the larger support in Fig. 3.9.(b) as the wispy region surrounding the main object. After 100 iterations, however, the average reconstruction has strongly converged, and after 1000 iterations the PRTF cutoff extends to approximately 0.5 inverse pixels. At this point, tightening the estimate of the support and additional iterations would generate an improved reconstruction.

CHAPTER IV

COHERENT IMAGING IN REFLECTION GEOMETRY

4.1. Introduction and Motivation

Nearly the entirety of the coherent imaging literature, including the papers cited earlier, describes experiments conducted in a transmission or forward-scattering geometry. Some exceptions to this rule exist [55, 96, 97], but generally only in the case of imaging nanoparticles in a Bragg geometry in which case the samples provide a support constraint endogenously, or with optical light and a very simple sample in a manner which logically replicates the requirements of a transmission experiment.

An extension of coherent imaging techniques in reflection geometries to extended and more arbitrary samples beyond nanoparticles would vastly increase the range of interesting physical samples amenable to coherent techniques. As a canonical example of our goals in this regard, we highlight the orbitally-ordered phase in half-doped manganite [98]. In this phase, the lattice, charge, spin, and orbital degrees of freedom in the 3d electrons of the manganese atoms become coupled, but on length-scales which are incommensurate and for reasons not yet fully understood. Previous work in our group by Josh Turner [32] focused on measuring the dynamics of this phase through XPCS, but the techniques did not exist to invert those speckle patterns to form images of the field leaving the crystal. For this and other purely electronic phases which are characterized by charge or orbital ordering, such as the spin-spiral state of dysprosium, magnetite below the Verwey transition [99], and the charge stripes in cuprates and nickelates [100, 101],

coherent imaging provides a unique opportunity to directly image phases accessible to few other techniques.

In this chapter, we develop a technique which could image extended samples in reflection geometries. We first consider various possible imaging geometries, then how to mount the sample properly to ensure best image fidelity in the reconstruction. Next, we explain in detail the steps to collect and condition the diffraction data to make it suitable for phase reconstruction using the iterative algorithms discussed in the previous chapter. Because the imaging geometry we use in this experiment separates the sample and the support-defining apertures, we then reconstruct the sample and back-propagate it to the original sample plane, developing a metric to judge the correct propagation distance. Finally, we spend considerable time to understand the effect which separating the sample and apertures exerts on the resolution of the final propagated image. The techniques we describe in this chapter were partially published earlier [102].

4.2. Choosing a Geometry for Reflection Imaging

In reflection geometry, we find a much higher degree of difficulty in establishing the support constraint necessary for diffractive imaging.

In Figure 4.1. we show cartoon schematics of three possible sample geometries for imaging in reflection. On the basis of the location of the aperture, we broadly label these geometries "On sample," "Upstream," and "Downstream." In the following sections, we consider the advantages and disadvantages of these three geometries, paying particular attention to light-in-light-out conditions in both low-angle and high-angle scattering situations.

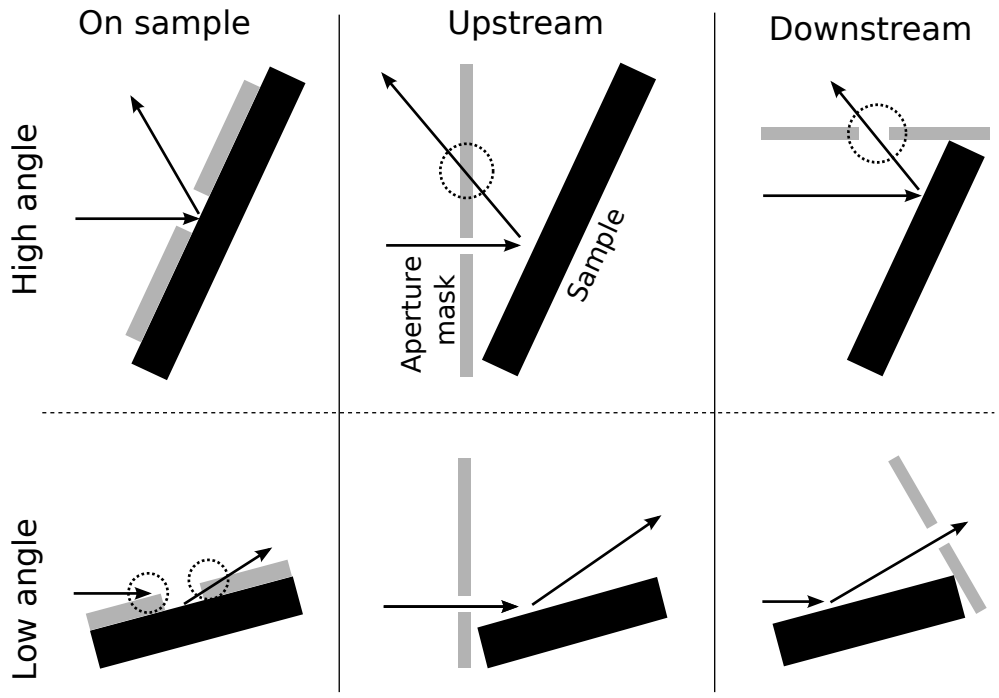

FIGURE 4.1.. Three candidate geometries for coherent imaging in reflection. Dashed circles indicate potential light-in-light-out violations.

4.2.1. Pinhole on Sample

The most direct, and most obvious, strategy to apply coherent imaging techniques developed in transmission geometries to the reflection geometries of interest by placing a pinhole directly on the sample. An experiment in which apertures were produced by means of photolithography on a known test-pattern sample for coherent imaging in the visible regime using lasers was reported earlier by researchers [97]. At x-ray energies, however, fabricating a pinhole directly on the surface of a sample poses a set of unique challenges.

First, the high penetrating power of x-rays requires a relatively thick coating of gold over the surface of the sample to block all scattering except from within the aperture. The apertures fabricated on the surface of the sample must fit within the coherence length of the beam for the coherent-scattering assumption

to remain valid. Consequently, for some range of small incident angles, the ratio of the thickness of the gold coating to the size of the aperture introduces a light-in-light-out problem due to the shadows cast over the aperture by the layer of gold.

Second, many of the samples available for imaging orient such that the scattering plane lies in the same plane specular reflection. In these cases, we record an incoherent superposition of the desired signal from within the pinhole and the undesired diffuse signal from the gold and the specular reflection. At small incidence angles, the specular reflection from a gold coating would almost certainly overwhelm the relatively weak coherent diffraction pattern, poisoning the reconstruction.

However, at large incidence angles, the approach of putting a pinhole aperture directly on the sample would avoid both problems more fully, as moving near normal incidence ameliorates both the the aspect ratio and shadowing problems and the strength of the specular reflection drops with increasing angle [10].

Additionally, making good pinholes on a sample will generally require some sort of lithographic method, either photo- or electron-beam assisted. In either case, the combination of photoresist and the strong chemicals used to remove it may damage the sample.

4.2.2. Pinhole Upstream of Sample

We next consider the issues around a pinhole upstream of the sample, as researchers often use photo-correlation experiments to restrict the illumination to a mutually coherent area without regard for the form the illumination takes on the sample.

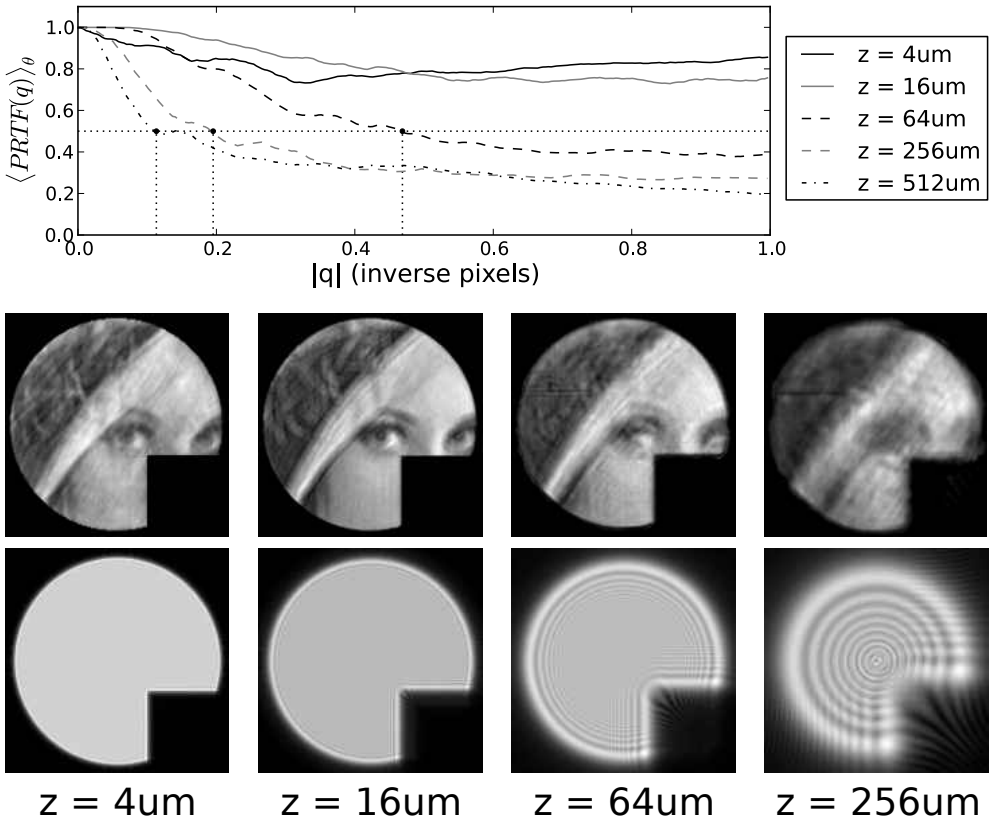

FIGURE 4.2.. Reconstructions fail in an upstream-pinhole geometry as the illumination becomes more diffuse with increasing distance. Top, PRTF for reconstructions with an upstream pinhole; bottom, near-field illumination functions and the resulting averaged reconstructions.

The light-in-light-out problem present in the case of high incidence angle is obvious. Because the beam is large compared to the coherence area, the extent of the mask surrounding the aperture must be very large so that the only light reaching the sample is that which passes through the aperture instead of passing around the sides of the mask. Consequently, at high angle the aperture mask blocks not only the incident x-ray beam but the diffracted x-ray beam as well. We could possibly solve this problem by fabricating a complicated set of apertures on the mask for both entry and exit of the illumination. Because of the angular relationship between exit and entry, however, the correct separation distance between the two apertures would depend strongly on the separation distance between the pinhole and the sample surface. We would struggle mightily to control that parameter with the level of precision required for this geometry.

In the case of low incidence angle, no light-in-light-out problem exists. However, a second and more fundamental problem takes its place: while the edge of the pinhole provides a support when considering only the pinhole plane, by the time the illumination reaches the sample it has already diffracted substantially and become diffuse. We simulate the outcomes of imaging experiments using a forward-propagated wavefield in Figure 4.2.. The simulation parameters here are an asymmetric pinhole of radius $3\mu m$ with illumination energy $640eV$. We show the propagation distance z on the Figure. As z increases, the illumination (bottom row) becomes more diffuse and the averaged reconstruction, formed by the same procedure as in Fig. 3.3. with several rounds of support refinement, becomes less clear. The PRTF for the simulations, shown in the top row, quantifies the degree to which the resolution suffers under diffuse illumination.

The lack of a well-defined support constraint is the primary cause of the loss of resolution. As the illumination becomes diffuse, contributions to the speckle pattern come from all parts of the sample instead of just the central illumination spot. Consequently, no support constraint whether supplied by hand or optimized by Equation 3.15. will accurately capture the illuminated region in a manner consistent with the requirements of the iterative algorithms.

Because of these limitations, we consider an upstream pinhole the worst geometry for imaging experiments.

4.2.3. Pinhole Downstream of Sample

Finally, we consider the limitations of a downstream pinhole. Of the three arrangements considered, a downstream pinhole diverges most strongly from the expectations of transmission coherent imaging by establishing the support constraint and selecting the coherent portion of the beam only after the x-rays have diffracted from the sample.

In the case of small incidence angle, no light-in-light-out problem exists.

In the case of large incidence angle, we encounter two separate light-in-light-out problems. First, if the mask over-rotates it will block the incoming beam. For this reason, we cannot keep the normal of the aperture plane parallel to the outgoing beam for incidence angles greater than forty-five degrees. This introduces the second problem, identical to the "On sample" arrangement: because we fabricate the apertures in the mask through lithography or focused-ion-beam milling, the orientation of the pinholes is typically along with normal of the mask instead of cutting through at some angle, and consequently above forty-five degrees we again find an aspect ratio problem with the thickness of the gold film and the

size of the aperture. In Fig. 4.1., this aspect ratio problem appears minor due to the exaggeration of the cartoon; in reality the aspect ratio problem becomes more serious.

In either case, this arrangement does provide the strong support constraint so necessary for coherent imaging and does not modify the sample, destructively or otherwise. For these reasons, we pursue this strategy for the experiment described next. However, meeting the support and no-modify conditions requires a trade-off: the solution procedure becomes two-step. First, we must use the coherent imaging algorithms to recover the complex wavefield passing through the apertures. Second, we must propagate the recovered wave-field back to the sample plane from the aperture plane. While we can achieve both steps, the limited coherence length of the beam ultimately means that we must place the apertures as close to the sample surface as possible. Next, we describe how to mount the sample and apertures to minimize the separation distance in reflection, and how that distance may be measured with at least some accuracy.

4.3. Sample Mounting

We show the basic geometry for reflection imaging with an aperture in the near field in Figure 4.3.. Fig. 4.3.(a) shows the scattering geometry. The x-ray beam approaches from the left onto a sample mounted on the standard beamline puck, which we have rotated to some incident angle θ. We fabricate the apertures in the silicon nitride membrane on the backside of a commercially-available silicon wafer. We mount the silicon wafer in a slot cut into the body of the puck at the angle $90^\circ - \theta$. This angle orients the wafer normal to the scattered x-rays, and consequently maximizes the signal transmitted through the apertures by

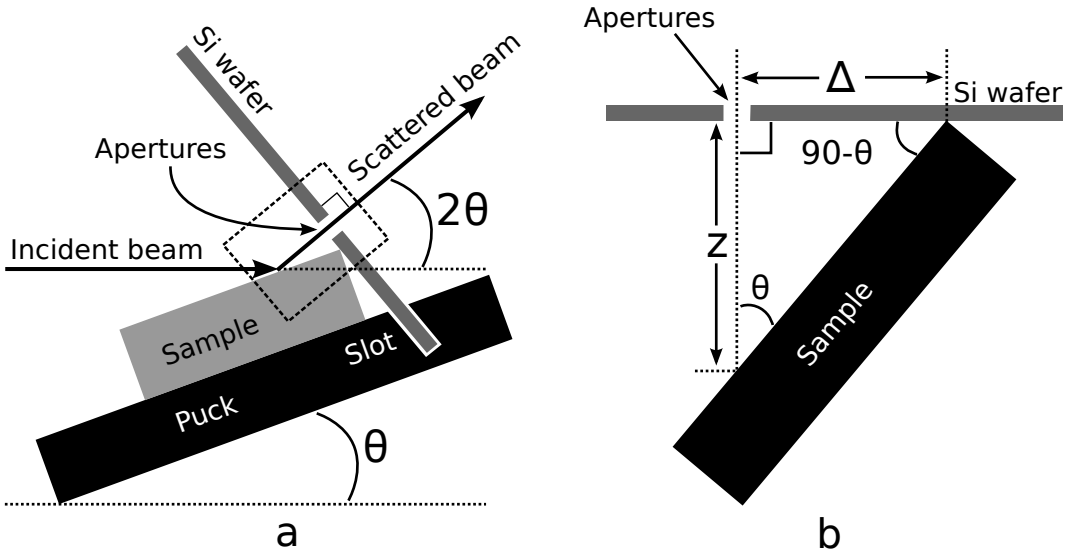

FIGURE 4.3.. The mounting geometry for reflection imaging. (a) shows the incoming x-rays incident on the sample with angle θ, passing through the pinholes, and reflecting to the detector in the far field at 2θ. (b) diagrams the separation distance z between the sample and the apertures; we measure Δ, not z.

presenting the full aspect of the apertures to the scattered beam in the near field. The scattered light passes through the apertures and diffracts onto the detector at scattering angle 2θ.

The most critical aspect of the sample mounting process is minimizing the distance between the surface of the sample and the near field apertures along the path of the scattered light. Fig. 4.3.(b) reorients the boxed region of Fig. 4.3.(a) to show how the angle of incidence and the height of the sample relative to the apertures effect the near-field propagation distance. Mounting the sample in such a way that it stays in direct physical contact with the wafer so that no gap exists helps minimize the propagation distance z. Labeling the distance between the sample-wafer point of contact and the apertures Δ, the propagation distance

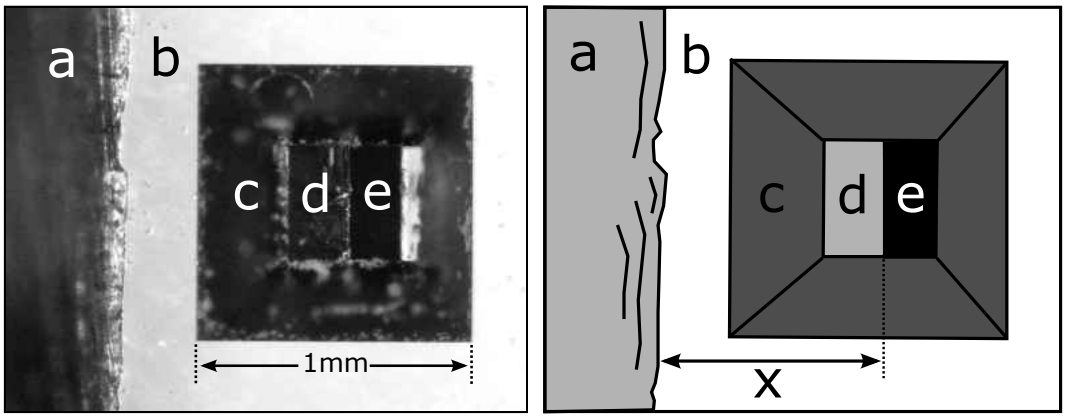

FIGURE 4.4.. The aperture plane and the sample viewed through the window of the silicon wafer with an optical microscope. Left, a photograph taken with the microscope; right, a cartoon reduction emphasizing the salient features.

follows the simple trigonometric relationship:

$$z = \frac{\Delta}{\tan(\theta)} \qquad \text{(Equation 4.1.)}$$

We require the formulation of the distance z in terms of the distance Δ as given in Equation 4.1. because while we have no method for directly measuring z after putting the apertures in place, we can easily measure Δ using standard microscopes.

In Figure 4.4. we illustrate measuring the quantity Δ using an optical microscope with encoded translation stages. This figure shows the sample and puck viewed along the z axis of Fig. 4.3.(b) with the puck held in a special mount cut such that the aperture wafer rests parallel to the ground and viewable from normal incidence. The left panel of Fig. 4.4. shows a micrograph of the puck, wafer, and sample taken while in the mounting jig; the right panel shows a simplified cartoon of the same image. We label the salient features a through e: a is the tilted surface of the puck, b is the silicon wafer made parallel to the ground, c is

the window etched into the silicon wafer, d is the sample, and e is empty space. As the first step in measuring Δ, we use a "dummy" silicon wafer similar to the one which contains the apertures but whose silicon nitride membrane we have removed. With the sample visible through the popped window, we measure the slot-sample separation x by centering the edge of the slot (the a/b boundary) in the microscope's field of view, zeroing the coordinates on the microscope's translation encoder, then re-centering on the edge of the sample; this gives x on the encoder readout. Replacing the "dummy" wafer with the actual apertures and measuring the distance from the slot edge to the pinholes gives Δ simply as the difference of the two measurements:

$$\Delta = x_{apertures} - x_{dummy} \qquad \text{(Equation 4.2.)}$$

Several obvious sources of error can lead to inaccuracies in Δ. First, the puck and its mounting jig freely rotate on the optical table of the microscope. As a result, the jig may be slightly misaligned with respect to the translation axis, and the measurement of the distance from the slot edge to either the sample edge or the pinholes therefore less than true by a factor of the cosine of the misalignment angle. Second, the rough edge left by cutting the slot into the puck makes defining the precise location of the slot problematic. Typically, we attempt to zero the translation coordinates on the same easily-identifiable feature. Because of these two difficulties we consider any particular measurement of Δ good only to within several microns.

Figure 4.5. shows the physical implementation of the puck with a sample and apertures correctly aligned. Upper left shows a photo from the side with the puck, sample, and dummy wafer in profile. In the cartoon schematic to the right of the photo, a marks the sample, b the silicon wafer, and d the puck. Lower left shows

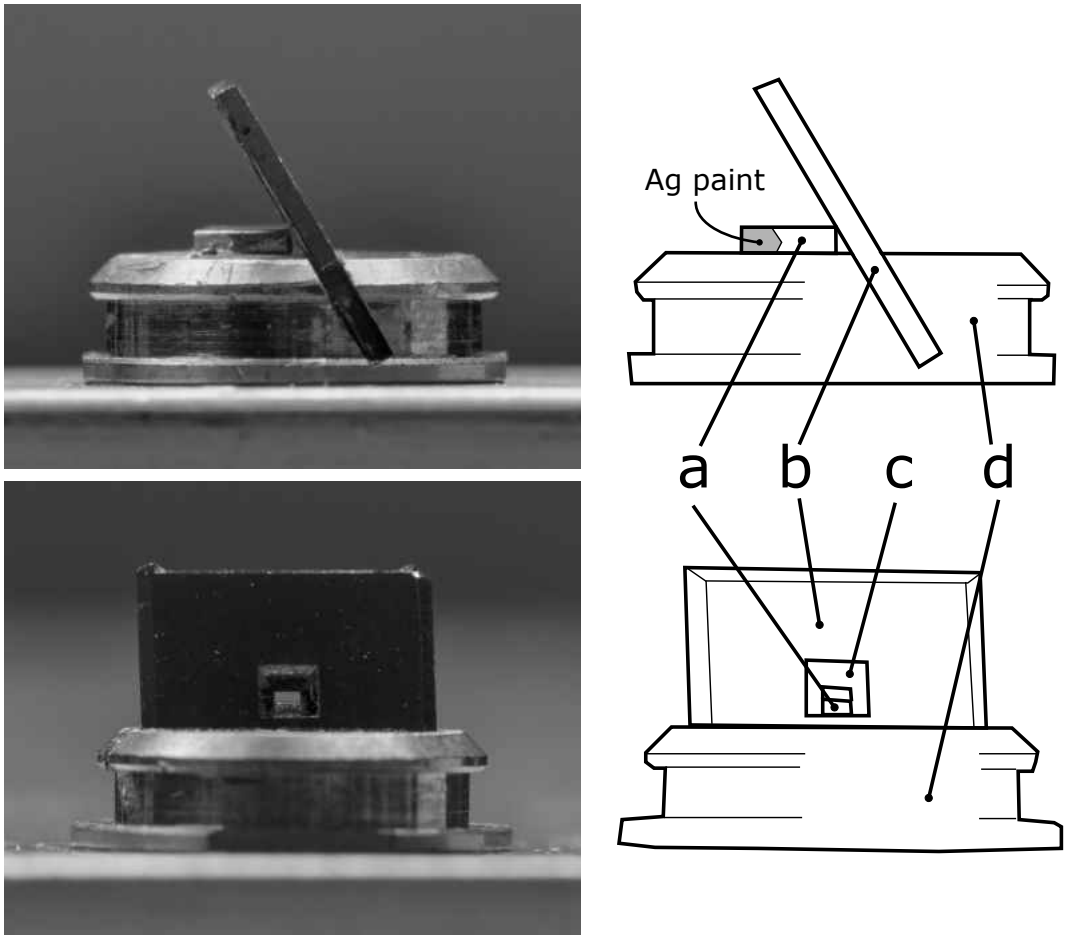

FIGURE 4.5.. A sample and "dummy" aperture wafer correctly mounted on a puck. *a* marks the sample, *b* the dummy wafer, *c* the window etched into the silicon, and *d* the puck. We see no gap between the wafer and sample, and the sample sits about halfway up the window.

the same sample rotated so as to view it from the upstream point of view. Here we see the etched window and through it the sample. In the cartoon schematic of this photo, we mark the window c. In the upper photo, we see no gap between the corner of the sample and the silicon wafer, the first condition for minimizing the propagation distance. In the lower photo, close examination shows that the sample comes up to about halfway within the window, indicating that it is nearly the correct height to minimize Δ; this follows from most of our pinhole apertures being located nearly in the center of the window.

To minimize Δ, we must ensure no gap exists between the aperture wafer and the sample edge. We must carefully manage the height of the sample above the puck, as we lack an easy way to adjust the height of the apertures. In other words, $x_{apertures}$ is fixed but x_{sample} has some freedom to vary, albeit with some difficulty. In aligning samples, the lack of a puck with a continuously variable height surface meant that adjustments to the height of the sample came through manual discrete variation of the adhesives used to fix the sample to the puck and inert shims placed between the puck and the sample. We first measured $x_{apertures}$ for the four orientations of the wafer, then measured x_{sample} using various combinations of double-sided scotch tape, aluminum foil, and thin stainless steel shims provided by the machine shop until Δ reached an acceptable value. Given an upper limit on the acceptable value of z and the incidence angle of the experiment (set, for example, by the resonant Bragg condition), Equation 4.1. sets a range of acceptable Δ values between approximately $5\mu m$ and $z\tan(2\theta)$. In the case of $\Delta < 5\mu m$, we typically assume that, given the precision in the measurements of $x_{apertures}$ and x_{sample}, such a small distance risk blocking the apertures with the sample. In Fig. 4.5., no tape or shims are visible as we found the sample fortuitously at the correct height even

in their absence. In this case, we mounted the sample to the puck by means of silver paint in the back corners; we marked this in the cartoon on the portion of the sample farthest from the wafer.

Although we attempted to mount samples systematically, the courseness of the available materials and the variability of the final measurement even under nominally identical conditions meant that such *ex-situ* mounting became fundamentally a process of trial and error.

4.4. Aperture Design Criteria

The set of apertures we place downstream from the sample must balance several competing factors, namely: flux, coherence, final image fidelity and ease of sample mounting, and in the case of holographic imaging the holographic separability condition.

Two factors argue for large apertures. First, the limited flux available at the beamline and the rather high number of photons required to form an image invertible to high spatial resolution argue for large apertures in order to decrease integration time. Second, at a given separation distance between the aperture and the sample, the recovered wavefield propagated from the aperture to the sample plane will retain higher fidelity with a large aperture. Equivalently, a large aperture allows a greater separation distance between aperture and sample at a given level of fidelity, and consequently allows for easier mounting of the sample with less trial and error. An in-depth discussion of the effect of aperture size and separation distance will occur later.

Coherence considerations argue for smaller apertures. Because the imaging algorithms assume fully coherent illumination and a Fourier transform propagator,

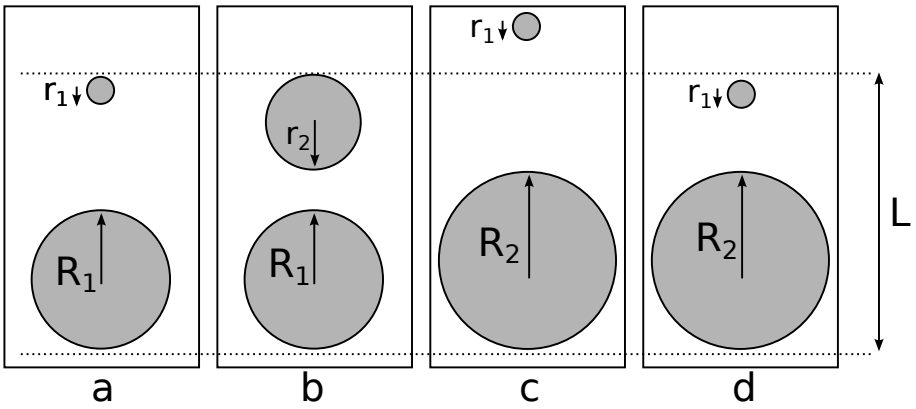

FIGURE 4.6.. Several candidate multi-partite aperture designs illustrating different balances of illumination criteria.

we must limit the extent of the aperture or set of apertures to within the beam's coherence length at the energy of interest. For typical coherence lengths available at beamline 12.0.2, this means that the apertures must all fit within a circle of approximately 4μm.

Finally, pursuit of a holographic imaging scheme, whether for easier reconstruction using iterative algorithms or in order to avoid using them entirely, requires that the object and reference aperture meet the holographic separability condition expressed in Equation 3.21..

We show four candidate aperture designs which balance these criteria in different ways in Figure 4.6.. In Fig. 4.6.(a), we maintain holographic separability and fully coherent illumination by making the object aperture relatively small. With the coherence length 4μm and the holographic separability condition $3R + r$, we assume $R_1 \approx 1\mu m$. Here, we also assume reference aperture size r_2 is small enough to approach a delta function. In order to meet these requirements, we sacrifice flux and propagation fidelity or easy sample mounting.

In Fig. 4.6.(b) we keep the object aperture R_1 at the previous $1\mu m$ size but enlarge the reference aperture substantially with $r_2 \gg r_1$. This increases the

total flux in the experiment, but in order to remain fully coherent we now clearly violate the holographic separability condition. In addition, a very large "reference" does not help with fidelity or mounting. Finally, as the size of the "reference" approaches that of the "object," we lose the valuable symmetry-breaking supplied by the second aperture as the apertures regain centro-symmetry.

In Fig. 4.6.(c) we keep the reference small and enlarge the object so that $R_2 > R_1$. To maintain separability with the larger R_2, we move the reference aperture farther from the object aperture. In comparison to (a), this increases total flux. Maintaining separability, however, requires that the apertures fall out of the bounds of the coherence length marked L. For this reason, we also must discount the improved fidelity afforded by the larger aperture, as this refers only to the propagated solution and we would consider untrustworthy a reconstructed image with apertures known to accept incoherent light.

In Fig. 4.6.(d), we again consider the larger object aperture with radius R_2. In contrast to (c), we keep the apertures within the coherence length but in doing so violate the separability condition. Such an aperture arrangement requires iterative phasing algorithms which are assisted by the multipartite nature of the support. In exchange, we achieve higher flux and better fidelity than the arrangement in (a).

When this project was developed, interest in the group was very high in pursuing an explicitly holographic imaging scheme. For this reason, we selected an aperture design most similar to that in Fig. 4.6.(a). However, in hindsight the reflection imaging experiment would have been more successful with an arrangement of apertures most similar to Fig. 4.6.(d).

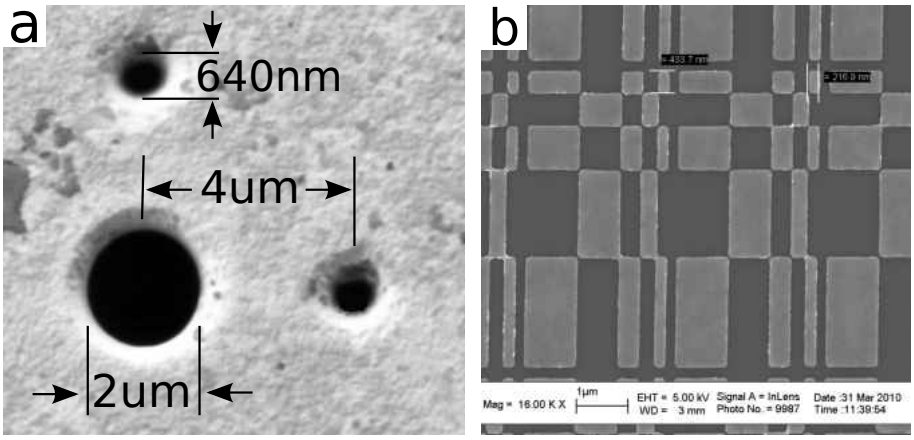

FIGURE 4.7.. The aperture set and experimental sample used for proving imaging in reflection.

In Figure 4.7.(a) we show an electron micrograph of the experimental apertures fabricated by means of focused ion-beam milling into a 1μm layer of gold evaporated onto a silicon nitride membrane. The object aperture measures approximately 1μm in radius, and along the two principal axes we placed a nominal reference aperture. While we requested references as small as feasible, our collaborator who fabricated the apertures reported that very small apertures are difficult with FIB. At approximately 640nm in diameter, the references approach the large-reference limit discussed earlier. However, as the supplied micrograph of the apertures provides a view only from the beam-side of the gold film and the apertures exhibit a tapered structure along the beam direction, we consider the aperture size measurements somewhat unreliable. The object and reference apertures have a center-center separation distance of around 4μm due to our assumption of 5μm horizontal coherence length.

4.5. Reconstruction of a Known Test Sample

We now show results of the experiment in which we demonstrate the efficacy of downstream-pinhole arrangement for imaging in reflection geometry.

4.5.1. Description of the Sample

To prove the validity of the downstream-pinhole imaging technique, we demonstrate the successful imaging of a known test pattern sample. We show an electron micrograph of the known sample in Figure 4.7.(b). Fabricated by collaborators at the Center for X-Ray Optics, the test sample consists of a two-dimensional series of nickel islands (lighter) deposited onto a silicon substrate (darker) using photolithography. A Barker code of sequence seven describes the position and size of the nickel regions [103, 104]. This function was recommended to use to avoid problems with the near-field Talbot effect seen from more regular patterns such as checkerboards [105, 106].

The size of the smallest element in the image's vertical direction measures approximately 434nm, and the size of the smallest element in the image's horizontal direction measures approximately 217nm. The largest features measure 1μm horizontally and 2μm vertically. These measurements all refer to the size when measured at normal incidence. We purposely distorted the feature size ratio in order to correct for the geometric foreshortening effect when operating in small-angle geometry. We wanted to set the features sizes such that the image features in the reconstruction became nearly square when setting the incidence angle of the x-rays to twenty degrees.

In this sample, the difference in reflectivity between the nickel and silicon regions provide the contrast mechanism for the reconstructed image.

4.5.2. Data Acquisition

After minimizing the distance between the apertures and the sample surface, we aligned the sample in the beamline 12.0.2 endstation to give maximum signal with $\theta = 20^{\circ}$ and an incident energy of $500eV$. We chose that energy to maximize both signal and coherence.

With the sample aligned and the position optimized for maximum signal, we collected data in a series of acquisitions rather than a single very long acquisition to allow for correction of drift of the speckle pattern on the detector or change in the speckle pattern due to fluctuations in the beam. During each exposure of the detector, we exposed for fifteen seconds which accumulated signal up to near the saturation point of the most intensely exposed pixels. We added twelve such exposures to create a single frame in the data series, and we took sixty total frames. The total acquisition time of the data collection was therefore three hours, not counting the approximately five seconds required to read the data from the detector after each fifteen second exposure. We acquired signal for so long to ensure a sufficient signal in the face of uncertainty regarding the level of necessary signal. After we finished acquiring signal from the sample, we closed the main endstation valve to block the beam and collected a dark frame for subtraction with identical acquisition parameters. The dark frame contains low levels of background signal from the chamber's ion gauge and small quantities of stray light which enter through various windows.

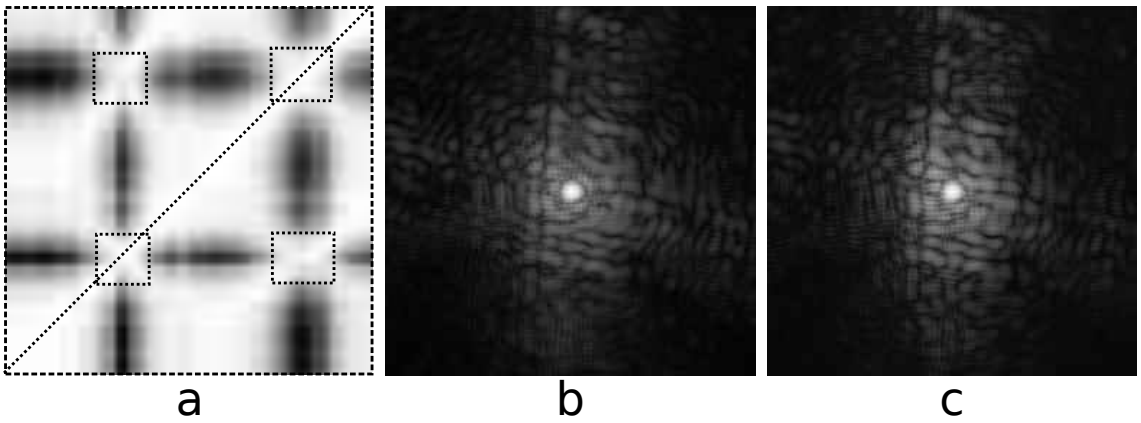

FIGURE 4.8.. Sorting experimental speckle pattern configurations to correct for fluctuations. In (a), the pixel at the coordinate (i, j) represents the peak value of the normalized cross-correlation between acquisitions i and j. (b) and (c) show the sum of the two resulting configurations after further conditioning (square root scale).

4.5.3. Data Conditioning

We put each of the sixty signal frames through several steps of conditioning prior to reconstruction. In order, these steps are: configuration sorting, dust removal, hot pixel removal, dark frame subtraction, and frame alignment.

4.5.3.1. Configuration Sorting

Although the we knew sample to be static and we ran the experiment at room temperature, we still observed morphological fluctuations in the speckle pattern distinct from variations in overall intensity. Given the known fluctuations in sample position relative to the beam caused primarily by undamped vibrations, we hypothesize that the sample moving slightly within the beam, resulting in a small change in the illumination function across the sample, caused these fluctuations in the speckle pattern. To divide the series of speckle patterns into groups of self-similar configurations acquired during periods of stability, we calculated the

normalized covariance, first defined in Equation 3.14. between all possible pairs of acquisitions. We show the result of these calculations in Figure 4.8.(a). In this plot, the pixel at image coordinate (i, j) represents the correlation coefficient between the i-th and j-th acquisitions in the series, with white pixels corresponding to more similar pairs speckle patterns and black pixels corresponding to less similar pairs of speckle patterns. The hypothesized instability of the sample relative to the beam can be easily visualized by tracing the image intensity across the bottom row, which plots the correlation of the first acquisition against all 59 subsequent acquisitions. The correlation coefficient stays high until approximately acquisition 15, at which point the images rapidly decorrelate. However, several frames later the patterns recorrelate, presumably as the sample returns to the most stable equilibrium position from whatever small excursion it underwent. A second short decorrelation begins at approximately acquisition 44, but the sample again recorrelates several acquisitions later. Interestingly, comparing the correlation of the frames in the first decorrelation region to the frames in the second decorrelation region shows a second region of mutual similarity; we mark these regions with the dotted boxes in Fig. 4.8.(a).

Fig. 4.8.(b) and (c) show the summed acquisitions from the primary and secondary speckle configuration after the additional conditioning described below. In comparing (b) and (c) side-by-side, we find the differences in the speckle configuration difficult to spot. However, comparing them by rapidly flipping between the two shows exchange of intensity between the large speckles, generated by the object aperture, as well as variation in the intensity fringes caused by interference from the two smaller reference apertures. As we find the majority of

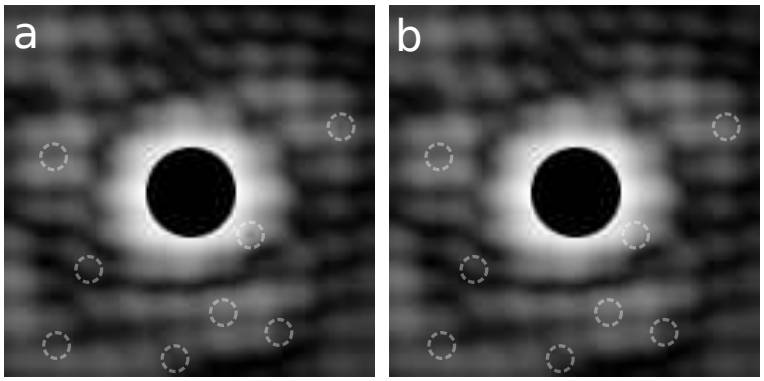

FIGURE 4.9.. Removing dust and similar distortions from the speckle pattern. (a) shows the speckle pattern afflicted by dust; (b) shows the same pattern after replacing the dust with interpolated intensity. We zero the bright central pixels to improve the visibility of the surroundings.

the signal in the primary configuration Fig. 4.8.(b), the following analysis will use only that data unless explicitly stated otherwise.

4.5.3.2. Dust Removal

Small dust particles or bits of fiber which have accumulated on the detector surface can distort the measurement of the speckle pattern by partially or wholly attenuating the transmission of the x-rays to the detector. We show examples of dust on the detector surface in Figure 4.9.(a), although the reduced contrast of the image makes them difficult to see. The highly oversampled nature of the diffraction pattern on the CCD leads to smoothly-varying speckle on the length scale of the important dust specks near the bright central speckles. We exploit this smooth variation to correct for the dust by replacing the data within specified dust-afflicted pixels with a spline interpolation of the intensity generated from clean neighboring pixels. Currently, this requires us to mark dust by hand, typically using a bitmap image editor to generate a binary mask of dust locations, as developing an algorithm which reliably distinguishes between dust and speckle

minima poses great difficulty. Fig. 4.9.(b) shows the same speckle pattern after successful dust removal. Each acquisition uses the same dust locations.

4.5.3.3. Hot Pixel Removal

After dust removal in each acquisition, we remove hot pixels created when high energy particles such as cosmic rays hit the detector or where the CCD damage leads to spurious current leakage. We use a simple median filter to remove hot pixels, replacing any pixel which exceeds a certain multiple t of the median pixel value in the surrounding environment withthat median value. Given a median filter $\hat{M}$ we define the hot pixel removal operator $\hat{H}$ as

$$\hat{H}\left(I(x,y);t\right) = \begin{cases} \hat{M}\left(I(x,y)\right), & I(x,y) > t\hat{M}\left(I(x,y)\right) \\ I(x,y), & \text{otherwise} \end{cases} \qquad \text{(Equation 4.3.)}$$

Next, we subtract a background dark image from each frame. In this particular data set, we acquired a series of dark images with the same acquisition parameters as the signal. Because the dark frames do not drift or reconfigure as the signal frames do, we performed the interpolative dust removal and hot pixel filtering after averaging the dark frames along the time axis. Subtracting the conditioned average dark frame $\langle D(x,y)\rangle$ from one of the sixty signal frames $I_n(x,y)$ is then simple:

$$I'_n(x,y) = |I_n(x,y) - \langle D(x,y)\rangle| \qquad \text{(Equation 4.4.)}$$

Often, however, we do not collect a dark frame with the same acquisition parameters as the signal. In these circumstances, we must consider the acquisition

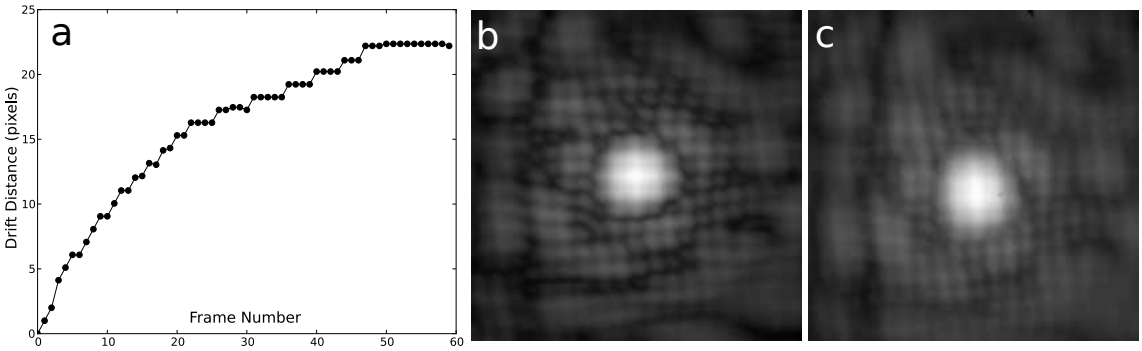

FIGURE 4.10.. Aligning experimental speckle patterns to compensate for drift on the detector. (a) shows the distance in pixels each frame drifted relative to the first frame, (b) the center of the frames sum after aligning, (c) the center of the frames sum before aligning.

time of the signal τ_n and the acquisition time of the dark images τ_d, and the dark current DC background I_{DC} of the CCD. With these additional parameters we generalize Equation 4.4.:

$$I'_n(x,y) = \left| |I_n(x,y) - I_{DC}| - \frac{\tau_n}{\tau_d} |\langle D(x,y)\rangle - I_{DC}| \right| \qquad \text{(Equation 4.5.)}$$

We most easily measure I_{DC} by averaging over several tens of pixels in the corner of the image where the signal is very low. On average, we find a dark current of 410 counts at the detector's operating temperature of $-50°C$ and a per-pixel readout time of $1\mu s$.

4.5.3.4. Frame Alignment

In the last step of conditioning the data for phase retrieval, we align and sum the conditioned frames from each of the two configurations. Instability in the sample or in the endstation led to the intensity pattern drifting on the detector over the course of the series of acquisitions. To correct for the drift of the speckle pattern, we cross-correlated the first frame in each of the two speckle

configurations with the subsequent members of the configuration. We used the location of the cross-correlation peak to shift the drifted speckle pattern back into alignment with the reference image; using numerical FFT algorithms, we find the cross-correlation peak of two aligned images at pixel (0,0) and the cross-correlation peak of two images displaced by a vector $(\Delta x, \Delta y)$ at either $(\Delta x, \Delta y)$ or $(-\Delta x, -\Delta y)$ depending on which Fourier transform we conjugate. Figure 4.10. shows the necessity of this step of the conditioning. In Fig. 4.10.(a), we show the drift distance, defined as $\sqrt{(\Delta x)^2 + (\Delta y)^2}$, between the first frame of the acquisition and all subsequent frames as a function of frame number. We calculate that the speckle pattern had drifted by more than 20 pixels on the detector by the end of the acquisitions. In Fig. 4.10.(b) and (c), we compare the effect of aligning frames. By not aligning the frames, the large amount of drift over the detector severely reduces the contrast in a manner analogous to reducing the coherence of the pattern, hampering the effectiveness of the reconstruction algorithms. In comparison, aligning the frames maintains the high degree of contrast between the speckles. We notice this reduction in contrast most particularly in the cross-hatched pattern in the intensity which comes from interference with the reference waves.

Fig. 4.8.(b) and (c) show the sums of the acquisitions separated into the two configurations.

4.5.4. Reconstruction of Conditioned Data

With the data conditioned we estimate the initial support for the phase reconstruction. As explained earlier, we base our initial estimate of the support on measurements of the auto- and cross-correlation terms in the inverse Fourier

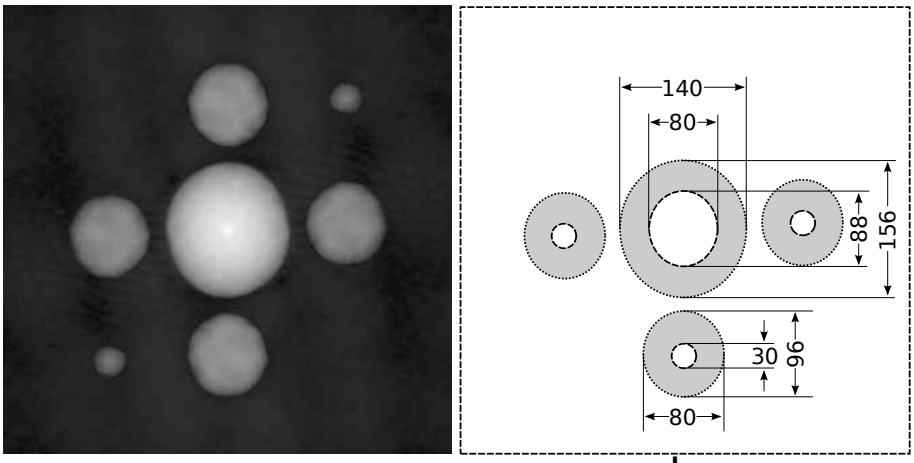

FIGURE 4.11.. Estimating the initial support using the inverted hologram as a guide. (a) shows the inverted hologram with the various correlation terms (log scale), (b) the dimensions of the hologram terms and the support estimate derived from them.

transform of the conditioned far-field intensity. We show the magnitude component of the correlation terms in Figure 4.11.(a). At center we see the autocorrelation; the four circles in the plus configuration are the object-reference cross-correlation terms and their rotated conjugates, and the two small dots along the diagonal are the reference-reference cross-correlation and its rotated conjugated. In the background where the signal should be zero, we see some fluctuations caused primarily not by counting statistics in the speckle pattern but rather by unresolved distortions in the detector response from dust or dead pixels. However, the magnitude inside the cross-correlation terms exceeds the average magnitude of the surrounding background by approximately a factor of seventy-five, so we do not worry about this signal in the reconstruction.

In Fig. 4.11.(b) we show a cartoon representation of the elements of (a) which contribute to the support estimate. We find that an ellipse with major and minor axes of approximately 156 and 140 pixels, respectively, fits the autocorrelation well.

The major and minor axes of the cross-correlation terms are approximately 96 and 88 pixels. We estimate the size of the object aperture by dividing the axes of the autocorrelation in half. Nominally, this gives an ellipse with major and minor axes of 78 and 70 pixels, but because we will refine this initial estimate further we set the object aperture at 88 by 80 pixels instead. We have more difficulty estimating the size of the reference apertures, but the size of the cross-correlations compared to half the size of the autocorrelation argues for a circle of approximately 20 pixels in diameter. The reference apertures have the further difficulty of position, so in the support estimate we make them circles with diameter 30 pixels, co-centered with the cross-correlation terms. Finally, because each reference generates two cross-correlation terms, we must properly select the correct pair of cross-correlations in order to correctly place the references in the support; selecting the primary cross-correlation of one reference and the conjugate of the other leads to a poorly converged solution. To resolve this dilemma, we include in the support a reference for *both* horizontal correlations, but only a single vertical reference. This arrangement allows the reconstruction algorithms to find which of the horizontal correlations correctly pairs with the selected vertical correlation.

The prior efforts to ensure a high degree of coherence in the experiment, to condition the data into a state suitable for reconstruction, and to generate a good initial estimate of the support constraint place the reconstruction into a well-formed state that successfully completes with no major intervention. Beginning with the initial support derived from the correlation terms of the hologram, we followed the reconstruction procedure described earlier for the simulated test pattern. We reconstructed 100 independent trials from random seeds by alternating 99 iterations of the hybrid input-output algorithm with 1 iteration of the error-

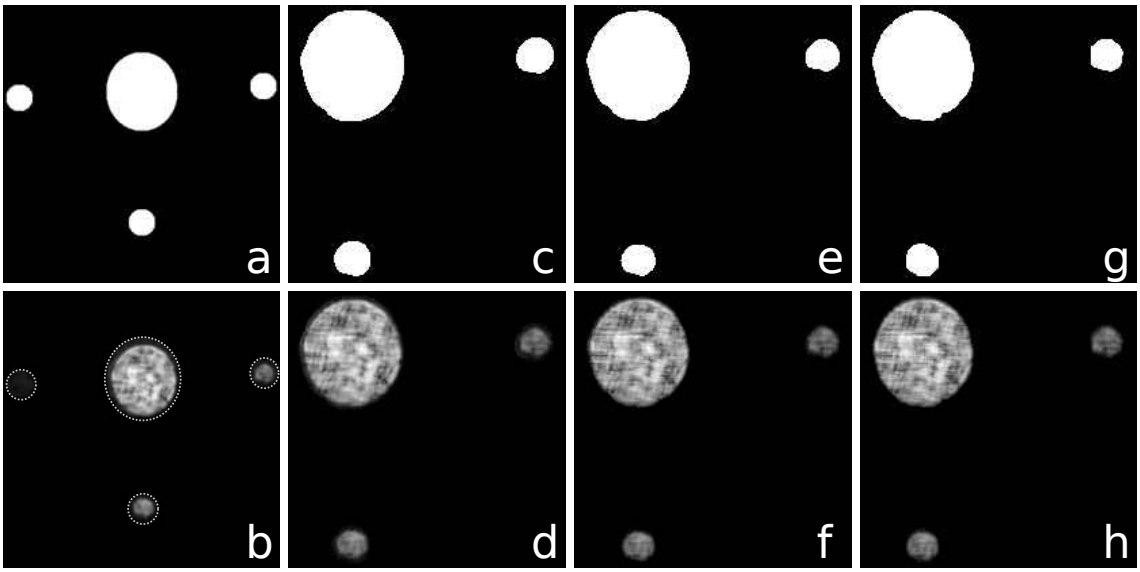

FIGURE 4.12.. Progression of support refinement and image reconstruction in the barker code data. (a) and (b) show the initial support estimated from the hologram and reconstruction; (c) and (d) show the first autorefined support and reconstruction; (e) and (f) show the final autorefined support and reconstruction; (g) and (h) show the hand-refined support and reconstruction. All reconstructions show only the square root of the magnitude component.

reduction algorithm for 1000 total iterations per independent trial. After all the trials had completed, we aligned the magnitude components and averaged the complex results. Using the averaged reconstruction, we refined the estimate of the support using Marchesini's blur-and-threshold algorithm, then repeated the reconstruction procedure with the refined support. We repeated the refinement loop until the support became self-consistent after five updates, at which point we performed an additional refinement of the support by hand on a pixel-by-pixel basis using a bitmap image editor.

In Figure 4.12. we show details from various stages within the reconstruction. Fig. 4.12.(a) and (b) show the initial support and the square root of the magnitude of the averaged reconstruction. As expected from the simulations, even with an intentionally loose support the average reconstruction is well-defined and

localized within the support region, which we mark in (b) with a white dotted line. Supplying the algorithm with a single location for the vertical reference but two locations for the horizontal reference also behaves as expected, with the reconstruction placing power in only one of the two options. Refinement of the support eliminated the alternative horizontal reference automatically. In Fig. 4.12.(c) and (d), we show the first algorithmically refined support and the resulting average reconstruction. The refinement algorithm substantially tightens the support, particularly around the object, although the difference in scale makes direct comparisons to (a) difficult. Small features become more evident in (d) compared to (b) as the quality of the reconstruction improves and sharpens. In Fig. 4.12.(e) and (f), we show the last algorithmically refined support and the resulting average reconstruction. Compared to the first refinement, slight changes appear in the support but the average reconstruction remains nearly identical. This story persists in examining Fig. 4.12.(g) and (h), which show the hand-optimized support and average reconstruction. From a qualitative standpoint, most of the improvement in the reconstruction comes from the first refinement of the support, with little additional improvement.

We calculate the quantitative degree of improvement in the reconstruction in Figure 4.13., which shows the PRTF and RFTF for each of the reconstructions in Fig. 4.12.. The average reconstruction in the case of the initial support passes the PRTF cutoff at approximately 0.39 inverse pixels. This improves substantially after the first round of support refinement, passing the cutoff at approximately 0.49 inverse pixels. Further refinement of the support until self-consistency of the update squeezes additional resolution from the reconstruction, reaching 0.52 inverse pixels. The additional hand-optimizations of the support constraint hardly move the

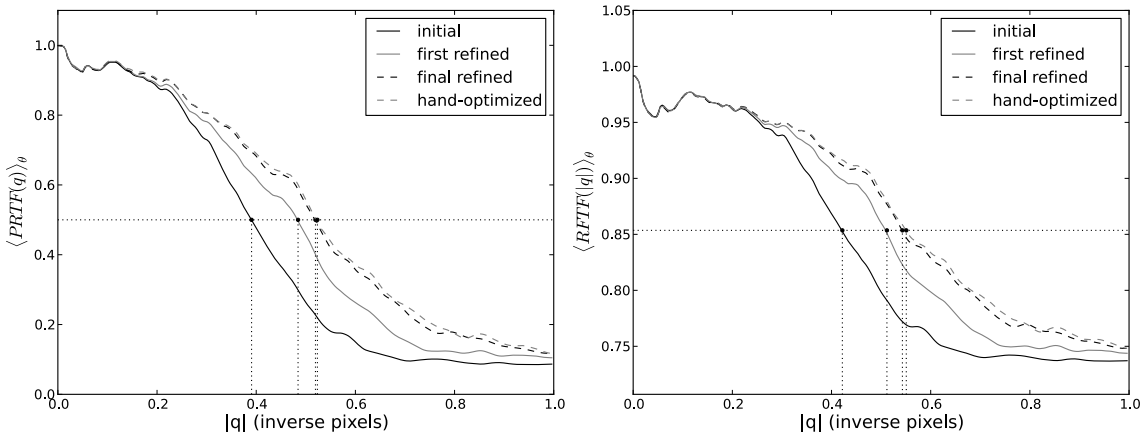

FIGURE 4.13.. Resolution estimates (PRTF and RFTF) for the experimental phase reconstruction shown in Figure 4.12..

PRTF cut-off value. This analysis confirms that discussed in qualitative terms from simple visual inspection of the reconstructions in Fig. 4.12.; the initial estimate from the hologram correlation terms gives a reasonable reconstruction which support refinement improves, but not dramatically. However, support refinement presents diminishing returns, and convergence of the reconstruction occurs quickly due to the strongly convergent nature of the separated and multipartite apertures. As typical, the RFTF generates somewhat different numbers, but the trend in the quality of the reconstruction does not change from that seen in the PRTF.

4.6. Propagation of the Reconstruction

The *ex situ* alignment technique we use to minimize the distance between the near-field apertures and the sample surface ultimately means that the true distance between the apertures and the surface *in situ* remains unknown. By the optical microscope measurements discussed earlier, we can estimate the correct propagation distance. However, various factors conspire to lower the accuracy of this estimate. In particular, the sample-aperture configuration may shift slightly

when being transferred to the experimental position, and the divergence of the beam past the focal point of the beamline's optics may introduce a phase curvature in the wavefront which alters the "true" back-propagation distance away from that which, when put into the propagation algorithms, gives the correctly back-propagated image. For these reasons, we require a numerical method to judge when we have found the correct back-propagation distance of the wavefield recovered at the apertures.

4.6.1. The Acutance Metric

We base our focusing metric on the general tendency of the diffraction phenomenon to spread out sharp features of the wavefield as it propagates away from the sample plane. In evaluating the correctness of the back-propagation, we therefore use a quantity called acutance which detects the amount of derivative content in the magnitude of the back-propagated wavefield:

$$\text{Acutance}\{\psi(z)\} = \iint_{\text{space}} \left|\nabla \left|\psi(z)\right|\right|^2 \, d^2r \qquad \text{(Equation 4.6.)}$$

In Equation 4.6., ψ is the wavefield, z the propagation distance, and ∇ the gradient operator. The square of the gradient operator is expressed in the usual cartesian coordinates as:

$$\left|\nabla \left|\psi(z)\right|\right|^2 = \left(\frac{d|\psi(z)|}{dx}\right)^2 + \left(\frac{d|\psi(z)|}{dy}\right)^2 \qquad \text{(Equation 4.7.)}$$

Equation 4.7. defines the gradient through analytic derivatives, but in our calculations the we represent the wavefield by a discrete numerical array. We therefore implement discrete numerical derivatives through Sobel filters, defined

as:

$$\frac{d\psi(z)}{dx} \approx \begin{bmatrix} -1 & 0 & +1 \\ -2 & 0 & +2 \\ -1 & 0 & +1 \end{bmatrix} * \psi(z) \qquad \text{(Equation 4.8.)}$$

$$\frac{d\psi(z)}{dy} \approx \begin{bmatrix} -1 & -2 & -1 \\ 0 & 0 & 0 \\ +1 & +2 & +1 \end{bmatrix} * \psi(z) \qquad \text{(Equation 4.9.)}$$

The matrices in Equation 4.8. and Equation 4.9. define discrete convolution kernels which act on the discretized $\psi(z)$ through the convolution operator $*$. The calculation of the derivative along either principal axis therefore requires the array element where we will calculate the derivative as well as its eight nearest neighbors. A number of software packages provide straightforward methods of implementing such discrete convolution kernels.

The acutance metric works by squaring the gradient of the back-propagated wavefield $\psi(z)$, then summing the result over the entire back-propagation plane. As $\psi(z)$ comes into correct focus at the sample, the amount of derivative content increases and the acutance peaks. We first examine simulations of back propagated wavefields to verify the behavior of the acutance metric, then turn attention to the back propgation of the experimental barker code data.

4.6.2. Finding the Correct Propagation Distance: Simulated Data

In Figure 4.14. we show the acutance curves calculated for the propagation of the wavefield recovered for a simulated test object of randomly distributed, perfectly absorptive gold balls on a uniformly transmissive substrate. The sample-

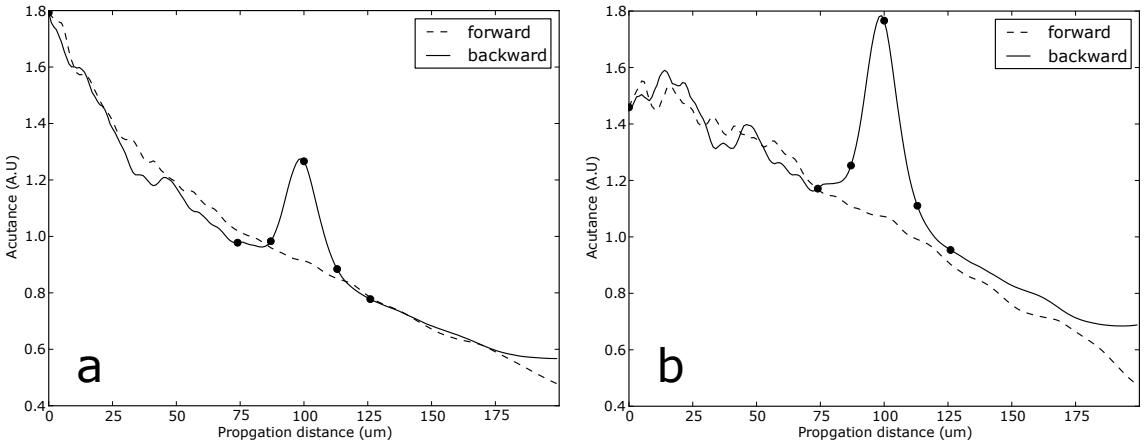

FIGURE 4.14.. Acutance calculation for a simulated test object as a function of propagation distance. In (a), we integrate the calculation for the forward and backward propagation over all space. In (b), we integrate only within the subregion of the simulated aperture. Black dots mark distances in Fig. 4.15.

aperture separation distance is $z = 100\mu m$, the pinhole radius $1.4\mu m$, and the illumination energy $500eV$. In Fig. 4.14.(a), we calculate the acutance strictly according to Equation 4.6. by integrating the square of the gradient over all space. We perform the calculation for both forward and backward propagated fields in order to qualitatively isolate the solution against the background behavior of the acutance; in both directions, the acutance starts high due to the large derivative signal generated at the edge of the aperture, then decreases as the aperture edge becomes diffuse. In only the backward direction, however, do we see a peak at the known solution distance $z = 100\mu m$. Fig. 4.14.(b) shows the same calculation repeated after we set as region of integration a circular disk co-centered with the near-field aperture but with a radius of $1.2\mu m$. With this modification, we aim to remove the influence of the relatively sharp aperture edge by not including it in the integration. In comparison to the series in (a), discarding the aperture edge greatly suppresses the acutance at low z and improves the visibility of the solution peak.

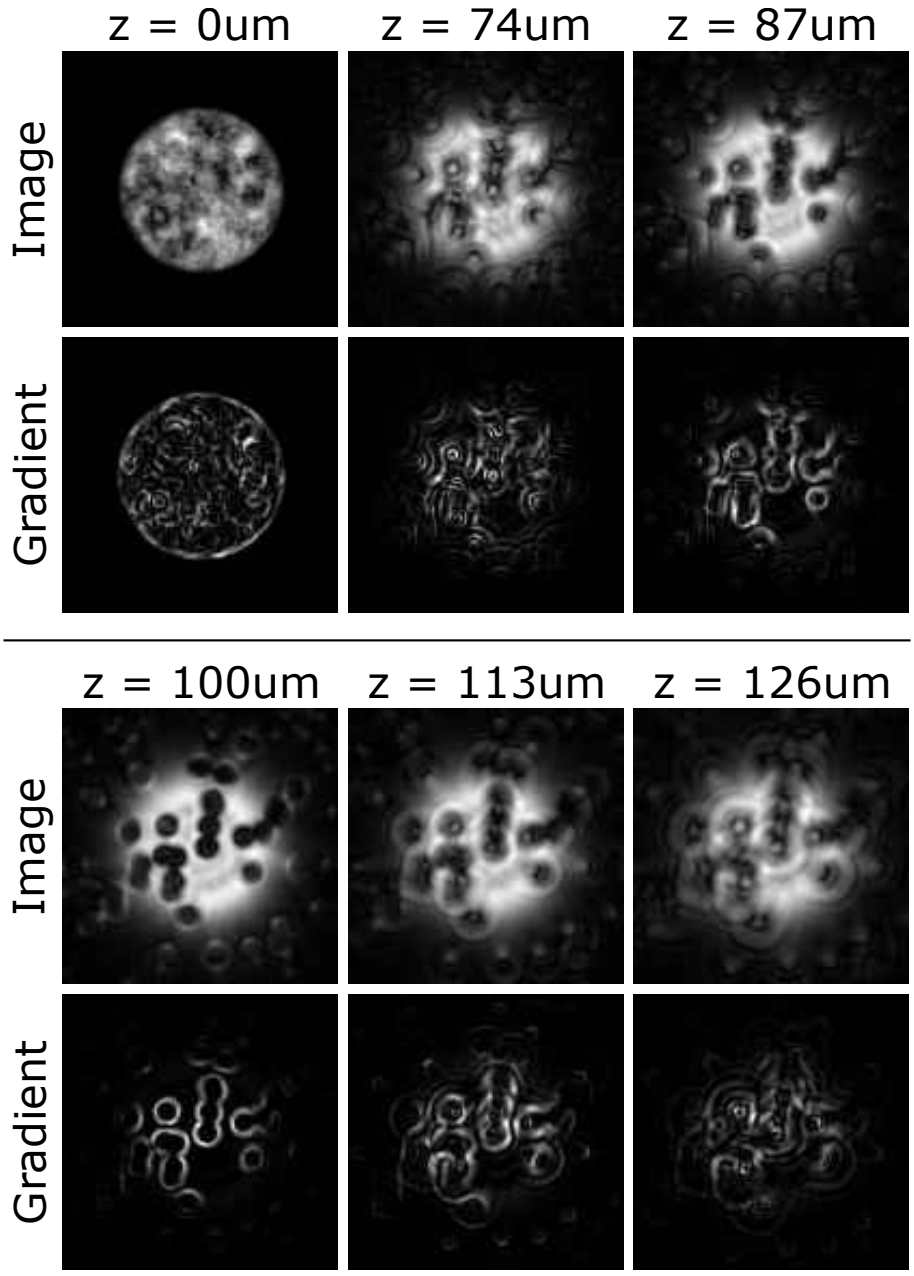

FIGURE 4.15.. Inputs to the acutance calculation of Fig. 4.14. as a function of propagation distance. Top images show the magnitude of the propagated wavefield; bottom images the square of the gradient of the wavefield.

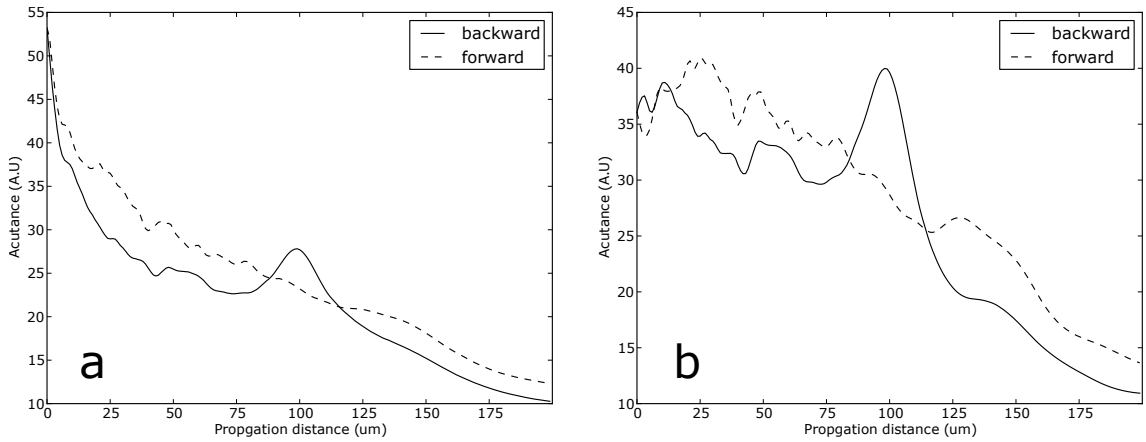

FIGURE 4.16.. Acutance calculation for the recovered Barker code image as a function of propagation distance. (a) shows calculation with integration over all space, (b) with integration over original aperture only.

The black dots in Fig. 4.14. mark the propagation distances where we examine particular propagated wavefields.

Figure 4.15. shows the magnitude component of these propagated fields and the gradient as computed by Sobel filter. At zero propagation distance away from the aperture, the edge and the interior near-field diffraction pattern all contribute to the gradient and the acutance. As z increases towards the solution at $z = 100\mu m$, the diffraction from the aperture edge becomes diffuse and the simulated test object begins to come into focus. The acutance peak spans approximately the range between $z = 75\mu m$ and $z = 125\mu m$. As expected, the solution at $z = 100\mu m$ has the most well-defined edges and consequently the highest acutance signal. Moving past the peak to the high-z side, we again defocus the sample and reduce the sharpness of its edges; the acutance drops.

4.6.3. Finding the Correct Propagation Distance: Experimental Data

With an expectation of the behavior of the acutance when back propagating from a small aperture to the sample plane, we return to the experimental data and

the recovered wavefield at the aperture plane. We repeat the analysis performed for the simulated test sample nearly exactly, propagating the wavefield in both directions to identify anomalous peaks and integrating first over all space, then over a restricted subregion of the aperture. Figure 4.16. shows the results of the calculation, with the integration over all space in Fig. 4.16.(a) and over the restricted region in Fig. 4.16.(b). Compared to the results from the simulated test sample, the experimental data does not surprise. The acutance starts high in both the forward and backward directions, then drops with increasing z. Only in the backward direction near $z = 100\mu m$ do we see a possible solution peak. When calculating the acutance over all space, the edge of the pinhole contributes a large signal at small z which mostly dissipates by the distance where solution comes in to focus; when calculating the acutance over the subregion, the solution peak becomes more prominent.

In Figure 4.17. we show the wavefield and its squared gradient at selected propagation distances. The uppers rows in Fig. 4.17. show the results from propagation in the backward direction, towards the sample plane. As with the simulated sample, the result comes into focus within several tens of microns and disappears over approximately the same distance. The distance of the peak acutance, $98\mu m$, is close to the $80\mu m$ separation distance estimated *ex situ* by optical methods. As explained earlier, we consider the initial estimate imprecise for several reasons. In an additional test of the solution, the lower rows show the wavefield and gradient at the same propagation distances when propagating in the opposite direction, away from the sample plane. We find no solution when propagating the wavefield in this direction.

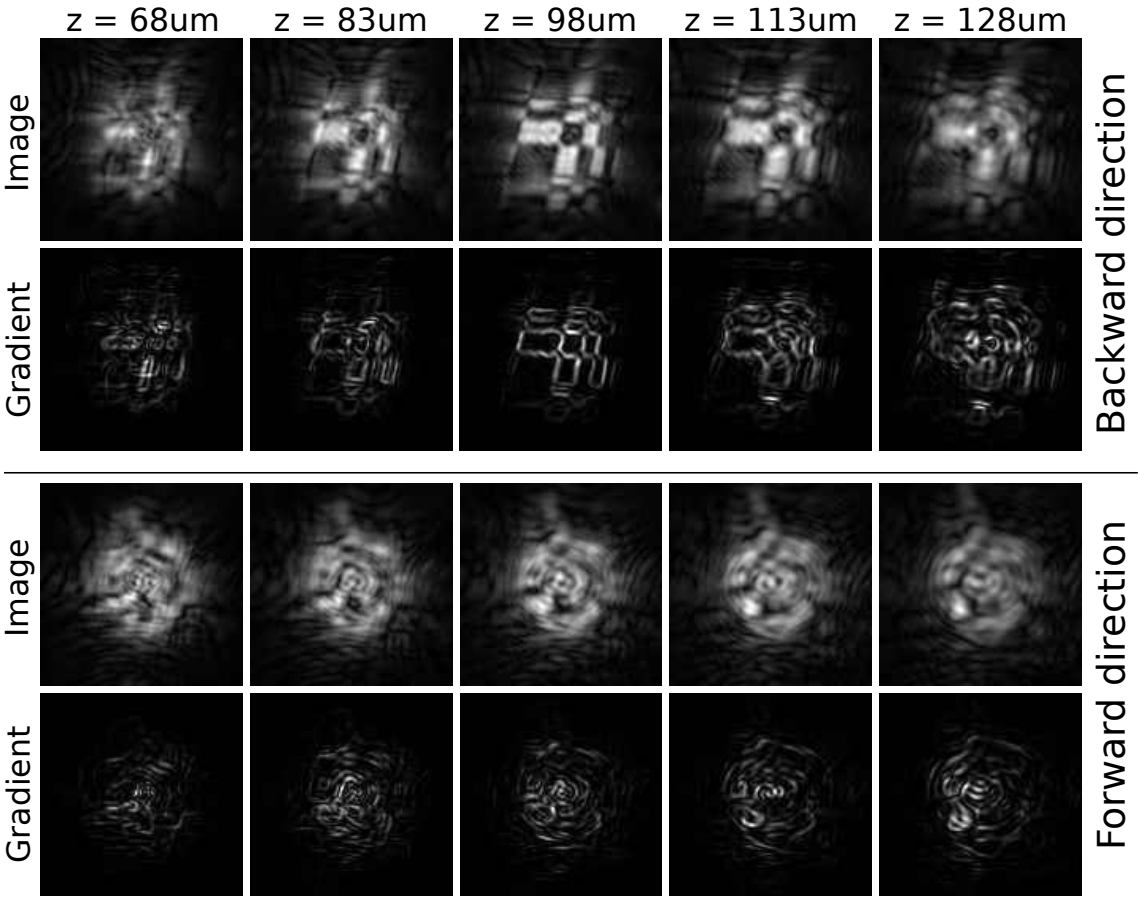

FIGURE 4.17.. Selected propagated images in the backwards direction (magnitude component) and their gradients. We find best acutance at $z = 98\mu m$.

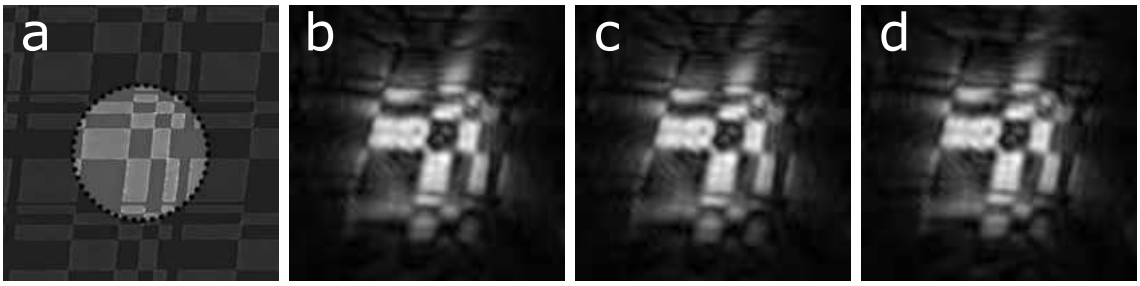

FIGURE 4.18.. Comparing differently-propagated images to the known solution. (a) shows an SEM image of the test sample, with the approximate field of view of the solution highlighted, (b) the back propagation in the case of the sample plane parallel to the aperture plane, and (c) and (d) tilt the sample plane to the experimental geometry.

4.6.4. Comparison of Propagated Solution to Known Sample

Because we performed the experiment with a known sample, the ultimate proof of the reconstruction and back propagation comes in comparing the final recovered image to an image of the sample obtained through other means, such as electron microscopy. We show this comparison in Figure 4.18.. Fig. 4.18.(a) shows an SEM image of the sample including the geometric foreshortening correction to account for the small-angle scattering geometry. We have highlighted the approximate field of view of the back-propagation, which we show in (b); we have not matched the length scale of the images. The high degree of fidelity between (a) and (b) provides indisputable experimental evidence that the two-step solution of first recovering the wavefield at the aperture plane, then back-propagating to the sample plane provides a viable technique for lensless imaging in reflection geometry. Comparing the known solution to the recovered solution also confirms that due to the near-field bandpass effect, features which lie strictly outside the nominal field of view at $z = 0$ can still be observed as high momentum-like signal diffracts into the aperture.

4.6.5. Propagating to a Tilted Sample Plane

In implementing this back-propagation focusing procedure, we have assumed that the tilt of the sample plane relative to the aperture plane does not seriously distort the final image. Here, we repeat the calculation for $z = 98\mu m$ but include a correction for the relative tilt of the two planes. Because the sample plane inclines relative to the aperture plane only about the θ axis, all pixels in each row of the image have the same propagation distance, but each row has a different propagation distance. We therefore calculate the propagation to the tilted plane through a composite set of propagations in which we perform an independent propagation for each of the rows in the image The true back-propagation distance for each row of the propagated image is

$$z(n) = z_0 \pm \frac{\delta \times n_r}{\cos(90^\circ - \theta)} \qquad \text{(Equation 4.10.)}$$

where z_0 is the best distance in the absence of inclination, n_r the index of the row running from -N/2 to N/2, δ the pixel pitch, and θ the angle of incidence in degrees. We use the $\pm$ symbol because of the solution degeneracy between the correctly-orientated apertures and their complex-conjugate rotation. In either case, we show the + correction in Fig. 4.18.(c), and the - correction in Fig. 4.18.(d). Only with very close inspection do any differences become visible, and none obviously distort the image within the nominal field of view. We attribute the lack of distortion to the small size of the aperture and distance correction relative to z_0. Compared to the $98\mu m$ back propagation distance before correction and the width of the acutance peak in Fig. 4.16., the correction is negligible. However, in experiments where we position the apertures closer to the sample or use much

lower angle of incidence, the effect of the distance correction may become more significant.

Algorithms have been published in the literature which claim to implement near-field propagation between tilted source and observation planes [107, 108], but the limited use of the calculation made more intensive efforts at implementation unworth the effort.

4.7. Estimating the Resolution of the Propagated Solution

As part of becoming a useful and viable technique, lensless reflection imaging requires an estimate of the resolution of the final image under variation of the several relevant experimental parameters. The well-known difficulty of calculating exact solutions to the Fresnel integral for all but the simplest integrands prevents analytical solutions to the question of image resolution. Instead, in this section we use numerical simulation to develop an empirical understanding of how the key parameters of aperture size, sample-aperture distance, and illumination wavelength combine to effect the resolvability of sharp edges in this imaging geometry. For simplicity, we restrict the simulated objects and apertures to one dimension, and discuss the complications of extrapolating the results to more realistic two dimensional objects. Finally, we check the consistency of the simulation results by comparing against an estimate of the resolution in the final recovered image of the barker-code test pattern.

In the near-field Fresnel regime where our imaging geometry encodes the wavefield, the wavefield exhibits both space- and momentum-like aspects. Broadly speaking, however, we expect that as the size of the pinhole decreases or the distance between the sample and pinhole increase, the resolution will worsen due

to decreased acceptance of momentum-like signal. In other words, the pinhole will behave as a type of low-pass filter.

4.7.1. The Simulated Imaging System

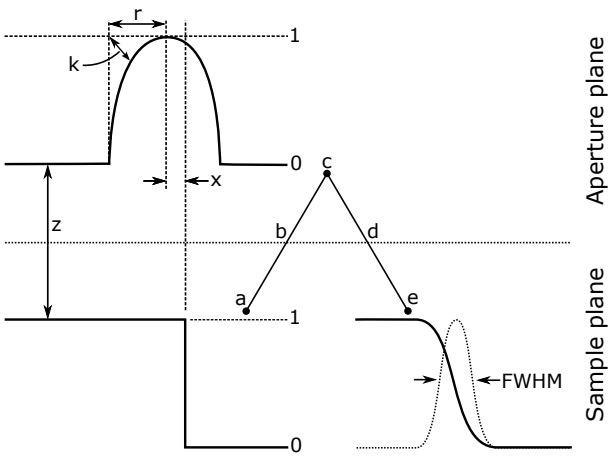

FIGURE 4.19.. Schematic representation of the numerical simulations conducted to estimate the final resolution in the reflection imaging experiment.

Figure 4.19. shows the configuration of the simulations we use to estimate the resolution of the final image. We label the steps of the simulation *a*-*e*. First, we create a wavefield in the sample plane with some wavelength λ; following tradition, we make the sample a knife-edge with maximum value one and minimum value zero (a). Second, we forward-propagate the wavefield a distance z to the aperture plane (b), where the propagated wavefield encounters a semi-transmissive pinhole function with radius r and a soft edge controlled by parameter k. We model the pinhole as entirely absorptive with no refractive component; the pinhole fully transmits the wavefield at the center, fully attenuates the wavefield a distance greater than r from the center, and partially attenuates it near the edge (c). This soft-edge acts as an apodizer to improve the visual quality of the propagation. We then propagate the product of the pinhole and wavefield back to the sample plane

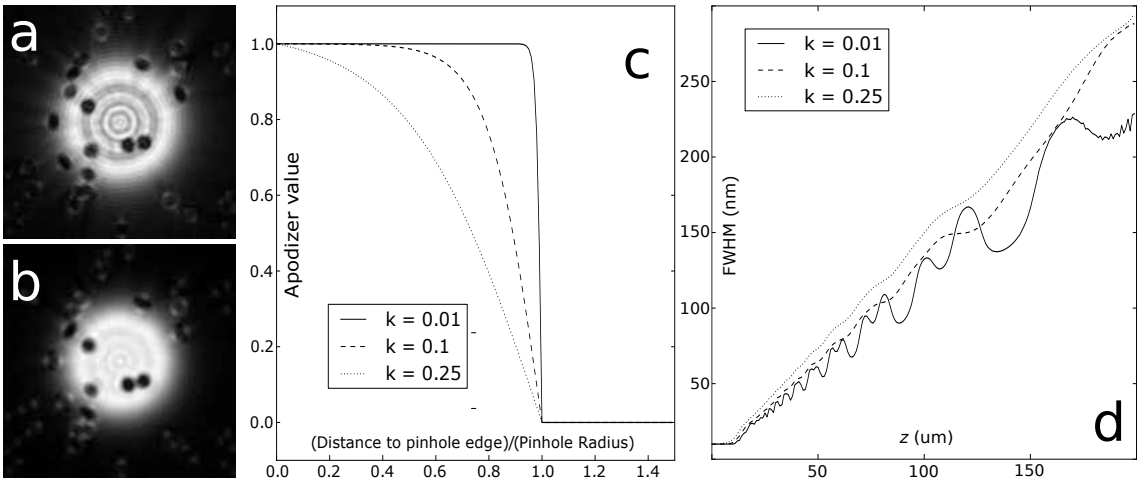

FIGURE 4.20.. Illustration of the effect of including a soft edge in the aperture function. (a) shows propagation with a hard edge pinhole, (b) with soft-edge pinhole, (c) the form of the apodizer function, and (d) the impact of the apodizer strength k on the resolution of the propagated image.

(d) where the loss of momentum-like signal blurs the knife-edge. To calculate the resolution of the back-propagated wavefield, we find the full-width at half-max (FWHM) of the absolute value of a discrete derivative of the propagated image (e). Simulating the effect of realistic two-dimensional apertures on two-dimensional wavefields requires a number of additional simulation parameters to describe the shape of the apertures and the orientation of the samples. For simplicity, we therefore restrict our simulations to a single in-plane dimension x; we will consider some effects of two-dimensional apertures later.

4.7.2. Effect of the Imaging System Parameters on Image Resolution

In these simulations, the soft-edged pinholes intentionally deviate from the experimental reality of hard-edged pinholes. Figure 4.20. illustrates the motivation for including the soft edge. In Fig. 4.20.(a), we see back propagation from a hard-edged pinhole, and in Fig. 4.20.(b) from a soft-edged pinhole. The soft-edged

pinhole substantially suppresses the Fresnel ringing from the aperture's hard edge. The soft edge of the aperture consequently functions as an apodizer which we can use both in simulations and in the analysis of experimental results after reconstructing the wavefield at the aperture plane. The apodizer can take any functional form which satisfies the boundary conditions of unity at the aperture center and zero at the aperture edge. In Equation 4.11., we give the exact form of the function used in these simulation, the normalized top half of a Fermi-Dirac function, where the radius of the aperture r replaces the chemical potential and the thermal energy kT becomes a unitless description of the apodization strength k. Figure 4.20.(c) shows the apodizer function with three different values of the strength parameter.

$$\text{Apodizer}(x) = \max\left(0, \frac{\left[e^{\left(\frac{x}{r}-1\right)/k}+1\right]^{-1} - \frac{1}{2}}{\left[e^{-1/k}+1\right]^{-1} - \frac{1}{2}}\right) \qquad \text{(Equation 4.11.)}$$

We show the effect of the apodizer strength on the resolution of the back-propagated image in Fig. 4.20.(d) with the pinhole radius set to 1μm, the energy 650eV, and the pixel pitch 10nm. As expected, the FWHM of the knife edge increases monotonically with z. However, the slopes of individual data series remain close, indicating that the apodizer has little effect on the sharpness of the knife-edge feature. In the case of minimal apodization (k = 0.01), the wild swings in the FWHM result from Fresnel ringing dominating as z increases. The apodizer must, of course, attenuate the momentum-like signal near the edge of the aperture coming from the sharp sample feature, an effect most easily seen in the slight increase in slope between k = 0.1 and k = 0.25. However, the tremendous suppression of aperture ringing makes up for the slight loss of image resolution at apodization

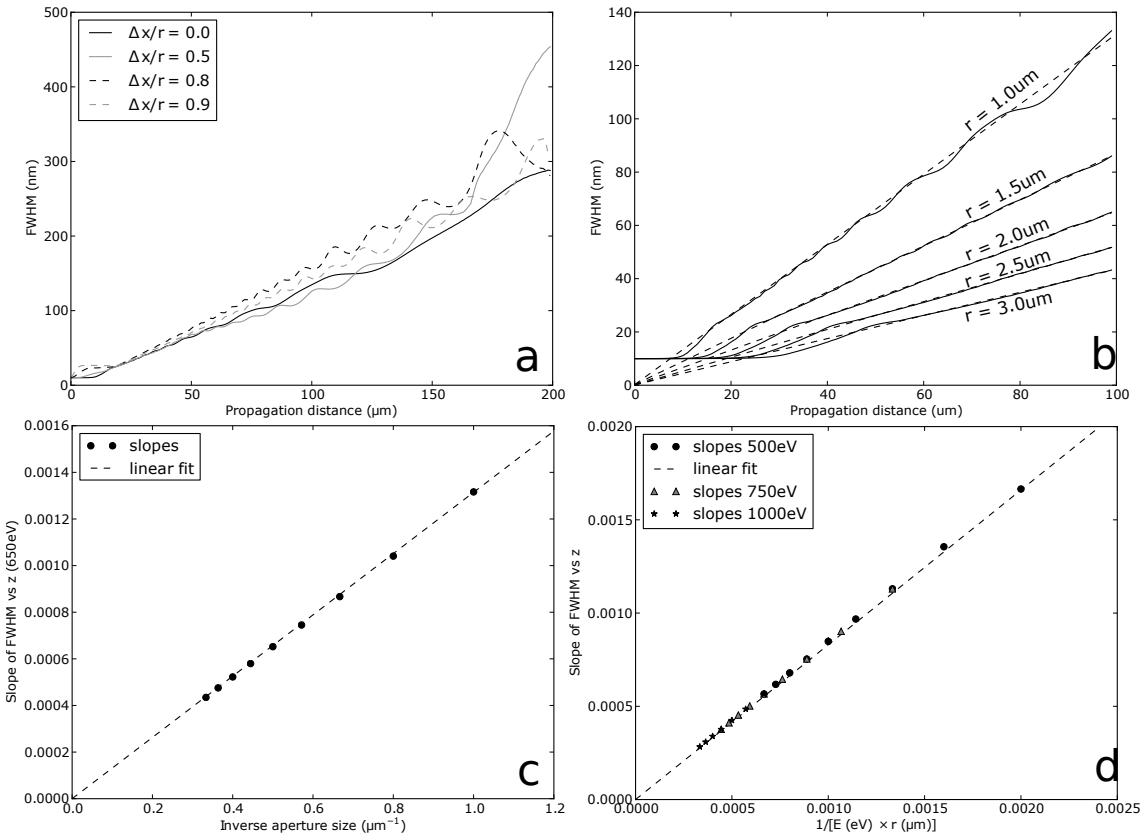

FIGURE 4.21.. Calculating the effect of the imaging system on resolution. (a) shows the FWHM as a function of distance from aperture edge and aperture distance; (b) shows the FWHM as a function of aperture radius and aperture distance; (c) shows slopes of the linear fits in (b) at a single energy; and (d) repeats (c) with several apertures.

strengths near k = 0.1, and we use this default apodization value in all remaining simulations.

Next we examine the effect of moving the knife-edge away from the center of the aperture's field of view by decreasing the distance labeled x in Fig. 4.19.. To make the measurement invariant to the size of the aperture, plot FWHM as a function of x/r, where r is the aperture radius. During the design of the experiment and the initial analysis of the first experimental results, we expected that proximity to the edge of the aperture's field of view would strongly effect the

resolvability of the image element due to a presumed higher loss of momentum-like signal. As the data in Figure 4.21.(a) shows, however, if such an effect is present in these one dimensional simulations it looks much weaker than anticipated. In particular, the FWHM when $x/r = 0.8$ exceeds the FWHM when $x/r = 0.9$ while we expect the opposite. Because of these results, we assume that in these simulations the final resolution of the image element does not depend on distance to the edge of the aperture field of view.

Finally and most importantly among the principal experimental parameters, we investigate the effect on the knife-edge FWHM from changing the size of the aperture. Figure 4.21.(b) shows the FWHM as a function of z for a series of pinhole sizes which we could realistically use in reflection imaging experiments, subject to coherence limitations. As expected, increasing the size of the aperture improves the resolution of the final image due to the increased acceptance of momentum-like signal at any given sample-aperture separation distance. Linear fits in the same panel extrapolate down to zero separation. In all cases, the excellent linear fit demonstrates the direct relationship between the propagation distance and the FWHM of the knife-edge derivative. At small propagation distances, the deviation of the extrapolated FWHM from the simulated FWHM results from the "true" value of the FWHM falling below the 10nm resolution of the simulation. To extract the dependence of the FWHM on the aperture size, we note that the slope of the linear fits to the FWHM vs z data decrease with increasing aperture size and so we plot the slope as a function of reciprocal aperture in Figure 4.21.(c). A linear function of the inverse aperture size clearly describes the slopes of the FWHM vs z data series.

The functional dependence on the FWHM of the derivative of the final propagated image therefore varies proportionally to z and inversely to r. We anticipate the effect of the remaining free variable, the energy, from its appearance in the quadratic phase factor of the Fresnel integral. In that calculation, λ and propagation distance z appear together as a product, and the FWHM must depend inversely on the energy. The full functional dependence on the experimental parameters is then given by:

$$\text{FWHM}(r, z, E) = c\frac{z}{rE} \qquad \text{(Equation 4.12.)}$$

Lastly, we calculate the constant of proportionality in Equation 4.12. by plotting the slope of a FWHM vs z data series as a function of rE, systematically varying both inputs. The linear fit to the data in Figure 4.21.(d) has slope $8.3 \times 10^{-7} eV \cdot m$, and Equation 4.12. becomes

$$\text{FWHM}(r, z, E) = \frac{8.3 \times 10^{-7}(eV \cdot m)z(m)}{r(m) \times E(eV)} \qquad \text{(Equation 4.13.)}$$

As a sanity check, we verify Equation 4.13. with the values $z = 100\mu m$, $E = 650eV$, $r = 1\mu m$, as we chose this energy and aperture radius for the simulations in Figure 4.20. We expect the result, $128nm$, by examining the $k = 0.1$ series at $z = 100\mu m$.

With the exception of the phenomenological proportionality constant, the general form for the FWHM in Equation 4.13. does not surprise. In terms of resolution, ratio z/r behaves as essentially a numerical aperture, and the energy comes in only because the rotation of information from the space-like into the

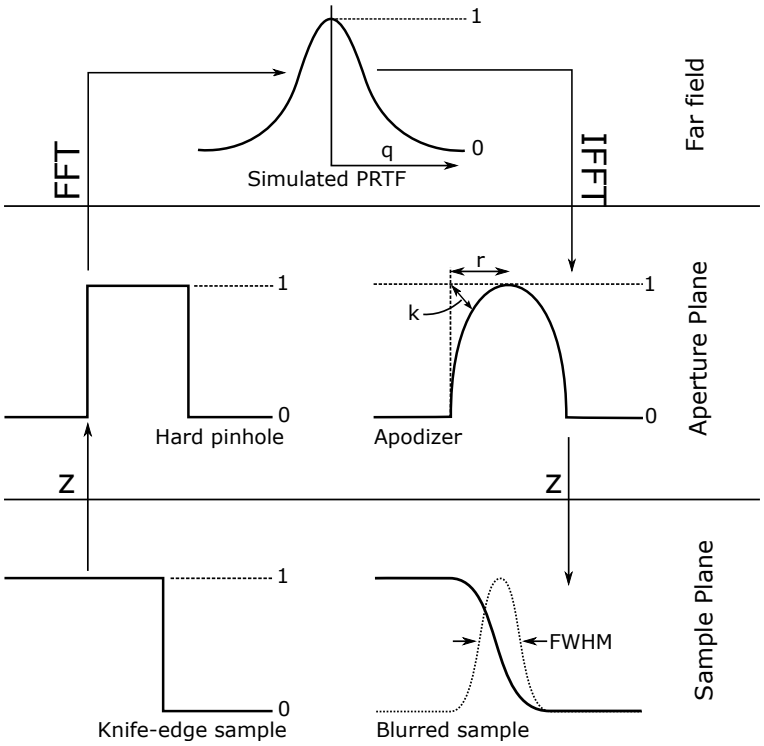

FIGURE 4.22.. The simulated imaging system modified to include the PRTF-related loss of resolution in the far field.

momentum-like basis happens as a function of both propagation distance z as well as wavelength.

4.7.3. Including Reconstruction Effects in the Resolution Estimate

Considering the imaging experiment as a whole, a second principal contribution to the loss of resolution comes from the phase retrieval algorithms. In the above investigation, we assumed that the phase-retrieval process perfectly estimated the exact solution to the phase problem, but a more accurate simulation must include the lost resolution as measured by the PRTF. We modify the experimental schematic originally shown in Figure 4.19. into that shown in Figure 4.22.. The extended simulation proceeds as follows. We first forward

propagate the same simulated knife-edge sample to a hard-edged pinhole in the near field aperture plane, then propagate the modulated wave to the far field with the Fourier transform. In the far field, we reduce the high-frequency content of the diffraction pattern by multiplying with a low-pass filter. We then inverse Fourier transform the low-passed signal to bring it back to the aperture plane, where we multiply by the same apodizer described in Equation 4.11.; after that, we back-propagate the apodized wave-field from the aperture plane to the sample plane. As before, we measure the FWHM of the magnitude of the derivative taken along the in-plane coordinate at the known location of the knife edge feature.

Given the now-vast range of possible parameters, we restrict the simulation to a few realistic values. We again set the apodizer strength $k = 0.10$, the energy $E = 650eV$, the radius of the near field aperture $r = 1.0\mu m$, and place the knife edge exactly in the center of the aperture's field of view. For the far-field low-pass filter which simulates the PRTF, we use a gaussian with variable standard deviation σ. As $z \to 0$, the simulation measures just the effect of the far-field PRTF. As $\sigma \to \infty$, the simulation measures just the effect of the near-field aperture.

Figure 4.23.(a) shows the effect of including a proxy PRTF in the simulation. Because the PRTF destroys high-frequency signal with no regard for sample-aperture separation distance, we most easily identify its effect at small z, where we find the trivial result that decreasing σ leads to a broader FWHM. As z increases away from zero, linearly-increasing contribution to the FWHM from the near-field aperture overwhelms the contribution from the PRTF. In Fig. 4.23.(b) we attempt to quantify this relationship by adding in quadrature the FWHM value at $z = 0$ to the FWHM value as a function of z when $\sigma = \infty$. While the behavior of the model in Fig. 4.23.(b) tracks the numerical simulations in Fig. 4.23.(a) in a qualitative

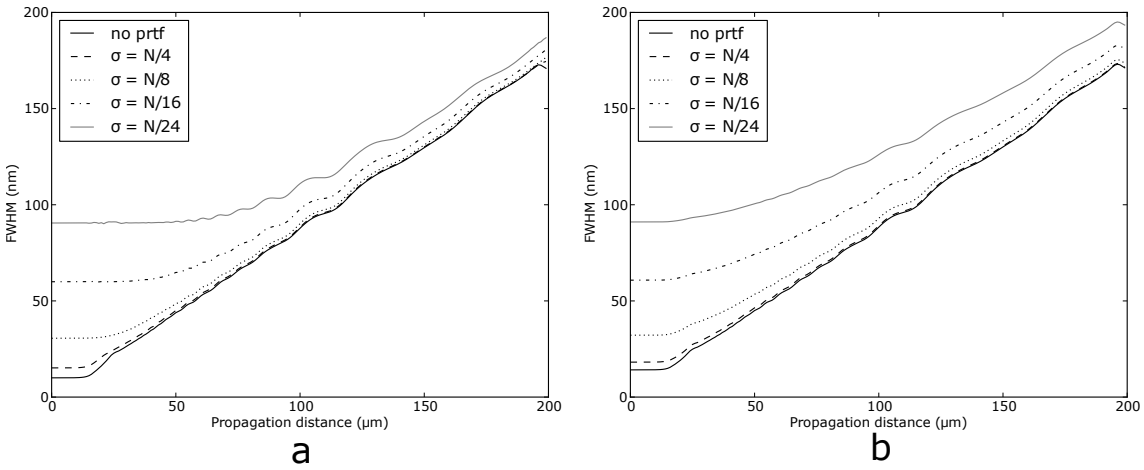

FIGURE 4.23.. Effect on image resolution of including a simple phase-retrieval transfer function. (a) shows the results of one-dimensional simulations with array length N with near-field filter and PRTF. (b) shows the results of adding in quadrature the FWHM at $z = 0$ for the various σ series.

sense, we do not see an exact correspondence. We model the PRTF explicitly as a gaussian, but from a band-pass point of view the behavior of the near-field aperture is more complicated.

4.7.4. Resolution Estimates for a Two-Dimensional Image

To conclude the investigation into the resolution possible with this imaging geometry, we note some of the complications which arise in the more general case of two-dimensional images.

We illustrate the main difficulty through a pair of two-dimensional simulations in Figure 4.24.. In Fig. 4.24.(a), we show the back-propagated image (magnitude component) at the sample plane when using a circular aperture of radius $2um$, and in Fig. 4.24.(b) we show the derivative along the axis perpendicular to the knife edge sample. Similarly, Fig. 4.24.(e) and (f) show a repeat of the simulation, but using a square aperture with side-length $400\mu m$ in

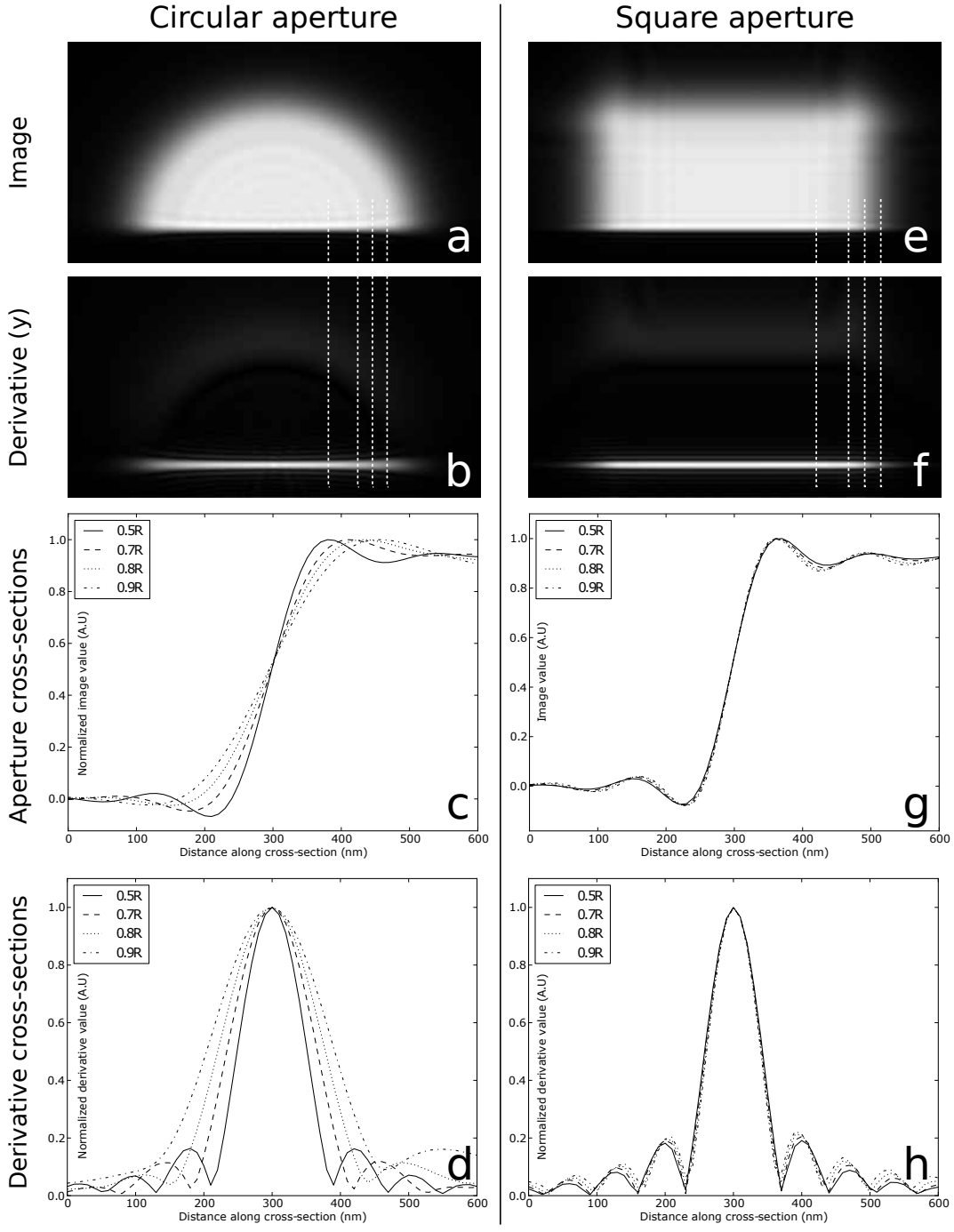

FIGURE 4.24.. In two dimensions, the resolution as measured by the FWHM depends on the aperture geometry. (a) shows a knife-edge object after interacting with a circular aperture in the near field; (b) shows the derivative along the image's vertical axis. (e) and (f) show analogous simulations in the case of a square aperture. Dashed lines in (a), (b), (e) and (f) show linecut locations used in (c), (d), (g), and (h).

place of the original circular aperture. The dashed lines in all figures mark the cuts through which we will examine the resolution.

We first consider the resolution in two dimensions when using the square aperture. In Figure 4.24. we show the value of the both the image in (e) and its derivative in (f), taken along a series of linecuts at increasing distances from the center. In the one-dimensional case, moving the feature towards the edge of the aperture seemed to have little, it any, effect on the outcome of the FWHM measurement. We see the same behavior repeated here, with the linecuts through the image as shown in (g) and through the derivative as shown in (h) displaying no strong dependence on proximity to the aperture edge. We find some small changes visible in the fringe structure, but attribute this to the complicated two-dimensional ringing near the edge rather than characterize it as a loss of resolution. In both plots, we normalize the linecuts to highlight the similarity of the data.

We present linecuts at the same position relative to the aperture edge but through the circular aperture data Figure 4.24.(c) and (d) and, in marked contrast to both the expectations of the one-dimensional simulations and the two-dimensional square aperture, they display a strong dependence on proximity of the feature to the edge of the aperture. Direct visual inspection of the data in Fig. 4.24.(a) also shows the effect in the broadening of the derivative as the linecut marker moves farther from center.

As we consider the part of the knife edge closer to the edge of the circular aperture, the momentum-like signal diffracting from that portion of the sample falls outside the acceptance of the aperture more quickly. Consequently, that portion of the knife-edge feature essentially experiences a smaller effective aperture. This does not happen with the square aperture, whose constant width preserves

the diffracted signal. In two dimensions, the shape of the aperture becomes an additional component to incorporate in the estimate of the final image resolution. As with other calculations in the Fresnel regime, however, analytic solutions seem unlikely, and Equation 4.13. should be used with the understanding that additional complexities lurk in the shape of the aperture and the orientation of the sample feature. More exact understanding of a particular experiment will therefore depend on numerical modeling.

4.7.5. Comparing the Resolution Model to Experiment

Finally, we apply our resolution model against the data acquired in the actual imaging experiment. Figure 4.25.(a) shows the wavefield after back-propagating to the sample plane while Fig. 4.25.(b) and (c) show the derivative of the propagated image along the x and y axes, respectively. In this calculation, we used the same apodizer as in the earlier two-dimensional simulations to help suppress Fresnel ringing from the hard edge of the aperture. Based on the energy of the illumination used to form the diffraction pattern, the known distance from the sample to the CCD detector, and the size of the CCD detector, we calculate a pixel size of $32nm$ in Figure 4.25.(a). Dashed lines in Fig. 4.25.(b) and (c) show the approximate location of the data used to measure the FWHM.

We show the measurement of the FWHM from the two derivative images in Figure 4.25.(d) and (e). In contrast to the simulations done to understand the resolution possible in the experiment, we do not know the exact location of the derivative peak. For this reason, we fit the derivative data with cubic splines to interpolate both the peak location and the closest value of the FWHM points. We measure the FWHM of the derivative along the x axis at $146nm$, while along

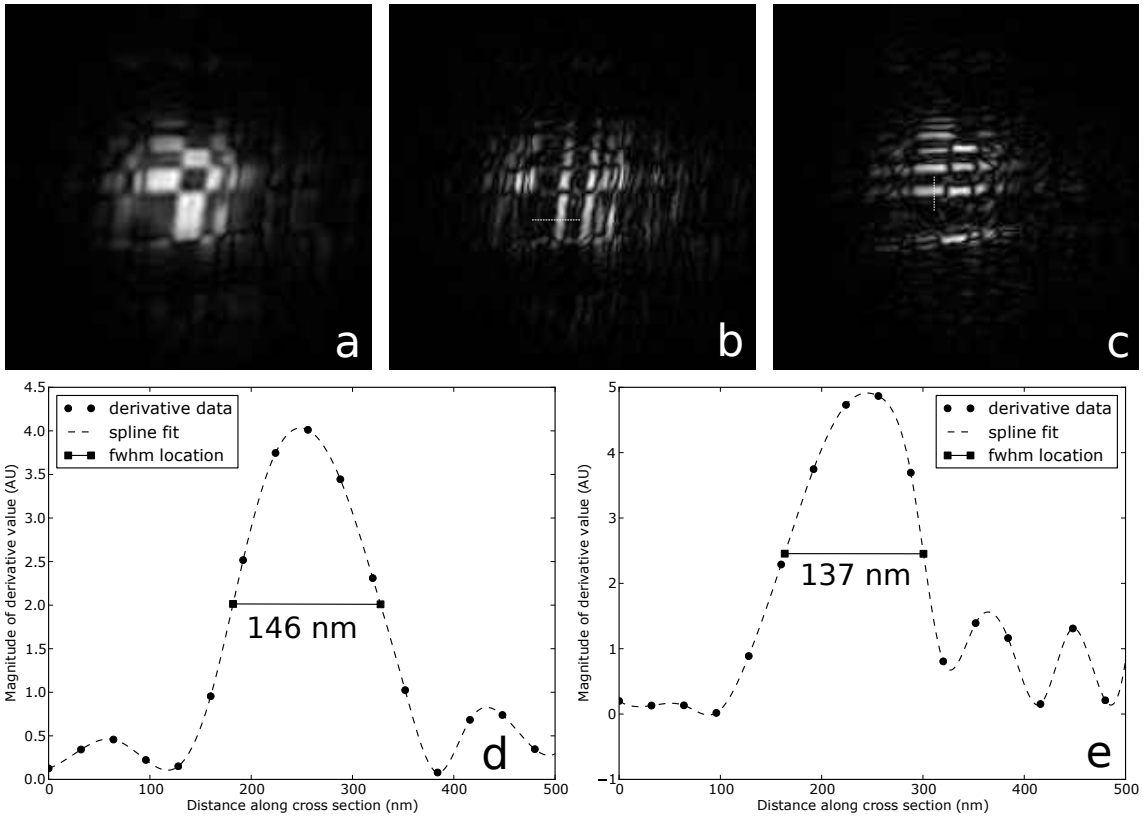

FIGURE 4.25.. Comparison of resolution prediction and measurement. (a) shows the back propagated image, (b) and (c) the square of the derivative along the two principal axes, (d) and (e) the cross-section taken along the marked sections of (b) and (c) and estimated FWHM.

the y axis at $137nm$. This discrepancy could reflect either a standard variation as we might expect in interpolated experimental data or the result of a slightly larger effective aperture along the y axis due to the geometric foreshortening of the aperture resulting from misalignment of the aperture plane relative to the CCD. Analyzing the derivative near the center of the field of view likely suppresses the complications associated with feature orientation and edge proximity. In any case, according to Equation 4.13., the expected FWHM at $E = 500ev$, $z = 98\mu m$, $r = 1\mu m$ is $163nm$.

Given the calculated $32nm$ pixel pitch, the actual pinhole radius may slightly exceed the nominal value. Measuring the semi-major and semi-minor axis lengths of the recovered wavefield at the aperture plane as approximately 40 and 35 pixels, we get a pinhole radius of approximately $1.1\mu m$ to $1.3\mu m$. With these values, we expect a FWHM between $148nm$ and $127nm$.

Including the PRTF calculated previously changes the result only slightly, as the effect of the near field filter dominates the loss of resolution measured by the FWHM. Based on the calculated pixel pitch of $32nm$ and the 0.53 inverse pixel resolution achieved in the reconstruction, the real-space resolution at the aperture plane is approximately $60nm$. Adding this in quadrature to the FWHM calculated for $r = 1\mu m$, $r = 1.1\mu m$, and $r = 1.3\mu m$, we estimate the anticipated resolution in the final propagated image as $174nm$, $160nm$, or $141nm$, respectively. We believe these predictions sufficiently match the experimental measurement to consider the simulations of the expected resolution of the reflection imaging geometry valid.

CHAPTER V

HOLOGRAPHIC IMAGING OF THE DEGREE OF COHERENCE

5.1. Introduction and Motivation

Future X-ray sources under investigation or proposed for construction exhibit high degrees of both longitudinal and transverse coherence. As researchers adapt existing experiments or develop entirely new experiments with these brilliant and highly coherent light sources in mind, they will require good methods of characterizing and precisely measuring the spatial coherence of the X-ray beam. In this chapter we will demonstrate a method of leveraging the Fourier transform holography techniques discussed earlier to quickly image the modulus of the complex coherence factor in two dimensions with diffraction-limited resolution. We will first explain the technique, then demonstrate an experimental realization, and finally present a path towards future improvement. In addition to the holography techniques already explained, the high-precision nature of this scattering experiment means that we will also repeat many of the data conditioning steps used for the imaging experiment as well.

5.2. Theory of Holographic Imaging of the Coherence Factor

Recalling Schell's Theorem Equation 2.28., we see that the deconvolution of the apertures becomes extremely simple under certain conditions. In particular, apertures with arbitrarily-extendable and locally-flat autocorrelation will provide a trivial measurement of $\mu(\Delta u, \Delta v)$ over the extent of the autocorrelation. Such apertures are known to exist in the form of a special type of coded-aperture array

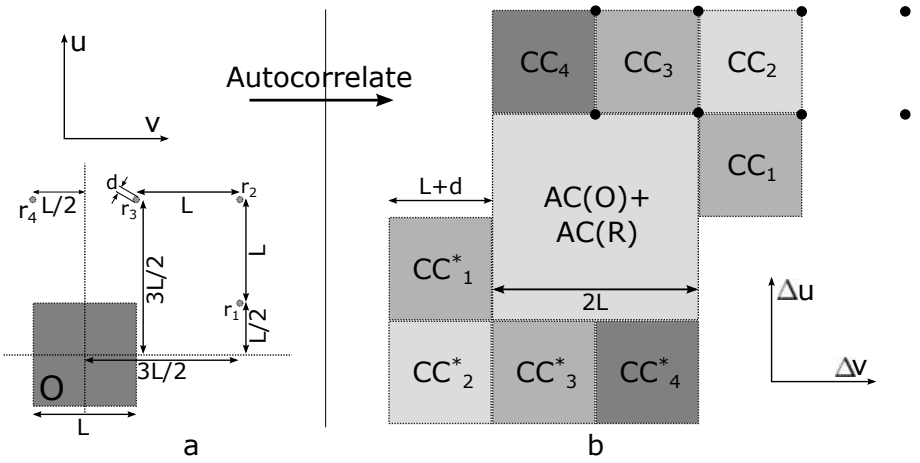

FIGURE 5.1.. Schematic representation of a set of pinholes suitable for measuring the coherence function in two dimensions with a single diffraction pattern. At left, the apertures; at right, their autocorrelation.

called uniformly redundant arrays [109–115], but we show here an alternative approach adapted from Fourier-transform holography which meets the same requirements.

We show the basic holography scheme in Figure 5.1.. An array of small apertures, labeled r_i with nominal characteristic size d, surround a larger square hole of length L, labeled O. We fabricate the apertures so that the separation between any given small hole r_i and a nearest-neighbor matches the size L of large aperture O. Additionally, we place small apertures to only one side of the large aperture; in Fig. 5.1.(a), we show this by placing no small apertures below the dashed horizontal line, but allow apertures on both sides of the vertical dashed line. Although Fig. 5.1. shows only four small holes, in principle we allow an infinite number so long as they maintain the separation condition. All together, we label the ensemble aperture function $A(u, v)$. The combination of O and any of the r_i forms an independent hologram; for this reason we will refer to the r_i as the references and O as the object. Alternatively, a set of apertures of this type

may be thought of as massive collection of double pinhole experiments, in which each r_i and some point in O form a pinhole pair. By choosing the inter-reference spacing to be the same as the size of O, we construct a set of apertures which form a continuous and extendable set of double pinhole separation vectors.

We derive an expression for the autocorrelation of the set of apertures by a simple extension to the prior theoretical treatment of the Fourier transform holography experiment (earlier equation); $\tilde{f}$ indicates the Fourier transformed version of real-space function $f(u,v)$ and $\star$ is the correlation operator:

$$\begin{aligned} A(u,v) &= O(u,v) + \sum_{i=1}^{N} r_i(u,v) \\ |\tilde{A}|^2 &= \left(\tilde{O} + \sum_{i=1}^{N} \tilde{r}_i\right)\left(\tilde{O}^* + \sum_{i=1}^{N} \tilde{r}_i^*\right) \\ &= \tilde{O}\tilde{O}^* + \tilde{O}\sum_{i=1}^{N} \tilde{r}_i^* + \tilde{O}^*\sum_{i=1}^{N} \tilde{r}_i + \sum_{i=1}^{N}\sum_{j=1}^{N} \tilde{r}_i^*\tilde{r}_j \end{aligned}$$

Grouping terms and recognizing the Fourier representation of the cross-correlation, an inverse Fourier transform brings this back to real space as

$$\begin{aligned} A \star A = O \star O + \sum_{i=1}^{N} (r_i \star r_i) + \sum_{i=1}^{N} (r_i \star O) + \sum_{i=1}^{N} (O \star r_i) + \\ \sum_{i=1}^{N}\sum_{j\neq i}^{N} (r_i \star r_j + r_j \star r_i) \end{aligned} \qquad \text{(Equation 5.1.)}$$

In analogy with (earlier equation), we identify the terms in the aperture autocorrelation $A \star A$ left to right as: the autocorrelation of O, the autocorrelations of the references r_i, the object-reference cross-correlations, their rotated complex conjugates, and finally the reference-reference cross-correlations and their rotated complex conjugates. These terms all appear variously in Fig. 5.1.(b). The

autocorrelation terms AC(O) and AC(R) exists in the central region of size $2L \times 2L$. We label the cross-correlations between O and r_i as CC_i and they tesselate to fill space outside the AC region; the conjugates CC_i^* appear rotated in the lower half plane, which is why we restrict the placement of the r_i to only one side of O. The cross-correlations between r_i and r_j appear in the corners of the CC_i as black dots and we do not individually label them because we do not use them in the analysis. In the experiment, the reference-reference cross-correlations appear as large but highly localized spikes in the signal which we can safely ignore.

Under the assumption that the illumination exhibits no significant structure across O, a set of apertures of this sort presents the extensible and locally-flat autocorrelation necessary to directly image the complex coherence factor via Equation 2.28..

5.3. Numerical Simulation of the Experiment

We now develop a basic numerical model of the experiment which we will use to build analytical techniques for the interpretation of the experimental data.

5.3.1. Non-ideal Reference Apertures

Our primary interest lies in the spectrum of $O \star r_i$ terms. An assumption of ideal references is unrealistic, as we saw in the fabrication of the holography mask for the reflection imaging experiment. Although convenient to treat the references as uniform, actual fabrication techniques create sub-100nm apertures with significant variations in size and shape. Additionally, we may misalign the apertures relative to the illumination and the beam intensity may vary over the reference array. For these reasons we assign an overall amplitude to each reference

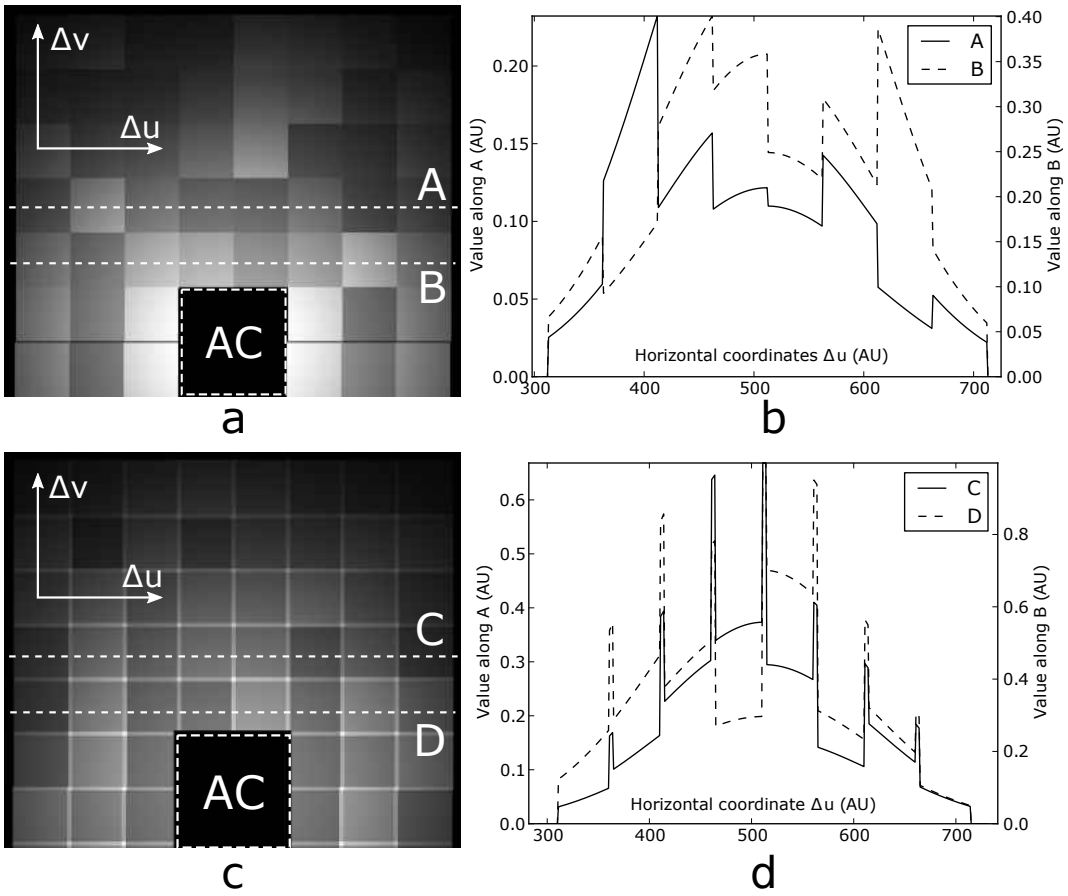

FIGURE 5.2.. Numerical simulations of the Fourier transform holography coherence measurement, including randomly weighted reference apertures. (a) and (c): autocorrelations (object-autocorrelation region zeroed); (b) and (d): cross-sections through the dashed lines showing effect of reference weights and overlaps.

function. However, we do assume that the apertures stay below the minimum simulation length-scale. We therefore model the references as:

$$r_i = a_i \delta(u - u_i + \epsilon, v - v_i + \epsilon) \qquad \text{(Equation 5.2.)}$$

Figure 5.2. shows results from a numerical simulation of the proposed set of apertures, simulated in accordance with the layout shown in Fig. 5.1.. We have assumed uniform illumination over O in the simulation, but we have included

Equation 5.2. in the model with random coefficients a_i. To start, we have set any positional jitter as described by ϵ to zero. The complex coherence factor we assume to be a simple gaussian function.

In Fig. 5.2.(a), we show the top half of the-autocorrelation of the exit wave accounting for partial coherence. Because of the extreme brightness of the autocorrelation compared to the cross-correlations, we have set the autocorrelation region, marked as the dashed box AC, to zero for visibility. Cross-correlations surrounding the autocorrelation, here appearing as a mosaic of tiles due to their random scalar multiplication by the a_i. In Fig. 5.2.(b), we plot the value of the autocorrelation taken along cross-sections A and B. Both cross-sections demonstrate both the multiplication of each cross-correlation by its random weight as well as the overall curvature imparted to the autocorrelation by the gaussian coherence function.

Fig. 5.2.(a) intentionally lacks realism to illustrate the effect of the random aperture weights. A more realistic model of the apertures includes jitter in their positions, leading to gaps or overlaps between neighboring cross-correlations. Because we use the same technique to account for gaps and overlaps, we show in Figure 5.2.(c) a simulation in which we have made the reference spacing smaller than the object size in order to introduce overlaps between all cross-correlations. These overlaps create spikes in the cross-sections shown in Fig. 5.2.(d). If we had instead created gaps by making the inter-reference spacing larger than the aperture, we would see zeroes between the cross-correlations instead.

5.3.2. Removal of Random Weights

We now consider how the random weights a_i may be removed to restore a smooth image of the coherence factor. Because the coherence function has a different value at all points in the $(\Delta u, \Delta v)$ plane while the scalar multipliers a_i are uniform across a given CC_i, apertures of the type now considered have sufficiently redundant information that the effects of the illumination and coherence separate. In the case of overlapping cross-correlations as in Fig. 5.2.(c) we regularize the relative illumination between two neighbors by requiring that linear fits performed over some range of each of the neighbors intersect at the midpoint of the overlap. We define an operator $\mathscr{L}$ which operates on some function $f(x)$ to return the slope and intercept of a best-fit linear approximation:

$$m, b = \mathscr{L}\left\{f(x_1) : f(x_2)\right\} \qquad \text{(Equation 5.3.)}$$

where x_1 and x_2 are the endpoints of the range over which $\mathscr{L}$ fits f. Any suitable fitting procedure or algorithm can supply $\mathscr{L}$. Considering the cross-sections along the Δu direction in Fig. 5.2.(c), we apply Equation 5.3. over two neighboring object-reference cross-correlations CC_i and CC_j to generate a slope and intercept for each:

$$m_i, b_i = \mathscr{L}\left\{CC_i(\Delta u_0, \Delta v_0) : CC_i(\Delta u_1, \Delta v_0)\right\}$$
$$m_j, b_j = \mathscr{L}\left\{CC_j(\Delta u_2, \Delta v_0) : CC_j(\Delta u_3, \Delta v_0)\right\}$$

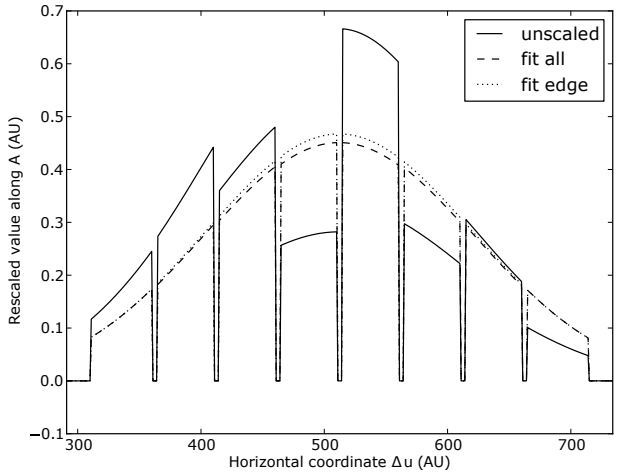

FIGURE 5.3.. Regularization of illumination factors in the case of overlapping cross-correlations, using either a few pixels near the edge of each region or the entirety of each region for the linear fit.

Calling the overlap midpoint Δu_{mid}, we calculate the ratio of the relative illuminations as:

$$\frac{a_i}{a_j} \approx \frac{m_i \Delta u_{mid} + b_i}{m_j \Delta u_{mid} + b_j} \qquad \text{(Equation 5.4.)}$$

The ratio a_i/a_j then multiplies CC_j, or equivalently the reciprocal may multiply CC_i.

In these equations, we have left the particulars of the input points unspecified as they will depend on experimental specifications, but some obvious considerations are universal. It is required that the range of each CC_i input be entirely over that CC_i and contain no part of an overlap. Due to the expected curvature of the coherence function, using smaller rather than larger ranges of inputs gives better results, as does using a range of inputs nearer to, rather than farther from, the overlap. However, while a small number of points better resists the effect of curvature, a larger number of points will better resist noise in the autocorrelation.

Figure 5.3. shows results of regularizing the relative illumination by linear interpolation; these data have gaps instead of overlaps, but we perform the same

analysis as we ignore both gaps and overlaps equally-well. In this simulation, we perform a chained analysis, picking an "anchor" cross-correlation term and regularizing the illumination of its neighbors through Equation 5.4., then treating those neighbors as new anchors and regularizing their neighbors and so forth until no neighbors remain. In Fig. 5.3.(a) we show the outcome of selecting as input range the entire extent of whichever cross-correlation was under analysis, labeled "fit all," as well as selecting smaller regions only several pixels in width near the overlap, labeled "fit edge." In both cases, we traversed the set of cross-correlations once with the left-most cross-correlation as anchor and again with the right-most cross-correlation as anchor, then averaging the results from both trajectories. Averaging across results with different starting points helps limit the effect of systematic errors which can accumulate due to the chained nature of the regularization process.

Both sets of fit ranges restore a gaussian profile. However, the two series differ near the center, as a linear fit taken over the full extent of the cross-correlation fails to replicate the curvature of the coherent function and consequently misestimates the illumination factor. Further improvement in this respect would be possible by doing a third fitting starting at center to include in the average.

5.4. Experimental

5.4.1. Apertures

The aperture scheme used in this experiment, which we show in Figure 5.4. essentially reproduces that proposed in Fig. 5.1.(a). The central object aperture has a side length $L \approx 1.5\mu m$. The smaller reference apertures have inter-reference spacing $1.5\mu m$, and an approximate diameter of 100nm each. However, as the

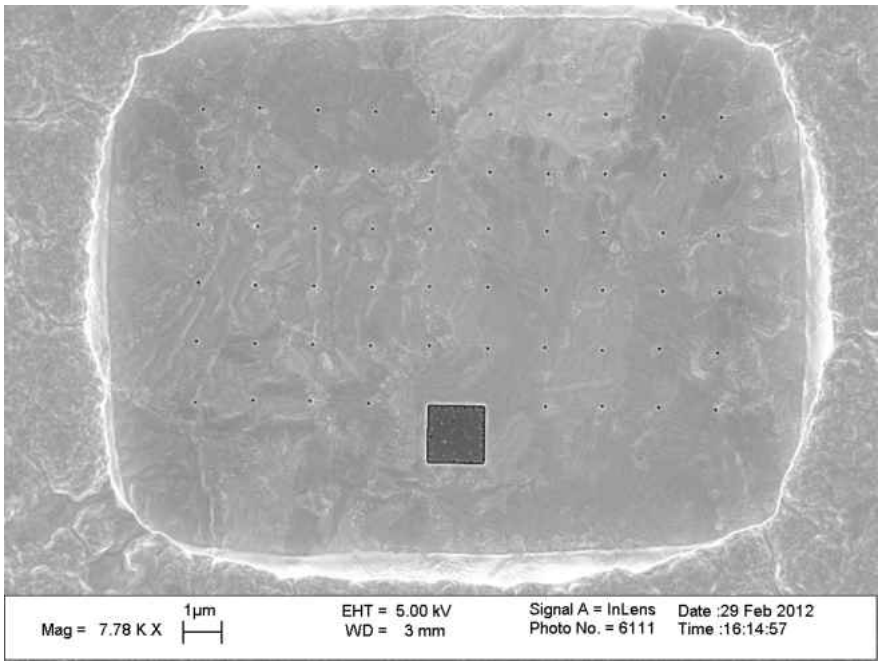

FIGURE 5.4.. SEM of the set of apertures used to measure the beam's degree of coherence. The object aperture measures approximately 1.5 μm, while the references have a diameter of approximately 100nm and are separated by 1.5 μm.

100nm size of the references approaches the minimum feature size possible in 800nm-thick gold, some variation exists in size which reflects in the random weight a_i for the corresponding cross-correlations. The reference grid has six rows and ten columns.

The apertures were fabricated by Weilun Chao at the Center for X-ray Optics using photolithographic processes for the mask; gold was deposited by electroplating.

5.4.2. Data Collection and Conditioning

Data collection and conditioning for this transmission-geometry experiment broadly follows the procedures explained earlier for the reflection imaging experiment with some differences. In particular, the extreme aspect ratio of the reference apertures makes them into tubes through the gold film which require precise angular alignment in the ϕ and θ coordinates to ensure maximum transmission. Also, the very bright signal which occurs in transmission geometry requires the use of a beam-block over the center of the diffraction pattern; however, as the experiment shows high sensitivity to signal in the central maximum, we must record behind the blocker as well. This requires merging exposures to extend the dynamic range of the detector.

We collected the data presented here at 640eV, near the L_3 resonance of manganese. Given the incident energy, the distance between the sample and detector, and the angle subtended by the detector, the maximum recorded $|\mathbf{q}|$ gives a per-pixel resolution of approximately 42nm.

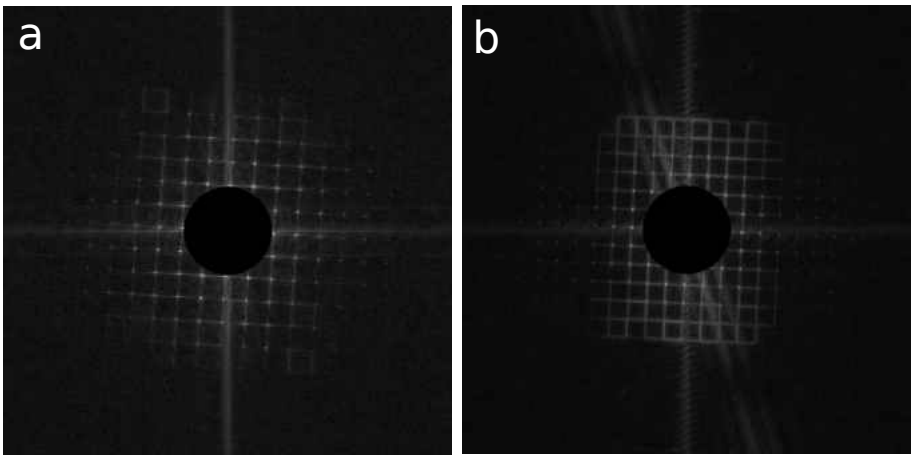

FIGURE 5.5.. Alignment of the experimental apertures with high-pass filters. (a) shows the high-passed correlation spectrum before alignment (incident energy 500eV), and (b) after (incident energy 640eV).

Compared to the reflection imaging experiment, improvements in beamline stability mean we can skip frame alignment or configuration sorting on the recorded images.

5.4.2.1. Angular Alignment

Prior to collecting data, we first align the sample in angles ϕ and θ in order to maximize the signal transmitted through the reference apertures. While optimization of θ proceeds rapidly due to the motorization of the coordinate, we must tediously optimize ϕ manually and with no readback. To evaluate the quality of transmission through the references, we form the image of the cross-correlation spectrum then run it through a high pass filter. When all the references transmit, the high pass signal shows an outline of all the correlations in the spectrum. When a reference transmits no light, its location in the spectrum appears dark. We illustrate this effect in Figure 5.5.. Fig. 5.5.(a) shows the high-passed correlation spectrum with the sample in its initial position, while (b) shows the correlation

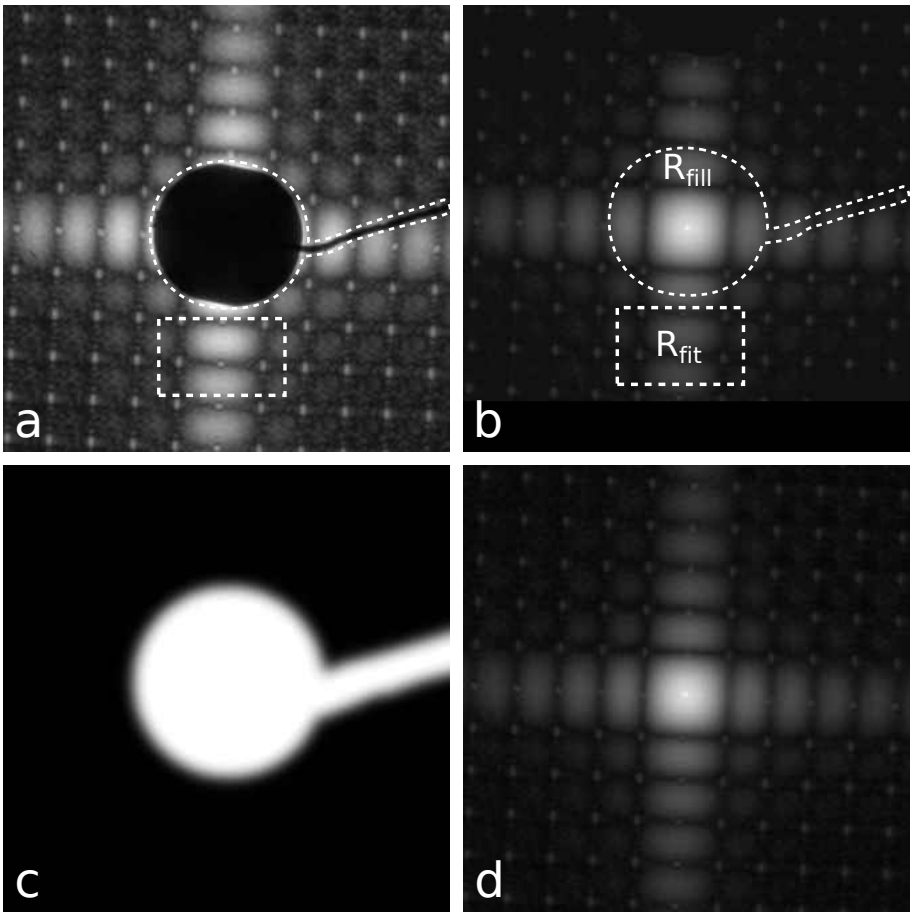

FIGURE 5.6.. Blending datasets to extend the dynamic range of the detector. (a) and (b) show the input datasets, (c) the blending function, and (d) the merged data.

spectrum after alignment. We attribute the increase in visible edges within the correlation spectrum to increased transmission of light through the references.

5.4.2.2. High Dynamic-Range Exposure Merging

Due to the limited dynamic range available on most CCD detectors and the slow read time of the CCD at beamline 12.0.2, in this experiment we take separate sets of data a low $|\mathbf{q}|$ and at high $|\mathbf{q}|$, then merge them together into a single continuous dataset. The beamblock which we use to protect the detector from the

direct beam in experiments with high flux makes a natural delineation between the two regions.

We show the two datasets in Figure 5.6.(a) and (b). In (a), we have moved the blocker over the bright central portion of the diffraction pattern, allowing for long exposures to record large $|\mathbf{q}|$ without saturating the detector. We label this data I_1. In (b), we have removed the blocker to collect data from the low $|\mathbf{q}|$ section of the diffraction pattern; because we are only interested in those pixels not illuminated in (a), we reduced the vertical readout region in order to quicken acquisitions. This may be seen in the black strip at the bottom portion of (b) which marks the end of the readout. We label this data I_2.

First, we match the signal levels in a region of the diffraction pattern where the two datasets overlap, marked in Fig. 5.6.(a) and (b) with dashed box R_{fit}. In the matching region, we attempt a least-squares optimization in order to solve a minimization problem in three variables:

$$\text{minimize}\,\{I_1 - sI_2 + (sD_2 - D_1); s, D_1, D_2\} \qquad \text{(Equation 5.5.)}$$

Here, we optimize: s, an overall scale factor; D_1, a constant offset to intensity pattern I_1; and D_2, a constant offset to intensity pattern I_2. D_1 and D_2 differ because I_1 and I_2 may have a different number of total exposures or a different exposure time per exposure, leading to differing amounts of signal from the chamber ion gauge or the CCD dark current. After optimizing s, D_1, and D_2, we match I_1 and I_2 by

$$I_2' = s \times (I_2 - D_2) + D_1 \qquad \text{(Equation 5.6.)}$$

We then merge exposures I_1 and I_2' through a spatially weighted average near R_{fill}, the region to be filled. In this case, R_{fill} corresponds to the blocker visible in Fig. 5.6.(a), which we estimate by tracing a mask in a bitmap image editor. We construct the blending function B from R_{fill} through two convolutions:

$$B = K_2 * \min(K_1 * R_{fill}, 1) \qquad \text{(Equation 5.7.)}$$

where the convolution kernels K_1 and K_2 are given by:

$$K_1 = \text{circ}(w) \qquad \text{(Equation 5.8.)}$$

$$K_2 = A \exp\left[-r^2/(2w^2)\right] \qquad \text{(Equation 5.9.)}$$

The merged image is then straightforward:

$$I_{1,2} = BI_1 + (1 - B)I_2' \qquad \text{(Equation 5.10.)}$$

The mechanism of Equation 5.7. is simple. The first convolution with K_1, the circle function, simply expands R_{fill}. The second convolution with K_2 gives the expanded fill region a soft edge to eliminate stitching artifacts between I_1 and I_2. The final sum, Equation 5.10., weights more heavily I_2 near R_{fill}. We show the final blended image in Fig. 5.6.(d); we see no blending artifacts.

5.4.2.3. Dedusting and Debeaming

As in the reflection imaging experiment, dust on the detector distorts the signal in undesirable ways and we must remove it via interpolation. In Figure 5.7.(a), we show the central portion of the merged data, and in (b) we

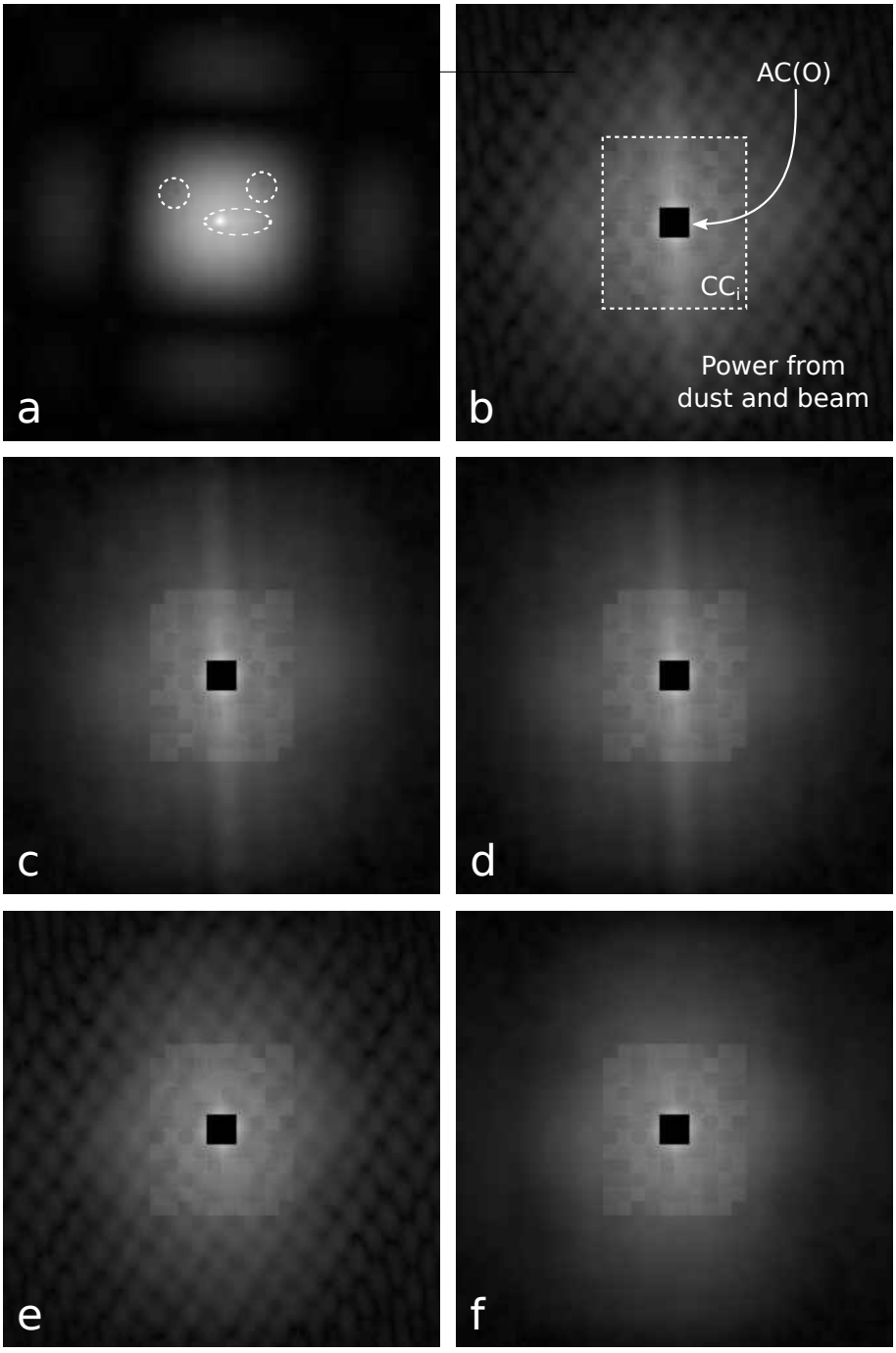

FIGURE 5.7.. Both the dust on the surface of the detector and the direct transmission from the beam distort the autocorrelation in undesirable ways. (a) shows the central diffraction maximum with dust and beam; (b) the autocorrelation with no conditioning; (c), (d), (e), and (f) the autocorrelation after various conditioning strategies.

show the magnitude component of its inverse Fourier transform. Dark spots in the central maximum result from dust; we also see a superimposed image of the beam, which has punched its way through the 800nm gold coating to contribute a spurious signal near $|\mathbf{q}| = 0$. We mark two dust spots and the beam with its long horizontal tail in (a). At the center of Fig. 5.7.(b) we have zeroed the bright object-object autocorrelation as we did earlier in Fig. 5.2.. The object-reference cross-correlations surround the center and contain the envelope of the complex coherence factor. Outside of that, we expect a uniform region of zeroes resulting from the oversampling of the diffraction pattern. Instead, we see a large amount of signal representing the power spectrum of the distortions introduced into the diffraction pattern by the dust and beam. This power diffuses throughout the autocorrelation plane, overlapping and interfering with the true cross-correlation signal.

We show various attempts to remove the dust and spurious beam signal in Fig. 5.7.(c)-(f). In (c), we interpolate around just those dust particles within in the first-order diffraction peaks; this removes the vast majority of the "checkerboard" effect. In (d), we interpolate around all visible dust particles anywhere in the diffraction pattern; this presents no particular improvement to the strength of the noise spectrum, as dust particles in the high-order diffraction peaks create very small distortions to the diffraction signal when compared to those particles near the center of the image. In (e), we attempt to remove through interpolation just the long horizontal tail of the direct beam; most of the power of the beam signal remains, but we cannot remove it through interpolation both because the interpolation control points are always somewhat contaminated by the beam but also because the beam peak and diffraction peak coincide, making accurate interpolation therefore more difficult. In (f), we combine the (d) and (e) to generate

the flattest background signal possible. The residual background in (f) shows the power spectrum of the partially removed direct beam signal, and we probably can do no better through operations on the diffraction data.

We also attempted to remove the beam during the data acquisition by taking an image of just the direct beam transmitted through an identically prepared gold film lacking any apertures. However, we found the morphology of the beam extremely sensitive to the position of the blank film, and therefore we could not use any of the images to correctly subtract the beam signal.

5.4.3. Extracting the Coherence Function

The slowly-varying nature of the beam signal overlapping the cross-correlations means that at the edge of the cross-correlation array we can subtract the beam signal with a relatively high degree of accuracy. In Figure 5.8.(a), we show the top portion of the cross-correlation region and draw through it two dashed lines showing where we take sections of the data for comparison. The upper line lies just outside the correlation region and measures only the signal provided by the beam. The lower line lies just inside the correlation region and measures the sum of the beam signal and the unpolluted cross-correlation signal. Both series of data are complex-valued. In Fig. 5.8.(b), we plot the magnitude component of the two sections and the magnitude of their complex-valued difference. The difference signal shows the isolated cross-correlation signal. The phase of the difference signal at any given point results from a combination of phase structure in the illumination, a phase difference introduced as part of the scalar multiplication via the reference, and misalignment of the diffraction pattern prior to the inverse

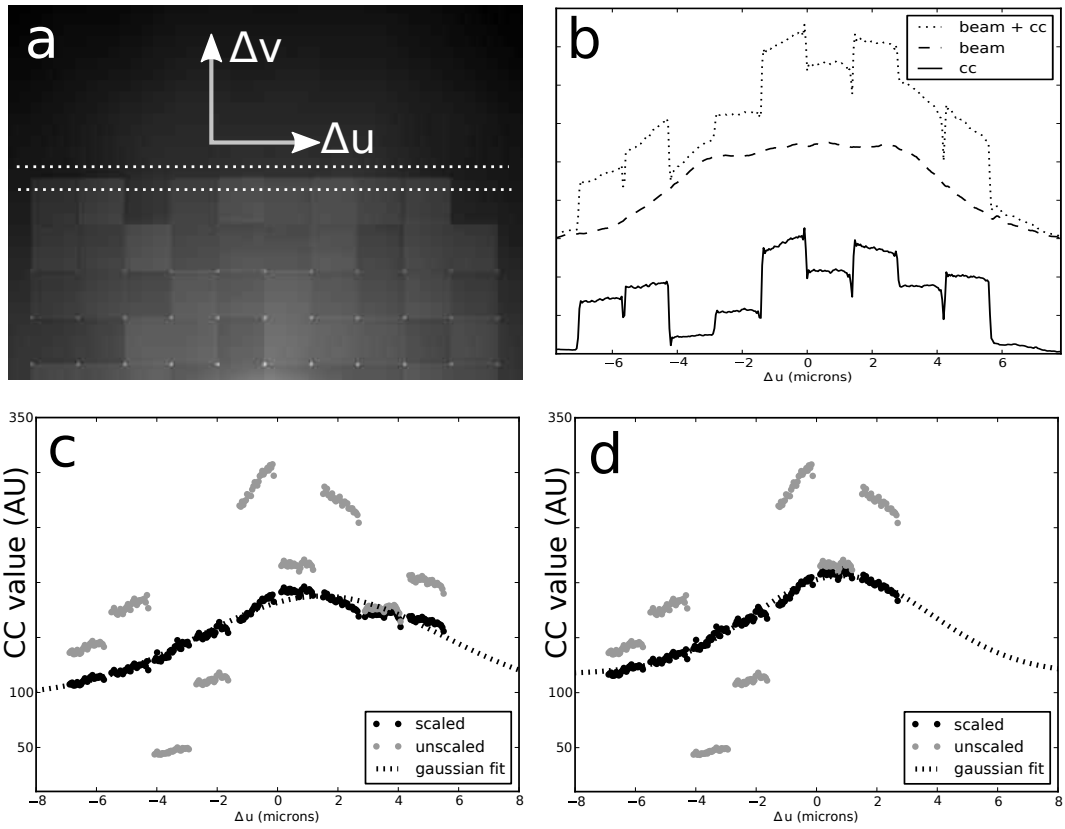

FIGURE 5.8.. Extracting the coherence factor for the horizontal (Δu) direction. (a) shows the cross-correlations; (b) shows plots the data taken along the two dashed lines in (a), and also their difference; (c) shows the rescaled data; (d) shows the rescaled data less the apparently unreliable correlations at $+\Delta u$. We fit the rescaled data to a gaussian.

Fourier transform which introduces a linear phase ramp; none of these are relevant to measuring the modulus of the coherence factor.

We show the data across the whole range of Δu before and after rescaling according to Equation 5.4. in Fig. 5.8.(c), excepting the cross-correlation at the far right of the Δu coordinate as insufficient signal through the reference generated an unusable signal in that $(\Delta u, \Delta v)$ range. Given the nearly gaussian profile of the synchrotron x-ray source and its relatively incoherent nature, we expect from the Van Cittert-Zernike theorem [8, 116–120] a nearly gaussian profile to the coherence factor. In general, the rescaled data conforms to this expectation, although with

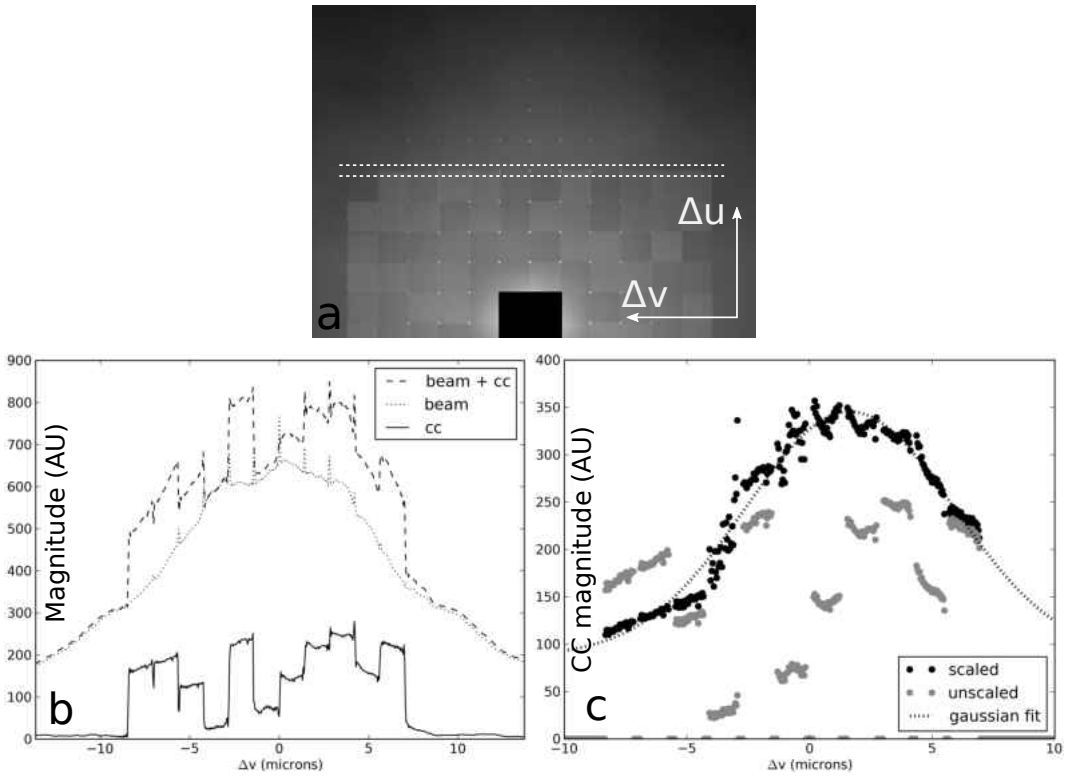

FIGURE 5.9.. Extracting the coherence factor for the vertical (Δv) direction. (a) shows the cross-correlations; (b) shows plots the data taken along the two dashed lines in (a), and also their difference; (c) shows the rescaled data.

some asymmetry in tails. Lacking a theoretical justification for a beam with more coherence in one direction in Δu than another, we repeat the gaussian fit excluding the two right-most cross-correlations in Fig. 5.8.(d). In this case the gaussian fit seems very good, and has a standard deviation of about 3.8μm.

We repeat the bulk of the process for the vertical axis in Figure 5.9.. First, we subtract the beam signal from the superposition of the beam and correlation signal near the positive Δu edge of the cross-correlation array. In this instance, we must put more of a gap between the two series as the bright reference-reference cross-correlations get in the way of the signal. We plot the magnitude of the two cross-sections and the magnitude of their difference in Fig. 5.9.(a). We rescale the

magnitude of the isolated cross-correlation signal identically to the method in the horizontal data, then again fit to a gaussian. Fig. 5.9.(b) shows the unscaled data, the rescaled data, and the gaussian fit. Again, the gaussian seems a good match, with standard deviation 4.4μm. As expected, we find the coherence greater in the vertical direction due to the greater filtering of the beam along the vertical direction, particularly at the exit slits of the monochromator (lower divergence of the source?).

However, as in the Δu case, the data has artifacts. In particular, after subtraction we observe "bowing" in the central portion of many of the cross-correlations. This effect matches with simulations in which we measure the beam signal too far away from the cross-correlation signal, and the subtraction introduces large errors relative to the value of the correlation signal. We believe the general behavior of the extracted coherence factor in the vertical direction reliable, but treat the behavior within any particular cross-correlation region with suspicion.

5.4.4. Data Interpretation Difficulties

In attempting to interpret this result, certain aspects of the fitting remain unclear. While we may explain the offset of the peaks of both fits from $(\Delta u, \Delta v) = (0, 0)$ as resulting from relative misalignment of the aperture axes, detector axes, and beam axes, the constant offset of the gaussian fit is troubling. As all wavefront have only finite coherence, we fully expect the obvious limiting condition

$$\lim_{\Delta u \to \infty} \mu(\Delta u) = 0 \qquad \text{(Equation 5.11.)}$$

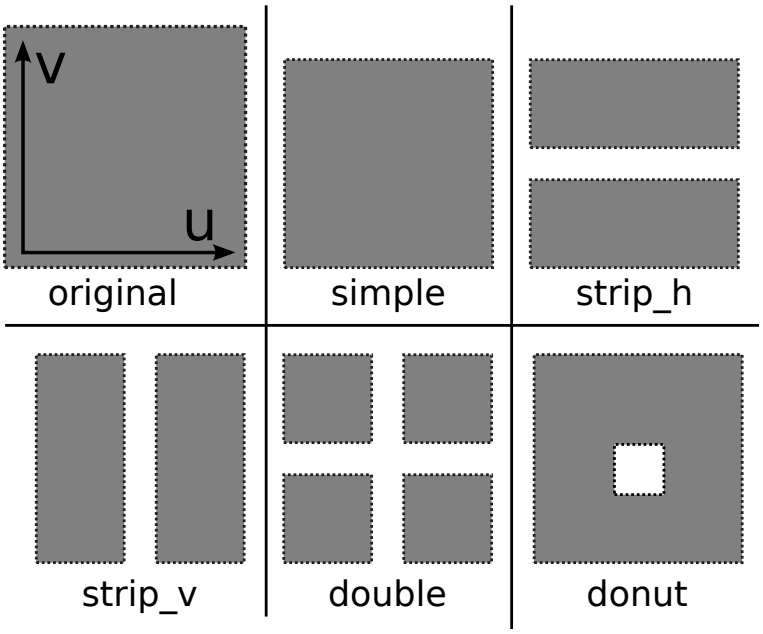

FIGURE 5.10.. Possible object aperture designs for an improved iteration of the measurement. "Original" refers to the aperture from the shown experimental results. Dark grey indicates the transmissive region of the aperture.

While we are tempted to dismiss the offset as an artifact of the rescaling process, which might drag some poorly subtracted background up to a significant value, the fact that we can easily distinguish the edge-most cross-correlations against the background contradicts this argument. Due to the limited extent of the measurement in both direction, we cannot rule out other possibilities such as a form of the coherence factor with a longer tail than a gaussian. Until we reconduct the experiment with a more extensive set of apertures to allow a measurement at greater $|\Delta u|$ and $|\Delta v|$, we assume the above limit must always be in force, and that any non-zero offset is spurious.

5.5. Possibilities for Future Improvements

During the design of the aperture array, we did not anticipate the incomplete attenuation of the direct beam by the gold and the consequent spurious signal in

the central maximum of the diffraction pattern. The presence of this signal poses a serious challenge to the experiment as we can only subtract the power spectrum of beam from the correlation signal very near a location where we measure the beam signal alone. For this reason, the current aperture design can measure the coherence factor $\mu(\Delta u, \Delta v)$ in two dimensions simultaneously, but only in the extremely restricted sense of two orthogonal one-dimensional measurements as done above. As we do not expect separable coherence functions in general, we require a better set of apertures which allow interpolation of the slowly-varying beam signal at far more points in the $(\Delta u, \Delta v)$ plane. Such a design would allow a fine-grained interpolation of the beam and isolation of the cross-correlation signal in a true two-dimensional fashion.

5.5.1. New Aperture Designs

We show a cartoon of several such design in Figure 5.10.. In comparison with the original square aperture used in the experimental results already presented, we shrink the size of all five designs below the inter-reference spacing. This size discrepancy introduces gaps between all the cross-correlations where we can measure the signal from the beam in isolation. While the aperture design labeled "simple" is merely a smaller version of the aperture used in the earlier experiment, "strip-h", "strip-v", "double", and "donut" all slice through the aperture to introduce additional points for measuring the power spectrum of the beam. Assuming that the beam signal varies slowly in $(\Delta u, \Delta v)$, sufficient sampling points allow an interpolation of the beam in two-dimensions even with irregularly spaced data via a cubic Clough-Tocher algorithm [121–123].

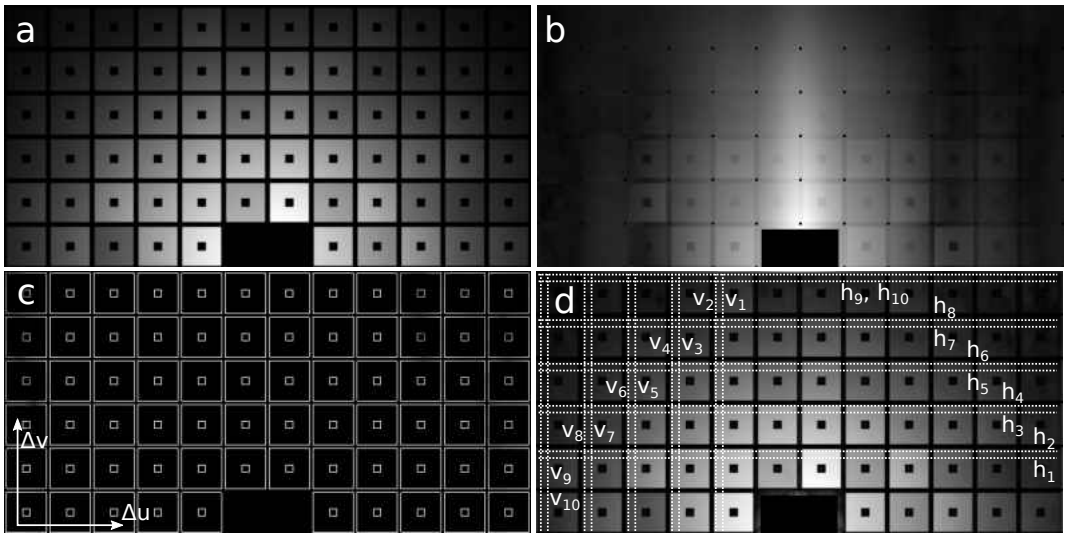

FIGURE 5.11.. A simulation of using improved aperture designs to handle pollution by the beam. (a) shows the partially coherent cross-correlation spectrum, including random weights and coherence function. (b) shows the same with semi-empirical beam signal. (c) shows the locations where we measure the beam for interpolation. (d) shows (b) after subtraction of the interpolant, and h_i and v_i cross sections for coherence recovery.

We show elements from the scattering simulation with the hypothetical "donut" design in Figure 5.11.. Fig. 5.11.(a) shows the cross-correlation spectrum with the central autocorrelation zeroed as usual; this image includes random reference weight and a gaussian coherence factor of standard deviation $4\mu m$. In Fig. 5.11.(b), we show the cross-correlation spectrum following the inclusion of a realistic direct-beam signal in the diffraction pattern. In this simulation, we took the form of the beam directly from the series of measurements of the beam on the CCD detector undertaken in an attempt to directly subtract a portion of the direct-beam signal. Based on the known cross-correlation spectrum in (a), we measure just the beam's power spectrum at the locations marked white in Fig. 5.11.(c). These pixels provide the anchor points for a complicated interpolation available in scipy.interpolate.griddata. In Fig. 5.11.(d), we show the magnitude

of the difference between the data in Fig. 5.11.(b) and the beam signal estimated through interpolation. In the cross-correlations at the top of the image, the beam signal overwhelms the true cross-correlation signal and introduces serious artifacts into the difference. The labels $h_1 ... h_{10}$ and $v_1 ... v_{10}$ and their corresponding dashed lines indicate where we will measure the performance of the aperture designs.

5.5.2. Comparison of Aperture Performance

To compare the performance of the various aperture designs, we repeat the rescaling and fitting procedure used to extract the coherence length from the experimental data. The cross-sections we use to recover the known coherence factor we label in Fig. 5.11.(d) as h_1 through h_{10} and v_1 through v_{10}. Cross sections with even numbers measure near the edge of the cross-correlations, while those with odd numbers measure the interiors; we expect all the designs to recover the coherence factor well near the edge of the correlation where we can measure the beam signal, artifacts from poor interpolation of the beam more seriously distort measurements on the interior. In the experimental data set, we recorded twelve unique beam profiles, which we combine in pairs to generate seventy-two unique beam signals polluting the true correlation signals. In addition, we simulate the recovery of the coherence factor using eight randomly generated sets of reference weights a_i, giving five hundred seventy six unique simulations of the coherence factor recovery along each cross-section for each aperture. To judge the performance of each aperture, we plot the average and standard deviation of the recovered coherence factor at each aperture and cross-section. Because we know the true coherence factor in the simulation, we condition the lists of recovered coherence factors by removing those obvious outliers which result from failed fits to the rescaled cross-correlations.

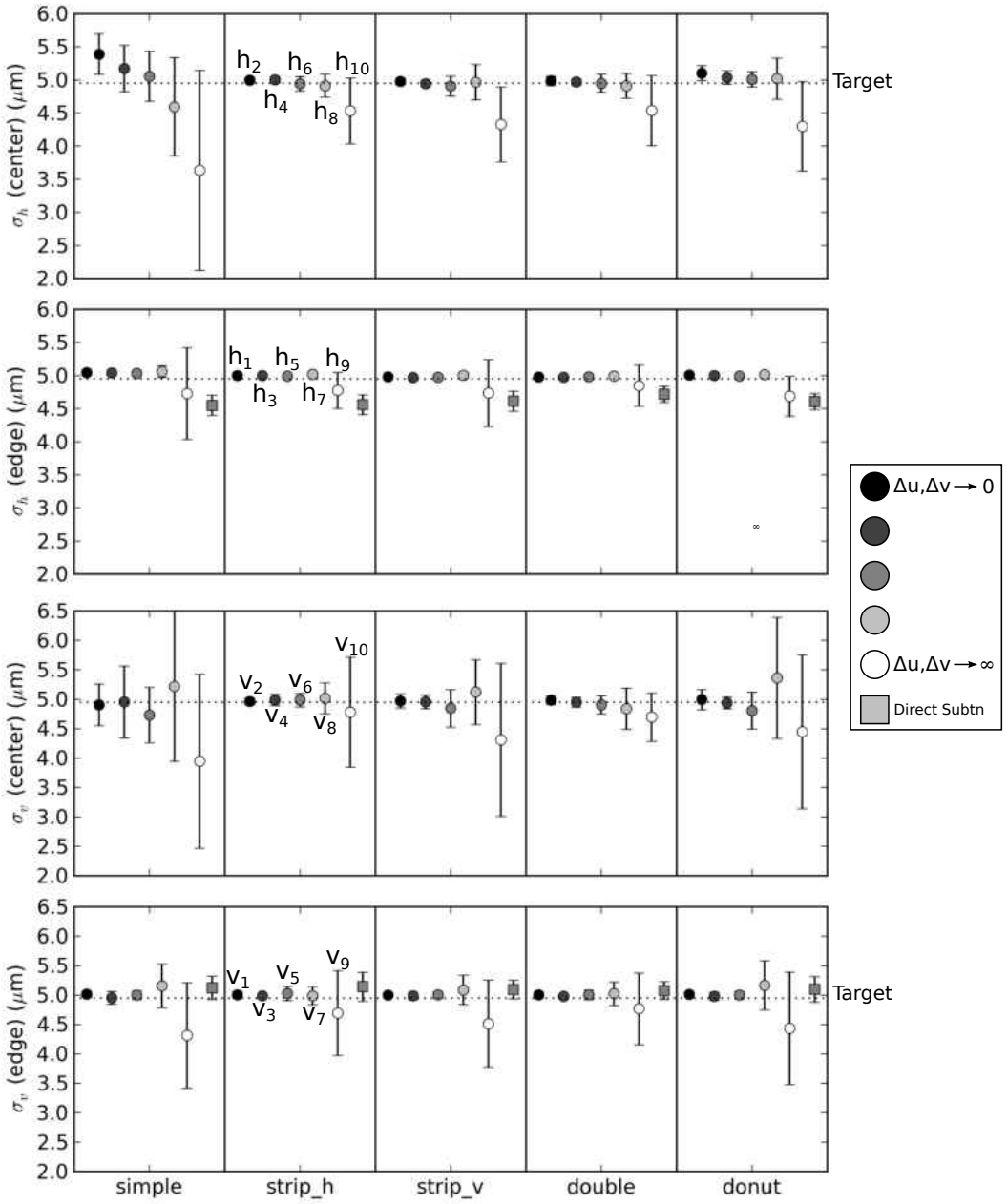

FIGURE 5.12.. Measuring the performance of the improved apertures in recovering the known degree of coherence. The top two plots show recovery along the horizontal direction at the various cross-sections marked in Fig. 5.11.(d). The bottom two plots show recovery along the vertical direction. The dashed line shows the target recovery; all advanced apertures outperform the aperture design used in the experiment.

We plot the performance of each aperture in Figure 5.12.. In the upper two images, we show the mean and standard deviation of the recovered horizontal coherence length σ_h, as measured on the edge cross-section or in the interior of the correlations. The darker dots show the performance of the recovery near $\Delta v = 0$, and the lighter dots the performance as Δv increases. The lower two plots show the same data organization as the upper two, but present the statistics of the recovered σ_v. We plot the recovery target of $5\mu m$ in all four plots as a dashed horizontal line.

In both directions, the performance of the apertures presents no real surprises. As expected, the simplest aperture fares the worst in recovering the coherence factor in the interior of the correlations. However, the more sophisticated designs which increase the density of sampling points for the beam recover the coherence factor with a high degree of accuracy all the way to the outer regions of the correlation spectrum, at which point the signal from the beam becomes too bright in comparison to the correlations and interpolation artifacts hinder the recovery. Importantly, the sophisticated "double" aperture with slices along both axes seems to fare no better than the simpler "strip-h" aperture, which has a slice only along the horizontal axis.

We additionally compare the recovery from the complicated two-dimensional interpolation to the method used in the experimental data earlier, when we directly subtracted the beam signal from the polluted correlation signal a few pixels away. This simpler method is represented by the square boxes of the second and fourth plots, and was performed at the h_5 and v_5 cross-sections. Notably, we observe that, at least in simulations, the recovered coherence lengths are self-consistent but in the horizontal direction they systematically underestimate the coherence. From this result, we conclude that even at the very edge of the aperture where only

a few pixels separate the beam and cross-correlation data, the two-dimensional interpolation provides a much better estimate of the beam.

5.5.3. Larger References

The ratio of the correlation signal to the spurious beam signal is the limiting factor in recovering the coherence factor. As Δu and Δv increase, the beam signal seems to fall off more slowly than the coherence factor, and consequently the beam signal dominates near the edge of the correlation spectrum.

For this reason, we anticipate that increasing the size of the references from their current δ-like size would substantially improve the recovery of the coherence factor. Larger references would lead to blurrier cross-correlations, but would leave the coherence function alone, Equation 2.27. shows. Several obvious factors limit the upper size of the references. First, the correlations cannot become so blurred that the gaps introduced by the more sophisticated apertures close entirely, as we must measure the beam signal in isolation. Second, the illumination over the references must remain approximately uniform so that the effect of the reference on the correlation signal can be approximated as a scalar multiplication.

CHAPTER VI

SIMULATION OF DOMAIN PATTERNS IN MAGNETIC THIN FILMS WITH PERPENDICULAR ANISOTROPY

In this chapter, we develop an algorithm for the simulation of labyrinthine magnetic domain patterns in thin films with perpendicular anisotropy. At least one algorithm already exists for the simulation of domain patterns of this type [124], and has been used in various applications including hysteresis loops and return-point memory [125–127], Barkhausen instabilities [128], and magnetic domain pattern formation and growth dynamics [129, 130]. Here, we develop a similar but independent model which eschews the explicit time dependence which comes from the usual approaches to minimizing the system's Hamiltonian in favor of very precise control over the scattering lineshape, which we use as the Fourier constraint. Iterative phasing algorithms of the type presented earlier, which repeatedly enforce constraints in real- and Fourier-space until a solution converges, have strongly influenced the algorithm developed in this Chapter.

We pursue this work to enable the statistical interpretation of magnetic speckle patterns with possible rotational symmetries at specific length-scales, which we will discuss in the next chapter.

6.1. Magnetic Thin Film Physics, in Brief

All ferromagnetic materials, whether single-crystal or thin-film, require differing energies to magnetize depending on the orientation of the applied field relative to the crystal axes. We refer to this orientational dependence as the magnetic anisotropy of the sample. For a detailed review of the microscopic

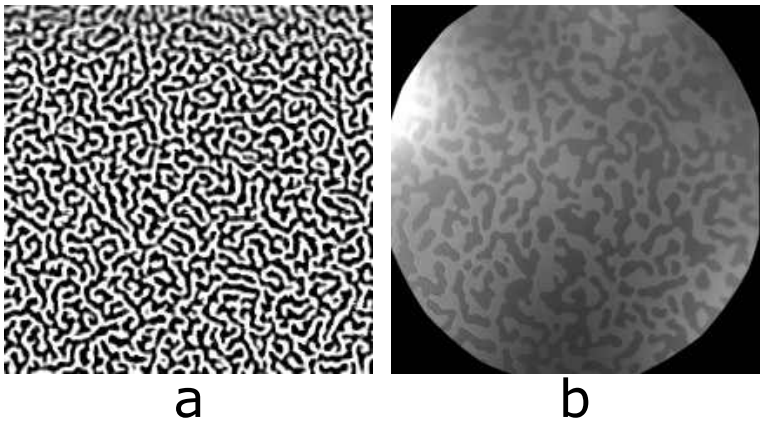

FIGURE 6.1.. Two real magnetic multilayer samples show potential goal domain configurations. (a) shows domains in a Co/Pd multilayer, (b) in Tb/Co.

contributions to the magnetic anisotropy, see Johnson [131]. In very brief mention, key contributions to the anisotropy include: the long-range dipolar interaction; electronic spin-orbit coupling, which reflects the material's crystal symmetry; the magneto-elasticity, whereby strain in a sample may favor a particular magnetic alignment to reduce stress-energy; and importantly the geometry of the sample, as the behavior of spins at a surface or interface may depart significantly from their behavior in bulk due to the change in symmetry. In multilayer samples grown by sputtering, which provide the basis for this simulation work, the extreme thinness of the layers in the multilayer structure and the sputtering technique promote through strain and interfacial change of symmetry an easy axis of magnetization perpendicular to the plane of the sample; the magnetization in the sample strongly favors alignment parallel or anti-parallel to the field.

Within the thin film, two competing interactions establish the characteristic length-scale and morphology of the domain configuration. The ferromagnetic interaction between neighboring spins promotes the parallel alignment of neighbors, while the dipolar interaction favors the anti-parallel alignment of neighboring spins.

Competition between the ferromagnetic interaction, which favors maximal domain size, and the dipolar interaction, which favors minimal domain size, results in domains of intermediate size. In Figure 6.1. we show the domain patterns in two different types of multilayer samples. Fig. 6.1.(a) (courtesy Jimmy Kan and Eric Fullerton, UCSD) shows perpendicular domains in a cobalt-palladium multilayer, imaged using magnetic force microscopy [132]. Fig. 6.1.(b) (courtesy Joshua Turner and Peter Fischer) shows perpendicular domains in a terbium-cobalt multilayer, imaged using full-field x-ray microscopy with zone plates [133, 134]. With these simulations we endeavour to produce domains of the labyrinthine type shown in Fig. 6.1.(a).

6.2. Solution Classes for Iterative Algorithms

In coherent imaging experiments, the modulus of the complex far-field diffraction pattern supplies the Fourier constraint. If we label the estimate of the solution wavefield at some iteration n as E_n, the Fourier transform of E_n as $\mathscr{F}\{E_n\} = |\tilde{E}_n| \exp(i\phi_n)$, and the experimentally measured far-field intensity I, enforcement of the Fourier constraint replaces the estimated Fourier modulus with the measured modulus:

$$\hat{F}(E_n) = \mathscr{F}^{-1}\left\{\sqrt{I}\exp\left(i\phi_n\right)\right\} \qquad \text{(Equation 6.1.)}$$

In conjunction with the real-space constraint, Equation 6.1. ultimately leads to a unique solution because of the one-to-one relationship between the real-space and the Fourier representations of a two-dimensional function; two different real-space functions cannot generate the same fully coherent and adequately sampled speckle

pattern. We seek a modification of Equation 6.1. which allows the generation of a class of similar solutions rather than a particular unique solution.

We illustrate the idea of unique members of a class of solutions in Figure 6.2.; Fig. 6.2. (a) and (c) show two coherent speckle patterns taken from a scattering experiment at the Co L_3 edge of a Co/Pd multilayer sample. In Fig. 6.2.(b) and (d), we show the intensity in the speckle patterns at a given radius from center, averaged along the azimuthal coordinate (marked θ) to "despeckle" the data. In both (b) and (d), the dashed line plots a least-squares fit to the despeckled average with the functional form of a squared lorentzian:

$$\langle I(|\mathbf{q}|)\rangle_\theta = \frac{s}{\left([(|\mathbf{q}| - |\mathbf{q}|_0)/w]^2 + 1\right)^2} \qquad \text{(Equation 6.2.)}$$

Here, $|\mathbf{q}|_0$ is the radial distance of the peak away from center, w the width of the peak, and s an overall scaling factor. The width factor w relates to the FWHM of the peak by FWHM $= 2w\sqrt{\sqrt{2}-1} \approx 1.29w$. For scattering patterns from magnetic samples such as this, we interpret the central radius $|\mathbf{q}|_0$ as describing the average domain periodicity and the width w as relating to the domain correlation length. The difference between the speckle patterns reflects the differing underlying domain configuration and the one-to-one relationship between the scatterer and the Fourier modulus. Although structure persists in the azimuthal average because of the limited number of speckles at each value of the radial coordinate, from one speckle pattern to another the least-squares fit to the despeckled scattering envelope remains essentially unchanged. The underlying domain configuration uniquely determines the precise arrangement of the speckle, but the statistical averages expressed in the scattering lineshape describe the configurations in a non-

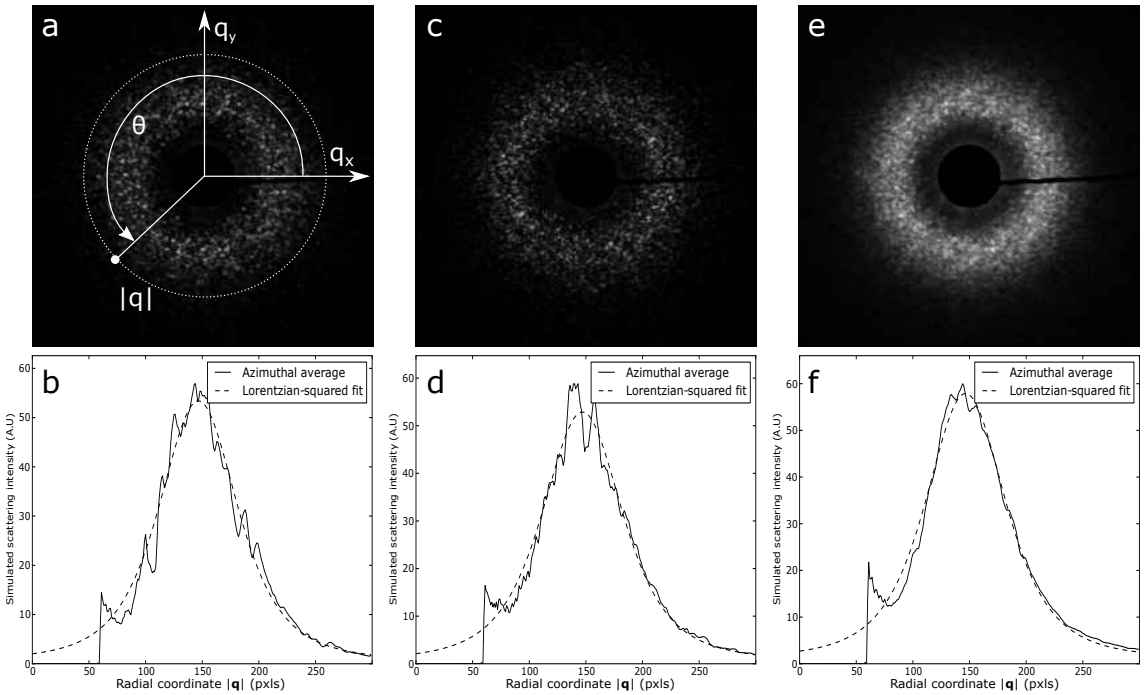

FIGURE 6.2.. Scattering lineshapes describe solution classes. Two different domain configurations generate two different speckle patterns (a) and (c), which share respective lineshapes (b) and (d). Summing many speckle patterns in (e) reduces the speckle contrast and clarifies the average lineshape.

particular way. By adding together many independent speckle patterns, we wash out the particulars of the individual configurations and leave behind the average incoherent scattering lineshape. In Fig. 6.2.(e), we show the average of twenty-six scattering patterns taken with the same beam over different points on the same sample, and in Fig. 6.2.(f) we show the azimuthal average in analogy to (b) and (d). In this sense, the azimuthally-averaged scattering lineshape describes a class of configurations, to which both Fig. 6.2.(a) and (c) belong.

When interpreting experimental speckle patterns, we use inverse meters (or fractions thereof) for the units of the scattering wave vector $\mathbf{q}$, and the size of reciprocal space subtended by each pixel on the detector depends on the wavelength of the illumination and the distance between the sample and the detector. In the simulations of domain patterns we will conduct later, the Fourier transform of the domain pattern still generates the reciprocal representation, but the simulation does not require a true physical length scale and instead we use pixels as the unit directly. Consequently, a domain pattern simulation of size $N \times N$ with a scattering profile given by Equation 6.2. and with radius $|\mathbf{q}|_0 = N/l$ will have an average domain periodicity in the real space image of l pixels.

6.3. Modification of the Fourier Constraint

We now consider how to modify Equation 6.1. to accept as a solution not a unique diffraction pattern but rather an arbitrary member of the class of solutions described by a scattering lineshape such as that shown in Fig. 6.2.(b), (d), and (f). Such a modification must meet several requirements. First, the incoherent scattering class must be two dimensional to allow for structure in the rotation coordinate; this requirement forbids applying the azimuthal average used in

Figure 6.2. as a despeckling procedure. Second, the updated estimate of the Fourier modulus must belong to the despeckled scattering class. Third, the updated modulus estimate must retain the speckle characteristic of the underlying real-space estimate; this requirement forbids a trivial modification of Equation 6.1. in which we simply replace $\sqrt{I}$ with the desired despeckled scattering envelope. Finally, as in coherent imaging, self-consistency under enforcement of the constraints defines a solution.

Given a goal despeckled scattering intensity profile G and a despeckling operator D, a modification to Equation 6.1. which meets these requirements is:

$$\hat{F}(E_n) = \mathscr{F}^{-1}\left\{\sqrt{\frac{G}{D(|\tilde{E}_n|^2)}}|\tilde{E}_n|\exp\left(i\phi_n\right)\right\} \qquad \text{(Equation 6.3.)}$$

The update operation in Equation 6.3. merely multiplies the previous complex Fourier estimate $\tilde{E}_n$ by the ratio of the goal scattering profile and the current scattering profile. When the current scattering profile reaches the goal scattering profile, the estimate becomes self consistent. By operating only on the despeckled profiles, we preserve the speckle specific to the underlying domain configuration. Multiplying by the ratio of the goal scattering profile to the current scattering profile ensures matching the goal scattering profile during every iteration when finding a solution.

The simulation can use neither of the two strategies used in Fig. 6.2. to despeckle the scattering pattern; the azimuthal average because it assumes azimuthal symmetry, and the sum of many speckle patterns because $|E_n|$ gives only a single speckle pattern. Instead, we calculate an estimate of the incoherent scattering pattern by a convolution of the fully coherent speckle pattern with some

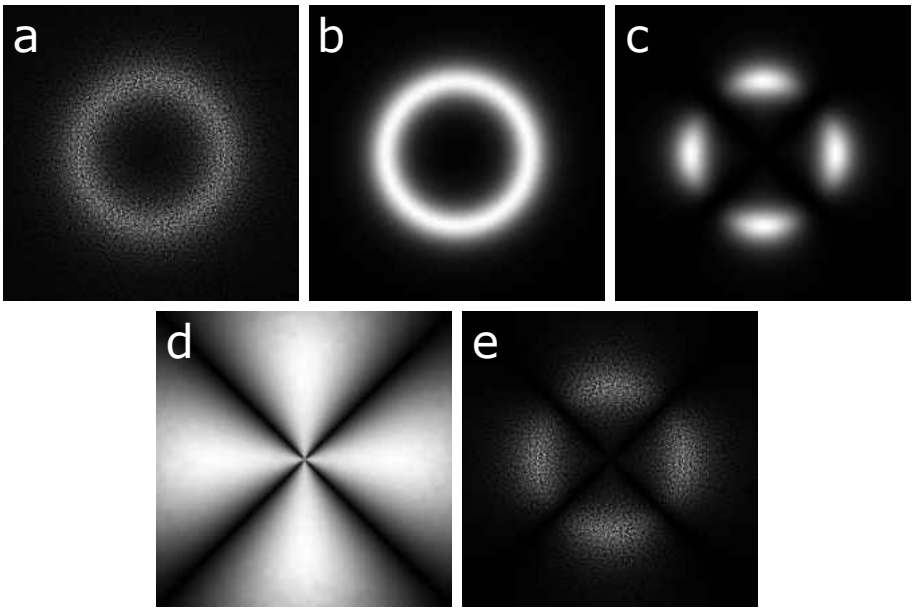

FIGURE 6.3.. Applying the modified Fourier-space constraint of 6.3. to a simulated speckle pattern. (a) shows the incoming Fourier modulus $|\tilde{E}|$, (b) the speckle blurred according to Equation 6.4., (c) the goal scattering profile with four-fold symmetry, (d) the rescaler function, and (e) the updated fourier modulus.

reasonable blurring kernel K. We define the despeckling operator as

$$D(|\tilde{E_n}|^2) = |\tilde{E_n}|^2 * K \qquad \text{(Equation 6.4.)}$$

and so

$$\hat{F}(\tilde{E_n}) = \sqrt{\frac{G}{|\tilde{E_n}|^2 * K}}|\tilde{E_n}| \exp(i\phi_n) \qquad \text{(Equation 6.5.)}$$

Finally, to satisfy Parseval's Theorem we require conservation of the total power of the speckle pattern before and after the application of Equation 6.5.. We therefore multiply the rescaled Fourier representation by an overall scaling factor p:

$$p = \sqrt{\frac{\sum |\tilde{E_n}|^2}{\sum |\hat{F}(\tilde{E_n})|^2}} \qquad \text{(Equation 6.6.)}$$

We break down the operation of Equation 6.5. in Figure 6.3.. The incoming fourier modulus $|\tilde{E}|$ (a) gets blurred by the convolution kernel K according to Equation 6.4. to give the despeckled intensity pattern in (b). Fig. 6.3.(c) shows the goal intensity profile; we use a squared lorentzian with the same center and $|\mathbf{q}|_0$ as the despeckled pattern in (b) but with an additional four-fold symmetry. The ratio of (b) and (c) calculated at all points in space give the rescaling ratio in (d). At the brightest azimuths of (c), the rescaler reaches unity because the speckles along those axes do not require modulation. However, along the minima azimuths in (c), (b) contains too much intensity, and consequently the rescaler suppresses the values at those locations. We show the updated Fourier modulus in (e), as the product of the incoming fourier modulus (a) and the rescaler (d). We leave the phase component of the Fourier estimate unchanged, as in imaging.

Notably, Fig. 6.3.(a) displays much smaller speckles than the experimental speckle patterns in Figure 6.2.. We do this purposefully to minimize the extent of the despeckling convolution kernel K and despeckle the intensity without significantly distorting the lineshape. In these simulations, we use for K a gaussian with standard deviation one-quarter the FWHM of the scattering lineshape. Because the degree of oversampling in Fourier space or equivalently the extent of zero-padding around the sample in real-space sets the size of the speckles in simulations such as these, minimizing the speckle size corresponds to simulating a sample which fills the entire real-space image. Due to the cyclic behavior of the discrete Fourier transform, solutions to the speckle class will have toroidal boundary conditions.

The calculations in Fig. 6.3. take place in a simulation with no net magnetization, making the value of the central pixel in the speckle pattern zero.

In simulations with a non-zero net magnetization, we must modify the incoming speckle pattern before rescaling the intensity envelope so that a convolution of the DC component does not pollute the nearby speckles. We perform this small correction by replacing the central speckle with the average of its nearest neighbors prior to rescaling; after rescaling the intensity envelope, we restore the original value of the central speckle to maintain the net magnetization of the simulation. In terms of preserving the power of Fourier transform, we do not include the DC component in the sums of Equation 6.6..

6.4. Real-Space Constraints on the Magnetization

While modifying the traditional Fourier modulus constraint familiar from imaging to accommodate a class of solutions requires only relatively straightforward changes, the constraints applied to the real-space representation of the domain pattern contain more complexity and freedom. In diffractive imaging, the real-space constraints typically involve the compactness of the solution; for simulating magnetic domains, however, minimizing the distortion applied by the Fourier constraint requires a small K and consequently no oversampling. For this reason we use no support constraint. Instead, we make assumptions regarding other aspects of the sample.

First, we model the real-space representation as a scalar field whose value represents the out-of-plane component of the magnetization; we require the field to be real-valued and range between negative one and positive one, the former implying out-of-plane magnetization antiparallel to the propagation of the beam and the latter parallel. Second, we encourage the real-space representation to favor fully saturated magnetization values of either negative one or positive one to reflect

the perpendicular anisotropy of the sample. Finally, apart from biasing the local magnetization, we also constrain the overall magnetization of the sample in order to simulate the magnetization configuration all the way from the initial reversal point through remnance.

Deciding which constraints to enforce in the real-space representation presents the primary difficulty, as enforcing them typically becomes just a matter of coding efficiency. Given an estimate of the out-of-plane magnetization E_n at some iteration n, we label and satisfy the above constraints as follows:

Bounds constraint:	$\hat{B}(E_n) = \text{sgn}(E_n) \times \min(\lvert E_n \rvert, 1)$	(Equation 6.7.)
Saturation constraint:	$\hat{S}(E_n) = (1+\alpha)E_n - \alpha E_n^3$	(Equation 6.8.)
Magnetization constraint:	$\hat{M}(E_n) = E_n + (W(E_n) \times m_0)$	(Equation 6.9.)

These constraints operate on each site in the simulation independently, and in numerical codes we implement them through fast vectorized functions. In comparison to the easily-understood reality constraint and bounds constraint $\hat{B}$, the saturation constraint $\hat{S}$ and the net magnetization constraint $\hat{M}$ require additional explanation.

6.4.1. The Saturation Constraint

In explaining the saturation constraint, we assume that the magnetization has local minima of free energy which occur when the magnetization points entirely out of plane, or when $|E_n| = 1$. This restates the perpendicular anisotropy of the thin

film. The simplest polynomial free energy which models the desired behavior is

$$F = F_0 - \frac{1}{2}E_n^2 + \frac{1}{4}E_n^4 \qquad \text{(Equation 6.10.)}$$

and the "force" felt by a local spin which undergoes an excursion away from the energy minima at $E_n = \pm 1$ is

$$-\frac{dF}{dE_n} = E_n - E_n^3 \qquad \text{(Equation 6.11.)}$$

Consequently, when updating the estimate of the real-space representation we bias the current estimate E_n towards saturated local spins by adding in some fraction of Equation 6.11.:

$$\hat{S}(E_n) = E_n + \alpha\left(-\frac{dF}{dE_n}\right) = (1+\alpha)E_n - \alpha E_n^3 \qquad \text{(Equation 6.12.)}$$

In the simulations we will show, we keep the bias parameter α set to 0.5 but the results do not seem particularly sensitive to the specific value.

6.4.2. The Magnetization Constraint

As Equation 6.8. rapidly biases the value of the individual sites in the simulation towards ± 1, we naturally modify the value of domain walls to satisfy the global magnetization constraint. Here, we define a simulation site as being along a magnetic domain wall if at least one of its nearest neighbors differs in sign and find domain walls in the current estimate E_n at some site indexed i with the following

binary function:

$$W(E_{n,i}) = \min\left(1, \sum_{j}^{\text{Neighbors}} \left[1 - \frac{1 + \text{sgn}(E_{n,i} \times E_{n,j})}{2}\right]\right) \qquad \text{(Equation 6.13.)}$$

The wall function W_i evaluates to zero if all the neighbors j of site i have the same sign as i, but evaluates to one if one or more of the neighbors have a differing sign. We calculate the value by which to promote the spins in the domain walls by comparing the current net magnetization to the desired average magnetization M_0, with N the number of sites in the simulation:

$$m_0 = \frac{M_0 N + \sum_i E_{n,i}}{\sum_i W_i} \qquad \text{(Equation 6.14.)}$$

In a strict sense, altering the value of spins in the domain walls via Equation 6.8., Equation 6.13., and Equation 6.14. will satisfy the net magnetization constraint. However, if the desired average magnetization M_0 differs too much from the current average magnetization $\sum E_{n,i}/N$, application of Equation 6.9. may break the bounds constraint Equation 6.7.. For this reason, we apply the bounds constraint a second time at little computational cost compared to the four Fourier transforms required to implement $\hat{F}$.

6.5. Self-consistency Determines Iterate Convergence

Given the various constraint operators $\hat{F}$, $\hat{B}$, $\hat{S}$, $\hat{M}$, we generate a new estimate by:

$$E_{n+1} = \hat{B}\hat{M}\hat{B}\hat{S}\,\text{Re}\,\hat{F}E_n \qquad \text{(Equation 6.15.)}$$

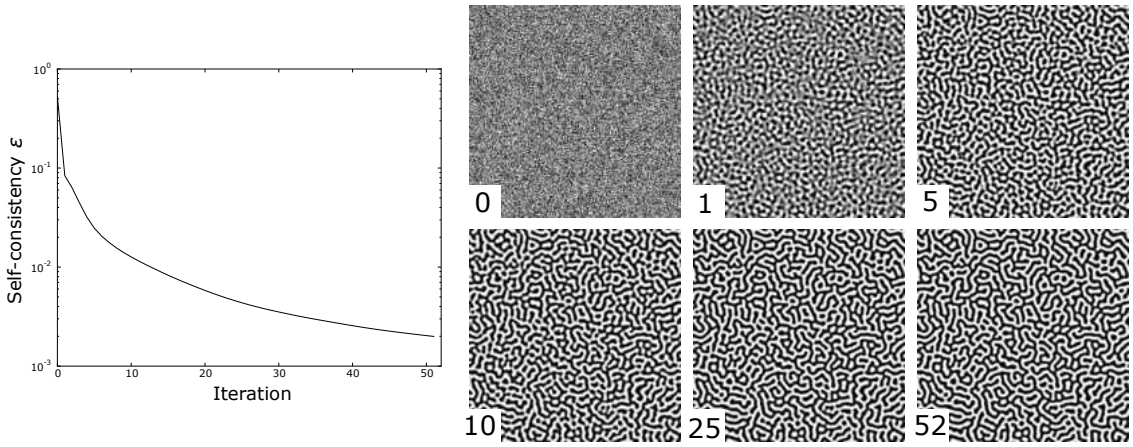

FIGURE 6.4.. Converging a magnetic domain pattern from a seed of random numbers. Left, the self-consistency parameter ϵ vs iteration number; right, the domain pattern after the marked number of iterations.

With the various constraint operators defined, the simulation iterates to a self-consistent solution. Here, we define self-consistency as the degree to which two sequential estimates differ:

$$\epsilon = \frac{1}{N} \sum_{\text{space}} |(E_n - E_{n-1})| \qquad \text{(Equation 6.16.)}$$

In the simulations in this chapter, we accept as sufficiently self-consistent $\epsilon < 0.002$.

We show the simulation of a labyrinthine magnetic domain pattern in Figure 6.4.. In this simulation, we set as the initial real-space estimate E_0 a field of random numbers uniformly distributed between negative one and positive one. Evolution of the domain pattern occurs by repeated application of the operator sequence Equation 6.15., with the real-space estimate after each iteration being used to compute the degree of self-consistency ϵ according to Equation 6.16.. In the left panel of Fig. 6.4. we show the logarithm of the degree of self-consistency as a function of iteration number. The simulation rapidly converges according to the self-consistency parameter, and inspection of the domain patterns confirms this

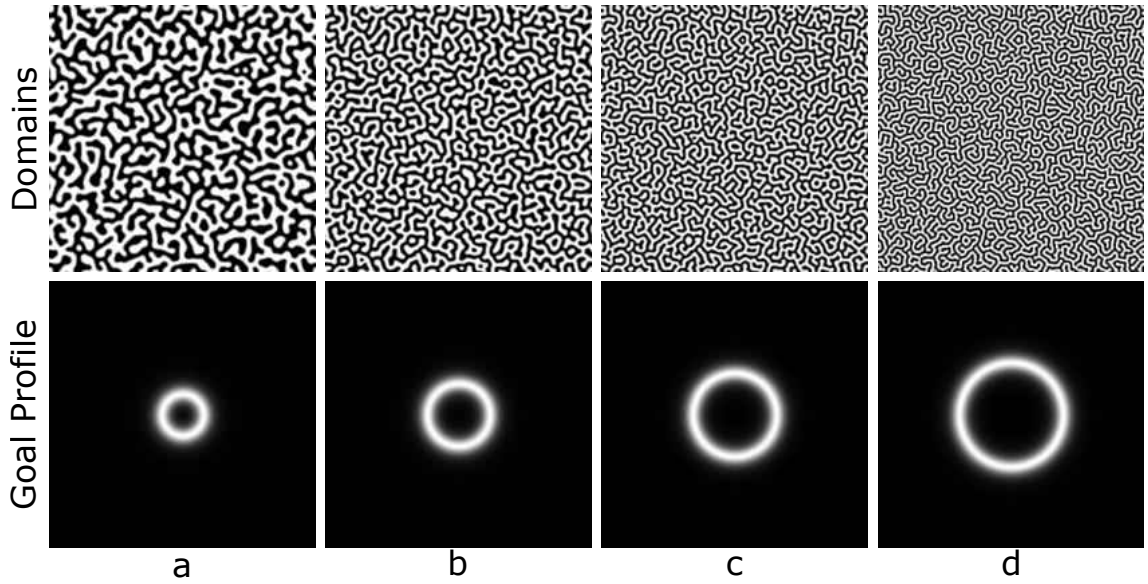

FIGURE 6.5.. Chained simulations allow movement between solution classes. First, we converge a domain pattern from a random seed (a), then sequentially change the goal profiles to generate different solutions (b) (c) and (d).

conclusion. Along with each domain pattern we show the iteration number of the simulation; after even only five iterations, the features of the labyrinth have already become apparent and the spins have segregated into well-defined parallel and anti-parallel domains. As the simulation proceeds, refinements take place across the labyrinth until eventually the calculation terminates after (in this case) the fifty-second iteration. However, the vast majority of the iterations occur in a highly-converged regime; without close inspection, the differences between iterations ten, twenty-five, and fifty-two become nearly invisible.

6.6. Varying Solution Classes in Chained Simulations

Once a simulation has converged, we can use it as the starting point in a second simulation in which we slightly adjust the scattering profile. A chained simulation of this sort allows an "apples-to-apples" comparison of the effect of

different scattering profiles as opposed to the "apples-to-oranges" approach of comparing two simulations which start from independent random seeds. We show a set of simulations where we use a converged domain pattern as the starting point in a second stage in Figure 6.5.. Simulating on a 256×256 grid, we converge a domain pattern with scattering lineshape given by Equation 6.2. with central radius $|\mathbf{q}|_0 = 20$ pixels and width $w = 9.7$ pixels. This value of the central radius leads to domains with average periodicity $256/20 = 12.8$ pixels. We then systematically increase the central radius $|\mathbf{q}|_0$ from 20 to 50 pixels, generating the domain pattern in column (b) with $|\mathbf{q}|_0 = 30$ pixels, in column (c) with $|\mathbf{q}|_0 = 40$ pixels, and column (d) with $|\mathbf{q}|_0 = 50$ pixels. The average domain size in these cases becomes 8.6, 6.4, and 5.2 pixels, respectively. Between the results presented in Fig. 6.5., we converged unshown intermediates to avoid drastic and unrealistic perturbations of the domain configuration. In all these simulations, we held the width of the scattering profile constant and the net magnetization zero.

However, we must take care in re-evolving the domain pattern to a changed goal scattering profile. By eschewing the requirement of inverting a specific speckle pattern to allow a class of solutions, we accept not only instances of domain patterns which generally look similar but also solutions which display obvious morphological differences in the real-space representation. We show in Figure 6.6. a set of simulations in which a scattering lineshape of form Equation 6.2. with $|\mathbf{q}|_0 = 25$ pixels and $w = 7.8$ pixels re-converges using a lineshape with $|\mathbf{q}|_0 = 25$ pixels but $w = 19.4$ pixels. Fig. 6.6.(a) shows the two profiles in cross-section, (b) the simulation converged to the first, narrower, profile, and (c) through (g) the re-convergence under a variety of simulation trajectories and procedures. We identify three broadly distinct morphologies: (c) alone; (d) alone; and (e), (f), and (g) as

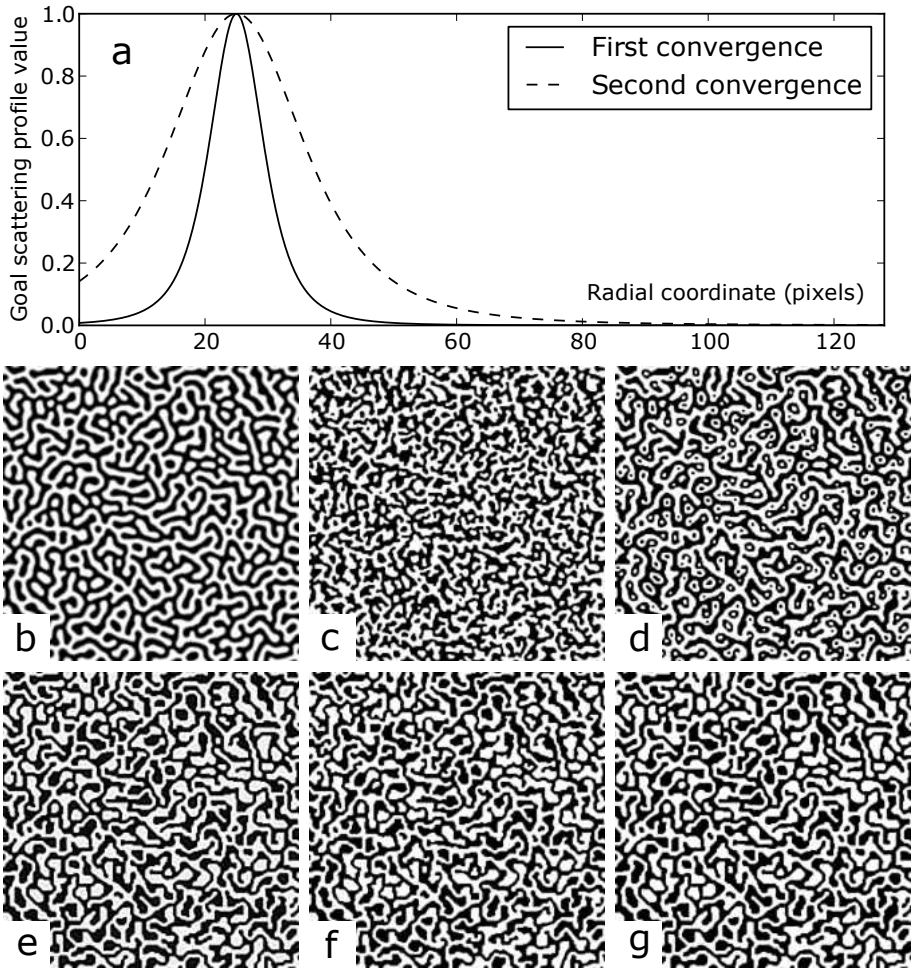

FIGURE 6.6.. Different simulation trajectories lead to different solution morphologies. (a) shows the two scattering lineshapes used in the growth simulation with fixed center but variable width, (b) the domains converged to the first lineshape, and (c)-(g) the domains reconverged under various simulation procedures; details in text body.

a set. The difference between these outcomes lies not in the constraints but in the methods of their enforcement.

In Fig. 6.6.(c), we do not directly re-converge the simulation after the primary convergence shown in (b), but instead perform an independent convergence from the same random seed. This simulation provides the clearest insight into how broadening the scattering profile might effect the real-space configuration, or what it means to reduce the domain correlation length. To satisfy the lineshape's demand of both larger feature sizes (scattering signal near center of diffraction pattern) and smaller features sizes (scattering signal near edges of diffraction pattern), the domain configuration adopts a more disordered appearance.

In Fig. 6.6.(d), we move directly from the narrow primary profile to the wide second profile in a single step, demanding rapid and drastic changes in the domain pattern. The simulation most easily meets the demand for the smaller features required by the scattering profile through the nucleation of small, isolated domains within existing domain of the opposite orientation. While the simulation constraints strictly permit this type of morphology, it does not conform to the general expectations of domain formation supplied by experimental microscopies that we get from Fig. 6.1.. Energetic considerations disfavor the formation of island domains in the center of an already saturated region, especially when compared to a simpler reconfiguration of domain walls.

In Fig. 6.6.(e) we see this latter strategy pursued by the simulation when the path from the narrow primary profile to the broad second profile passes through many intermediate profiles in which the width w changes slowly. Under this approach, expanding and contracting domain walls, rather than spurious nucleation deep in domains, provide the needed diversity of feature sizes. Fig. 6.6.(f) and (g)

confirm this effect modifying the Fourier constraint $\hat{F}$ in Equation 6.3.. Rather than accepting all the changes implemented by an the Fourier rescaling, we choose to keep only those which act within the domain walls regions:

$$E_{n+1} = \hat{B}\hat{M}\hat{B}\hat{S}\,\mathrm{Re}\,\hat{F}_2 E_n$$
$$\hat{F}_2(E_n) = W(E_n)\hat{F}(E_n) + [1 - W(E_n)]E_n \qquad \text{(Equation 6.17.)}$$

The wall function W comes from Equation 6.13. and the other constraint operators remain unchanged. Using this modified Fourier constraint, shifting between the goal profiles in a single step as in Fig. 6.6.(f) or a series of small steps as in (g) produces nearly identical outcomes.

As the results in (c), (f), and (g) all satisfy the available constraints and lack the obvious implausibility of (d), we lack clear rules on how to distinguish between the solution morphologies without greater input from microscopy of actual domain patterns. The difficulties of evolving a domain pattern between two very different scattering profiles with no concurrent change in net magnetization may also reflect an inherently unrealistic possibility. We take as the primary lesson from such simulations that, as with all models, blind application can lead to poor results, and we must employ caution in their interpretation.

6.7. Creating Angular Symmetries With the Solution Class

Next, we explore the impact of introducing angular symmetries into the goal scattering profile, which we will use in interpreting data in the following Chapter.

We build rotational symmetries into the scattering profile $G(\mathbf{q})$ according to

$$G(\mathbf{q}) = G_0(|\mathbf{q}|)\left(1 + \sum_m \alpha_m \cos(m\theta) R_m(|\mathbf{q}|)\right) \qquad \text{(Equation 6.18.)}$$

where θ is the azimuthal coordinate, m the symmetry order, $G_0(|\mathbf{q}|)$ the isotropic scattering profile which has already been demonstrated, $R_m(|\mathbf{q}|)$ are the $|\mathbf{q}|$ envelopes within which the cosine terms are confined, and α_m, valued between 0 and 1, sets the strength of the symmetry. This multiplicative modulation of the scattering profile modifies simulation constraints in the simplest way which generates angular symmetries in reciprocal space and the only modification which does not require complicated intervention on a per-speckle basis in order to generate the correlation. Using this formulation, we can easily simulate arbitrary symmetry orders at arbitrary length scales.

Figure 6.7. demonstrates the effect on the real-space representation of introducing a four-fold symmetry ($m = 4$) at various length scales $|\mathbf{q}|$. We first converged each simulation from the same seed using the same isotropic goal scattering profile; this seed and scattering profile converge to give Fig. 6.6.(b). After convergence, we changed the goal profile in a single step to include the four-fold symmetry with $\alpha_4 = 1.0$. In column (a), the simulation modulates all length scales equally by setting $R_4(|\mathbf{q}|) = 1$. This modulation leads to pronounced changes in the real space representation as the domains now preferentially align along the principal axes of the simulation and no longer align along the diagonals. The bottom image in the column shows the magnitude of the difference between the ordered domain pattern and the isotropic pattern of Fig. 6.6.(b); the bright spots in the image indicate where domains have flipped orientation in order to satisfy the new scattering profile. Some of the changes involve where two domains of the same

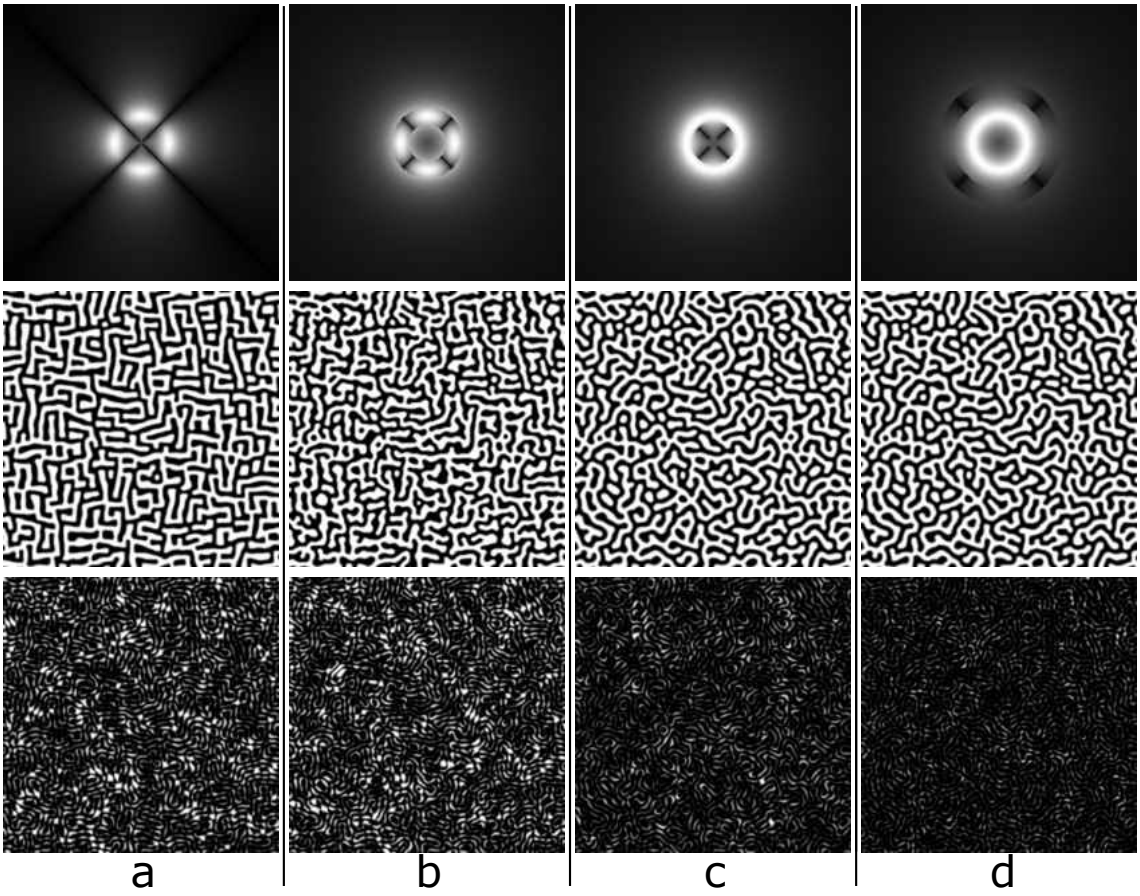

FIGURE 6.7.. Introducing rotational symmetries in the Fourier profile leads to reconfigurations of the domain pattern. In (a), we modulate all $|\mathbf{q}|$ with a four-fold symmetry. In (b), (c), and (d) we restrict the modulation to narrower ranges of $|\mathbf{q}|$. The bottom row shows the difference between the above results and the isotropic domains in Fig. 6.6.(b).

sign combine by bridging and splitting a domain of the opposite sign; the remainder of the changes consist of minor modifications to the domain wall configuration which straighten sides and square corners.

The simulation in column (b) restricts the symmetry to length scales near the center of the scattering ring through radial envelope

$$R_4(|\mathbf{q}|) = \begin{cases} 1, & |\mathbf{q}|_0 + w > |\mathbf{q}| > |\mathbf{q}|_0 - w \\ 0, & \text{otherwise} \end{cases}$$

In this case, the domains still realign along the principal axes but the restricted modulation range lowers the visual impact. While the realignment of the domains remains evident, features which place more spectral power in higher $|\mathbf{q}|$, such as domain corners, experience less evolution. As in the case of modulation at all length scales, changes to the domain configuration involve both bridging and splitting as well as minor domain wall realignment.

The simulation in column (c) restricts the symmetry to large length scales on the interior of the scattering ring through the radial envelope

$$R_4(|\mathbf{q}|) = \begin{cases} 1, & |\mathbf{q}|_0/2 + w > |\mathbf{q}| > |\mathbf{q}|_0/2 - w \\ 0, & \text{otherwise} \end{cases}$$

In this case, changes to the real space domain configuration remain essentially invisible without the aid of the explicit differences. No domains bridge in making this modulation in the scattering profile, and minor reconfigurations of domain walls seem the only changes in the pattern.

Similarly, column (d) restricts the symmetry to small length scales at larger radial coordinates than the center of the scattering ring; the radial envelope is

$$R_4(|\mathbf{q}|) = \begin{cases} 1, & 2|\mathbf{q}|_0 + w > |\mathbf{q}| > 2|\mathbf{q}|_0 - w \\ 0, & \text{otherwise} \end{cases}$$

As with modulating the domain pattern below $|\mathbf{q}|_0$, we find no changes in the domain pattern except minor modification of domain walls; we see no major bridging points where domain polarity reverses in order to satisfy the new scattering profile.

These simulations produce no startling results. Even with the maximum strength symmetry ($\alpha_m = 1$), the effect of the symmetry depends strongly on its location in $|\mathbf{q}|$ relative to the center of the scattering ring $|\mathbf{q}|_0$. We understand this easily: the intensity of the Fourier transform at any particular radius $|\mathbf{q}|$ describes the importance of that length scale in the real-space configuration, so we cannot expect modulations to regions of $|\mathbf{q}|$ lacking appreciable scattering intensity to produce readily visible alterations in the real-space configuration.

CHAPTER VII

A SYMMETRY MICROSCOPE FOR DISORDERED MATERIALS

7.1. Introduction and Motivation

Condensed matter physics is rich with systems which display only short range order [135], such as the labyrinthine domains in perpendicular magnetic thin films [136], as well as superconductors [100, 137, 138], liquid crystal and copolymer films [139, 140], biological membranes, granular flows, reaction-diffusion systems [141–143], and Rayleigh-Benard convection [144]. The lack of long-range order in these and other systems precludes translational symmetry but does allow different local, or short-range, ordering within the same sample. Scientists have essentially solved the structure problem of ordered materials, with even crystals of proteins or other complex biological samples often solvable to atomic resolution through highly refined electron and x-ray diffraction methods [145–147]; in contrast, the lack of long-range order in liquid, amorphous, or glassy materials makes the determination of the microstructure exceptionally challenging [148–150]. Coherent diffraction, through its sensitivity to the unique configuration of the sample at the point of illumination, offers a path forward on characterizing and understanding the local structure of disordered materials [151]. In particular, coherent scattering from isotropic systems enables the search for otherwise hidden rotational symmetries preserved by the Fourier transform during the diffraction process.

We motivate the forthcoming analysis with an example of an apparent hidden rotational symmetry in a perpendicular magnetic thin film, shown in Figure 7.1.. In Fig. 7.1.(a) we show the speckle pattern containing the candidate; the isotropy

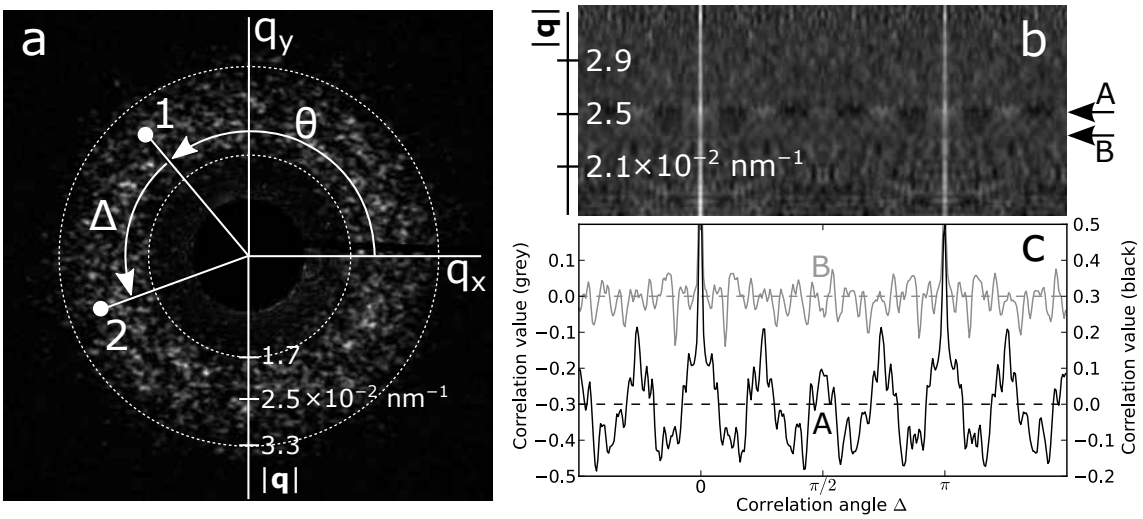

FIGURE 7.1.. A candidate rotational symmetry in a magnetic speckle pattern from a cobalt-palladium thin film. (a) shows the speckle pattern with the coordinates and length scales marked; points labeled 1 and 2 have the same $|\mathbf{q}|$ but a relative angle Δ separates them. (b) shows the angular correlation within the dashed bands of (a). (c) shows two cross-sections through (b) at the arrows labeled A and B. A cuts through the symmetry candidate and B outside the ordered lengthscale.

of the domain labyrinth scatters x-rays to all azimuths θ, and the dominance of a single characteristic length-scale within the labyrinth means that the lineshape in $|\mathbf{q}|$ peaks at some non-zero value. Here, we find the maximum scattering intensity at approximately $2.5 \times 10^{-2}\text{nm}^{-1}$, corresponding to a feature size of $2\pi/|\mathbf{q}| \approx 250\text{nm}$. To search the pattern for hidden rotational symmetries, we adopt the angular cross-correlation defined by Wochner [152]:

$$C(|\mathbf{q}|, \Delta) = \frac{\langle I(|\mathbf{q}|, \theta) I(|\mathbf{q}|, \theta + \Delta) \rangle_\theta - \langle I(|\mathbf{q}|, \theta) \rangle_\theta^2}{\langle I(|\mathbf{q}|, \theta) \rangle_\theta^2} \qquad \text{(Equation 7.1.)}$$

Equation 7.1. describes the degree of correlation between the original speckle pattern and the same pattern rotated about the center by some angle Δ. This correlator maintains the structure of the familiar cartesian correlation function but rotates rather than translates.

Applying Equation 7.1. to the dashed region of Fig. 7.1.(a) generates Fig. 7.1.(b). Two main features require explanation. First, we note the stripes across $|\mathbf{q}|$ at $\Delta = 0$ and $\Delta = \pi$; these correspond to the autocorrelation peak and the spatial inversion peak, respectively. The latter results from the strong absorption contrast present in the magnetic sample when we tune the illumination to the L_3 resonance, which in turn makes the exiting illumination strongly real-valued and gives the speckle pattern approximate inversion symmetry; both phase retardation in the sample and phase structure in the incident illumination partially break this symmetry. Second, we note the pronounced eight-fold oscillation visible by eye at approximately 2.5×10^{-2} nm^{-1}, near the center of the scattering ring. While some amount of structure pervades the entirety of the correlation image, the strength of the oscillation suggests the existence of a hidden rotational symmetry within the nominally disordered sample. We emphasize the strength of the eight-fold feature by plotting in Fig. 7.1.(c) a pair of cross-sections taken along the Δ coordinate at the $|\mathbf{q}|$ values marked A and B in Fig. 7.1.(b). The magnitude of the eight-fold oscillation in cross-section A dominates the residual structure present nearby in cross-section B.

Such pronounced structure raises two basic questions. First, how do nominally disordered magnetic domains differ from those ordered only within a narrow annular band of reciprocal space? Second, how can we distinguish between the sort of trivial statistical structure caused by correlating a small number of speckles and the sort of structure in the correlation which indicates a true local ordering mechanism at work? To illustrate the critical importance of the latter question, we show examples of applying the angular correlation in Equation 7.1. to simulated realistic speckle patterns generated from a real-space object composed

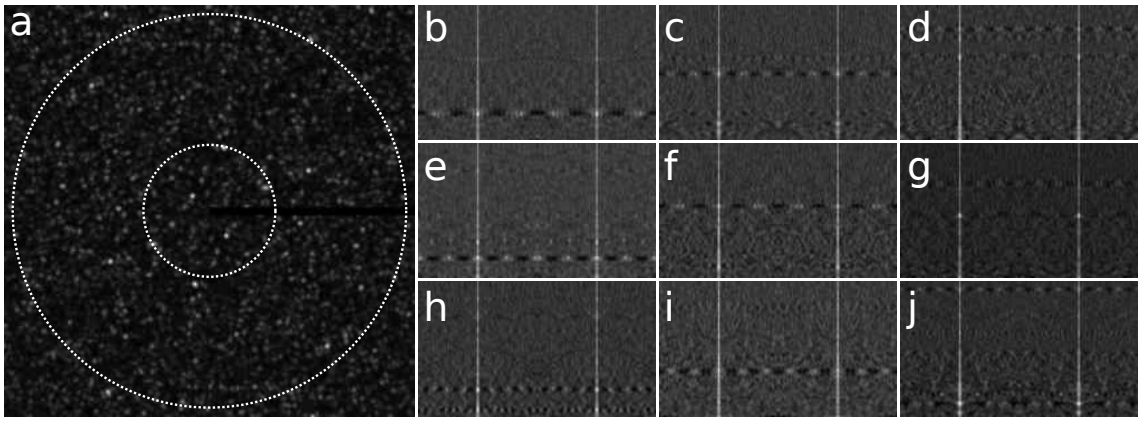

FIGURE 7.2.. Finding symmetries in completely random speckle patterns. (a) shows a partially coherent speckle pattern generated from an array of random numbers and a circular illumination function. (b)-(j) show angular correlation functions from speckle patterns like (a), correlated within the marked region of $|\mathbf{q}|$.

of random numbers in Figure 7.2.. Fig. 7.2.(a) shows the type of speckle pattern being correlated and the dashed lines the approximate range of $|\mathbf{q}|$ used in the calculation; as we will explain later, we optimized the simulation parameters to closely match the speckle morphology to that in Figure 7.1.(a). Fig. 7.2.(b)-(j) show a variety of apparent angular symmetries visually similar to those identified as the experimental candidate; however, because we design the real-space object to lack all symmetry, we understand these symmetry signatures as a small-size effect from the limited number of speckles being correlated at any particular $|\mathbf{q}|$. For the same reason that a string of coin flips landing as heads does not prove a coin biased, we must therefore remain skeptical of any particular candidate speckle symmetry and interpret it in the context of the expected correlation statistics rather than through appeals to its appearance.

Directly imaging the structure of the domains producing this signal would clearly provide great insight into the nature of local ordering with disorder, but our lensless reflection imaging work demonstrates that imaging experiments can present

serious challenges and difficulties in terms of design, execution, and data acquisition and analysis. In circumstances where the material under investigation undergoes subtle changes in ordering or configuration, the tremendous effort required to achieve a single image quickly becomes prohibitive as such experiments may require a large number of data points in order to establish statistical patterns of behavior. In this chapter, we use the domain simulation algorithms developed perviously to rapidly simulate the labyrinthine domain patterns characteristic of magnetic thin films with perpendicular anisotropy, and then in turn use the simulated patterns first to help understand how the magnetic domain configuration of an ordered sample might differ from a wholly disordered one and next to help sufficiently understand the statistics of the angular correlation function to judge whether the candidate speckle pattern in Fig. 7.1.(a) shows evidence of an ordering mechanism or mere statistical fluctuation.

7.2. Simulation of Candidate Symmetry

We now simulate the candidate symmetry using the algorithms developed earlier. The candidate symmetry lies at the center of the scattering ring ($2.5 \times 10^{-2}\text{nm}^{-1}$), with a width on the 1024×1024 detector of approximately 10 pixels. We therefore model the radial envelope $R_8(|\mathbf{q}|)$ similarly to that used in Fig. 6.7.(b), but with a narrower annulus. Figure 7.3. shows the results of a chained simulation, first converging the domain pattern from a random seed to the disordered state then slowly increasing the strength of the symmetry order parameter α to unity.

Although the symmetry under investigation here most resembles that previously simulated in Fig. 6.7.(b) due to placing the modulation at the peak

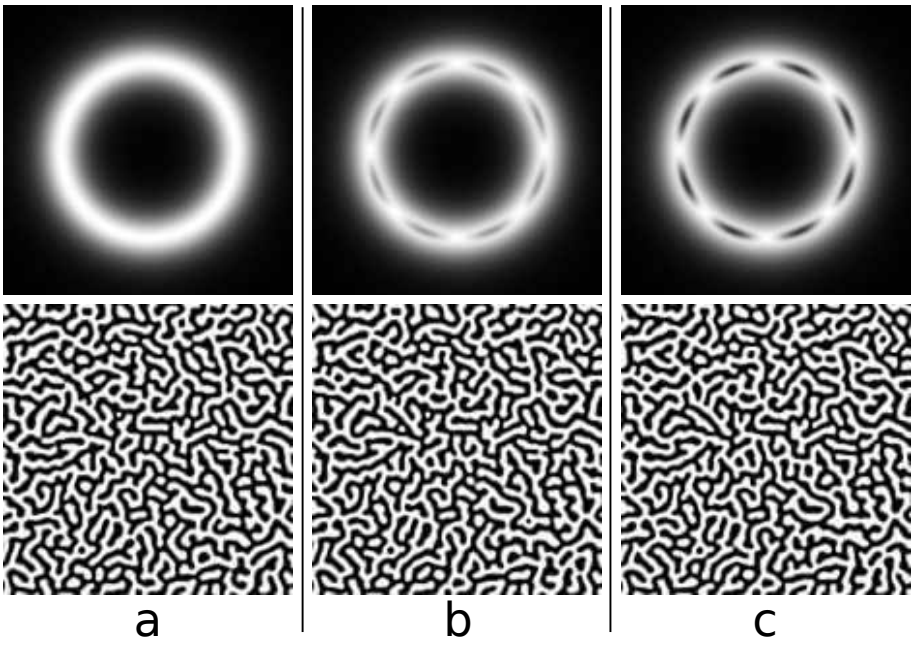

FIGURE 7.3.. Simulating the candidate rotational symmetry observed in Fig. 7.1.. (a) shows domains with $\alpha_8 = 0$, (b) $\alpha_8 = 0.5$, (c) $\alpha_8 = 1.0$.

of the scattering intensity, the results in Fig. 7.3.(b) and (c) are not nearly so dramatic as in the earlier $m = 4$ simulation. As Fig. 6.7.(c) and (d), in which the modulation occurred in a low-intensity region of the scattering pattern and was consequently did not drive any significant changes to the domain configuration, in the case of the experimental candidate symmetry the apparent symmetry region in $|\mathbf{q}|$ is simply too thin to induce noticeable changes in the real-space representation.

7.3. A Realistic Scattering Model

To use simulated domain patterns as a statistical basis to judge apparent rotational symmetries in experimental speckle patterns, we must develop a scattering model which transforms them into simulated speckle patterns as realistically as possible. We broadly separate the scattering model into two domains: the accuracy of the sample transmittance function, and the accuracy

of the illumination function. In the case of the illumination function, we find a variety of parameters to investigate, including the size of the upstream pinhole, the distance between the pinhole and the sample, the degree of partial coherence, and the blocker prior to the detector which protects the detector from the intense direct beam.

7.3.1. Sample Transmittance and Magnetic Circular Dichroism

First, we consider the transmittance of the sample. In the Born approximation, the relationship between the field incident on the sample and the field leaving the sample is given by:

$$U_{out}(u,v) = U_{in}(u,v)\exp\left[ikt(u,v)n(u,v)\right] \qquad \text{(Equation 7.2.)}$$

where k is the usual wavevector $2\pi/\lambda$, $t(u,v)$ is the thickness of the sample, and $n(u,v)$ is the index of refraction. For thin film samples such as those we simulate, the thickness remains approximately constant over the whole extent. However, the index of refraction exhibits magnetic circular dichroism and so the index of refraction changes as a function of the magnetization and the polarization state.

We implement the dichroic scattering formalism of Equation 2.34. in Figure 7.4.. The domain pattern used as scattering object has $|\mathbf{q}|_0 = 290$ pixels and $w = 120$ pixels, approximately what we find for experimental diffraction patterns. As illumination function, we use a circle of radius 95 pixels; we slightly deform the circle to introduce the radial intensity flares at high $|\mathbf{q}|$. To set the correct transmission function, we used a thickness t of 60nm, a wavelength of 1.93nm corresponding to the cobalt L_3 resonance, and obtained the values of δ and β from

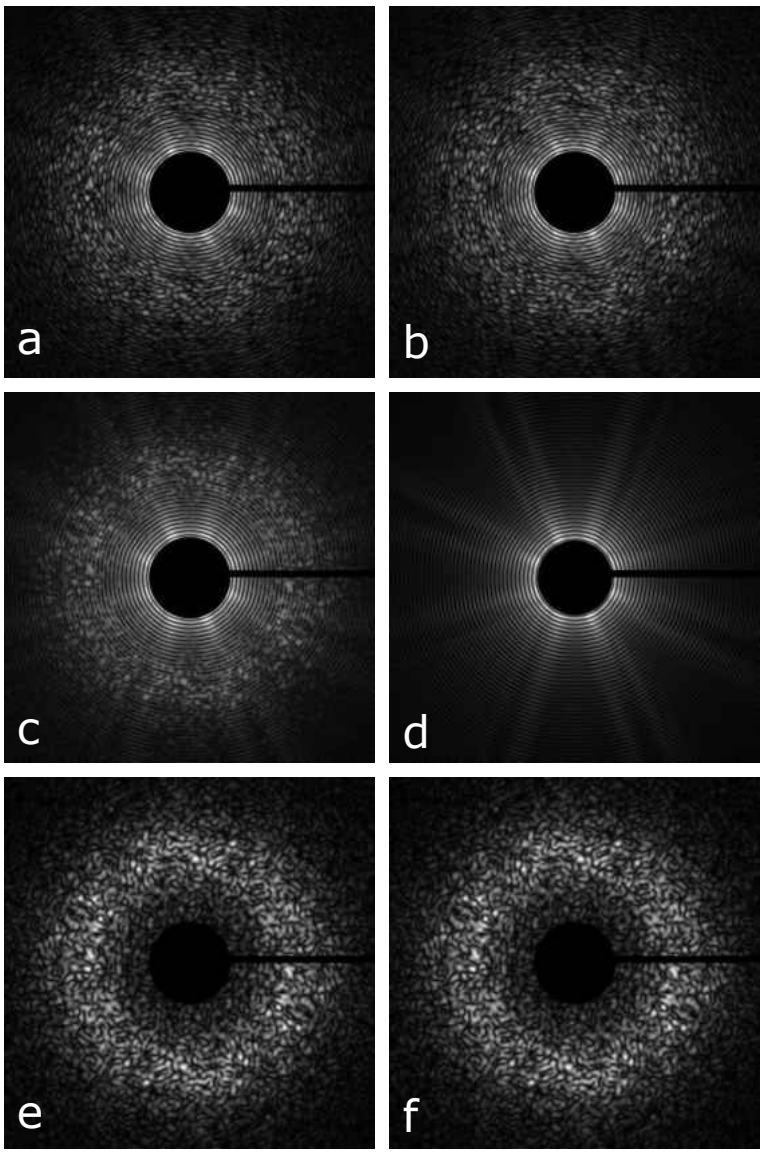

FIGURE 7.4.. Simulation of realistic dichroic speckle patterns. (a) and (b) show the speckle from left- and right- polarizations; (c) the sum of (a) and (b); (d) the charge scattering alone by $m(u,v) = const.$; (e) the isolated magnetic speckle by the difference of (c) and (d); (f) the Fourier modulus of the domain configuration directly.

the CXRO material database website [29]. The free parameter Δ corresponds to the degree of magnetic contrast, and after some variation we found that a value around $\Delta = 0.2$ gives good qualitative agreement with experimental speckle patterns; conceivably, we could obtain a more accurate measure of Δ from XMCD spectra of magnetized cobalt.

Fig. 7.4.(a) and (b) show the intensity patterns corresponding to the two circular polarizations. In each (a) and (b), the magnetic-scattering speckles around $|\mathbf{q}|_0$ and the Airy fringes from the pinhole intertwine such that the Airy fringes appear discontinuous, and cannot be followed around all azimuths. Fig. 7.4.(c) simulates the diffraction pattern from linearly polarized light in accordance with Equation 2.34. by adding the patterns from (a) and (b). In (c), the Airy fringes become continuous. Fig. 7.4.(d) shows the diffraction pattern obtained by setting $m(u, v)$ to a constant, simulating the effect of just the charge component of the scattering. Fig. 7.4.(e) shows the difference of (c) and (d), clearly demonstrating that when simulating the dichroic diffraction pattern through the optical constants method, the charge and magnetic scattering become separable as predicted by the scattering factor formalism and Equation 2.30.. We may therefore isolate the magnetic scattering by subtracting a signal which contains charge scattering only. Fig. 7.4.(f) shows the result of skipping the dichroic scattering model, which requires a Fourier transform for both polarization, and instead directly forming the speckle pattern by the Fourier transform of the domain pattern with parallel and anti-parallel spins relative to the beam propagation vector set to ± 1. Up to a multiplicative scaling constant, the speckle pattern formed through the full dichroic scattering model matches identically the speckle pattern formed by the Fourier transform of the domain pattern. As the formation of the speckle

pattern in Fig. 7.4.(e) requires two Fourier transforms and that in (f) only one, we therefore model the dichroic scattering process through the Fourier transform of the magnetization alone.

7.3.2. Optimization of the Illumination Function Parameters

With the scattering model for the sample established, we next consider the impact of the illumination function and the degree of coherence on the appearance and statistics of the speckle pattern. We try to optimize three variables so that the angular correlation of a simulated speckle pattern matches the angular correlation of the candidate symmetry in terms of the height and width of both the autocorrelation peak at rotation coordinate $\Delta = 0$ and the spatial inversion peak at $\Delta = \pi$. Assuming a perfectly circular aperture filtering the beam, we optimize the radius of the pinhole and the separation distance between the pinhole and the sample. Assuming an azimuthally-symmetric gaussian as the coherence function, we optimize the width of the gaussian. Changing the several parameters gives the following primary effects: increasing the pinhole radius decreases the average speckle size and narrows the width of the correlation peaks; decreasing the coherence length decreases the speckle contrast, decreasing the height of both correlation peaks; increasing the sample-pinhole separation distance increases the phase curvature in the illumination at the sample plane, decreasing the inversion symmetry of the speckle pattern and decreasing the height of the correlation peak at $\Delta = \pi$ relative to that at $\Delta = 0$. As can be seen in Fig. 7.1., the value of the correlation peaks can vary substantially over $|\mathbf{q}|$, and for that reason we match an average of the correlation taken over a range of $|\mathbf{q}|$ near the $|\mathbf{q}|$ of the candidate.

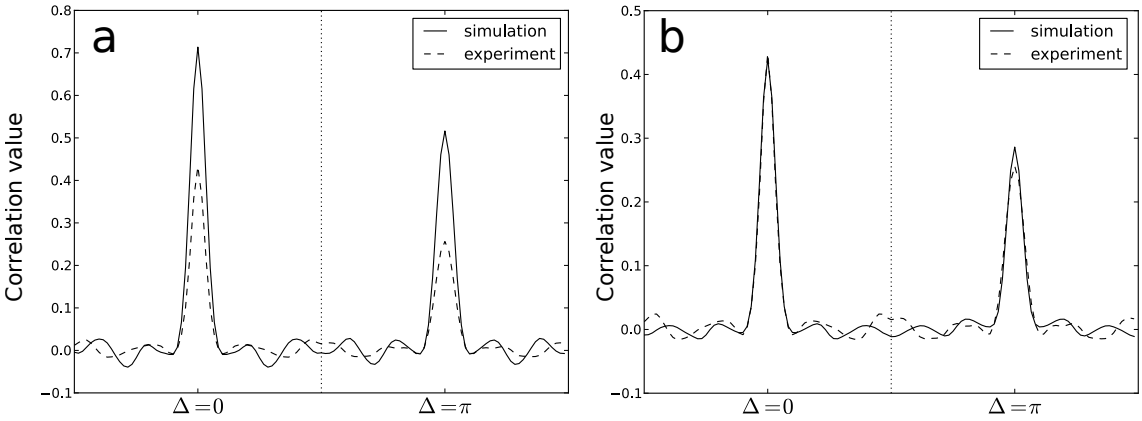

FIGURE 7.5.. Optimizing the illumination function in the scattering model; parameters to optimize include pinhole radius, pinhole distance, and coherence length. (a) shows a portion of the angular correlation before optimization, (b) after optimization.

Figure 7.5. shows cross-sections through the angular correlation functions near $|\mathbf{q}|_0$, the length-scale of the candidate symmetry, for two points in the illumination parameter space. In Fig. 7.5.(a), we used pinhole 3.2μmin radius, an illumination coherence length of 5.7μm, and a the pinhole-sample separation of 3mm. Under this set of parameters, the simulated angular correlation mismatches the experimental data at both peaks. Qualitatively, we note the peaks are too wide, so the pinhole is too small; the peaks are too tall, so the coherence length is too long, and the ratio of the $\Delta = \pi$ peak to the $\Delta = 0$ peak is too high, so the pinhole propagation distance is too short. In Fig. 7.5.(b), we show the best attained match between the simulated and experimental correlations, with pinhole radius 4.2μm, coherence length 4.1μm, and pinhole-sample separation distance 7mm. These values all closely agree with known or estimated endstation and beamline parameters. Further increasing the simulated pinhole-sample separation distance does not improve the match of the $\Delta = \pi$ peak, implying either some phase structure to the beam incident on the upstream pinhole as a result of the beamline optics or the

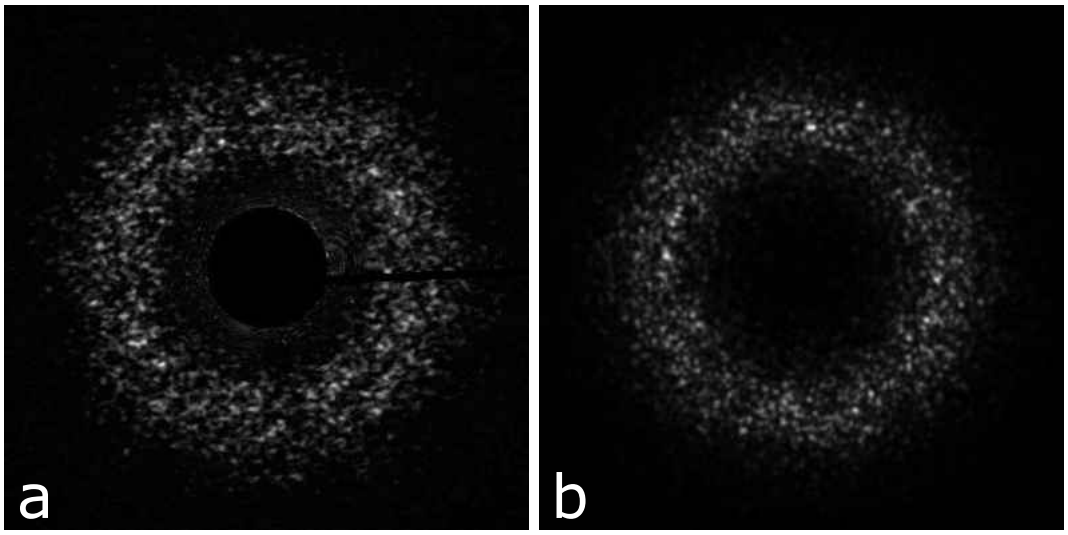

FIGURE 7.6.. Comparison of real (a) and simulated (b) magnetic speckle patterns

direct Fourier transform of the magnetization does not fully capture the complex modulation of the illumination passing through the magnetic domains. Neither explanation would be surprising.

We directly compare the candidate speckle pattern to a realistic simulation using the optimized illumination parameters in Figure 7.6.. Qualitatively, the resemblance seems very good. In Figure 7.6.(b), we have not included an approximation of the beamblock, which in future simulations we model as a rectangular region of width approximately twenty pixels on the detector, extending from the center to the very edge of the speckle pattern. Within the blocker region we set the scattering intensity to zero. The blocker does not effect in a significant way the simulation results shown in Figure 7.5..

7.4. Statistics of the Angular Correlations

With the correct simulations parameters established, we now prepare to interpret the candidate experimental symmetry in the context of statistical

expectations regarding the angular correlation of magnetic speckle patterns developed from a large number of speckle patterns simulated as realistically as possible. In contrast to highly analytical derivations of speckle statistics[6], we here adopt a semi-empirical approach based in analysis of simulated speckle patterns.

For this judgment, we adopt relatively simple metrics. First, we will consider the robustness of decomposing the angular correlation of the candidate at each $|\mathbf{q}|$ into a cosine series, assuming that the presence of an order-forming mechanism will lead to cosine coefficients well outside the range seen from simulations in which we restrict the domain configuration to the disordered state. Because inspecting components in this way supposes a symmetry of a particular order m, we will also consider a second metric for reducing the cosine spectrum at a given $|\mathbf{q}|$ across the m axis, measuring the concentration of the power of the spectrum in any m without regard for which particular m.

7.4.1. Cosine Decomposition of Angular Correlation

Figure 7.7. illustrates the steps of the cosine decomposition process. The simulation algorithm and scattering model described earlier generate the realistic simulated speckle patterns displayed in Fig. 7.7.(a) and (b). The patterns in (a) and (b) show the scattering from a disordered configuration and a configuration ordered within the main scattering ring with order parameter $\alpha = 0.5$, respectively. In Fig. 7.7.(c) and (d), we show the angular correlation of each of the two speckle patterns calculated by the correlation equation Equation 7.1.; the region of correlation lies within the dashed annulus. As seen in Fig. 7.5., the scattering model used here has difficulty exactly reproducing the spatial inversion peak of the correlation, which may consequently distort the cosine decomposition of the

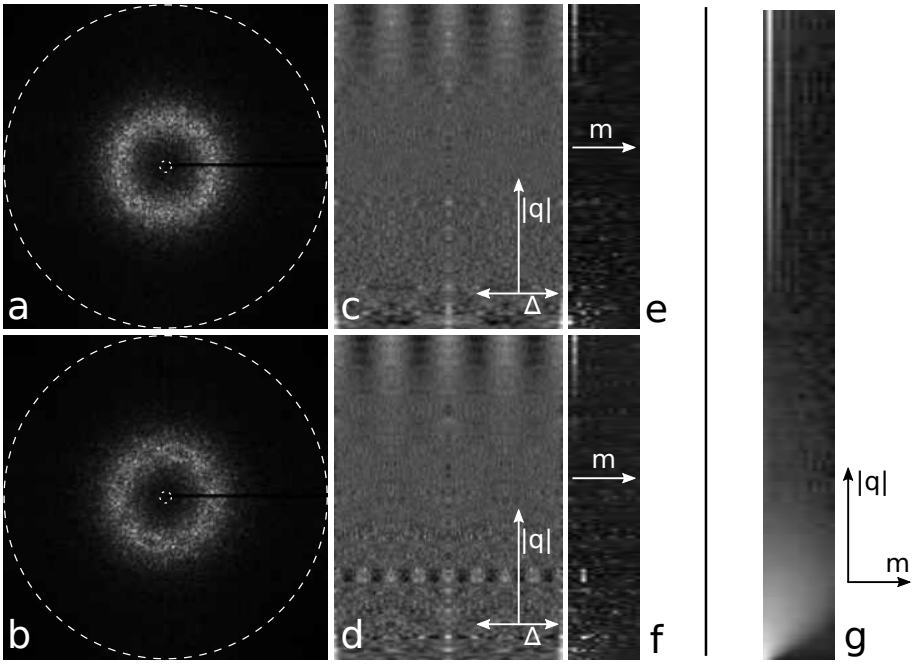

FIGURE 7.7.. Example angular correlation and cosine decomposition of two different speckle patterns. (a) and (b) show speckle patterns from domain configurations without and with intentional ordering, respectively; (c) and (d) their angular correlations; (e) and (f) the corresponding cosine decompositions of the correlations. (g) shows the average cosine decomposition (log scale) from many simulations. The range of cosine components m is the even numbers between two and thirty-two.

simulated correlations in comparison to the cosine decompositions of experimental data. For this reason, we replace the region of the autocorrelation and spatial-inversion peaks in the correlation with a cubic spline interpolation. Because all cosine orders are unity at the narrow autocorrelation and spatial inversion peaks, removing the peaks primarily corrects a DC offset in the cosine series. In Fig. 7.7.(e) and (f), we decompose the correlations at each $|\mathbf{q}|$ according to the usual cosine expansion given by

$$a_{|\mathbf{q}|,m} = \frac{1}{N} \sum_{\Delta=0}^{N} C(|\mathbf{q}|, \Delta) \cos(2\pi m \Delta / N) \qquad \text{(Equation 7.3.)}$$

where N is the number of pixels along the Δ coordinate of the correlation and the $1/N$ prefactor keeps $a_{|\mathbf{q}|,m}$ independent of N. We calculate the cosine series for the even symmetry orders between two and thirty-two; Friedel symmetry of the correlation function forbids odd orders. For speed, we calculate Equation 7.3. by selecting components of the Fourier transform.

At small $|\mathbf{q}|$, we see in both the correlations and their respective cosine series the tell-tale signs of small-size fluctuations at low $|\mathbf{q}|$. The small number of speckles being correlated near the lower bound of the correlation region, marked as a dashed annulus in Fig. 7.7.(a) and (b), leads to large oscillations in the values of the cosine coefficients. These oscillations rapidly damp as $|\mathbf{q}|$ increases and with it the number of speckles correlated. At large $|\mathbf{q}|$ near the edge of the array, a pronounced four-fold symmetry appears even in the disordered domain configuration. This unavoidable artifact results from the discrete lattice on which we conduct the domain simulation; features of approximately one pixel in size must naturally exhibit a four-fold symmetry. In Fig. 7.7.(f) we also see the intentional $m = 8$

symmetry near the center of the scattering ring. This symmetry dominates the spectrum of the correlation within the scattering ring.

In Fig. 7.7.(g) we show with log scaling the average cosine spectrum taken from decomposing several thousand independent speckle patterns generated through the same process as those shown in (a) and (b). In this plot, the small-size fluctuations as $|\mathbf{q}| \rightarrow 0$ become evident in the large residual signal which remains after the averaging of so many cosine series. As $|\mathbf{q}|$ increases, however, the average cosine component rapidly tends to zero. At very high $|\mathbf{q}|$ we again see the lattice artifact with a more complicated harmonic structure revealed by the averaging process.

In judging the likelihood of a candidate symmetry, we want to know its relationship to the $a_{|\mathbf{q}|,m}$ ensemble. Next, we consider how the variation of the various simulation parameters and consequent variation of speckle size and shape changes the distribution of cosine component values. In the following analysis, we examine only those components within approximately the central scattering ring, which for the optimized experimental parameters lies between the residual small-size signal at low $|\mathbf{q}|$ and the lattice artifact at high $|\mathbf{q}|$ shown in Fig. 7.7.(g). To plot their occurrence, we sort the component values sort into forty equally-spaced bins and normalize by dividing the total count in each bin by the total count of all bins. In the following Figures we plot the histograms on both linear and log scales to emphasize the behavior of the distribution at the peak and along the long tail.

7.4.2. Effect of Varying Pinhole Radius

First, we consider the effect of changing the size of the illumination function in Figure 7.8.. Here, we assume a perfectly circular pinhole in direct contact

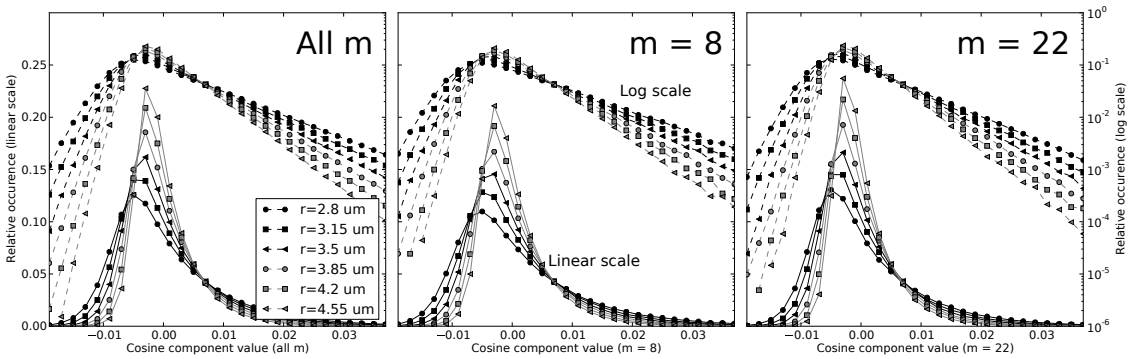

FIGURE 7.8.. Cosine component frequency vs pinhole radius. At left, the occurrence of all symmetry orders; at center and right, only the $m = 8$ and $m = 22$ symmetry orders, respectively.

with the sample ($z = 0$), in contrast to the usual scattering model. However, we retain a realistic coherence length of $4\mu m$. Variation of the size of the upstream pinhole exerts a powerful effect on the distribution of the cosine coefficients. Generally speaking, smaller apertures lead to a greater spread in coefficient values. This relationship holds whether examining the entire ensemble of coefficients in Fig. 7.8.(a), or the $m = 8$ or $m = 22$ components individually in Fig. 7.8.(b) and Fig. 7.8.(c). The cause of this broadening: a smaller illumination function illuminates fewer domains, which in turn leads to fewer and larger speckles. At any given $|\mathbf{q}|$, correlating a smaller number of speckles leads to greater fluctuation in the angular correlation and its cosine decomposition solely due to finite-size effects.

7.4.3. Effect of Varying Pinhole Distance

Next, we consider variation of the pinhole-sample separation distance z in Figure 7.9.. We vary this in 1mm steps between 2mm and the value found to produce the most realistic speckle for the scattering model, 7mm. The radius of the pinhole for these calculations was $4.2\mu m$ and the coherence length $4\mu m$. In comparison to the variation of the radius, variation of the separation distance

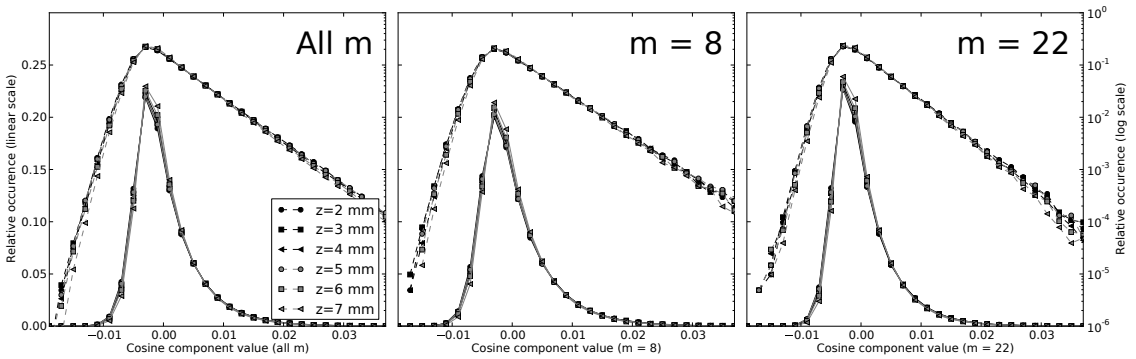

FIGURE 7.9.. Cosine component frequency vs pinhole-sample distance. At left, the occurrence of all symmetry orders; at center and right, only the $m = 8$ and $m = 22$ symmetry orders, respectively.

produces almost no discernible change in the coefficient distribution. The same explanation for the major changes in coefficient distribution under variation of the radius hold equally well for variation of the separation distance: forward propagation of the pinhole does not significantly change the size of the speckles, as the majority of the illumination function's power remains in the central spot which in this separation regime remains of approximately constant size. Instead, both the speckle morphology and the inversion symmetry of the pattern change, but this does not change the cosine decomposition of the angular correlation after removing the autocorrelation and spatial inversion peaks.

7.4.4. Effect of Varying Coherence Length

We vary the final parameters of the illumination, the coherence length, in Figure 7.10. to either side of its estimated value of $4\mu m$. While variation of the pinhole radius directly effects the size of the speckles, variations in the coherence length near the size of the pinhole radius primarily change the speckle contrast, as was seen in Fig. 7.5. when optimizing the illumination properties of the scattering model for maximum realism. Imagining a fully coherent speckle pattern and the

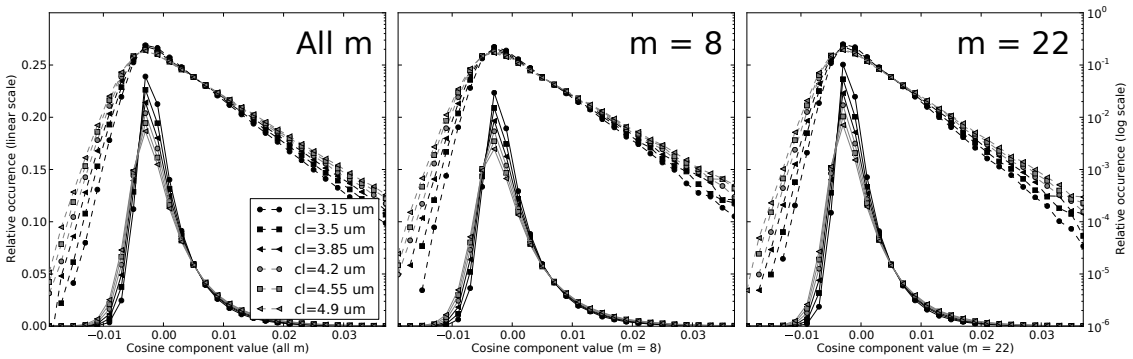

FIGURE 7.10.. Cosine component frequency vs degree of coherence as expressed through the coherence length. At left, the occurrence of all symmetry orders; at center and right, only the $m = 8$ and $m = 22$ symmetry orders, respectively.

incoherent goal profile used in the domain simulations, we would expect that a decrease in coherence leads to a tightening of the coefficient distributions as the reduced contrast gives the speckle pattern less freedom to fluctuate. Figure 7.10. confirms this effect, showing a broadening of the coefficient distribution as we increase the coherence length of the illumination. As under variation of the pinhole radius, this effect does not discriminate between symmetry orders, and may be observed as well in $m = 8$ (Fig. 7.10.(b)) as in $m = 22$ (Fig. 7.10.(c)).

7.4.5. Effect of Varying Blocker Size

Finally, we address the role of the beam block, whose wire casts a shadow onto the detector and places spurious zeros in the speckle pattern. In the scattering model, we model the wire of the blocker as a rectangle of zeros with a width of some number of pixels. In Figure 7.11., we observe only minor changes to the coefficient distribution for $m = 8$ and essentially no change in the $m = 22$ distribution, and even then only for unrealistically thick blockers (experimental blocker size is approximately 10 pixels). For this reason, we can safely neglect this aspect of the scattering model for any value within shouting distance of reality.

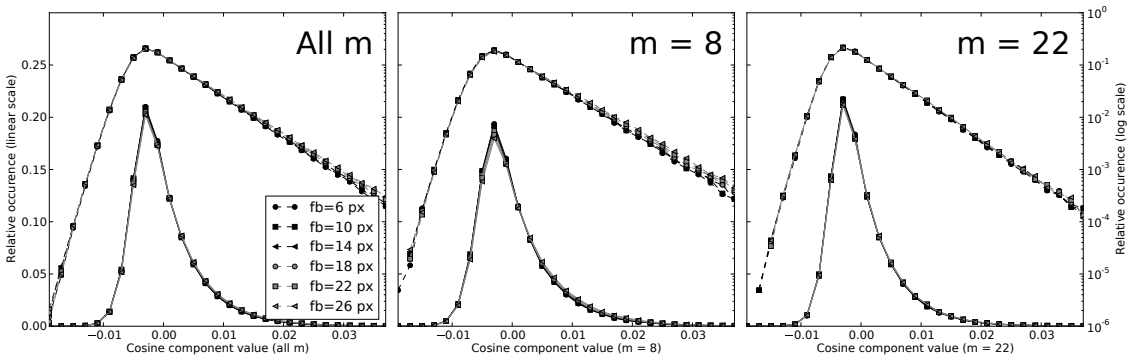

FIGURE 7.11.. Cosine component frequency vs size of beam block. At left, the occurrence of all symmetry orders; at center and right, only the $m = 8$ and $m = 22$ symmetry orders, respectively.

7.4.6. The Concentration Metric

In all parameter variations, the skew-symmetric distribution of the cosine coefficients appears highly similar, but we have failed to find a common analytic form which accurately describes the distribution to either side of the peak. However, as the linear behavior of the distribution on the log-scale plots demonstrate, a simple stretched exponential must describe the limiting form of the distribution at high coefficient value. Fitting the tail of the distribution in the case of the more sparse experimental data allows extrapolation of the distribution so that we can judge the relative occurrence of supposed rare components, such as experimental candidate, at a more reliable precision. Judgments based on the statistical basis provided by simulations of the $a_{|\mathbf{q}|,m}$ distributions require very close agreement of the pinhole radius and the coherence length between the experiment as performed and the scattering model used to generate the speckle patterns. As Fig. 7.5. shows, however, we cannot completely match the experimental speckle patterns with the current scattering model, and as Fig. 7.8. and Fig. 7.10. demonstrate, small variations in the scattering model may have serious effects

on evaluating the likelihood of rare candidates which fall far on the tail of the component value distribution. For this reason, we next examine a more robust metric which measures the degree to which the power of the cosine decomposition concentrates in a few components:

$$\mathscr{C}(|\mathbf{q}|) = \left(\sum_{m=0}^{M} a_{|\mathbf{q}|,m}^2\right) / \left(\sum_{m=0}^{M} a_{|\mathbf{q}|,m}\right)^2 \qquad \text{(Equation 7.4.)}$$

Equation 7.4., which evaluates to between $1/M$ and unity, achieves its maximum value when only one of the M components in the decomposition has a non-zero value, and its minimum value when all the components in the decomposition have the same value.

7.4.7. Invariance of Concentration to Illumination Parameters

We apply Equation 7.4. to the same spectra whose cosine components we plotted earlier to investigate the effect of the same parameter variations on this concentration metric, and show the results in Fig. 7.12.. In Fig. 7.12.(a), we show the distribution of concentration values under variation of the pinhole radius; in Fig. 7.12.(b) we vary the propagation distance z; in Fig. 7.12.(c) we vary the coherence length of the illumination; and in Fig. 7.12.(d) we vary the width of the blocker where it passes through the scattering ring. The values of the parameters other than that being varied remain unchanged from earlier. In contrast to the variability seen in the cosine component distribution under variation of the pinhole radius and the coherence length of the illumination, the concentration metric exhibits essentially no dispersion under variation of any of the scattering model parameters. As in the histograms of the cosine components, the limiting behavior

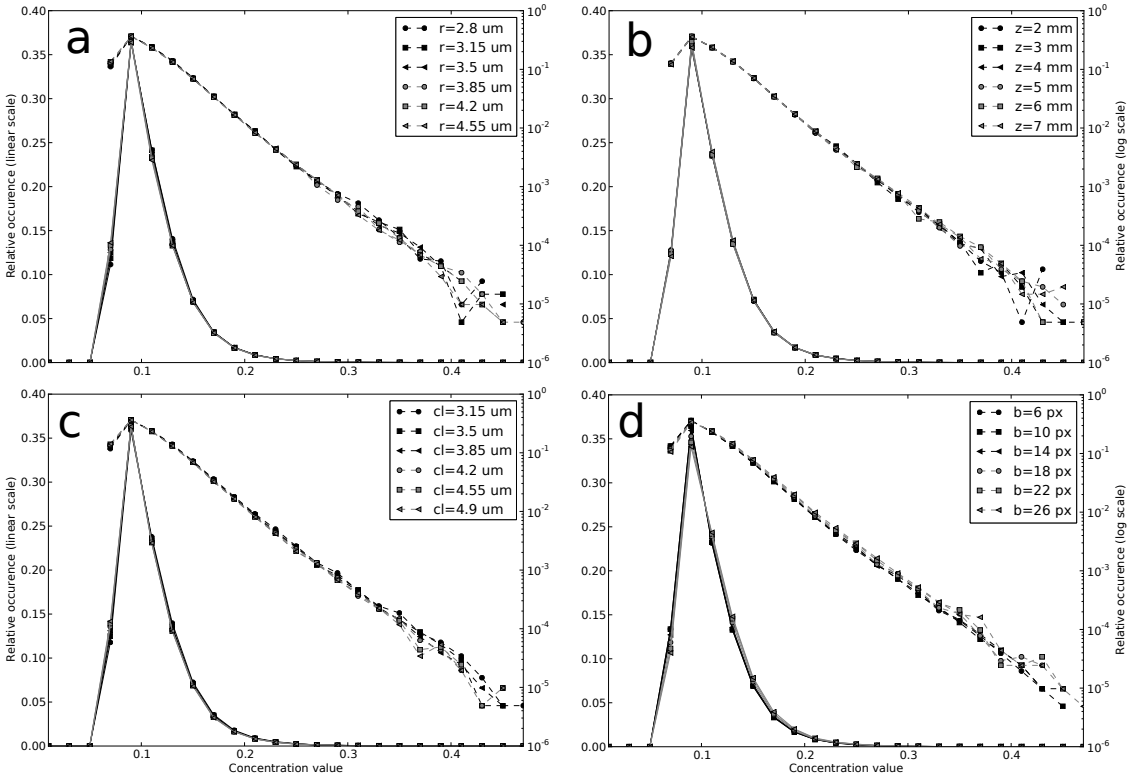

FIGURE 7.12.. Relative occurrence histograms for the concentration metric. Parameter varied: (a) pinhole radius; (b) pinhole distance; (c) coherence length; (d) blocker size.

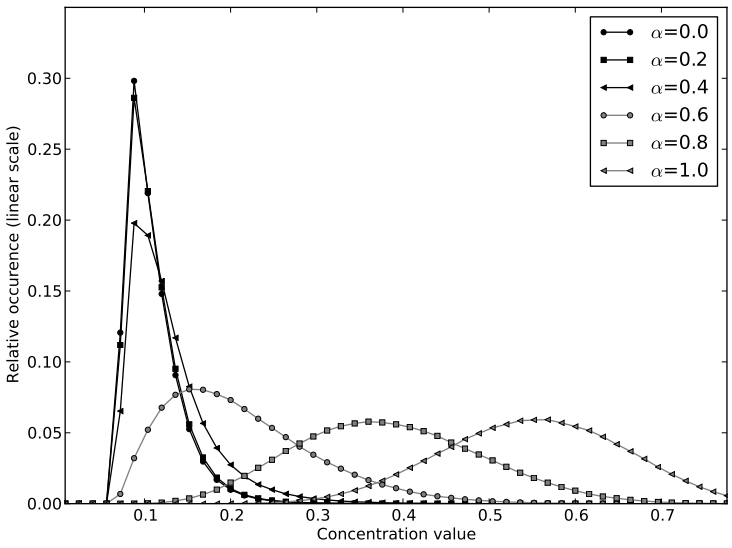

FIGURE 7.13.. Relative occurrence histograms for the concentration metric under variation of the ordering strength α.

of the distribution as the concentration value increases becomes a stretched exponential as seen by the linear behavior of the log-scaled series. At the extreme right-hand side of the log-scaled series we see some Poisson noise caused by the finite number of simulated speckle patterns.

From such distributions we may easily calculate the relative occurrence probability of a candidate at some $|\mathbf{q}|$ through the value of its concentration $\mathscr{C}(|\mathbf{q}|)$.

7.4.7.1. Effect of Varying Ordering Parameter

In Figure 7.13. we show the effect of varying the ordering parameter α, originally defined in Equation 6.18.. For extremely weak ordering ($\alpha = 0.2$), we notice essentially no variation in the concentration metric. At $\alpha = 0.4$, we begin to see a distinct rightward shift and broadening of the distribution, and at $\alpha = 0.6$ we would consider the modal value of the concentration rather unlikely in the isotropic

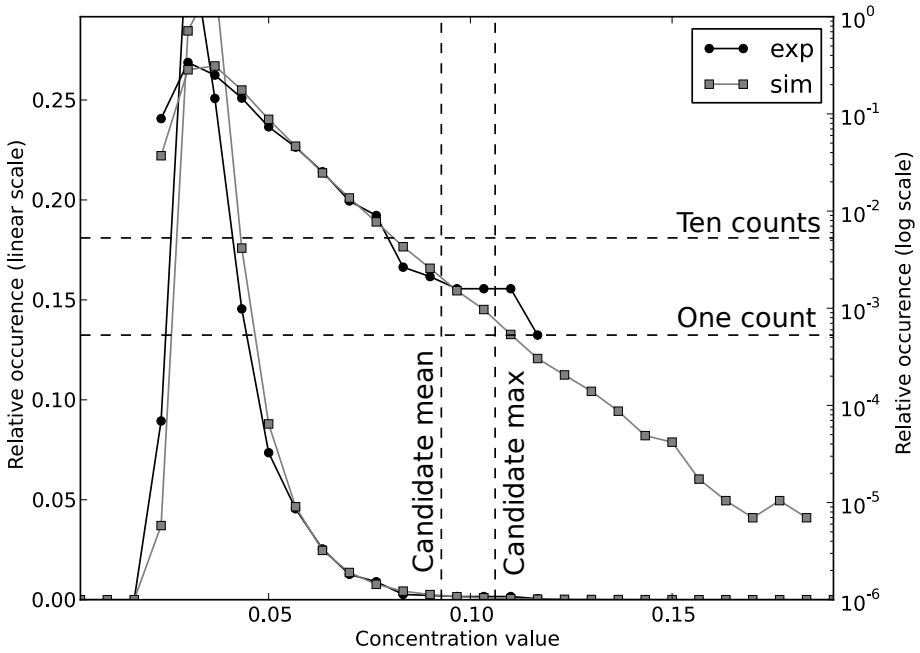

FIGURE 7.14.. Statistical evaluation of candidate symmetry. Simulated concentration data (grey) and experimental concentration data (black) taken from within the central scattering ring. Experimental data comes from the ensemble of speckle patterns collected contemporaneously with the candidate in Fig. 7.1..

$\alpha = 0$ case. Nevertheless, even using this designed metric, sensitivity to rotational symmetries seems rather low due to the natural fluctuation of speckle patterns.

7.4.8. Evaluation of Experimental Candidate

We now evaluate the experimental candidate in terms of the component concentration of Equation 7.4.. Contemporaneously with the speckle pattern presented as experimental candidate, we recorded twenty-six additional speckle patterns in an attempt to do a ptychographic image reconstruction of the domain pattern. This data set allows us to compare the distribution of experimental speckle concentrations to the simulated basis. We show a plot of the concentration from both the experimental and simulated speckle patterns in Figure 7.14.; we

plot only the concentration from the center portion of the ring, with $|\mathbf{q}|_{min} = 2.07 \times 10^{-2} nm^{-1}$ and $|\mathbf{q}|_{max} = 3.26 \times 10^{-2} nm^{-1}$.

The experimental and simulated concentrations match extremely well. In comparison to the data shown earlier, for the precise comparison with the experimental data we calculated the concentration after decomposing the speckle pattern into all even cosine orders between two and one-hundred eighty, the Nyquist limit. This lowers the concentration relative to that seen in Fig. 7.12. Both the simulated and experimental data peak at $\mathscr{C} \approx 0.03$ and undergo a stretched-exponential decline with increasing concentration. The misalignment of the experimental and simulated concentrations at large $\mathscr{C}$ finds an easier interpretation: Poisson noise. With only a few thousand pixels in the experimental dataset, extreme small-size fluctuations will afflict concentrations which the simulated basis places at an expected occurrence of one in one thousand or less. The two dashed vertical lines show the relative occurrence value on the log-scale we expect to see from a single pixel and from ten pixels in the experimental concentration data. Between these two lines, we treat the occurrence value as quite imprecise.

In evaluating the experimental candidate, we consider both the mean and maximum value within the $|\mathbf{q}|$ range of the candidate. We plot these values as the vertical lines in Fig. 7.14.. Neither measure of the concentration, mean or max, finds the candidate statistically remarkable. While both measures place the candidate among the most spectrally-concentrated pixels in the data, all ordered lists must have elements at the top and this merely confirms earlier suspicions based on visual judgment alone. Indeed, both measures evaluate the candidate symmetry at approximately the occurrence rate at which we expect to find a handful of pixels in a data set the size of that collected.

For several reasons, we therefore conclude that the preponderance of evidence supports the interpretation that the candidate symmetry shown in Fig. 7.1. does *not* reflect an ordering mechanism, but rather a "lucky" alignment of speckles expected within the statistics of the angular correlation. First, as shown above, the average concentration within the candidate symmetry certainly evaluates higher than the modal concentration value in either the simulated or experimental dataset, but not profoundly so. Second, the width of the candidate correlation closely matches the average size of a single speckle; the likelihood of a lucky speckle alignment drops considerably when speckles must align in $|\mathbf{q}|$ as well as Δ. Finally, the presence of symmetries in speckle patterns generated from pure random numbers, as in Fig. 7.2., highlights the ease with which we may by chance find deceptive angular symmetries; these noise-based symmetries also shown a width of approximately a single speckle.

7.5. Symmetry Microscope in Two Dimensions

By performing the same sort of analysis in as a function of position on the sample, we construct a sort of "symmetry microscope" specifically sensitive to otherwise hidden rotational ordering. We show the basic sequence of operations for such a microscope in the top half of Figure 7.15.. First, we collect a sequence of coherent speckle patterns by rastering the illumination across the sample in a position-resolved fashion. At each location, we collect a unique speckle pattern. We then perform the rotational autocorrelation of Equation 7.1., decompose the correlation into a cosine spectrum with Equation 7.3., and reduce the correlation along each resolvable $|\mathbf{q}|$ to the concentration given in Equation 7.4.. As Equation 7.4. reduces the spectrum along only the m axis, we require a further reduction

along the $|\mathbf{q}|$ axis to reduce the entire speckle pattern to a single number which describes the amount of rotational structure present in the speckle pattern. With this single metric in place, we plot its value vs the raster motor positions at which we took each speckle pattern. In this way, we plot the degree of rotational symmetry present across the sample. For a hypothetical sample in which the ordering signals such as that seen in Figure 7.1. indicate an ordering mechanism at work, the map of the reduced concentration vs the probe position allows us to find the ordered region.

In the bottom half of Figure 7.15. we show results from a large-scale two-dimensional simulation in which we embed two ordered regions inside an otherwise disordered sea of magnetic domains, then run the symmetry microscope as described above. The scattering lineshape from the disordered domains matches that seen in the experimental data, and the simulated illumination uses the optimal parameters found earlier. The thermometer-shaped ordered region in the lower left of the sample expresses symmetry $m = 8$, while the annular region in the upper right of the sample expresses $m = 4$; the ordering signal had center and width approximately that seen in the experimental candidate. We performed several instances of the domain generator to vary the order parameter α between zero and unity. The simulated domains are of size 2048×2048 pixels, and each simulated speckle pattern was calculated after displacing the illumination function by 16 pixels for a total of 16384 speckle patterns. After decomposing each speckle pattern, we calculated the concentration $\mathscr{C}(|\mathbf{q}|)$ within the main scattering ring, $|\mathbf{q}|_0 - w/2 < |\mathbf{q}| < |\mathbf{q}|_0 + w/2$.

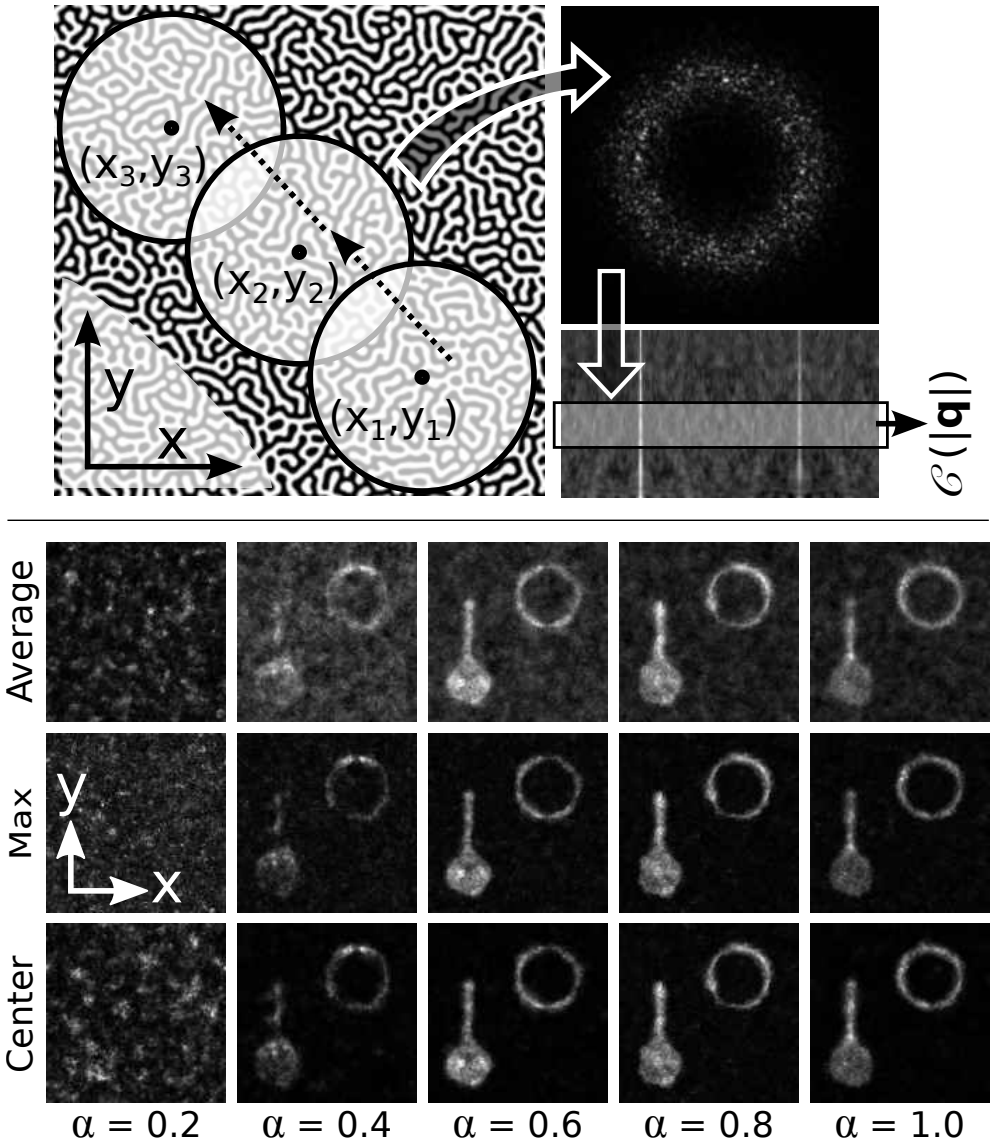

FIGURE 7.15.. Mode of operation for a hypothetical "symmetry microscope". By running the rotational analysis on a set of position-resolved scattering patterns, we build a symmetry microscope. Top: basic scan procedure collects, correlates, and decomposes at each scan location. Bottom: Position-resolved simulation of concentration using three different reductions of $\mathscr{C}(|\mathbf{q}|)$.

We tried three different ways of reducing $\mathscr{C}$ along the $|\mathbf{q}|$ axis to generate a single figure of merit $\overline{\mathscr{C}}$.

1. Arithmetic mean: $\overline{\mathscr{C}} = \frac{1}{N} \sum_{|\mathbf{q}|_{min}}^{|\mathbf{q}|_{max}} \mathscr{C}(|\mathbf{q}|)$
2. Maximum value: $\overline{\mathscr{C}} = \max \{\mathscr{C}(|\mathbf{q}|_{min}) : \mathscr{C}(|\mathbf{q}|_{max})\}$
3. Central value: $\overline{\mathscr{C}} = \mathscr{C}(|\mathbf{q}|_0)$

Of these three methods, the mean performs the worst at all values of α, as the size of the calculation region dominates that of the supplied symmetry and the arithmetic mean gets dragged down by low values of $\mathscr{C}$. However, in analyzing experimental data, we could not presuppose the location and width of the symmetry. Examining just the center concentration $\mathscr{C}(|\mathbf{q}|_0)$ and the maximum value $\max\{\mathscr{C}(|\mathbf{q}|_0 - w/2 < |\mathbf{q}| < |\mathbf{q}|_0 + w/2)\}$ within the calculation region shows no great deviation. The reason for this is straightforward: in the simulated sample, the value of the concentration at center will by design nearly match maximum value seen anywhere in the analysis. However, this represents a naïve idealization of possible experimental data. In reality, we would probably expect a sample with hidden rotational symmetry to exhibit some dispersion in the length-scale $|\mathbf{q}|$ of the ordering signature, and in this case plotting the concentration from a single presumed length scale would risk missing the signal. For these reasons plotting the maximum value within the calculation region seems the most robust reduction of $\mathscr{C}$ along $|\mathbf{q}|$. Additionally, the concentration metric makes no distinction between m, and so both the $m = 4$ and $m = 8$ regions show equally with no additional specification in the analysis.

In contrast to evaluating a single experimental candidate with respect to a statistical basis, a position-resolved measurement achieves a significant advantage in terms of interpretation: if a speckle pattern taken from an ordered region shows little ordering signal due to fluctuations, its neighbors will likely regress to the mean and keep the region visible. We can see this effect most strongly in comparing the $\alpha = 0.4$ images in Fig. 7.15. to the distribution of concentrations for $\alpha = 0.4$ in Fig. 7.13.. When evaluating a single image at this value of the order parameter, we must constantly remain aware that the distribution of concentrations remains similar to the isotropic case of $\alpha = 0$; in a position-resolved scan, however, we observe the ordered region quite distinctly due to the aggregating effect of neighboring sites.

Close examination of all three maps in the $\alpha = 0.2$ case also holds an important lesson. In plotting just $\mathscr{C}$ as a function of position, we create a blotchy image in which illusory islands of ordering may appear. Without the anchor of a statistical expectation for what an ordering signal may look like, the aggregated fluctuations of the disordered sample present a misleading signal analogous to that seen in the correlations of speckle patterns from random numbers in Fig. 7.2.. The same effect would appear if plotting only a single symmetry component. In this sense, we can strictly ascribe a designation of "more ordered" to portions of the domain pattern which generate the higher correlation concentration, but only in the same way that a fair coin may generate a string of several heads or tails in a row.

In any case, implementing a symmetry microscope on a real sample may be a daunting task. If implemented as a purely scattering experiment, the collection of thousands of speckle patterns with good counts and well-subtracted backgrounds would constitute an enormous undertaking. If implemented by in a manner

analogous to the simulation here, in which we transform sections of a high-fidelity real-space image into speckle patterns, such an analysis would require a real-space image with large field of view and high fidelity. However, most real-space imaging techniques, such as the MFM in Figure 6.1.(a), capable of resolving small features are poorly suited to the task of imaging a large area. It seems likely that the best hope for this sort of microscope is a restricted one-dimensional scan with fine steps in the illumination between collected speckle patterns, or to use ptychographic techniques to first image the domains with relatively sparse illumination, then do the fine analysis from the reconstructed image. For an example of ptychography applied to magnetic domains, see Tripathi [153].

CHAPTER VIII

SUMMARY AND OUTLOOK

In this dissertation, we have discussed three experiments dedicated to advancing coherent techniques both at present light sources as well as future high-brightness, high-coherence light sources. Each of the three experiments functions as a novel form of microscopy, exploiting the one-to-one correspondence between a scatterer of coherent illumination and the far-field intensity pattern to perform a type of lensless imaging or look for hidden symmetries revealed by the Fourier transform.

In Chapter IV, we designed, built and tested a novel lensless microscope specifically geared towards coherent imaging in reflection geometry. An effective coherent imaging technique suitable for reflection and Bragg geometry opens the door to applying three decades of development in iterative algorithms to the vast range of samples in condensed matter physics whose behavior is still poorly understood.

Additionally, our numerical modeling work in determining the resolvability of features in the final recovered image shows we fully understand the trade-offs involved in this imaging geometry. The rather unimpressive resolution demonstrated in the proof-of-principle experiment here can be primarily attributed to the limited coherence of the present light source and the desire to initially pursue an explicitly holographic imaging strategy. However, future developments promise great improvement in the resolution achievable in this geometry. First, the ever-improving coherence at present light sources due to accelerator upgrades and the promise of fully-coherent future light sources will allow much larger object

apertures to be used in the experiment; as our modeling demonstrates that the resolution increases linearly with the radius of the object aperture, we expect improved resolution from coherence considerations along. Second, the efficacy of the holographic aperture arrangement in conjunction with the iterative phasing algorithms shows the holographic separability condition to be unnecessary; future work may use a larger object aperture which violates holographic separability to achieve higher resolution. Third, in the time since our initial work on the experiment, we have dramatically improved our skills in positioning the apertures close to the surface of the sample, which also improves the resolution of the final image; it may also be possible in future work to engineer a special puck which allows the height of the sample to be precisely adjusted, allowing arbitrarily close alignment of the sample surface and apertures without tedious manual mounting and remounting of the sample.

One critical requirement in applying this imaging technique to more interesting physical samples is improving our understanding of the focusing metric during back propagation. For the test pattern, the acutance metric we used to determine when we had found the sample plane succeeded in large part due to the large amount of derivative content in the sample owing to its binary nature. Samples of real physical interest will certainly contain less derivative content and focusing will correspondingly be more difficult unless an alternative metric is developed.

In Chapter V, we demonstrated a novel use of holographic techniques to image the coherence factor of the synchrotron x-ray beam, adjusting the magnitude of the object-reference cross-correlations in order to recover the coherence factor embedded in the curvature of the autocorrelation intensity as

predicted by rigorous theories of partial coherence. In doing numerical modeling of the experiment prior to its physical realization, we did not understand the extent to which the direct beam would pass through even nearly a micron of gold and disrupt the measurement with spurious signal at the center of the diffraction pattern. To improve the measurement, we have shown additional extensive modeling of modified apertures which allow the spurious beam signal to be measured independently of the coherence signal. However, an honest evaluation of this technique shows that while it may be pedagogically interesting to use holographic ideas to encode the coherence factor into an autocorrelation pattern, coded aperture techniques are more efficient and better suited to performing the measurement quickly and with precision.

More intense future development of this technique may be warranted if the nanofabrication of efficient coded aperture designs proves too difficult, or if further development of analysis strategies shows it is possible to use this sort of holography mask to image a sample as in Chapter IV while simultaneously measuring the coherence of the illumination.

In Chapter VI and Chapter VII, we showed how the speckle pattern obtained by coherent scattering from a specific part of a sample could be analyzed for hidden rotational symmetries, and proposed coupling this measurement with position-resolution to form a symmetry microscope specifically sensitive to ordering invisible to other techniques. To perform the judgment, we modified the iterative phasing algorithms used to invert speckle patterns to instead accept as a Fourier constraint an incoherent scattering lineshape. This new algorithm allows the generation of a nearly unlimited number of different configurations which display the same scattering statistics. Using the statistical basis provided by a large number of

speckle patterns, we examined the statistics of the two-point angular correlation function introduced by Wochner. We then used those statistics to interpret an experimental speckle pattern taken from a magnetic thin film which displayed a potential "hidden" rotational symmetry. Based on several factors, including that statistical basis and highly similar candidate symmetries in speckle patterns generated from random numbers, we concluded that the experimental candidate reflected a rare but not statistically unexpected fluctuation in the speckle pattern. We concluded by showing that operating the measurement as a form of microscopy by evaluating speckle patterns in position-resolved fashion could more robustly identify regions of otherwise hidden rotational ordering in domain patterns.

The outlook for this technique depends on both technological as well as fundamental factors. Technologically, to build a true symmetry microscope we must be able to quickly image a large area of a sample in order to scan for regions with high hidden symmetry. The most promising technique for this capability is ptychography, which reconstructs an extended real-space image from speckle patterns with overlapping illuminations. Beamline 12.0.2 is ill-equipped to implement this technique due to low brightness and slow detector readout time; future beamlines and light sources will be much brighter, and much faster detectors are now available. Additionally, the choice of magnetic domains instead of the similar patterns in other systems makes recording speckle patterns very time-consuming due to the low efficiency of magnetic scattering even at resonance.

The most important factor for a symmetry microscope is the degree to which hypothetical ordering mechanisms in samples such as magnetic thin-films actually do create rotational symmetries only within narrow ranges of wavevectors. In cases where a rotational symmetry extends across all reciprocal space magnitudes, the

real-space image becomes identifiably ordered without resort to Fourier techniques, and in cases where the symmetry is localized, our simulations show the differences in the real-space image to be nearly invisible. For this reason, whether the signal this technique is designed to find actually exists or not is still an unanswered question. However, work published from our group did indicate a marked change in the angular correlation statistics in an exchange-biased magnetic thin-film when cooled below the blocking temperature.

APPENDIX

DERIVATION OF OPTICAL AND SYNCHROTRON FORMULAE

A.1. Derivation of the Kirchoff Diffraction Formula

From Maxwell's Equations it is a straightforward exercise to derive the scalar wave equation an optical disturbance $U(x, y, t)$ must obey:

$$\nabla^2 U - \frac{n^2}{c^2}\frac{\partial^2 U}{\partial t^2} = 0 \qquad \text{(Equation A.1.)}$$

If we limit the form of $U(x, y, t)$ to the monochromatic wave $U(x, y, t) = U(x, y)e^{i\omega t}$, then Equation A.1. assumes the familiar form of the Helmhotz equation:

$$\nabla^2 U - \frac{n^2\omega^2}{c^2}U = 0$$

$$\left(\nabla^2 + k^2\right) U = 0 \qquad \text{(Equation A.2.)}$$

Because we need to derive the relationship between the wavefield at an aperture and wavefield at some observation plane, the task at hand now becomes using the bare bones of the Helmholtz equation to describe the relationship of the wave at some point of observation P_0 to the value of the electric field over some arbitrary surface S enclosing volume V. The two quantities are illustrated in Figure A.1.(a). This derivation requires the additional mathematical tool of Green's theorem, which states that if $U(P)$ and $G(P)$ are two complex-valued functions of position and if $U(P)$, $G(P)$, and their first and second partial derivatives are all

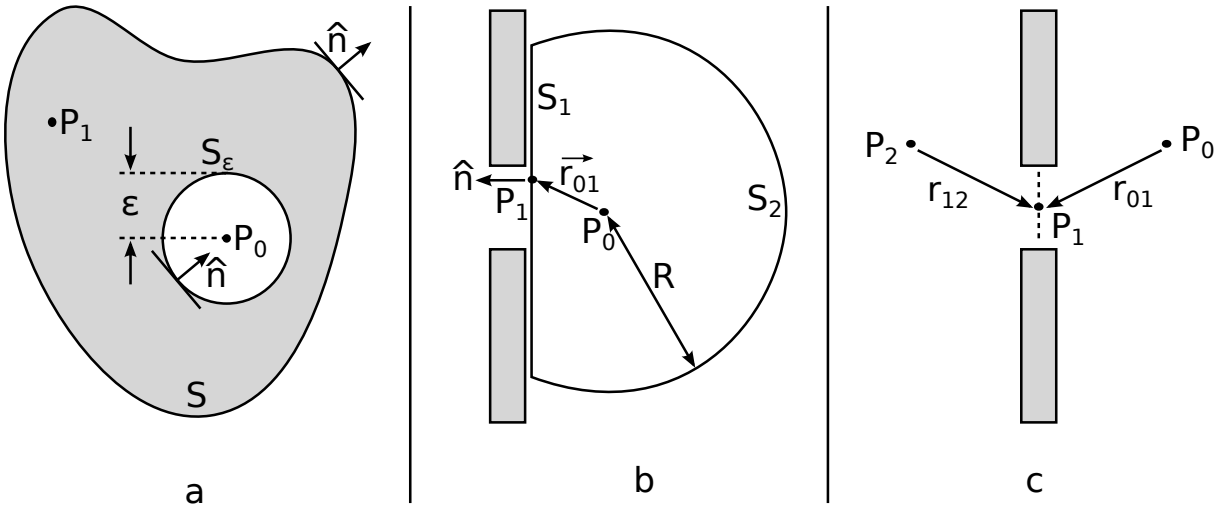

FIGURE A.1.. Geometries used in the derivation of the Kirchoff diffraction formula. (a) shows the surfaces and volume in Green's Theorem, (b) transmission through an opaque screen, and (c) the geometry of the alternative Green's functions Equation A.10. and Equation A.11..

continuous within and on S, then the following relationship holds:

$$\iiint_V (U\nabla^2 G - G\nabla^2 U)ds = \iint_S \left(U\frac{\partial G}{\partial n} - G\frac{\partial U}{\partial n}\right) ds \qquad \text{(Equation A.3.)}$$

Here, the variable of differentation n refers explicitly to the "outward" direction from the surface.

To apply Equation A.3. to the diffraction problem, we must ensure no discontinuity in U or whatever function we choose for G at P_0, and to this end we carve out a small bubble around P_0 of radius ϵ; we will later take the limit of $\epsilon \to 0$. This creates a second surface of integration S_ϵ. Following Kirchoff, we use as the initial function of G an expanding spherical wave centered about P_0:

$$G(P_1) = \exp(ikr_{01})/r_{01} \qquad \text{(Equation A.4.)}$$

Here, P_1 is some test point within V and r_{01} is the distance between P_0 and P_1. Equation A.4. also has the virtue of satisfying the Helmholtz equation and as U satisfies it by definition, Equation A.3. becomes

$$\iint_S \left(U\frac{\partial G}{\partial n} - G\frac{\partial U}{\partial n} \right) = -\iint_{S_\epsilon} \left(U\frac{\partial G}{\partial n} - G\frac{\partial U}{\partial n} \right) \qquad \text{(Equation A.5.)}$$

We now take the limit of $\epsilon \to 0$. In this limit, the conditions of validity for Equation A.3. require that $U \to U(P_0)$ and $\frac{\partial U}{\partial n} \to 0$. Additionally, we evaluate the partial derivative $\frac{\partial G}{\partial n}$ on the surface S_ϵ as

$$\left.\frac{\partial G(P_1)}{\partial n}\right|_{P_1 \in S_\epsilon} = \frac{\exp(ik\epsilon)}{\epsilon}\left(\frac{1}{\epsilon} - ik\right) \qquad \text{(Equation A.6.)}$$

Equation A.6. includes a hidden minus sign which must be included to account for the antiparallel nature of $\hat{n}$ and r_{01} at all points on S_ϵ. With these three limiting behaviors in hand, we calculate the limit of the integral:

$$\begin{aligned}
&\lim_{\epsilon\to 0} \iint_{S_\epsilon} \left(U\frac{\partial G}{\partial n} - G\frac{\partial U}{\partial n} \right) \\
&= \lim_{\epsilon\to 0} 4\pi\epsilon^2 \left[U(P_0)\frac{\exp(ik\epsilon)}{\epsilon}\left(\frac{1}{\epsilon} - ik\right)\right] \\
&= 4\pi U(P_0)
\end{aligned}$$

So the wave at P_0 is given by the boundary conditions on S:

$$U(P_0) = \frac{1}{4\pi}\iint_S \left(G\frac{\partial U}{\partial n} - U\frac{\partial G}{\partial n} \right) \qquad \text{(Equation A.7.)}$$

Now we consider the field propagating forward from some aperture in an opaque screen, which we illustrate in Figure A.1.(b). Here, we divide the

surface S into two sections S_1 and S_2; S_1 lies parallel to the screen, while S_2 becomes approximately hemispherical as R increases. On the surface S_2, $G(P_1) = \exp(ikR)/R$, and as R becomes very large, the normal derivative becomes $\partial G/\partial n = \left(ik - \frac{1}{R}\right) e^{ikR}/R \approx ikG$. Therefore, the integral over surface S_2 becomes:

$$\iint_{S_2} G\left(\frac{\partial U}{\partial n} - ikUG\right) ds = \iint_{S_2} G\left(\frac{\partial U}{\partial n} - ikU\right) R^2 \, d\Omega \qquad \text{(Equation A.8.)}$$

where Ω is the solid angle of subtended by S_2. Because the magnitude $|RG|$ is always unity, the integral above will tend towards zero under the condition that

$$\lim_{R\to\infty} R\left(\frac{\partial U}{\partial n} - ikU\right) \to 0 \qquad \text{(Equation A.9.)}$$

This is simply a fancy way of saying that U must vanish at least as fast as an expanding spherical wave, and therefore all waves in the problem are outgoing. Consequently, we must evaluate the integral only over S_1.

To derive the diffraction formula, Kirchoff assumed that both the function U and its derivative $\partial U/\partial n$ vanished at the opaque screen. However, this requires that the wave be zero *everywhere* behind the screen in contradiction of the physical reality of the optical disturbance we are describing. Sommerfeld removed this contradiction by choosing two alternative Green's functions G_- and G_+ which maintain Equation A.7.. In addition, either G or $\partial G/\partial n$ vanishes at S_1, freeing U from non-physicality.

$$G_-(P_1) = \frac{\exp(ikr_{01})}{r_{01}} - \frac{\exp(ikr_{12})}{r_{12}} \qquad \text{(Equation A.10.)}$$

$$G_+(P_1) = \frac{\exp(ikr_{01})}{r_{01}} + \frac{\exp(ikr_{12})}{r_{12}} \qquad \text{(Equation A.11.)}$$

We show quantities described by G_- and G_+ in Fig. A.1.(c). G_- describes two source points P_0 and P_2 for G, equidistant from P_1 on each side of the screen; the sources emit out of phase. G_+ has the same arrangement with the sources emitting in phase.

We only consider G_-. Clearly, at any P_1 along the aperture G_- vanishes, and therefore the diffraction integral Equation A.7. becomes

$$U_-(P_0) = \frac{-1}{4\pi} \iint_{aperture} U \frac{\partial G_-}{\partial n} ds \qquad \text{(Equation A.12.)}$$

The derivative $\partial G_-/\partial n$ evaluates similarly to that of Kirchoff's G. First, we note that on surface S_1 and for the propagation distances we are considering at x-ray wavelengths:

$$\begin{aligned} r_{01} &= r_{12} \\ \cos(\vec{n}, \vec{r_{01}}) &= -\cos(\vec{n}, \vec{r_{12}}) \\ r_{01} &\gg \lambda \end{aligned}$$

With these considerations stated, we calculate the derivative:

$$\begin{aligned} \frac{\partial G_-}{\partial n}(P_1) &= \cos(\vec{n}, \vec{r_{01}}) \left(ik - \frac{1}{r_{01}} \right) \frac{\exp(ikr_{01})}{r_{01}} - \cos(\vec{n}, \vec{r_{12}}) \left(ik - \frac{1}{r_{12}} \right) \frac{\exp(ikr_{12})}{r_{12}} \\ &= 2\cos(\vec{n}, \vec{r_{01}}) \left(ik - \frac{1}{r_{01}} \right) \frac{\exp(ikr_{01})}{r_{01}} \\ &\approx 2ik \cos(\vec{n}, \vec{r_{01}}) \frac{\exp(ikr_{01})}{r_{01}} \qquad \text{(Equation A.13.)} \end{aligned}$$

Substituting Equation A.13. into Equation A.12. generates the diffraction integral we expect from a qualitative understanding of wave phenomena:

$$U(P_0) = \frac{1}{i\lambda} \iint_{aperture} U(P_1) \frac{\exp(ikr_{01})}{r_{01}} \cos(\vec{n}, \vec{r_{01}})\, ds \qquad \text{(Equation A.14.)}$$

Equation A.14. expresses the Huygens-Fresnel principle by stating that the disturbance at point P_0 may be expressed by treating each point P_1 in the aperture as the source of an expanding spherical wave which then adds in superposition at P_0. In fact, up to the cosine term, we could write down Equation A.14. directly from the Huygens-Fresnel principle. That cosine term, which Goodman calls "a relatively simple mathematical construct that allows us to solve diffraction problems without paying attention to the physical details of exactly what is happening at the edge of the aperture," is sometimes referred to as the obliquity factor, and changes somewhat depending on the choice of G. Different choices of G and thereby different obliquity factors lead to nearly identical results in the far field but may show small differences very close to the aperture [13], ultimately due to differences in the treatment of the complicated fringing fields near the rim of the aperture.

A.2. Derivation of Schell's Theorem

In this section we fully present the derivation of Schell's Theorem, Equation 2.27.. In the far field, Equation 2.24. gives the mutual intensity between two points J_{12}, from which we may obtain the usual intensity by setting points one and two equal. Substituting two instances of Equation 2.2. into Equation 2.24. (one for each point in the source plane) gives a four-dimensional integral as each of the two

points in the time average has two coordinates:

$$I(x,y) = \left\langle \frac{1}{(\lambda z)^2} \iint\limits_{aperture} P(u_1,v_1)U(u_1,v_1)\exp(-ikr_1)\,du_1\,dv_1 \right.$$
$$\left. \iint\limits_{aperture} P^*(u_2,v_2)U^*(u_2,v_2)\exp(ikr_2)\,du_2\,dv_2 \right\rangle$$
$$= \frac{1}{(\lambda z)^2} \iiiint\limits_{aperture} P(u_1,v_1)P^*(u_2,v_2)J(u_1,v_1;u_2,v_2)$$
$$\exp\left(-ik(r_2-r_1)\right)\,du_1\,dv_1\,du_2\,dv_2 \qquad \text{(Equation A.15.)}$$

We now introduce the following change of variables:

$$\Delta u = u_2 - u_1, \quad \bar{u} = \frac{u_1+u_2}{2}$$
$$\Delta v = v_2 - v_1, \quad \bar{v} = \frac{v_1+v_2}{2}$$

which facilitates the simplifying assumption

$$J(u_1,v_1;u_2,v_2) = I_0\mu(\Delta u,\Delta v) \qquad \text{(Equation A.16.)}$$

By assuming that the degree of coherence depends only on the difference in position of the two points, we assert that the degree of coherence has the same statistical properties everywhere on the wavefront. For example, in a double pinhole experiment with totally uniform illumination, under this assumption any positioning of the pinhole pair would satisfy the uniform illumination requirement and the fringe visibility would be unaffected by pinhole position because only pinhole separation matters. In practice, intensity variations make this assumption difficult to test.

We simplify the exponential in Equation A.15. by making the same approximations as in deriving the Fraunhofer approximation from the Kirchoff integral, only with more variables:

$$\begin{aligned} r_i &= \sqrt{(u_i - x)^2 + (v_i - y)^2 + z^2} \\ &= z\sqrt{1 + \left((u_i - x)^2 + (v_i - y)^2\right)/z^2} \\ &\approx z\left[1 + (u_i^2 + v_i^2 + x^2 + y^2 - 2u_i x - 2v_i y)/2z\right] \\ r_2 - r_1 &\approx \left[(u_2^2 + v_2^2) - (u_1^2 + v_1^2) + 2x(u_1 - u_2) + 2y(v_1 - v_2)\right]/(2z) \\ &= \left[\bar{u}\Delta u + \bar{v}\Delta v - x\Delta u - y\Delta v\right]/z \end{aligned}$$

Putting these simplifications back into Equation A.15. gives:

$$\begin{aligned} I(x,y) = \frac{I_0}{(\lambda z)^2} \iiiint & P\left(\bar{u} - \frac{\Delta u}{2}, \bar{v} - \frac{\Delta v}{2}\right) P^*\left(\bar{u} + \frac{\Delta u}{2}, \bar{v} + \frac{\Delta v}{2}\right) \\ & \times \mu(\Delta u, \Delta v)\ \exp\left[\frac{-2\pi i}{\lambda z}(\bar{u}\Delta u + \bar{v}\Delta v)\right] \\ & \times \exp\left[\frac{2\pi i}{\lambda z}(x\Delta u + y\Delta v)\right]\, d\bar{u}\, d\bar{v}\, d\Delta u\, d\Delta v \end{aligned}$$

While still a four-dimensional mess, the exponentials begin to look familiar. We again drop first exponential factor as its argument tends toward zero:

$$\begin{aligned} I(x,y) = \frac{I_0}{(\lambda z)^2} \iiiint & P\left(\bar{u} - \frac{\Delta u}{2}, \bar{v} - \frac{\Delta v}{2}\right) P^*\left(\bar{u} + \frac{\Delta u}{2}, \bar{v} + \frac{\Delta v}{2}\right) \\ & \times \mu(\Delta u, \Delta v)\ \exp\left[\frac{2\pi i}{\lambda z}(x\Delta u + y\Delta v)\right]\, d\bar{u}\, d\bar{v}\, d\Delta u\, d\Delta v \end{aligned}$$

The final step of the derivation of the far field intensity given an aperture and a degree of coherence in the source plane is to recognize the integral over coordinates $\bar{u}$ and $\bar{v}$ as the autocorrelation of the field exiting the aperture, albeit in a slightly

non-standard form:

$$
\begin{aligned}
I(x,y) &= \frac{I_0}{(\lambda z)^2} \iint \left[\iint P\left(\bar{u} - \frac{\Delta u}{2}, \bar{v} - \frac{\Delta v}{2}\right) P^*\left(\bar{u} + \frac{\Delta u}{2}, \bar{v} + \frac{\Delta v}{2}\right) d\bar{u}\, d\bar{v} \right] \\
&\qquad \times \mu(\Delta u, \Delta v)\ \exp\left[\frac{2\pi i}{\lambda z}(x\Delta u + y\Delta v)\right] d\Delta u\, d\Delta v \\
&= \frac{I_0}{(\lambda z)^2} \iint \mathscr{P}(\Delta u, \Delta v)\mu(\Delta u, \Delta v)\ \exp\left[\frac{2\pi i}{\lambda z}(x\Delta u + y\Delta v)\right] d\Delta u\, d\Delta v \\
&\propto \mathscr{F}\left\{\mathscr{P}(\Delta u, \Delta v) \times \mu(\Delta u, \Delta v)\ \right\} \qquad \text{(Equation A.17.)}
\end{aligned}
$$

Equation A.17. for the intensity in the far field is just the Fourier transform of the product of the autocorrelation of the wavefront passing through the aperture and the complex coherence factor. In the limiting case of $\mu(\Delta u, \Delta v) = 1$ which describes full coherence, we recover the expected result that the fully coherent far field intensity pattern is the Fourier transform of the autocorrelation of the wavefield leaving the aperture. Rewriting Equation A.17. with the convolution theorem gives

$$
\begin{aligned}
I_{pc}(x,y) &= I_{fc}(x,y) * \mathscr{F}\{\mu(\Delta u, \Delta v)\} \\
&= \left|\mathscr{F}\{P(u,v)\}\right|^2 * \mathscr{F}\{\mu(\Delta u, \Delta v)\} \\
&= \mathscr{F}\left\{\mathscr{F}^{-1}\left\{\left|\mathscr{F}\{P(u,v)\}\right|^2\right\} \times \mu(\Delta u, \Delta v)\right\} \qquad \text{(Equation A.18.)}
\end{aligned}
$$

where $I_{pc}(x,y)$ is the partially coherent intensity, $I_{fc}(x,y)$ is the intensity pattern which would be formed under fully coherent illumination, and $*$ denotes convolution. Equation A.18., referred to as Schell's Theorem, provides a powerful approach to calculating partially coherent diffraction patterns, simplifying the full four dimensional integral in Equation A.15. into a set of three Fourier transforms, all calculable by FFT. A slight rearrangement of Equation A.18. solves for the

coherence factor:

$$\mu(\Delta u, \Delta v) = \frac{\mathscr{F}^{-1}\left\{I_{pc}(x,y)\right\}}{\mathscr{P}(\Delta u, \Delta v)} \qquad \text{(Equation A.19.)}$$

Equation A.19. shows that an experimental measurement of the partially coherent diffraction pattern can combine with sufficiently good *a priori* knowledge of the aperture to directly measure the coherence function.

A.3. Undulator Radiation

In this section we will discuss the generation of undulator radiation and the several of its properties most applicable to the coherent scattering experiments presented in this dissertation. The main source for this discussion is Attwood [12]; an advanced and generally incomprehensible discussion of synchrotron radiation more broadly can be found in Jackson [154].

A.3.1. Undulator Fundamental Frequency and Harmonics

At beamline 12.0.2, an undulator source produces the x-rays for the experiments. The undulator consists of a periodic series of permanent magnets through which deflect a relativistic beam of electrons. As the electrons traverse the undulator, the magnetic field causes them to undulate transverse to their direction of motion and emit radiation. In Figure A.2. we show a cartoon of a basic undulator design and the coordinate system used in the derivation of the undulator equation. We construct a simple model of the magnetic field inside the undulator as

$$B_y(z) = B_0 \cos\left(\frac{2\pi z}{\lambda_u}\right) \qquad \text{(Equation A.20.)}$$

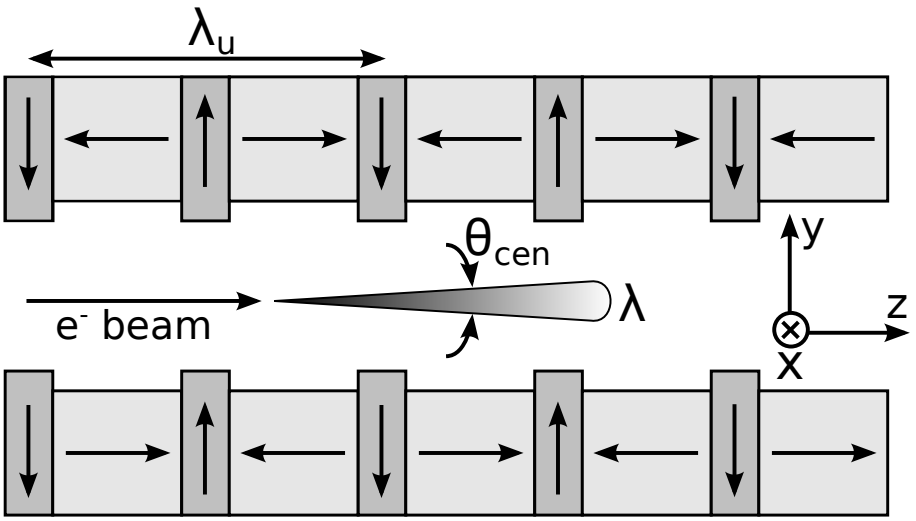

FIGURE A.2.. A basic schematic of undulator design. Incoming relativistic electrons undulate due to the force exerted by a periodic magnetic structure, and radiate in return. Relativistic effects compress the radiation into x-ray wavelengths.

where λ_u is the wavelength of the undulator.

The Lorentz force equation gives the usual expression for the force on the electrons:

$$\frac{dp}{dt} = q\left(\mathbf{E} + \mathbf{v} \times \mathbf{B}\right) \qquad \text{(Equation A.21.)}$$

Due to relatively short length of the undulator device, we may ignore the effect of the electric field; for longer undulator devices, retention of the electric field leads to the free-electron laser [155, 156]. Additionally, if we assume to first order that the only component of the velocity is v_z, then the only term of the cross product is the x component $-v_z B_y$. Equation A.21. then becomes:

$$\begin{aligned} m\gamma\frac{dv_x}{dt} &= ev_z B_y \\ \frac{dv_x}{dt} &= \frac{e}{m\gamma}\frac{dz}{dt}B_0 \cos\left(\frac{2\pi z}{\lambda_u}\right) \\ v_x &= \frac{Kc}{\gamma}\sin\left(\frac{2\pi z}{\lambda_u}\right) \end{aligned} \qquad \text{(Equation A.22.)}$$

In Equation A.22. we have collected various constants into the so-called deflection parameter K, which represents the strength of the magnetic field in the undulator. We use the usual definition of γ to transform Equation A.22. into an expression for v_z:

$$\begin{aligned}
\gamma &= 1/\sqrt{1-(v_x^2+v_z^2)/c^2} \\
\frac{v_z^2}{c^2} &= 1-\frac{1}{\gamma^2}-\frac{v_x^2}{c^2} \\
&= 1-\frac{1}{\gamma^2}-\frac{K^2}{\gamma^2}\sin^2\left(\frac{2\pi z}{\lambda_u}\right) \\
\frac{v_z}{c} &= \sqrt{1-\frac{1}{\gamma^2}-\frac{K^2}{\gamma^2}\sin^2\left(\frac{2\pi z}{\lambda_u}\right)} \\
&\approx 1-\frac{1}{2\gamma^2}-\frac{K^2}{4\gamma^2}\left[1-\cos\left(\frac{2\pi z}{\lambda_u}\right)\right] \qquad \text{(Equation A.23.)}
\end{aligned}$$

In the last step, we have assumed that K/γ is small enough for the binomial expansion of the square root to first order, and we have used a trigonometric identity for $\sin^2$.

So v_z is a function of z as the magnetic field shifts momentum between v_x and v_z but conserves energy. The relation between v_z and z through the cosine necessarily results in a series of harmonics for the emitted radiation, which is beyond the scope of this treatment. Instead, we focus on the fundamental by dropping the cos term, which is equivalent to the earlier assumption that $v_x \approx 0$

or the assumption that the average axial velocity $\langle v_z \rangle$ suffices to first-order:

$$\begin{aligned} \frac{\langle v_z \rangle}{c} &\approx 1 - \frac{2 + K^2}{4\gamma^2} \\ &= 1 - \frac{1}{2\gamma_K^2} \\ \gamma_K &= \gamma / \sqrt{1 + K^2/2} \end{aligned}$$

So when we consider the average axial velocity rather than the instantaneous velocity we must modulate γ by a factor which describes how much velocity is actually dispersed into the transverse component of the motion.

We now consider the wavelength of light emitted by the undulating charges. By the usual contraction factor, the periodicity of the undulator according to the electrons is $\lambda_e = \lambda_u / \gamma_K$, where we are using the γ_K defined immediately above, and the frequency is $f_e = c\gamma_K / \lambda_u$. According to the relativistic Doppler effect, the frequency f_e emitted by electrons within the moving frame of reference is observed in the laboratory frame of reference as

$$f = \frac{f_e}{\gamma_K (1 - \beta \cos\theta)} \qquad \text{(Equation A.24.)}$$

where θ is the angle between the direction of travel and the observer. In considering undulator radiation, we assume the angle θ to be small, and approximate $\cos\theta \approx 1 - \theta^2/2$. Consequently, the observed fundamental wavelength $\lambda_0 = c/f$ is given by

$$\lambda_0 = \lambda_u \left(1 - \beta + \beta\theta^2/2\right) \qquad \text{(Equation A.25.)}$$

As $\beta \to 1$, we approximate $1 - \beta \approx 1/2\gamma_K^2$, and the observed emitted wavelength is

$$\begin{aligned}\lambda_0 &= \frac{\lambda_u}{2\gamma_K^2}\left(1 + \gamma_K^2\theta^2\right) \\ &= \frac{\lambda_u}{2\gamma^2}\left(1 + \frac{K^2}{2} + \gamma^2\theta^2\right)\end{aligned} \qquad \text{(Equation A.26.)}$$

Therefore, we see that an undulator may be constructed to generate x-ray wavelengths even with a period of several centimeters due to the relativistic contraction of the period by a factor γ^2, which is set by the energy of the storage ring. However, as the observation angle increases, so does the fundamental wavelength; for this reason, we use only the on-axis radiation.

In treatments of undulator radiation which do not neglect the cosine term in Equation A.23., the resulting solution to the differential equation requires harmonics of the form

$$\lambda_n = \frac{\lambda_0}{n} \qquad \text{(Equation A.27.)}$$

Only odd harmonics ($n = 1, 3, 5...$) appear in the forward direction. The direction of emission of even harmonics is not parallel to the propagation axis of the electron beam.

A.3.2. Spatial Distribution of Undulator Radiation

Within the electron beam's frame of reference, the transverse motion caused by motion within the periodic magnetic field appears as standard dipole radiation, whose radiated power P per unit solid angle Ω is given by the well-known formula [154]:

$$\frac{dP}{d\Omega} = \frac{e^2 a^2 \sin^2\Theta}{16\pi^2\epsilon_0 c^3} \qquad \text{(Equation A.28.)}$$

where a is the acceleration (here along the laboratory x direction) and Θ is the angle between a and the direction of radiation propagation.

The relativistic transformation between an angle θ in the laboratory frame and θ' in the moving frame of the electrons is given by

$$\tan\theta = \frac{sin\theta'}{\gamma\left(\beta + \cos\theta'\right)} \qquad \text{(Equation A.29.)}$$

In the limit of large θ', for highly relativistic electrons with $\beta \approx 1$, $\theta \rightarrow 1/2\gamma$. This indicates that the radiated power of the undulator compresses to a narrow "searchlight" cone of small divergence, important for increasing brilliance and coherence. A more careful calculation predicts that for an undulator with N periods, this radiation cone is found within approximately a half-angle of

$$\theta_{cen} \approx \frac{1}{\gamma_K\sqrt{N}} \qquad \text{(Equation A.30.)}$$

A.3.3. Spectral Distribution of Undulator Radiation

Because beamline 12.0.2 performs many experiments at energies corresponding to electronic resonances, we now consider the approximate spectral width of the undulator radiation predicated by Equation A.26.. Directly on axis with $\theta = 0$, we find the wavelength λ. Somewhat off axis, with $\theta \neq 0$, we find a slighter different wavelength $\lambda + \Delta\lambda$:

$$\lambda = \frac{\lambda_u}{2\gamma^2}\left(1 + \frac{K^2}{2}\right) \qquad \text{(Equation A.31.)}$$

$$\lambda + \Delta\lambda = \frac{\lambda_u}{2\gamma^2}\left(1 + \frac{K^2}{2} + \gamma^2\theta^2\right) \qquad \text{(Equation A.32.)}$$

Solving this pair of equations for the dispersion $\Delta\lambda/\lambda$ gives

$$\frac{\Delta\lambda}{\lambda} = \gamma^2\theta^2\left(1 + \frac{K^2}{2}\right) \qquad \text{(Equation A.33.)}$$

For an undulator with N periods, in the central radiation cone θ_{cen} this becomes

$$\frac{\Delta\lambda}{\lambda} = \frac{1}{N}\left(1 + \frac{K^2}{2}\right)^2 \qquad \text{(Equation A.34.)}$$

The undulator radiation has a fairly narrow spectrum due to the large number of periods. The bandwidth may be further reduced by operating at a higher harmonic n, as $\lambda_n = \lambda_0/n$. In this case, the bandwidth is:

$$\frac{\Delta\lambda}{\lambda} = \frac{1}{nN}\left(1 + \frac{K^2}{2}\right)^2 \qquad \text{(Equation A.35.)}$$

In general, for resonant scattering we require still more energy resolution, so we use a grating monochromator to select just a portion of the incoming wavelengths.

REFERENCES CITED

[1] T. Young, *A course of lectures on natural philosophy and the mechanical arts.* London: Johnson, 1807.

[2] A. J. Fresnel, H. H. de Senarmont, E. Verdet, and L. F. Fresnel, *Oeuvres completes d'Augustin Fresnel.* Paris: Imprimerie imperiale, 1866.

[3] T. H. Maiman, "Stimulated optical radiation in ruby," *Nature*, vol. 187, pp. 493–494, 08 1960.

[4] A. Javan, E. A. Ballik, and W. L. Bond, "Frequency characteristics of a continuous-wave he-ne optical maser," *J. Opt. Soc. Am.*, vol. 52, pp. 96–98, Jan 1962.

[5] R. N. Hall, G. E. Fenner, J. D. Kingsley, T. J. Soltys, and R. O. Carlson, "Coherent light emission from gaas junctions," *Phys. Rev. Lett.*, vol. 9, pp. 366–368, Nov 1962.

[6] J. C. Dainty, *Laser speckle and related phenomena.* Berlin; New York: Springer-Verlag, 1975.

[7] J. W. Goodman, *Statistical optics.* New York: Wiley, 1985.

[8] J. W. Goodman, *Introduction to Fourier optics.* Englewood, Colo.: Roberts & Co., 3rd ed., 2005.

[9] M. Born and E. Wolf, *Principles of optics.* Oxford u.a.: Pergamon Pr., 1999.

[10] E. Hecht, *Optics.* Reading, Mass.: Addison-Wesley, 2002.

[11] E. G. Steward, *Fourier optics : an introduction (second edition).* Mineola, N.Y.: Dover Publications, 2004.

[12] D. T. Attwood, *Soft x-rays and extreme ultraviolet radiation : principles and applications.* Cambridge; New York: Cambridge University Press, 2000.

[13] E. Wolf and W. Marchand, "Comparison of the kirchhoff and the rayleigh-sommerfeld theories of diffraction at an aperture," *J. Opt. Soc. Am.*, vol. 54, pp. 587–594, May 1964.

[14] M. Frigo and S. G. Johnson, "The design and implementation of FFTW3," *Proceedings of the IEEE*, vol. 93, no. 2, pp. 216–231, 2005. Special issue on "Program Generation, Optimization, and Platform Adaptation".

[15] J. W. Cooley and J. W. Tukey, "An algorithm for the machine calculation of complex fourier series," *Math. Comp*, vol. 19, pp. 297–301, 1965.

[16] L. I. Bluestein, "A linear filtering approach to the computation of the discrete fourier transform," *Northeast Electronics Research and Engineering Meeting Record*, vol. 10, pp. 218–219, 1968.

[17] N. K. Govindaraju, B. Lloyd, Y. Dotsenko, B. Smith, and J. Manferdelli, "High performance discrete fourier transforms on graphics processors," in *Proceedings of the 2008 ACM/IEEE conference on Supercomputing*, SC '08, (Piscataway, NJ, USA), pp. 2:1–2:12, IEEE Press, 2008.

[18] D. Mas, J. Garcia, C. Ferreira, L. M. Bernardo, and F. Marinho, "Fast algorithms for free-space diffraction patterns calculation," *Opt. Commun.*, vol. 164, no. 4â"6, pp. 233 – 245, 1999.

[19] J. W. Cooley, P. Lewis, and P. Welch, "The finite fourier transform," *IEEE Trans. Audio Electroacoustics*, vol. 17, no. 2, pp. 77–85, 1969.

[20] E. Wolf, "A macroscopic theory of interference and diffraction of light from finite sources. i. fields with a narrow spectral range," *Proc. R. Soc. London, Ser. A*, vol. 225, no. 1160, pp. 96–111, 1954.

[21] L. Mandel and E. Wolf, "Coherence properties of optical fields," *Rev. Mod. Phys.*, vol. 37, pp. 231–287, Apr 1965.

[22] C. Chang, P. Naulleau, E. H. Anderson, and D. T. Attwood, "Spatial coherence characterization of undulator radiation," *Opt. Commun.*, vol. 182, pp. 25–34, 2000.

[23] A. Singer, I. A. Vartanyants, M. Kuhlmann, S. Duesterer, R. Treusch, and J. Feldhaus, "Transverse coherence properties of the free-electron-laster flash at desy," *Phys. Rev. Lett.*, vol. 101, no. 25, p. 254801, 2008.

[24] J. P. Hannon, G. T. Trammell, M. Blume, and D. Gibbs, "X-ray resonance exchange scattering," *Phys. Rev. Lett.*, vol. 61, pp. 1245–1248, Sep 1988.

[25] S. W. Lovesey and S. P. Collins, *X-ray scattering and absorption by magnetic materials*. Oxford; New York: Clarendon Press ; Oxford University Press, 1996.

[26] K. M. Chesnel, J. J. Turner, M. Pfiefer, and S. D. Kevan, "Probing complex materials with coherent soft x-rays," *Appl. Phys. A*, vol. 92, no. 431, 2008.

[27] K. M. Rosfjord, Y. Liu, and D. T. Attwood, "Tunable coherent soft x-rays," *IEEE J. Quantum Electron.*, vol. 10, no. 6, 2004.

[28] H. Daido, "Review of soft x-ray laser researches and developments," *Rep. Progress. Phys.*, vol. 65, no. 10, pp. 1513–1576, 2002.

[29] B. L. Henke, E. M. Gullikson, and J. C. Davis, "X-ray interactions: photoabsorption, scattering, transmission, and reflection at E=50-30000eV, Z=1-92," *Atomic Data and Nuclear Data Tables*, vol. 52, no. 2, pp. 181–342, 1993.

[30] P. Kirkpatrick and A. V. Baez, "Formation of optical images by x-rays," *J. Opt. Soc. Am.*, vol. 38, pp. 766–773, Sep 1948.

[31] D. T. Attwood, "Class notes, "synchrotron radiation for materials science applications"," 2007.

[32] J. J. Turner, *Probing dynamics of complex ordered phases in colossal magnetoresistive transition-metal oxides using coherent resonant soft x-ray scattering*. PhD thesis, University of Oregon, 2008.

[33] E. Arenholz and S. O. Prestemon, "Design and performance of an eight-pole resistive magnet for soft x-ray magnetic dichroism measurements," *Rev. Sci. Instrum.*, vol. 76, no. 8, p. 083908, 2005.

[34] J. R. Janesick, *Scientific charge-coupled devices*. Bellingham, Wash.: SPIE Press, 2001.

[35] J. Miao, P. Charalambous, J. Kirz, and D. Sayre, "Extending the methodology of x-ray crystallography to allow imaging of micrometre-sized non-crystalline specimens," *Nature*, vol. 400, pp. 342–344, 07 1999.

[36] G. J. Williams, H. M. Quiney, B. B. Dhal, C. Q. Tran, K. A. Nugent, A. G. Peele, D. Paterson, and M. D. de Jonge, "Fresnel coherent diffractive imaging," *Phys. Rev. Lett.*, vol. 97, p. 025506, Jul 2006.

[37] J. Miao, T. Ishikawa, B. Johnson, E. H. Anderson, B. Lai, and K. O. Hodgson, "High resolution 3d x-ray diffraction microscopy," *Phys. Rev. Lett.*, vol. 89, p. 088303, Aug 2002.

[38] D. Shapiro, P. Thibault, T. Beetz, V. Elser, M. Howells, C. Jacobsen, J. Kirz, E. Lima, H. Miao, A. M. Neiman, and D. Sayre, "Biological imaging by soft x-ray diffraction microscopy," *Proc. Natl. Acad. Sci.*, vol. 102, no. 43, pp. 15343–15346, 2005.

[39] J. Nelson, X. Huang, J. Steinbrener, D. Shapiro, J. Kirz, S. Marchesini, A. M. Neiman, J. J. Turner, and C. Jacobsen, "High-resolution x-ray diffraction microscopy of specifically labeled yeast cells," *Proc. Natl. Acad. Sci.*, vol. 107, no. 16, pp. 7235–7239, 2010.

[40] X. Huang, J. Nelson, J. Kirz, E. Lima, S. Marchesini, H. Miao, A. M. Neiman, D. Shapiro, J. Steinbrener, A. Stewart, J. J. Turner, and C. Jacobsen, "Soft x-ray diffraction microscopy of a frozen hydrated yeast cell," *Phys. Rev. Lett.*, vol. 103, p. 198101, Nov 2009.

[41] E. Lima, L. Wiegart, P. Pernot, M. Howells, J. Timmins, F. Zontone, and A. Madsen, "Cryogenic x-ray diffraction microscopy for biological samples," *Phys. Rev. Lett.*, vol. 103, p. 198102, Nov 2009.

[42] C. Song, H. Jiang, A. Mancuso, B. Amirbekian, L. Peng, R. Sun, S. S. Shah, Z. H. Zhou, T. Ishikawa, and J. Miao, "Quantitative imaging of single, unstained viruses with coherent x rays," *Phys. Rev. Lett.*, vol. 101, p. 158101, Oct 2008.

[43] M. M. Seibert, T. Ekeberg, F. R. N. C. Maia, M. Svenda, J. Andreasson, O. Jonsson, D. Odic, B. Iwan, A. Rocker, D. Westphal, M. Hantke, D. P. DePonte, A. Barty, J. Schulz, L. Gumprecht, N. Coppola, A. Aquila, M. Liang, T. A. White, A. Martin, C. Caleman, S. Stern, C. Abergel, V. Seltzer, J.-M. Claverie, C. Bostedt, J. D. Bozek, S. Boutet, A. A. Miahnahri, M. Messerschmidt, J. Krzywinski, G. Williams, K. O. Hodgson, M. J. Bogan, C. Y. Hampton, R. G. Sierra, D. Starodub, I. Andersson, S. Bajt, M. Barthelmess, J. C. H. Spence, P. Fromme, U. Weierstall, R. Kirian, M. Hunter, R. B. Doak, S. Marchesini, S. P. Hau-Riege, M. Frank, R. L. Shoeman, L. Lomb, S. W. Epp, R. Hartmann, D. Rolles, A. Rudenko, C. Schmidt, L. Foucar, N. Kimmel, P. Holl, B. Rudek, B. Erk, A. Homke, C. Reich, D. Pietschner, G. Weidenspointner, L. Struder, G. Hauser, H. Gorke, J. Ullrich, I. Schlichting, S. Herrmann, G. Schaller, F. Schopper, H. Soltau, K.-U. Kuhnel, R. Andritschke, C.-D. Schroter, F. Krasniqi, M. Bott, S. Schorb, D. Rupp, M. Adolph, T. Gorkhover, H. Hirsemann, G. Potdevin, H. Graafsma, B. Nilsson, H. N. Chapman, and J. Hajdu, "Single mimivirus particles intercepted and imaged with an x-ray laser," *Nature*, vol. 470, pp. 78–81, 02 2011.

[44] A. Scherz, W. F. Schlotter, K. Chen, R. Rick, J. Stöhr, J. Lüning, I. McNulty, C. Günther, F. Radu, W. Eberhardt, O. Hellwig, and S. Eisebitt, "Phase imaging of magnetic nanostructures using resonant soft x-ray holography," *Phys. Rev. B*, vol. 76, p. 214410, Dec 2007.

[45] J. J. Turner, X. Huang, O. Krupin, K. A. Seu, D. Parks, S. Kevan, E. Lima, K. Kisslinger, I. McNulty, R. Gambino, S. Mangin, S. Roy, and P. Fischer, "X-ray diffraction microscopy of magnetic structures," *Phys. Rev. Lett.*, vol. 107, p. 033904, Jul 2011.

[46] D. Stickler, R. Fromter, H. Stillrich, C. Menk, C. Tieg, S. Streit-Nierobisch, M. Sprung, C. Gutt, L.-M. Stadler, O. Leupold, G. Grubel, and H. P. Oepen, "Soft x-ray holographic microscopy," *Appl. Phys. Lett.*, vol. 96, no. 4, p. 042501, 2010.

[47] T. A. Duckworth, F. Ogrin, S. S. Dhesi, S. Langridge, A. Whiteside, T. Moore, G. Beutier, and G. van der Laan, "Magnetic imaging by x-ray holography using extended references," *Opt. Express*, vol. 19, pp. 16223–16228, Aug 2011.

[48] M. Sacchi, H. Popescu, N. Jaouen, M. Tortarolo, F. Fortuna, R. Delaunay, and C. Spezzani, "Magnetic imaging by fourier transform holography using linearly polarized x-rays," *Opt. Express*, vol. 20, pp. 9769–9776, Apr 2012.

[49] S. Flewett, S. Schaffert, J. Mohanty, E. Guehrs, J. Geilhufe, C. M. Günther, B. Pfau, and S. Eisebitt, "Method for single-shot coherent diffractive imaging of magnetic domains," *Phys. Rev. Lett.*, vol. 108, p. 223902, May 2012.

[50] I. A. Vartanyants, I. K. Robinson, J. D. Onken, M. A. Pfeifer, G. J. Williams, F. Pfeiffer, H. Metzger, Z. Zhong, and G. Bauer, "Coherent x-ray diffraction from quantum dots," *Phys. Rev. B*, vol. 71, p. 245302, Jun 2005.

[51] J. Miao, Y. Nishino, Y. Kohmura, B. Johnson, C. Song, S. H. Risbud, and T. Ishikawa, "Quantitative image reconstruction of gan quantum dots from oversampled diffraction intensities alone," *Phys. Rev. Lett.*, vol. 95, p. 085503, Aug 2005.

[52] H. N. Chapman, A. Barty, S. Marchesini, A. Noy, S. P. Hau-Riege, C. Cui, M. R. Howells, R. Rosen, H. He, J. C. H. Spence, U. Weierstall, T. Beetz, C. Jacobsen, and D. Shapiro, "High-resolution ab initio three-dimensional x-ray diffraction microscopy," *J. Opt. Soc. Am. A*, vol. 23, pp. 1179–1200, May 2006.

[53] A. Barty, S. Marchesini, H. N. Chapman, C. Cui, M. R. Howells, D. A. Shapiro, A. M. Minor, J. C. H. Spence, U. Weierstall, J. Ilavsky, A. Noy, S. P. Hau-Riege, A. B. Artyukhin, T. Baumann, T. Willey, J. Stolken, T. van Buuren, and J. H. Kinney, "Three-dimensional coherent x-ray diffraction imaging of a ceramic nanofoam: Determination of structural deformation mechanisms," *Phys. Rev. Lett.*, vol. 101, p. 055501, Jul 2008.

[54] X. Shi, G. Xiong, X. Huang, R. Harder, and I. Robinson, "Radiation-induced bending of silicon-on-insulator nanowires probed by coherent x-ray diffractive imaging," *New Journal of Physics*, vol. 14, no. 6, p. 063029, 2012.

[55] M. A. Pfeifer, G. J. Williams, I. A. Vartanyants, R. Harder, and I. K. Robinson, "Three-dimensional mapping of a deformation field inside a nanocrystal," *Nature*, vol. 442, pp. 63–66, 07 2006.

[56] K. A. Nugent, "Coherent methods in the x-ray sciences," *Adv. Phys.*, vol. 59, no. 1, pp. 1–99, 2010.

[57] H. Quiney, "Coherent diffractive imaging using short wavelength light sources," *J. Mod. Opt.*, vol. 57, no. 13, pp. 1109–1149, 2010.

[58] D. Sayre, "Some implications of a theorem due to Shannon," *Acta Cryst.*, vol. 5, p. 843, Nov 1952.

[59] S. Marchesini, H. He, H. N. Chapman, S. P. Hau-Riege, A. Noy, M. R. Howells, U. Weierstall, and J. C. H. Spence, "X-ray image reconstruction from a diffraction pattern alone," *Phys. Rev. B*, vol. 68, p. 140101, Oct 2003.

[60] R. W. Gerchberg and W. O. Saxton, "A practical algorithm for the determination of phase from image and diffraction plane pictures," *Optik*, vol. 35, no. 2, pp. 237–246, 1978.

[61] A. Levi and H. Stark, "Image restoration by the method of generalized projections with application to restoration from magnitude," *J. Opt. Soc. Am. A*, vol. 1, pp. 932–943, Sep 1984.

[62] L. M. Bregman, "The method of successive projection for finding a common point of convex sets," *Sov. Math. Dok.*, vol. 6, pp. 688–692, 1965.

[63] J. R. Fienup, "Phase retrieval algorithms: a comparison," *Appl. Opt.*, vol. 21, pp. 2758–2769, Aug 1982.

[64] J. P. Abrahams and A. G. W. Leslie, "Methods used in the structure determination of bovine mitochondrial F1ATPase," *Acta Cryst.*, vol. D52, pp. 30–42, Jan 1996.

[65] H. H. Bauschke, P. L. Combettes, and D. R. Luke, "Phase retrieval, error reduction algorithm, and fienup variants: a view from convex optimization," *J. Opt. Soc. Am. A*, vol. 19, pp. 1334–1345, Jul 2002.

[66] J. R. Fienup, "Reconstruction of an object from the modulus of its fourier transform," *Opt. Lett.*, vol. 3, pp. 27–29, Jul 1978.

[67] R. Luke, "Relaxed averaged alternating reflections for diffraction imaging," *Inverse Problems*, vol. 21, pp. 37–50, 2005.

[68] V. Elser, "Phase retrieval by iterated projections," *J. Opt. Soc. Am. A*, vol. 20, pp. 40–55, Jan 2003.

[69] S. Marchesini, "Phase retrieval and saddle-point optimization," *J. Opt. Soc. Am. A*, vol. 24, pp. 3289–3296, Oct 2007.

[70] S. Marchesini, "A unified evaluation of iterative projection algorithms for phase retrieval," *Rev. Sci. Instrum.*, vol. 78, no. 1, p. 011301, 2007.

[71] R. Bates *et al.*, "Fourier phase problems are uniquely solvable in more than one dimension. i: Underlying theory," *Optik*, vol. 61, no. 3, pp. 247–262, 1982.

[72] K. Garden and R. Bates, "Fourier phase problems are uniquely solvable in more than one dimension. ii: One-dimensional considerations," *Optik*, vol. 62, pp. 131–142, 1982.

[73] W. Fright and R. Bates, "Fourier phase problems are uniquely solvable in more than one dimension. iii: Computational examples for two dimensions," *Optik*, vol. 62, pp. 219–230, 1982.

[74] R. Barakat and G. Newsam, "Necessary conditions for a unique solution to two-dimensional phase recovery," *J. Math. Phys*, vol. 25, no. 11, pp. 3190–3193, 1984.

[75] G. J. Williams, H. M. Quiney, A. G. Peele, and K. A. Nugent, "Coherent diffractive imaging and partial coherence," *Phys. Rev. B*, vol. 75, p. 104102, Mar 2007.

[76] L. W. Whitehead, G. J. Williams, H. M. Quiney, D. J. Vine, R. A. Dilanian, S. Flewett, K. A. Nugent, A. G. Peele, E. Balaur, and I. McNulty, "Diffractive imaging using partially coherent x rays," *Phys. Rev. Lett.*, vol. 103, p. 243902, Dec 2009.

[77] J. N. Clark and A. G. Peele, "Simultaneous sample and spatial coherence characterisation using diffractive imaging," *Appl. Phys. Lett.*, vol. 99, no. 15, p. 154103, 2011.

[78] G. Williams, M. Pfeifer, I. Vartanyants, and I. Robinson, "Effectiveness of iterative algorithms in recovering phase in the presence of noise," *Acta Cryst.*, vol. A63, pp. 36–42, Jan 2007.

[79] R. A. Dilanian, G. J. Williams, L. W. Whitehead, D. J. Vine, A. G. Peele, E. Balaur, I. McNulty, H. M. Quiney, and K. A. Nugent, "Coherent diffractive imaging: a new statistically regularized amplitude constraint," *New J. Phys.*, vol. 12, no. 9, p. 093042, 2010.

[80] S. Marchesini, H. N. Chapman, A. Barty, C. Cui, M. R. Howells, J. H. Spence, U. Weierstall, and A. M. Minor, "Phase aberrations in diffraction microscopy," in *IPAP Conference Series 7*, 2006.

[81] C. Giacovazzo, *Fundamentals of crystallography*. Oxford: Oxford University Press, 2002.

[82] J. R. Fienup, "Reconstruction of a complex-valued object from the modulus of its fourier transform using a support constraint," *J. Opt. Soc. Am. A*, vol. 4, pp. 118–123, Jan 1987.

[83] X. Huang, J. Nelson, J. Steinbrener, J. Kirz, J. J. Turner, and C. Jacobsen, "Incorrect support and missing center tolerances of phasing algorithms," *Opt. Express*, vol. 18, no. 25, p. 26441, 2010.

[84] M. Guizer-Sicairos and J. R. Fienup, "Understanding the twin-image problem in phase retrieval," *J. Opt. Soc. Am. A*, vol. 29, no. 11, 2012.

[85] J. R. Fienup and C. C. Wackerman, "Phase-retrieval stagnation problems and solutions," *J. Opt. Soc. Am. A*, vol. 3, pp. 1897–1907, Nov 1986.

[86] G. W. Stroke, "Lensless fourier-transform method for optical holography," *Appl. Phys. Lett.*, vol. 6, no. 10, pp. 201–203, 1965.

[87] J. E. Trebes, S. B. Brown, E. M. Campbell, D. L. Matthews, D. G. Nilson, G. F. Stone, and D. A. Whelan, "Demonstration of x-ray holography with an x-ray laser," *Science*, vol. 238, no. 4826, pp. 517–519, 1987.

[88] I. McNulty, J. Kirz, C. Jacobsen, E. H. Anderson, M. R. Howells, and D. P. Kern, "High-resolution imaging by fourier transform x-ray holography," *Science*, vol. 256, no. 5059, pp. 1009–1012, 1992.

[89] S. Eisebitt, J. Luning, W. F. Schlotter, M. Lorgen, O. Hellwig, W. Eberhardt, and J. Stohr, "Lensless imaging of magnetic nanostructures by x-ray spectro-holography," *Nature*, vol. 432, pp. 885–888, 12 2004.

[90] W. F. Schlotter, J. Lüning, R. Rick, K. Chen, A. Scherz, S. Eisebitt, C. M. Günther, W. Eberhardt, O. Hellwig, and J. Stöhr, "Extended field of view soft x-ray fourier transform holography: toward imaging ultrafast evolution in a single shot," *Opt. Lett.*, vol. 32, pp. 3110–3112, Nov 2007.

[91] W. Schlotter, *Lensless Fourier Transform Holography with Soft X-rays*. PhD thesis, Stanford University, 2007.

[92] D. Gabor, "A new microscopic principle," *Nature*, vol. 161, pp. 777–778, 1948.

[93] D. Gabor, "Microscopy by reconstructed wave-fronts," *Proc. R. Soc. London, Ser. A*, vol. 197, no. 1051, pp. 454–487, 1949.

[94] S. Marchesini, S. Boutet, A. E. Sakdinawat, M. J. Bogan, S. Bajt, A. Barty, H. N. Chapman, M. Frank, S. P. Hau-Riege, A. Szoke, C. Cui, D. A. Shapiro, M. R. Howells, J. C. H. Spence, J. W. Shaevitz, J. Y. Lee, J. Hajdu, and M. M. Seibert, "Massively parallel x-ray holography," *Nat. Phot.*, vol. 2, pp. 560–563, 09 2008.

[95] M. Guizar-Sicairos and J. R. Fienup, "Holography with extended reference by autocorrelation linear differentialoperation," *Opt. Express*, vol. 15, pp. 17592–17612, Dec 2007.

[96] V. Chamard, J. Stangl, G. Carbone, A. Diaz, G. Chen, C. Alfonso, C. Mocuta, and T. H. Metzger, "Three-dimensional x-ray fourier transform holography: The bragg case," *Phys. Rev. Lett.*, vol. 104, p. 165501, Apr 2010.

[97] S. Marathe, S. S. Kim, S. N. Kim, C. Kim, H. C. Kang, P. V. Nickles, and D. Y. Noh, "Coherent diffraction surface imaging in reflection geometry," *Opt. Express*, vol. 18, pp. 7253–7262, Mar 2010.

[98] Y. Tokura, "Critical features of colossal magnetoresistive manganites," *Rep. Progress. Phys.*, vol. 69, no. 3, p. 797, 2006.

[99] F. Walz, "The verwey transition - a topical review," *J. Phys. Condens. Matter*, vol. 14, no. 12, p. R285, 2002.

[100] V. J. Emery, S. A. Kivelson, and J. M. Tranquada, "Stripe phases in high-temperature superconductors," *Proc. Natl. Acad. Sci.*, vol. 96, no. 16, pp. 8814–8817, 1999.

[101] E. Dagotto, "Complexity in strongly correlated electronic systems," *Science*, vol. 309, pp. 257–262, JUL 8 2005.

[102] S. Roy, D. Parks, K. A. Seu, R. Su, J. J. Turner, W. Chao, E. H. Anderson, S. Cabrini, and S. D. Kevan, "Lensless x-ray imaging in reflection geometry," *Nat. Phot.*, vol. 5, pp. 243–245, 04 2011.

[103] R. H. Barker, *Group synchronizing of binary digital systems*. Butterworth, 1953.

[104] J. Lindner, "Binary sequences up to length 40 with best possible autocorrelation function," *Electron. Lett.*, vol. 11, p. 507, 16 1975.

[105] H. F. Talbot, "Facts relating to optical science," *Philos. Mag.*, vol. 9, no. 4, 1836.

[106] L. Rayleigh, "On copying diffraction gratings and on some phenomenon connected therewith," *Philos. Mag.*, vol. 11, 1881.

[107] K. Matsushima, H. Schimmel, and F. Wyrowski, "Fast calculation method for optical diffraction on tilted planes by use of the angular spectrum of plane waves," *J. Opt. Soc. Am. A*, vol. 20, pp. 1755–1762, Sep 2003.

[108] G. B. Esmer and L. Onural, "Computation of holographic patterns between tilted planes," in *Holography 2005: International Conference on Holography, Optical Recording, and Processing of Information*, pp. 62521K–62521K–6, 2006.

[109] E. E. Fenimore, "Coded aperture imaging: predicted performance of uniformly redundant arrays," *Appl. Opt.*, vol. 17, pp. 3562–3570, Nov 1978.

[110] E. E. Fenimore and T. M. Cannon, "Coded aperture imaging with uniformly redundant arrays," *Appl. Opt.*, vol. 17, pp. 337–347, Feb 1978.

[111] K. A. Nugent, "Coded aperture imaging: a fourier space analysis," *Appl. Opt.*, vol. 26, pp. 563–569, Feb 1987.

[112] J. E. Trebes, K. A. Nugent, S. Mrowka, R. A. London, T. W. Barbee, M. R. Carter, J. A. Koch, B. J. MacGowan, D. L. Matthews, L. B. Da Silva, G. F. Stone, and M. D. Feit, "Measurement of the spatial coherence of a soft-x-ray laser," *Phys. Rev. Lett.*, vol. 68, pp. 588–591, Feb 1992.

[113] K. A. Nugent and J. E. Trebes, "Coherence measurement technique for short-wavelength light sources," *Rev. Sci. Instrum.*, vol. 63, no. 4, pp. 2146–2151, 1992.

[114] N. A. Moldovan, D. Paterson, R. Divan, D. C. Mancini, J. Lin, K. A. Nugent, and I. McNulty, "Fabrication of uniformly redundant arrays and young's slits for coherence measurements in x-rays," in *Proc. SPIE 4783 Design and Microfabrication of Novel X-Ray Optics, 165*, pp. 165–175, 2002.

[115] J. J. A. Lin, D. Paterson, A. G. Peele, P. J. McMahon, C. T. Chantler, K. A. Nugent, B. Lai, N. Moldovan, Z. Cai, D. C. Mancini, and I. McNulty, "Measurement of the spatial coherence function of undulator radiation using a phase mask," *Phys. Rev. Lett.*, vol. 90, p. 074801, Feb 2003.

[116] A. S. Ostrovsky, G. Martínez-Niconoff, P. Martínez-Vara, and M. A. Olvera-Santamaría, "The van cittert-zernike theorem for electromagnetic fields," *Opt. Express*, vol. 17, pp. 1746–1752, Feb 2009.

[117] P. H. Van Cittert, "Die wahrscheinliche schwingungsverteilung in einer von einer lichtquelledirekt oder mittels einer linse beleuchteten ebene," *Physica*, vol. 1, p. 201, 1934.

[118] P. H. Van Cittert, "Kohaerenz-probleme," *Physica*, vol. 6, p. 1129, 1939.

[119] F. Zernike, "The concept of degree of coherence and its application to optical problems," *Physica*, vol. 5, p. 785, 1938.

[120] F. Zernike, "Diffraction and optical image formation," *Proc. Phys. Soc. London*, vol. 61, p. 158, 1948.

[121] P. Alfeld, "A trivariate clough-tocher scheme for tetrahedral data," *Comput. Aided Geom. Des.*, vol. 1, p. 169, 1984.

[122] G. Farin, "Triangular bernstein-bezier patches," *Comput. Aided Geom. Des.*, vol. 3, p. 83, 1986.

[123] G. Nielson, "A method for interpolating scattered data based upon a minimum norm network," *Math. Comp*, vol. 40, no. 253, 1983.

[124] E. A. Jagla, "Numerical simulations of two-dimensional magnetic domain patterns," *Phys. Rev. E*, vol. 70, p. 046204, 2004.

[125] M. S. Pierce, C. R. Buechler, L. B. Sorensen, S. D. Kevan, E. A. Jagla, J. M. Deutsch, T. Mai, O. Narayan, J. E. Davies, K. Liu, G. T. Zimanyi, H. G. Katzgraber, O. Hellwig, E. E. Fullerton, P. Fischer, and J. B. Kortright, "Disorder-induced magnetic memory: Experiments and theories," *Phys. Rev. B*, vol. 75, p. 144406, 2007.

[126] J. M. Deutsch and T. Mai, "Mechanism for nonequilibrium symmetry breaking and pattern formation in magnetic films," *Phys. Rev. E*, vol. 72, p. 016115, 2005.

[127] M. S. Pierce, C. R. Buechler, L. B. Sorensen, J. J. Turner, S. D. Kevan, E. A. Jagla, J. M. Deutsch, T. Mai, O. Narayan, J. E. Davies, K. Liu, J. H. Dunn, K. M. Chesnel, J. B. Kortright, O. Hellwig, and E. E. Fullerton., "Disorder-induced microscopic magnetic memory," *Phys. Rev. Lett.*, vol. 94, p. 017202, 2005.

[128] A. Benassi and S. Zapperi, "Barkhausen instabilities from labyrinthine magnetic domains," *Phys. Rev. B*, vol. 84, p. 214441, 2011.

[129] K. Kudo, "Effects of an oscillating field on magnetic domain patterns: Emergence of concentric-ring patterns surrounding a strong defect," *Phys. Rev. E*, vol. 80, p. 016209, 2009.

[130] K. Kudo, M. Mino, and K. Nakamura, "Magnetic domain patterns depending on the sweeping rate of magnetic fields," *J. Phys. Soc. Jpn.*, vol. 76, no. 1, p. 013002, 2007.

[131] M. T. Johnson, P. J. H. Bloemen, F. J. A. den Broeder, and J. J. de Vries, "Magnetic anisotropy in metallic multilayers," *Rep. Progress. Phys.*, vol. 59, no. 11, p. 1409, 1996.

[132] U. Hartmann, "Magnetic force microscopy," *Annu. Rev. Mater. Sci.*, vol. 29, pp. 53–87, 1999.

[133] W. Meyer-Ilse, H. Medecki, L. Jochum, E. Anderson, D. Attwood, C. Magowan, R. Balhorn, M. Moronne, D. Rudolph, and G. Schmahl, "New high-resolution zone-plate microscope at beamline 6.1 of the als," *Synchrotron Radiation News*, vol. 8, no. 3, pp. 29–33, 1995.

[134] W. Meyer-Ilse, H. Medecki, C. Magowan, R. Balhorn, M. Moronne, and D. Attwood, "Advanced microscopy: The new high resolution zone-plate microscope at the advanced light source in berkeley," in *JMSA Proceedings Microscopy and Microanalysis 1995*, 1995.

[135] M. Seul and D. Andelman, "Domain shapes and patterns: The phenomenology of modulated phases," *Science*, vol. 267, no. 5197, pp. 476–483, 1995.

[136] R. Su, K. A. Seu, D. Parks, J. J. Kan, E. E. Fullerton, S. Roy, and S. D. Kevan, "Emergent rotational symmetries in disordered magnetic domain patterns," *Phys. Rev. Lett.*, vol. 107, p. 257204, 2011.

[137] M. Vershinin, S. Misra, S. Ono, Y. Abe, Y. Ando, and A. Yazdani, "Local ordering in the pseudogap state of the high-tc superconductor bi2sr2cacu2o8," *Science*, vol. 303, no. 5666, pp. 1995–1998, 2004.

[138] M. Izquierdo, S. Megtert, J. P. Albouy, J. Avila, M. A. Valbuena, G. Gu, J. S. Abell, G. Yang, M. C. Asensio, and R. Comes, "X-ray diffuse scattering experiments from bismuth-based high-T-c superconductors," *Phys. Rev. B*, vol. 74, no. 5, 2006.

[139] C. Harrison, D. H. Adamson, Z. Cheng, J. M. Sebastian, S. Sethuraman, D. A. Huse, R. A. Register, and P. M. Chaikin, "Mechanisms of ordering in striped patterns," *Science*, vol. 290, no. 5496, pp. 1558–1560, 2000.

[140] A. Knoll, A. Horvat, K. S. Lyakhova, G. Krausch, G. J. A. Sevink, A. V. Zvelindovsky, and R. Magerle, "Phase behavior in thin films of cylinder-forming block copolymers," *Phys. Rev. Lett.*, vol. 89, p. 035501, 2002.

[141] A. Yochelis, A. Hagberg, E. Meron, A. Lin, and H. Swinney, "Development of standing-wave labyrinthine patterns," *SIAM J. Appl. Dyn. Syst.*, vol. 1, no. 2, pp. 236–247, 2002.

[142] C. Muratov and V. Osipov, "Scenarios of domain pattern formation in a reaction-diffusion system," *Phys. Rev. E*, vol. 54, no. 5, pp. 4860–4879, 1996.

[143] Q. Ouyang and H. L. Swinney, "Transition from a uniform state to hexagonal and striped turing patterns," *Nature*, vol. 352, no. 6336, pp. 610–612, 1991.

[144] E. Bodenschatz, J. R. de Bruyn, G. Ahlers, and D. S. Cannell, "Transitions between patterns in thermal convection," *Phys. Rev. Lett.*, vol. 67, pp. 3078–3081, 1991.

[145] W. L. Bragg, "The structure of some crystals as indicated by their diffraction of x-rays," *Proc. R. Soc. London, Ser. A*, vol. 89, no. 610, pp. 248–277, 1913.

[146] W. H. Bragg and W. L. Bragg, "The Structure of the Diamond," *Nature*, vol. 91, p. 557, 1913.

[147] N. Grigorieff and S. C. Harrison, "Near-atomic resolution reconstructions of icosahedral viruses from electron cryo-microscopy," *Curr. Opin. Struct. Biol.*, vol. 21, no. 2, pp. 265 – 273, 2011.

[148] F. C. Frank, "Supercooling of liquids," *Proc. R. Soc. London, Ser. A*, vol. 215, no. 1120, pp. 43–46, 1952.

[149] J. D. Bernal, "Geometry of the structure of monatomic liquids," *Nature*, vol. 185, no. 4706, pp. 68–70, 1960.

[150] P. J. Steinhardt, D. R. Nelson, and M. Ronchetti, "Bond-orientational order in liquids and glasses," *Phys. Rev. B*, vol. 28, pp. 784–805, 1983.

[151] B. Lengeler, "Coherence in x-ray physics," *Naturwissenschaften*, vol. 88, pp. 249–260, 2001.

[152] P. Wochner, C. Gutt, T. Autenrieth, T. Demmer, V. Bugaev, A. D. Ortiz, A. Duri, F. Zontone, G. Grübel, and H. Dosch, "X-ray cross correlation analysis uncovers hidden local symmetries in disordered matter," *Proc. Natl. Acad. Sci.*, vol. 106, no. 28, pp. 11511–11514, 2009.

[153] A. Tripathi, J. Mohanty, S. H. Dietze, O. G. Shpyrko, E. Shipton, E. E. Fullerton, S. S. Kim, and I. McNulty, "Dichroic coherent diffractive imaging," *Proc. Natl. Acad. Sci.*, 2011.

[154] J. D. Jackson, *Classical electrodynamics*. New York: Wiley, 3rd ed., 1999.

[155] L. R. Elias, W. M. Fairbank, J. M. J. Madey, H. A. Schwettman, and T. I. Smith, "Observation of stimulated emission of radiation by relativistic electrons in a spatially periodic transverse magnetic field," *Phys. Rev. Lett.*, vol. 36, pp. 717–720, Mar 1976.

[156] P. Luchini and H. Motz, *Undulators and free-electron lasers*. Oxford: Clarendon Press ; Oxford University Press, 1990.